



UNIL | Université de Lausanne

Unicentre

CH-1015 Lausanne

<http://serval.unil.ch>

---

*Year : 2023*

## Nutritional and pharmacological strategies to limit Ischemia-Reperfusion Injury.

Agius Thomas

Agius Thomas, 2023, Nutritional and pharmacological strategies to limit Ischemia-Reperfusion Injury.

Originally published at : Thesis, University of Lausanne

Posted at the University of Lausanne Open Archive <http://serval.unil.ch>

Document URN : urn:nbn:ch:serval-BIB\_EFE474743B088

### **Droits d'auteur**

L'Université de Lausanne attire expressément l'attention des utilisateurs sur le fait que tous les documents publiés dans l'Archive SERVAL sont protégés par le droit d'auteur, conformément à la loi fédérale sur le droit d'auteur et les droits voisins (LDA). A ce titre, il est indispensable d'obtenir le consentement préalable de l'auteur et/ou de l'éditeur avant toute utilisation d'une oeuvre ou d'une partie d'une oeuvre ne relevant pas d'une utilisation à des fins personnelles au sens de la LDA (art. 19, al. 1 lettre a). A défaut, tout contrevenant s'expose aux sanctions prévues par cette loi. Nous déclinons toute responsabilité en la matière.

### **Copyright**

The University of Lausanne expressly draws the attention of users to the fact that all documents published in the SERVAL Archive are protected by copyright in accordance with federal law on copyright and similar rights (LDA). Accordingly it is indispensable to obtain prior consent from the author and/or publisher before any use of a work or part of a work for purposes other than personal use within the meaning of LDA (art. 19, para. 1 letter a). Failure to do so will expose offenders to the sanctions laid down by this law. We accept no liability in this respect.



**UNIL** | Université de Lausanne

Faculté de biologie  
et de médecine

Département de Chirurgie Vasculaire, CHUV

# **Nutritional and pharmacological strategies to limit Ischemia-Reperfusion Injury.**

**Thèse de doctorat ès sciences de la vie (PhD)**

présentée à la

Faculté de biologie et de médecine  
de l'Université de Lausanne

par

**Thomas AGIUS**

Biologiste diplômé ou Master de l'Université de Toulouse III Paul  
Sabatier.

## **Jury**

Prof. Alban Denys, Président  
Dr. Sébastien Déglise, Directeur de thèse  
Dr. Alban Longchamp, Co-directeur de thèse  
Prof. Déla Golshayan, Experte  
Dr. Korkut Uygun, Expert

Lausanne  
(2023)





**UNIL** | Université de Lausanne

Faculté de biologie  
et de médecine

Département de Chirurgie Vasculaire, CHUV

# **Nutritional and pharmacological strategies to limit Ischemia-Reperfusion Injury.**

**Thèse de doctorat ès sciences de la vie (PhD)**

présentée à la

Faculté de biologie et de médecine  
de l'Université de Lausanne

par

**Thomas AGIUS**

Biologiste diplômé ou Master de l'Université de Toulouse III Paul  
Sabatier.

## **Jury**

Prof. Alban Denys, Président  
Dr. Sébastien Déglise, Directeur de thèse  
Dr. Alban Longchamp, Co-directeur de thèse  
Prof. Déla Golshayan, Experte  
Dr. Korkut Uygun, Expert

Lausanne  
(2023)

# Imprimatur

Vu le rapport présenté par le jury d'examen, composé de

|                                 |          |       |           |                  |
|---------------------------------|----------|-------|-----------|------------------|
| <b>Président·e</b>              | Monsieur | Prof. | Alban     | <b>Denys</b>     |
| <b>Directeur·trice de thèse</b> | Monsieur | Dr    | Sébastien | <b>Dégli</b>     |
| <b>Co-directeur·trice</b>       | Monsieur | Dr    | Alban     | <b>Longchamp</b> |
| <b>Expert·e·s</b>               | Madame   | Prof. | Déla      | <b>Golshayan</b> |
|                                 | Monsieur | Dr    | Korkut    | <b>Uygun</b>     |

le Conseil de Faculté autorise l'impression de la thèse de

## **Thomas Paul Agius**

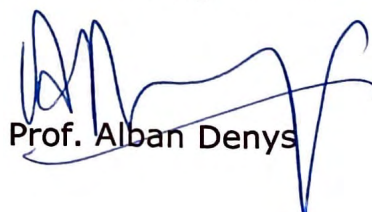
Master de Sciences, technologies, santé, mention biologie-santé, Université Paul Sabatier /  
Toulouse III, France

intitulée

## **Nutritional and pharmacological strategies to limit ischemia-reperfusion injury**

Lausanne, le 29 janvier 2024

pour le Doyen  
de la Faculté de biologie et de médecine



Prof. Alban Denys



# TABLE OF CONTENTS

|  |            |
|--|------------|
| <b>ACKNOWLEDGMENTS</b> .....   | <b>4</b>   |
| <b>ABSTRACT</b> .....  | <b>6</b>   |
| <b>RESUME</b> .....  | <b>7</b>   |
| <b>LIST OF ABBREVIATIONS</b> .....   | <b>8</b>   |
| <b>INTRODUCTION</b> .....  | <b>9</b>   |
| ORGAN SHORTAGE AND MARGINAL GRAFTS TRANSPLANT .....  | 9          |
| ISCHEMIA-REPERFUSION INJURY .....  | 9          |
| DIETARY PRECONDITIONING TO LIMIT ISCHEMIA-REPERFUSION INJURY .....   | 11         |
| HYDROGEN SULFIDE .....   | 13         |
| ACUTE KIDNEY INJURY AND DELAYED GRAFT FUNCTION .....   | 15         |
| THE STRESS OF MAJOR SURGERY .....  | 16         |
| TRANSLATIONAL STRATEGIES TO LIMIT SURGICAL STRESS .....  | 17         |
| ENHANCED RECOVERY AFTER SURGERY .....  | 18         |
| <b>REFERENCES</b> .....  | <b>20</b>  |
| <b>AIM OF THE STUDY</b> .....  | <b>27</b>  |
| <b>RESULTS</b> .....   | <b>29</b>  |
| CHAPTER 1: SUBNORMOTHERMIC EX VIVO PORCINE KIDNEY PERFUSION IMPROVES ENERGY METABOLISM:<br>ANALYSIS USING <sup>31</sup> P MAGNETIC RESONANCE SPECTROSCOPIC IMAGING ..... | 29         |
| CHAPTER 2: SODIUM HYDROSULFIDE TREATMENT DURING PORCINE KIDNEY EX VIVO PERFUSION AND<br>TRANSPLANTATION .....  | 42         |
| CHAPTER 3: SHORT-TERM HYPERCALORIC CARBOHYDRATE LOADING INCREASES SURGICAL STRESS<br>RESILIENCE BY INDUCING FGF21 .....  | 51         |
| <b>CONCLUSIONS</b> .....   | <b>86</b>  |
| <b>FUTURE DIRECTIONS</b> .....   | <b>90</b>  |
| BIOMARKERS OF ORGAN VIABILITY PRIOR TO TRANSPLANTATION .....   | 90         |
| IMPROVING ORGAN PRESERVATION .....   | 91         |
| TARGET IGF-1 TO REDUCE IRI .....   | 93         |
| UNDERSTAND IRI IN THE CONTEXT OF AGING .....   | 94         |
| <b>APPENDIXES</b> .....  | <b>102</b> |



## ACKNOWLEDGMENTS

I am deeply grateful to the jury, Prof. A. Denys, Dr. A. Longchamp, Dr. S. Déglise, Prof. D. Golshayan, and Prof. K. Uygun, who contributed and evaluated this work by providing their expertise and guidance throughout my thesis journey.

When I first joined the Laboratory of vascular surgery in 2019, I could never have imagined being where I am today. This would never have been possible without Dr. Alban Longchamp, who, beyond being an excellent mentor, guided and supported me both morally and financially throughout my thesis. Alban offered me incredible professional opportunities by initiating collaborations with outstanding scientists who taught me a lot and helped me grow as a young researcher. With an insatiable passion for research, he always knew how to resparkle my motivation during difficult times. By the end of 2022, he convinced me to follow him on his quest to the USA. Thanks to him, I was able to join one of the best environments in the world for pursuing impactful science and to meet inspiring scientists who excel in their fields. To me, he was not just an excellent mentor but also a good friend with whom I shared great moments (Hello to Tim and Justine) exploring Switzerland and the US.

I would also like to thank Prof. F. Lazeyras, without whom, this would have been impossible. Beyond being an exceptional collaborator I've had the privilege to work with, he has consistently provided financial and scientific support for our joint projects. I am grateful to everyone at Prof. Lazeyras' lab in Geneva: Julien, Jean-Pierre, and Raphael. Thank you for the long hours and weekends sacrificed for the MRI acquisitions and perfusions; without you, our fruitful collaboration would never have been as successful.

I would also like to express my gratitude to Professor K. Uygun, who welcomed me into his lab at Massachusetts General Hospital and Harvard with open arms and provided support and guidance from the moment I arrived in Boston. I had the opportunity to explore and learn the joy of organ perfusion engineering and cryopreservation. Beyond being an exceptional researcher, I was fortunate to encounter an incredibly kind person and a professional model. I have been lucky enough to connect and collaborate with outstanding scientists and colleagues who have become friends over time. Mo, Mclean, Irina, and Sila, thank you for sharing your expertise and collaborating with me. And Alexi, thank you for all our great times, releasing stress and playing childish games across the room during long working days. Laura, Maeva, and Yanis, thank you for bringing a little bit of France to Boston. Without you, I would have missed home even more.

Huge thanks to the members of the vascular surgery lab in Lausanne. Thank you, Florent, for spending so many hours training me and sharing your passion for science. Martine and Séverine, thank you for sharing your experience and advice, our motorcycle discussions, and recommending wonderful things to explore in Switzerland. And to my fellow Ph.D. students, but most importantly, my friends Kevin, Arnaud, Tania, Clémence, and Diane. Without you, my thesis wouldn't be what it is today. All the adventures we've had together, the laughs, the afterwork gatherings and beers, and the weekends exploring Switzerland made me realize that I didn't just find a Ph.D. program when I came to Lausanne, but also lifelong friendships too. Thank you!

I would like to thank my parents, Christine and Paul Agius, and my sister Julie. They have always been there to support me throughout my life and have always believed in me. My family has provided me with happiness, education, and culture, shaping me into a thoughtful and well-educated individual. I can never thank them enough for everything they have done for me.

Thank you to my girlfriend, Pia. You've always been there to keep me entertained and remind me to enjoy life when I've been working too much. Thank you for taking me to the other side of the world. Thank you for being there during tough times, for being understanding, and for giving me your time and moral support when I needed it the most.

## ABSTRACT

During transplantation, and more broadly during surgery, there's an urgent need to reduce ischemia-reperfusion (IR), improve graft outcomes, and ease recovery. During my thesis, we 1. optimized kidney graft preservation temperature and perfusate composition (including molecules such as hydrogen sulfide) 2. Identified novel biomarkers of graft viability 3. Examine the effects of carbohydrate loading before surgery to reduce IR injury (IRI).

In the first part, we hypothesized that kidney perfusion at subnormothermic temperature (22°C) might improve kidney mitochondrial function and viability and limit IRI. Indeed, kidney perfusion at 22°C improved cortical and medullary perfusion and reduced histological lesions after transplantation compared to 4°C. In addition, total adenosine triphosphate (ATP) content was 4 times higher during ex vivo perfusion at 22 °C than at 4 °C. Recent improvements in the detection and measurement of ATP have rendered it a reliable and valuable indicator of graft viability, capable of predicting immediate graft function. Interestingly, the addition of sodium hydrosulfide (NaHS) in the perfusate, previously shown to protect against renal IRI in several models of IR and during cold preservation before transplantation in rodents, did not affect porcine kidney graft function.

Lastly, we tested whether carbohydrate-rich drinks (part of a multimodal perioperative care pathway) could increase resistance to IRI / surgical stress. Despite widespread clinical use, preclinical and mechanistic studies on carbohydrate loading in surgical contexts are lacking. Here, we investigated the effects of carbohydrate loading, aiming to understand how it can influence post-operative recovery in multiple rodent models of IRI. Here we demonstrated in ad libitum-fed mice that liquid carbohydrate loading for 1 week reduces solid food intake while nearly doubling total caloric intake. Carbohydrate loading-induced protein dilution increased expression of hepatic fibroblast growth factor 21 (FGF21), resulting in protection in two models of surgical stress: renal and hepatic IRI. The protection was consistent across sex and age and was associated with the induction of the canonical integrated stress response (ATF3/4, NFkB) and oxidative metabolism (PPAR $\gamma$ ). Together, these data support carbohydrate loading drinks before acute surgical stress and reveal an essential role of protein dilution via FGF21.



## RESUME

Lors des transplantations, et plus largement pendant les chirurgies, il est urgent de réduire l'ischémie-reperfusion (IR), d'améliorer les résultats des greffes et de faciliter la récupération. Durant ma thèse, nous avons 1. Optimisé la température de conservation des greffes rénales et la composition du perfusat (incluant des molécules comme le sulfure d'hydrogène) 2. Identifié de nouveaux biomarqueurs de viabilité de la greffe 3. Examiné les effets d'une charge glucidique avant la chirurgie pour réduire les lésions d'ischémie-reperfusion (IRI).

Dans la première partie, nous avons émis l'hypothèse qu'une perfusion rénale à une température subnormothermique (22°C) pourrait améliorer la fonction mitochondriale et la viabilité du rein et limiter l'IRI. En effet, la perfusion rénale à 22°C a amélioré la perfusion corticale et médullaire et réduit les lésions histologiques après transplantation par rapport à 4°C. De plus, le contenu total en adénosine triphosphate (ATP) était 4 fois plus élevé lors de la perfusion ex vivo à 22°C qu'à 4°C. Les récentes avancées dans la détection et la mesure de l'ATP en ont fait un indicateur fiable de la viabilité de la greffe, capable de prédire une fonction immédiate du greffon. De façon intrigante, l'ajout de sodium hydrosulfide (NaHS) au perfusat, montré auparavant comme protecteur contre l'IRI rénal dans plusieurs modèles d'IR et pendant la conservation à froid avant transplantation chez les rongeurs, n'a pas affecté la fonction du greffon chez le cochon.

Enfin, nous avons testé si des boissons riches en glucides (intégrées dans un protocole périopératoire multimodal) pouvaient augmenter la résistance à l'IRI/au stress chirurgical. Malgré leur usage clinique courant, peu d'études précliniques se penchent sur ces charges en glucides. Nous avons analysé leurs effets. Chez des souris nourries à volonté, l'ajout d'une boisson riche en glucides pendant 1 semaine réduisait l'apport en nourriture solide tout en doublant presque la prise calorique totale. Cette surcharge glucidique induisait une dilution protéique, augmentant l'expression du facteur de croissance hépatique fibroblast growth factor 21 (FGF21), offrant une protection lors de deux modèles de stress chirurgical : IRI rénale et hépatique. La protection était cohérente quel que soit le sexe ou l'âge, associée à l'induction d'une réponse au stress (via ATF3/4, NFkB) et au métabolisme oxydatif (PPAR $\gamma$ ). Ces données soutiennent l'usage de boissons chargées en glucides avant un stress chirurgical et mettent en lumière le rôle crucial de la dilution protéique via FGF21.

## LIST OF ABBREVIATIONS

|                  |  |
|------------------|--|
| ACE              | Angiotensin-Converting Enzyme                      |
| AKI              | Acute Kidney Injury                                |
| AMP              | Adenosine Monophosphate                            |
| ATP              | Adenosine Triphosphate                             |
| ATN              | Acute Tubular Necrosis                             |
| BHMT             | Betaine Homocysteine Methyltransferase             |
| CBS              | Cystathionine Beta-Synthase                        |
| CGL              | Cystathionine Gamma-Lyase                          |
| CKD              | Chronic Kidney Disease                             |
| COXII            | Cyclooxygenase II                                  |
| DCD              | Donation after Circulatory Death                   |
| DBD              | Donation after Brain Death                         |
| DGF              | Delayed Graft Function                             |
| DR               | Dietary Restriction                                |
| ECD              | Extended-Criteria Donors                           |
| ERAS             | Enhanced Recovery After Surgery                    |
| ESRD             | End-Stage Renal Disease                            |
| Gd               | Gadolinium   |
| GFR              | Glomerular Filtration Rate                         |
| GSH              | Glutathione  |
| H <sub>2</sub> S | Hydrogen Sulfide                                   |
| HOPE             | Hypothermic Oxygenated Perfusion                   |
| IRI              | Ischemia-Reperfusion Injury                        |
| MAT              | Methionine Adenosyl Transferase                    |
| MRI              | Magnetic Resonance Imaging                         |
| MS               | Methionine Synthase                                |
| mPTP             | Mitochondrial Permeability Transition Pore         |
| NADH             | Nicotinamide Adenine Dinucleotide (Reduced)        |
| NAD <sup>+</sup> | Nicotinamide Adenine Dinucleotide (Oxidized)       |
| NaHS             | Sodium Hydrogen Sulfide                            |
| NSAIDs           | Non-Steroidal Anti-Inflammatory Drugs              |
| OxPhos           | Oxidative Phosphorylation                          |
| pMRSI            | Phosphorus Magnetic Resonance Spectroscopy Imaging |
| PME              | Phosphomonoesters                                  |
| Pi               | Inorganic Phosphate                                |
| ROS              | Reactive Oxygen Species                            |
| SAM              | S-Adenosylmethionine                               |
| SAH              | S-Adenosylhomocysteine                             |
| SAHH             | S-Adenosylhomocysteine Hydrolase                   |
| Taurine          | Taurine  |

# INTRODUCTION

## Organ shortage and marginal grafts transplant

Transplantation is the preferred treatment for end-stage disease, but it suffers from a severe shortage of available organs. Approximately 34 000 patients are added to the US waiting list every year, while only 20 000 kidney transplants are performed over the same period (survival of >80% at 5 years). The situation is especially concerning regarding end-stage renal disease (ESRD) since it affects at least two million and 750 000 patients worldwide in the United States<sup>1</sup>. For the most part, dialysis and low survival are the only remaining options for ESRD patients, whose 5-year survival rate is between 40% and 50% and is approximately 10 times more expensive than a transplant<sup>2</sup>.

To face this shortage, the donor pool was expanded beyond standard-criteria donors to include extended-criteria donors (ECD) and donation after circulatory death (DCD) donors<sup>3,4</sup>. ECD donor is defined as anyone over the age of 60 or over 50, with two of the following: a history of high blood pressure, a creatinine level greater than or equal to 1.5, or death because of a stroke<sup>5</sup>. Although organs from these donors allow a higher survival rate than dialysis, their use is complicated by an increased rate of delayed graft function (DGF)<sup>6</sup> and acute rejection<sup>7</sup>. During the transplantation procedure, the organs are subjected to several stresses, including surgical acts, such as inflammation, and all the stresses associated with ischemia-reperfusion injury (IRI). Unfortunately, DCD organs are particularly vulnerable to IRI and are at risk of transplant failure and subsequent poor long-term survival<sup>2,7</sup>.

## Ischemia-Reperfusion Injury

Ischemia-reperfusion injury involves the occlusion of blood flow to an organ or tissue for a certain period of time (ischemia) and subsequent restoration of blood supply (reperfusion)<sup>8</sup>. IRI represents a primary clinical concern in controlled elective surgery, which requires temporary restriction of blood flow (e.g., solid organ transplantation, vascular surgery) and uncontrolled settings (stroke, heart attack, limb trauma). IRI increases the probability of delayed graft function, acute graft rejection, and graft loss<sup>9,10</sup>. The current consensus is that the duration of ischemia greater than 30 minutes in the human kidney<sup>6</sup> primes the tissue for further injury upon reperfusion. Ischemic cells will die if blood flow is not restored, even though most damage occurs during reperfusion.

Mechanistically, ischemia leads to Adenosine Triphosphate (ATP) depletion, inhibition of mitochondrial Na<sup>+</sup>/K<sup>+</sup> ion channels, resulting in decreased mitochondrial membrane potential ( $\Delta\psi_m$ ), increased mitochondrial inner membrane permeability, influx of calcium ions, and subsequent swelling of mitochondria. Inner membrane permeability leads to alteration of the “redox state” by oxidation of pyridines and thiols and with the modification of the reduced/oxidized Nicotinamide Adenine Dinucleotide (NADH/NAD<sup>+</sup>) and Glutathione (GSH/GSSG) ratio<sup>11-13</sup>. Ischemia further affects the mitochondrial antioxidant system by decreasing the activity of antioxidant enzymes, such as mitochondrial antioxidant manganese superoxide dismutase (MnSOD)<sup>14</sup>, and/or depleting substrates, such as GSH, which render cells more susceptible to oxidative stress at reperfusion<sup>15-17</sup>. Anaerobic metabolism during ischemia also leads to the accumulation of lactic acid and the citric acid cycle intermediate succinate<sup>18</sup>.

Reperfusion is characterized by a further increased formation of reactive oxygen species (ROS), decreased ATP production, and cell death. The reintroduction of O<sub>2</sub> at reperfusion may lead to significant production of ROS. GSH depletion worsens the oxidation of thiols and hydroxyl radical (OH<sup>•-</sup>) formation<sup>18</sup> (Figure 1). ROS produced at reperfusion may also damage proteins, lipids, and DNA. This leads to further mitochondrial disruption, sterile immune activation<sup>19-23</sup>, and necrotic interaction of a dysfunctional respiratory chain with oxygen during reperfusion<sup>23-26</sup>. Recent work showed that at reperfusion, the accumulated succinate during ischemia is rapidly re-oxidized by succinate dehydrogenase, driving extensive ROS generation by reverse electron transport at mitochondrial complex I<sup>18</sup>. Significantly, mitochondrial ROS drives acute damage and initiates the pathology that develops over the minutes, days, and weeks following reperfusion<sup>25</sup>.

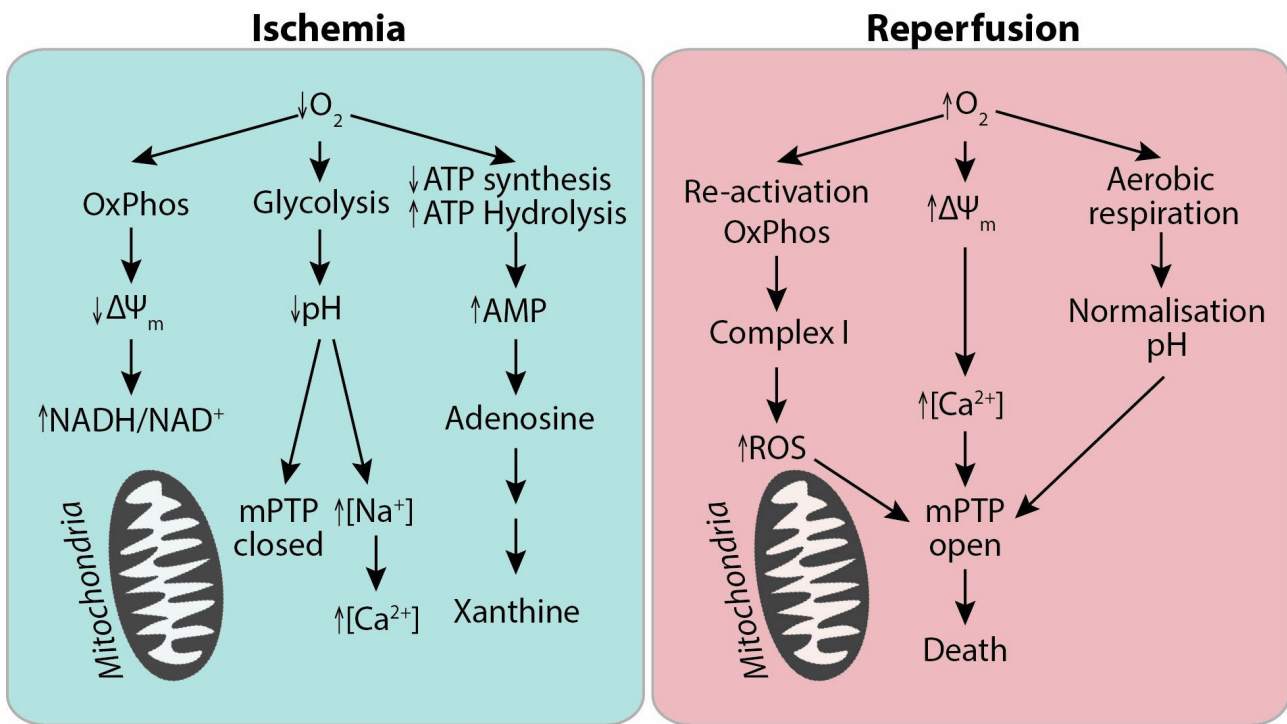


**Figure 1. Schematic illustrating the main component of IRI.** During ischemia, the lack of oxygen causes a switch to anaerobic respiration, resulting in the production of lactate and a drop in intracellular pH. This disrupts ion haemostasis resulting in  $\text{Na}^+$  and  $\text{Ca}^{2+}$  overload. The low pH also prevents the opening of the mPTP. Oxidative phosphorylation is inhibited, and  $\text{NADH}/\text{NAD}^+$  ratio increases. ATP stores are depleted as ATP is hydrolysed to AMP by ATP synthase to maintain  $\Delta\psi_m$ . During reperfusion, the electron transport chain is re-activated and restored resulting in the normalization of intracellular pH and  $\Delta\psi_m$  and a large influx of  $\text{Ca}^{2+}$  into the mitochondrion. Complex I is rapidly reactivated, resulting in a large burst of ROS. Opening of the mPTP is induced resulting in the collapse of the  $\Delta\psi_m$ , the triggering of cell death. OxPhoS, oxidative phosphorylation;  $\Delta\psi_m$ , mitochondrial membrane potential. Figure and legend adapted from Pell VR et al., *Cardiovasc Res* 2016.

## Dietary Preconditioning to limit Ischemia-Reperfusion Injury

Clive McCay, in 1935, described dietary restriction (DR) as reduced nutrient intake without malnutrition<sup>27</sup>. DR encompasses decreased daily caloric intake, removing or rebalancing specific macronutrients, such as amino acids, and/or intermittent fasting. Primarily studied for anti-aging interventions, DR extends both the lifespan and healthspan of laboratory rats<sup>27-29</sup>. Since then, longevity extension by DR has been established in various experimental organisms, from yeast to nonhuman primates<sup>28</sup>. DR is expected to increase longevity by slowing aging, making it an essential tool in aging research. However, because long-term adhesion is required for maximum lifespan extension, antigeronic clinical applications have been challenging due to long-term voluntary food restriction<sup>30,31</sup>. In addition to defending against aging-related diseases, DR offers stress resistance and metabolic fitness<sup>32-35</sup>. Short-term DR (2 days to 1 week) effectively protects against various acute stressors. Notably, short-term DR or fasting prior to surgery, with a return to normal food

intake post-surgery, improves recovery outcomes in mouse models. This encompasses surgical stress scenarios, from IRI to vascular restenosis (intimal hyperplasia)<sup>36-40</sup>.

From a nutritional standpoint, many of the pleiotropic benefits of calorie restriction can be triggered by dietary protein restriction or single amino acids<sup>41</sup>. These benefits include resistance to hepatic IRI<sup>42</sup>, improved recovery upon acute limb ischemia<sup>43</sup>, increased energy expenditure<sup>44</sup>, and improved glucose and lipid homeostasis, even during short-term interventions (Figure 3)<sup>45-47</sup>. This is a significant distinction when considering clinical translational potential, due to the difficulties inherent in enforcing food restriction, even for short periods of time. It is also worth noting that even when subjected to the same injury, different organs may require different levels of protection. In the renal IRI model, for example, protein and calorie restriction contribute additively to organ protection<sup>36</sup>, but protein restriction alone contributes disproportionately to organ protection against hepatic IRI<sup>48</sup>. Much more research is needed in the future to establish the ideal balance of calories from protein vs. sugar and fat, as well as overall calorie intake, for optimal stress resistance, which will likely depend on the specific surgery and patient-specific risk factors.

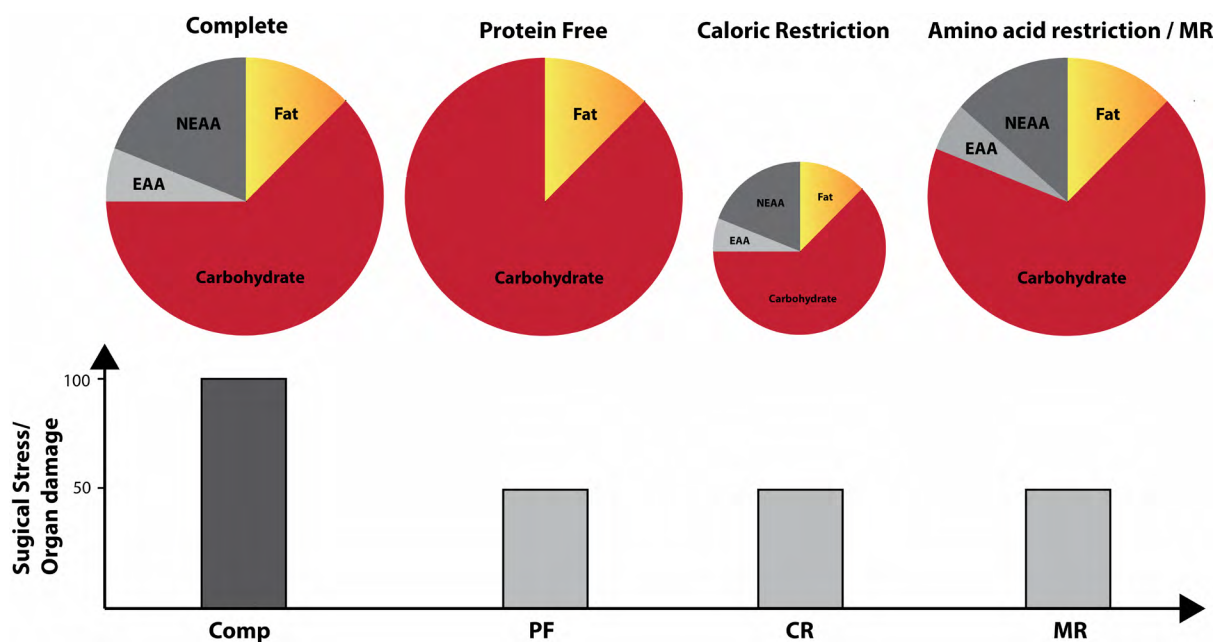


**Figure 3.** Schematic of diets in which 18% of calories are contributed by protein (complete), sucrose (PF), NEAAs (NEAA only), or EAAs (EAA only, top). Mice preconditioned with these diets were protected against various form of surgical stress (bottom), including ischemia reperfusion injury to the heart, brain, liver, kidney or limbs.

## Hydrogen Sulfide

Hydrogen sulfide (H<sub>2</sub>S) is an endogenous gaseous molecule characterized by its distinct rotten egg odor. H<sub>2</sub>S is historically classified as an environmental and occupational hazard due to its inhibition of mitochondrial respiration and lethality when exposed to high dose<sup>49,50</sup>. However, in the later part of the 20<sup>th</sup> and early part of the 21<sup>st</sup> centuries, functional and beneficial endogenous production of H<sub>2</sub>S, principally produced by cystathionine gamma-lyase (CGL or CTH), and cystathionine beta-synthase (CBS, [Figure 4](#))<sup>43,51</sup>, was discovered acting as a critical signaling molecule in various physiological functions, from vascular actions to its role in the brain<sup>52-54</sup>. It has been demonstrated that H<sub>2</sub>S reduces blood pressure<sup>55</sup>, prevents neurodegeneration<sup>56</sup>, and even increases the lifespan of worms<sup>57</sup>. In addition, it can induce a hibernation-like state in mammals<sup>58</sup> and has various cardiovascular effects in vitro and in vivo, such as a reduction in intimal hyperplasia<sup>59</sup>, anti-atherosclerotic activity<sup>60</sup>, and a diminution in neutrophil binding to blood vessel walls<sup>61</sup>.

It's noteworthy that H<sub>2</sub>S, either as a gas or through donor molecules, increases lifespan in model organisms<sup>57</sup>, prevents multi-tissue ischemic-reperfusion injury<sup>42,62</sup>, and improves cardiovascular health<sup>55,63</sup>. In contrast, endogenous H<sub>2</sub>S concentrations or production deficiencies correlate with and/or cause hypertension<sup>55</sup>. In contrast, during IRI, the genetic

deletion of CGL exacerbates damage and mortality in rodents with post-renal ischemia-reperfusion injury and eliminates DR protective effects<sup>42</sup>. However, both phenotypes can be rescued by delivering exogenous H<sub>2</sub>S (NaHS), notably in wild-type mice. Exogenous NaHS mitigated hepatic and renal ischemia-reperfusion injury<sup>42,64</sup>. This suggests that multiple DR benefits could be attributed to endogenous H<sub>2</sub>S gas produced in response to nutrient/energy scarcity. The exact role of free H<sub>2</sub>S as a paracrine or autocrine molecule remains under discussion<sup>65</sup>. However, H<sub>2</sub>S possesses antioxidant properties and could contribute to mitochondrial energy by giving electrons to the SQR protein in the mitochondrial electron transport chain, which could play a role in protecting against organ ischemia<sup>66</sup>.

Consequently, the field of H<sub>2</sub>S in biology, physiology, and medicine has expanded rapidly<sup>67</sup>, with endogenous H<sub>2</sub>S or the delivery of exogenous H<sub>2</sub>S with donor molecules serving as a therapeutic target, and the third functional gasotransmitter, in addition to carbon monoxide and nitric oxide<sup>68</sup>.

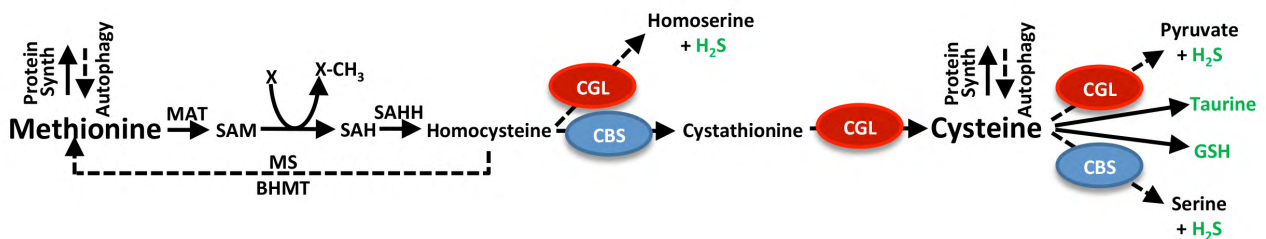


**Figure 4.** Model of the transmethylation and transsulfuration pathway (TSP). Arrows trace sulfur from Methionine to Cysteine through various metabolites and downstream cellular processes via the enzymes Cystathionine Beta-Synthase (CBS) and Cystathionine Gamma-Lyase (CGL). Metabolites in green (taurine, GSH and H<sub>2</sub>S) have demonstrated potential to protect against IRI. MAT: methionine adenosyl transferase, SAM: S-Adenosylmethionine, SAH: S-Adenosylhomocysteine, SAHH: S-adenosylhomocysteine hydrolase, MS: Methionine synthase, BHMT: Betaine homocysteine methyltransferase. Picture and Legend from Hine et al, Cell 2015.



## Acute Kidney Injury and Delayed Graft Function

Acute kidney injury (AKI) underlies a heterogeneous group of injuries, including transplantation, partial nephrectomy, shock, cardiac surgery, and vascular surgery<sup>69</sup>. AKI is defined as a rise in creatinine of  $\geq 50\%$  from its baseline value, and/or a fall in the glomerular filtration rate (GFR) by  $\geq 25\%$ , and/or a decrease in urine output below 0.5ml/kg/h for 6h or more. The acute element of the definition of AKI requires that creatinine rises within a specified time frame. RIFLE required the  $\geq 50\%$  rise was known or presumed to have developed over  $\leq 7$  days<sup>70</sup>. AKI affects more than 15 per 1000 people over the age of 65 in the United States in 2011, and 20% of hospitalized patients. In addition, the prevalence is

increasing significantly with age<sup>1</sup>.

Evidence also suggests that even mild forms of AKI (such as a 50% increase in serum creatinine) are associated with an increased risk of hospital mortality<sup>71,72</sup>.

Additionally, although AKI is considered reversible, patients who have recovered from AKI have a 25% increased risk of developing progressive chronic kidney disease (CKD) and even ESRD<sup>73</sup>.

At the onset of AKI, assuming a single isolated insult to the kidneys, such as a defined period of ischemia, the actual GFR will drop rapidly to a nadir. Serum creatinine will then rise over hours to days. When AKI occurs

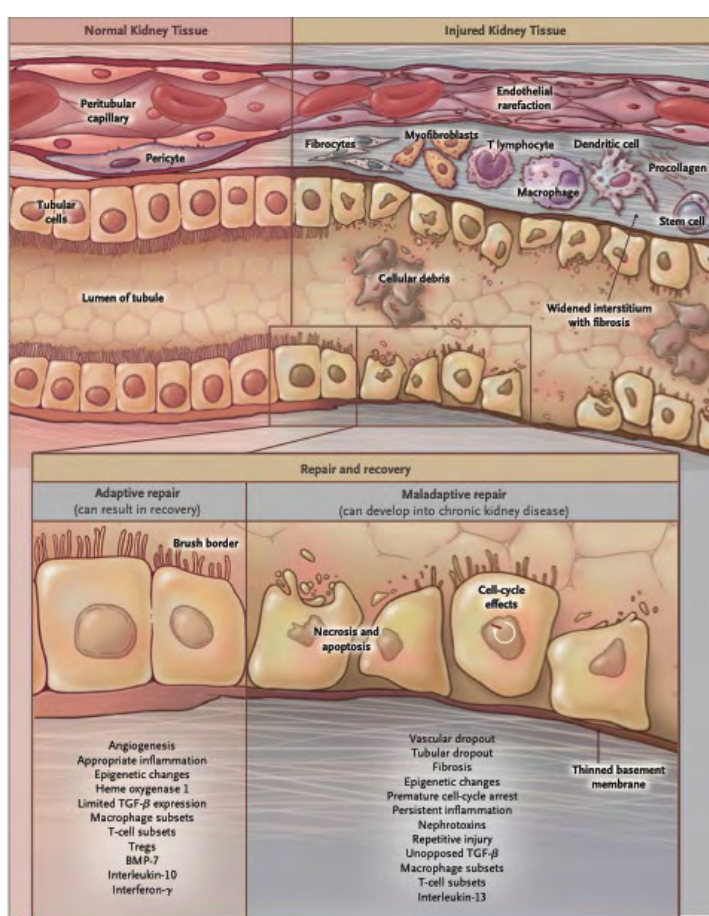


**Figure 5. Pathophysiological Feature of AKI.**

From NEJM 2014.

within the first week of kidney transplantation and necessitates dialysis, it is called DGF. The occurrence of DGF varies significantly among centers and according to donor types. In the US, DGF rates average 31% for deceased donors and range from 45-55% for DCDs<sup>74,75</sup>. The onset of DGF is associated with higher rates of acute cellular rejection and shorter graft survivals, where graft half-life is 3 to 5 years shorter<sup>75,76</sup>. The use of dialysis ranges anywhere from days to months and adds a significant cost impact to healthcare centers and patients<sup>77</sup>. It also

complicates post-transplant management of patients who need to maintain immunosuppressive therapy, specifically calcineurin inhibitors (CNI), which are associated with acute nephrotoxicity<sup>78</sup>.

AKI can affect many distinct cell types along the entire length of the nephron, resulting in various injuries. Tubulointerstitial fibrosis, particularly in the inner cortical and outer medullary regions, is the most common disease associated with AKI. Less often, AKI induces glomerular injury<sup>79</sup>. Although mildly damaged tubules restore normal structure and function following AKI, a fraction remains dedifferentiated and continues to generate profibrotic and pro-inflammatory mediators<sup>80-82</sup>. The delayed recovery of such tubules is related to pathological processes initiated during AKI<sup>83-85</sup>. Cell-cycle mechanisms and mediators, such as heme oxygenase 1, hypoxia-inducible factors, vascular endothelial growth factor, and transforming growth factor  $\beta$ 1, have been identified as protective factors in acute kidney injury. Still, some also may contribute to chronic kidney disease. The chronic dysregulation of such factors and the complex interactions between their expression and counter-regulation over time may determine the character and extent of fibrotic responses ([Figure 2](#)). The roles of these factors and the roles of vasoactive mediators and mediators of progressive fibrosis, such as transforming growth factor  $\beta$ , are only beginning to be delineated in animal models. Sublethally injured cells failed to recover due to the loss of nephrons and subsequent tubulointerstitial fibrosis that occurs fast after AKI (e.g., 1–4 weeks after injury), resulting in the shift from AKI to CKD<sup>80</sup>. These mechanisms all can interact, synergistically accelerating loss of function. Many mechanisms implicated in developing and progressing chronic kidney disease and cardiovascular disease after conventional therapies may target an episode of acute kidney injury. Current clinical management is still based on patient risk assessment, such as age, co-morbidities, and current drug treatment, and minimizing the risk of AKI by providing supportive care, such as optimization of volume with crystalloid volume, blood pressure control, and removal of nephrotoxic drugs (NSAIDs, COXII or ACE inhibitors, etc.)<sup>86</sup>.

## **The stress of major surgery**

Surgery is an invasive medical intervention involving an incision, with major surgery typically describing procedures in which a body cavity is entered. Like many types of acute injury, surgery perturbs metabolic and immune homeostasis through effects on afferent (autonomic and sympathetic) nerve input from the area of trauma, leading to local and systemic catecholamine release, increased levels of pro-inflammatory acute phase reactants,

metabolic adaptations, including glycogen mobilization, and vascular changes including vasoconstriction and increased heart rate. Parallel activation of the hypothalamic-anterior pituitary-adrenomedullary axis promotes the release of cortisol from the adrenal cortex, resulting in a partially counterbalancing response characterized by protein and fat mobilization, immunosuppression, and dampening of the action of anabolic hormones such as insulin and testosterone<sup>87</sup>.

From an evolutionary standpoint, the selective advantage conferred by these coordinated stress responses is likely related to stopping hemorrhage and redirecting stored energy to immune function and tissue repair to promote survival following acute injury. However, in any surgical patient, such vasoconstrictive, pro-thrombotic, and pro-inflammatory responses can lead to IRI, leading to various complications, from renal dysfunction to life-threatening heart attack or stroke.

Beyond the local and tissue-specific consequences, IRI causes a systemic inflammatory response, activating circulating leukocytes and causing a pro-thrombotic state, possibly contributing to multi-organ dysfunction<sup>88,89</sup>. Surgery also carries the risk of complications specific to the procedure. Repairing aortic lesions involving the renal arteries, for example, increases the risk of renal failure (due to inflow artery cross-clamping), proportional to the ischemic time<sup>90</sup>. Surprisingly, while risk assessment is common practice in determining whether the benefits of a particular surgery outweigh the risks, interventional prophylactic approaches to reduce patient-based risk factors prior to surgery are not.

## **Translational strategies to limit surgical stress**

The importance of energy metabolism, by which living cells acquire and use the energy needed to stay alive during organ transplantation, has been duly acknowledged<sup>91</sup>. Consequently, current methods of organ preservation aim to preserve the energy machinery<sup>92</sup> and reduce the rate of energy depletion<sup>93</sup>. Once energy levels have fallen beyond a critical point, the resulting injury is irreversible<sup>94</sup>. Respiratory defects were identified as early events of injury during preservation<sup>94</sup> and after ischemia-reperfusion<sup>95</sup>. For example, in livers, ATP content correlates with transplant outcome<sup>96,97</sup>. Today, limiting IRI during renal transplantation involves essentially cold storage of kidneys in an optimized preservation solution during the peri-transplant / transport period<sup>98</sup>. However, these strategies have been maximized, and prolonged periods (>24 h) of cold ischemia are still associated with tubular necrosis (ATN), DGF, and poor graft survival, especially DCD grafts<sup>7,99-102</sup>. Thus, novel

strategies are required to protect these fragile organs from IRI and to ensure their sustainability during transplantation.

## Enhanced recovery after surgery

Enhanced recovery after surgery (ERAS) protocols increasingly use multimodal perioperative care pathways designed to achieve early recovery after surgical procedures. The critical components of ERAS protocols include preoperative counseling, optimization of nutrition, standardized analgesic and anesthetic regimens, and early mobilization<sup>103</sup>. Interestingly, pre-operative 12.6% oral carbohydrate loading is one cornerstone of ERAS (Figure 5). Carbohydrate loading practices vary among institutions, encompassing simple carbohydrates (e.g., Gatorade) and complex carbohydrates (e.g., maltodextrin), with multiple commercial preparations available<sup>104</sup>. Carbohydrate loading practices vary among institutions, encompassing simple carbohydrates (e.g., Gatorade) and complex carbohydrates (e.g., maltodextrin), with multiple commercial preparations available<sup>104</sup>. In the context of surgery, carbohydrate loading may reduce insulin resistance and improve recovery<sup>105</sup>, although the exact mechanisms are unknown. Several studies report shorter lengths of stay and a reduction in patient discomfort. However, within ERAS, carbohydrate loading benefits are confounded by numerous interventions (e.g., analgesia, early removal of catheters, thromboprophylaxis, etc.<sup>106</sup>), making it challenging to evaluate its efficacy.

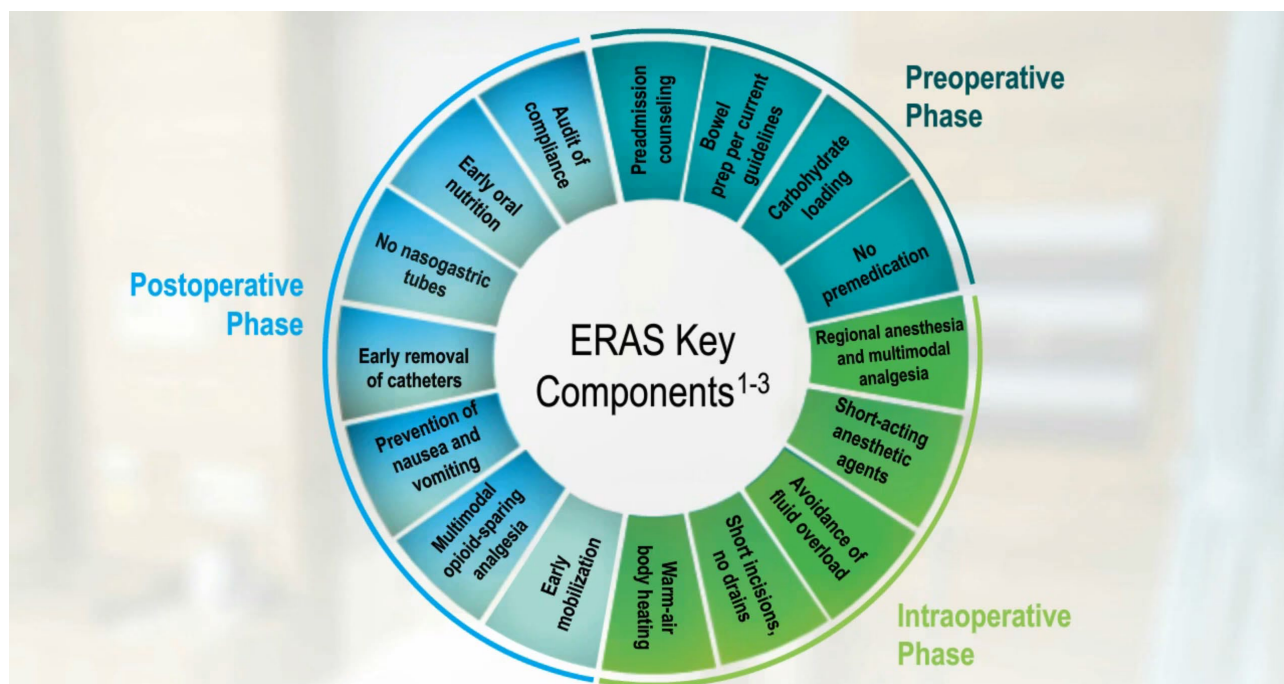


**Figure 6.** Key aspects of ERAS protocols. Adapted and modified from Melnyk Megan et al. *Can Urol Assoc J.* 2011 Oct;5(5):342-8. doi: 10.5489/cuaj.11002.

## REFERENCES

1. Collins, A.J., Foley, R.N., Chavers, B., Gilbertson, D., Herzog, C., Ishani, A., Johansen, K., Kasiske, B.L., Kutner, N., Liu, J., et al. (2014). US Renal Data System 2013 Annual Data Report. *Am J Kidney Dis* 63, A7. 10.1053/j.ajkd.2013.11.001.
2. Wu, W.K., Famure, O., Li, Y., and Kim, S.J. (2015). Delayed graft function and the risk of acute rejection in the modern era of kidney transplantation. *Kidney Int* 88, 851-858. 10.1038/ki.2015.190.
3. Zhao, H., Alam, A., Soo, A.P., George, A.J.T., and Ma, D. (2018). Ischemia-Reperfusion Injury Reduces Long Term Renal Graft Survival: Mechanism and Beyond. *EBioMedicine* 28, 31-42. 10.1016/j.ebiom.2018.01.025.
4. Ponticelli, C. (2014). Ischaemia-reperfusion injury: a major protagonist in kidney transplantation. *Nephrol Dial Transplant* 29, 1134-1140. 10.1093/ndt/gft488.
5. Ojo, A.O. (2005). Expanded criteria donors: process and outcomes. *Semin Dial* 18, 463-468. 10.1111/j.1525-139X.2005.00090.x.
6. Tennankore, K.K., Kim, S.J., Alwayn, I.P., and Kiberd, B.A. (2016). Prolonged warm ischemia time is associated with graft failure and mortality after kidney transplantation. *Kidney Int* 89, 648-658. 10.1016/j.kint.2015.09.002.
7. Dragan, D., Hoff, U., Park, J.K., Qun, Y., Schneider, W., Luft, F.C., and Haller, H. (2001). Prolonged cold preservation augments vascular injury independent of renal transplant immunogenicity and function. *Kidney Int* 60, 1173-1181. 10.1046/j.1523-1755.2001.0600031173.x.
8. Jaeschke, H. (2003). Molecular mechanisms of hepatic ischemia-reperfusion injury and preconditioning. *Am J Physiol Gastrointest Liver Physiol* 284, G15-26. 10.1152/ajpgi.00342.2002.
9. Ojo, A.O., Wolfe, R.A., Held, P.J., Port, F.K., and Schmouder, R.L. (1997). Delayed graft function: risk factors and implications for renal allograft survival. *Transplantation* 63, 968-974. 10.1097/00007890-199704150-00011.
10. Shoskes, D.A., and Halloran, P.F. (1996). Delayed graft function in renal transplantation: etiology, management and long-term significance. *J Urol* 155, 1831-1840. 10.1016/s0022-5347(01)66023-3.
11. Chouchani, E.T., Pell, V.R., James, A.M., Work, L.M., Saeb-Parsy, K., Frezza, C., Krieg, T., and Murphy, M.P. (2016). A Unifying Mechanism for Mitochondrial Superoxide Production during Ischemia-Reperfusion Injury. *Cell Metab* 23, 254-263. 10.1016/j.cmet.2015.12.009.
12. Lê-Quôc, D., and Lê-Quôc, K. (1989). Relationships between the NAD(P) redox state, fatty acid oxidation, and inner membrane permeability in rat liver mitochondria. *Arch Biochem Biophys* 273, 466-478. 10.1016/0003-9861(89)90506-7.
13. Pell, V.R., Chouchani, E.T., Frezza, C., Murphy, M.P., and Krieg, T. (2016). Succinate metabolism: a new therapeutic target for myocardial reperfusion injury. *Cardiovasc Res* 111, 134-141. 10.1093/cvr/cvw100.
14. Perrelli, M.G., Pagliaro, P., and Penna, C. (2011). Ischemia/reperfusion injury and cardioprotective mechanisms: Role of mitochondria and reactive oxygen species. *World J Cardiol* 3, 186-200. 10.4330/wjc.v3.i6.186.
15. Halestrap, A.P., Clarke, S.J., and Javadov, S.A. (2004). Mitochondrial permeability transition pore opening during myocardial reperfusion--a target for cardioprotection. *Cardiovasc Res* 61, 372-385. 10.1016/S0008-6363(03)00533-9.
16. Kotlyar, A.B., and Vinogradov, A.D. (1990). Slow active/inactive transition of the mitochondrial NADH-ubiquinone reductase. *Biochim Biophys Acta* 1019, 151-158. 10.1016/0005-2728(90)90137-s.

17. Zweier, J.L., Flaherty, J.T., and Weisfeldt, M.L. (1987). Direct measurement of free radical generation following reperfusion of ischemic myocardium. *Proc Natl Acad Sci U S A* *84*, 1404-1407. 10.1073/pnas.84.5.1404.
18. Chouchani, E.T., Pell, V.R., Gaude, E., Aksentijević, D., Sundier, S.Y., Robb, E.L., Logan, A., Nadtochiy, S.M., Ord, E.N.J., Smith, A.C., et al. (2014). Ischaemic accumulation of succinate controls reperfusion injury through mitochondrial ROS. *Nature* *515*, 431-435. 10.1038/nature13909.
19. Arslan, F., de Kleijn, D.P., and Pasterkamp, G. (2011). Innate immune signaling in cardiac ischemia. *Nat Rev Cardiol* *8*, 292-300. 10.1038/nrcardio.2011.38.
20. Chen, G.Y., and Nuñez, G. (2010). Sterile inflammation: sensing and reacting to damage. *Nat Rev Immunol* *10*, 826-837. 10.1038/nri2873.
21. Kawaguchi, M., Takahashi, M., Hata, T., Kashima, Y., Usui, F., Morimoto, H., Izawa, A., Takahashi, Y., Masumoto, J., Koyama, J., et al. (2011). Inflammasome activation of cardiac fibroblasts is essential for myocardial ischemia/reperfusion injury. *Circulation* *123*, 594-604. 10.1161/circulationaha.110.982777.
22. Loor, G., Kondapalli, J., Iwase, H., Chandel, N.S., Waypa, G.B., Guzy, R.D., Vanden Hoek, T.L., and Schumacker, P.T. (2011). Mitochondrial oxidant stress triggers cell death in simulated ischemia-reperfusion. *Biochim Biophys Acta* *1813*, 1382-1394. 10.1016/j.bbamcr.2010.12.008.
23. Murphy, E., and Steenbergen, C. (2008). Mechanisms underlying acute protection from cardiac ischemia-reperfusion injury. *Physiol Rev* *88*, 581-609. 10.1152/physrev.00024.2007.
24. Burwell, L.S., Nadtochiy, S.M., and Brookes, P.S. (2009). Cardioprotection by metabolic shut-down and gradual wake-up. *J Mol Cell Cardiol* *46*, 804-810. 10.1016/j.yjmcc.2009.02.026.
25. Eltzschig, H.K., and Eckle, T. (2011). Ischemia and reperfusion--from mechanism to translation. *Nat Med* *17*, 1391-1401. 10.1038/nm.2507.
26. Yellon, D.M., and Hausenloy, D.J. (2007). Myocardial reperfusion injury. *N Engl J Med* *357*, 1121-1135. 10.1056/NEJMra071667.
27. McCay, C.M., Crowell, M.F., and Maynard, L.A. (1989). The effect of retarded growth upon the length of life span and upon the ultimate body size. 1935. *Nutrition* *5*, 155-171; discussion 172.
28. Speakman, J.R., and Mitchell, S.E. (2011). Caloric restriction. *Mol Aspects Med* *32*, 159-221. 10.1016/j.mam.2011.07.001.
29. Fontana, L., and Partridge, L. (2015). Promoting health and longevity through diet: from model organisms to humans. *Cell* *161*, 106-118. 10.1016/j.cell.2015.02.020.
30. Ravussin, E., Redman, L.M., Rochon, J., Das, S.K., Fontana, L., Kraus, W.E., Romashkan, S., Williamson, D.A., Meydani, S.N., Villareal, D.T., et al. (2015). A 2-Year Randomized Controlled Trial of Human Caloric Restriction: Feasibility and Effects on Predictors of Health Span and Longevity. *J Gerontol A Biol Sci Med Sci* *70*, 1097-1104. 10.1093/gerona/glv057.
31. Fontana, L., and Klein, S. (2007). Aging, adiposity, and calorie restriction. *JAMA* *297*, 986-994. 10.1001/jama.297.9.986.
32. JA, M., RJ, C., TM, B., DB, A., JW, K., GS, R., DK, I., R, W., R, d.C., and RM, A. (2017). Caloric restriction improves health and survival of rhesus monkeys. *Nature communications* *8*. 10.1038/ncomms14063.
33. DA, S. (2005). Toward a unified theory of caloric restriction and longevity regulation. *Mechanisms of ageing and development* *126*. 10.1016/j.mad.2005.03.019.
34. Mitchell, J.R., Verweij, M., Brand, K., van de Ven, M., Goemaere, N., van den Engel, S., Chu, T., Forrer, F., Müller, C., de Jong, M., et al. (2010). Short-term dietary restriction

- and fasting precondition against ischemia reperfusion injury in mice. *Aging Cell* 9, 40-53. 10.1111/j.1474-9726.2009.00532.x.
35. S, F., N, S.-Z., D, R., C, V.-D., A, S.D., DJ, C., and M, T. (2016). Caloric Restriction Leads to Browning of White Adipose Tissue through Type 2 Immune Signaling. *Cell metabolism* 24. 10.1016/j.cmet.2016.07.023.
  36. Robertson, L.T., Treviño-Villarreal, J.H., Mejia, P., Grondin, Y., Harputlugil, E., Hine, C., Vargas, D., Zheng, H., Ozaki, C.K., Kristal, B.S., et al. (2015). Protein and Calorie Restriction Contribute Additively to Protection from Renal Ischemia Reperfusion Injury Partly via Leptin Reduction in Male Mice. *The Journal of Nutrition* 145, 1717-1727. 10.3945/jn.114.199380.
  37. Mauro, C.R., Tao, M., Yu, P., Treviño-Villarreal, J.H., Longchamp, A., Kristal, B.S., Ozaki, C.K., and Mitchell, J.R. (2016). Preoperative dietary restriction reduces intimal hyperplasia and protects from ischemia-reperfusion injury. *J Vasc Surg* 63, 500-509.e501. 10.1016/j.jvs.2014.07.004.
  38. Varendi, K., Airavaara, M., Anttila, J., Vose, S., Planken, A., Saarma, M., Mitchell, J.R., and Andressoo, J.O. (2014). Short-term preoperative dietary restriction is neuroprotective in a rat focal stroke model. *PLoS One* 9, e93911. 10.1371/journal.pone.0093911.
  39. Mitchell, J.R., Verweij, M., Brand, K., van de Ven, M., Goemaere, N., van den Engel, S., Chu, T., Forrer, F., Müller, C., de Jong, M., et al. (2010). Short-term dietary restriction and fasting precondition against ischemia reperfusion injury in mice. *Aging Cell* 9, 40-53. 10.1111/j.1474-9726.2009.00532.x.
  40. Verweij, M., van Ginhoven, T.M., Mitchell, J.R., Sluiter, W., van den Engel, S., Roest, H.P., Torabi, E., Ijzermans, J.N., Hoeijmakers, J.H., and de Bruin, R.W. (2011). Preoperative fasting protects mice against hepatic ischemia/reperfusion injury: mechanisms and effects on liver regeneration. *Liver Transpl* 17, 695-704. 10.1002/lt.22243.
  41. Green, C.L., Lamming, D.W., and Fontana, L. (2022). Molecular mechanisms of dietary restriction promoting health and longevity. *Nat Rev Mol Cell Biol* 23, 56-73. 10.1038/s41580-021-00411-4.
  42. Hine, C., Harputlugil, E., Zhang, Y., Ruckenstuhl, C., Lee, B.C., Brace, L., Longchamp, A., Trevino-Villarreal, J.H., Mejia, P., Ozaki, C.K., et al. (2015). Endogenous hydrogen sulfide production is essential for dietary restriction benefits. *Cell* 160, 132-144. 10.1016/j.cell.2014.11.048.
  43. Longchamp, A., Mirabella, T., Arduini, A., MacArthur, M.R., Das, A., Trevino-Villarreal, J.H., Hine, C., Ben-Sahra, I., Knudsen, N.H., Brace, L.E., et al. (2018). Amino Acid Restriction Triggers Angiogenesis via GCN2/ATF4 Regulation of VEGF and H2S Production. *Cell* 173, 117-129.e114. 10.1016/j.cell.2018.03.001.
  44. Maida, A., Zota, A., Sjöberg, K.A., Schumacher, J., Sijmonsma, T.P., Pfenninger, A., Christensen, M.M., Gantert, T., Fuhrmeister, J., Rothermel, U., et al. (2016). A liver stress-endocrine nexus promotes metabolic integrity during dietary protein dilution. *J Clin Invest* 126, 3263-3278. 10.1172/JCI85946.
  45. Malloy, V.L., Krajcik, R.A., Bailey, S.J., Hristopoulos, G., Plummer, J.D., and Orentreich, N. (2006). Methionine restriction decreases visceral fat mass and preserves insulin action in aging male Fischer 344 rats independent of energy restriction. *Aging Cell* 5, 305-314. 10.1111/j.1474-9726.2006.00220.x.
  46. Yu, D., Richardson, N.E., Green, C.L., Spicer, A.B., Murphy, M.E., Flores, V., Jang, C., Kasza, I., Nikodemova, M., Wakai, M.H., et al. (2021). The adverse metabolic effects of branched-chain amino acids are mediated by isoleucine and valine. *Cell Metab* 33, 905-922 e906. 10.1016/j.cmet.2021.03.025.
  47. Treviño-Villarreal, J.H., Reynolds, J.S., Bartelt, A., Langston, P.K., MacArthur, M.R., Arduini, A., Tosti, V., Veronese, N., Bertozzi, B., Brace, L.E., et al. (2018). Dietary protein



- restriction reduces circulating VLDL triglyceride levels via CREBH-APOA5-dependent and -independent mechanisms. *JCI Insight* 3. 10.1172/jci.insight.99470.
48. Harputlugil, E., Hine, C., Vargas, D., Robertson, L., Manning, D., Brendan, and Mitchell, R., James (2014). The TSC Complex Is Required for the Benefits of Dietary Protein Restriction on Stress Resistance In Vivo. *Cell Reports* 8, 1160-1170. 10.1016/j.celrep.2014.07.018.
  49. C, S., C, R., K, M., M, A., B, M., C, C., G, O., K, Y., and F, B. (2014). Regulation of mitochondrial bioenergetic function by hydrogen sulfide. Part I. Biochemical and physiological mechanisms. *British journal of pharmacology* 171. 10.1111/bph.12369.
  50. RG, H., A, C., and RJ, H. (2004). Co-worker fatalities from hydrogen sulfide. *American journal of industrial medicine* 45. 10.1002/ajim.10355.
  51. Hine, C., Kim, H.J., Zhu, Y., Harputlugil, E., Longchamp, A., Matos, M.S., Ramadoss, P., Bauerle, K., Brace, L., Asara, J.M., et al. (2017). Hypothalamic-Pituitary Axis Regulates Hydrogen Sulfide Production. *Cell Metab* 25, 1320-1333.e1325. 10.1016/j.cmet.2017.05.003.
  52. K, A., and H, K. (1996). The possible role of hydrogen sulfide as an endogenous neuromodulator. *The Journal of neuroscience : the official journal of the Society for Neuroscience* 16. 10.1523/JNEUROSCI.16-03-01066.1996.
  53. R, H., N, M., and H, K. (1997). The possible role of hydrogen sulfide as an endogenous smooth muscle relaxant in synergy with nitric oxide. *Biochemical and biophysical research communications* 237. 10.1006/bbrc.1997.6878.
  54. W, Z., J, Z., Y, L., and R, W. (2001). The vasorelaxant effect of H<sub>2</sub>S as a novel endogenous gaseous K(ATP) channel opener. *The EMBO journal* 20. 10.1093/emboj/20.21.6008.
  55. Yang, G., Wu, L., Jiang, B., Yang, W., Qi, J., Cao, K., Meng, Q., Mustafa, A.K., Mu, W., Zhang, S., et al. (2008). H<sub>2</sub>S as a physiologic vasorelaxant: hypertension in mice with deletion of cystathionine gamma-lyase. *Science* 322, 587-590. 10.1126/science.1162667.
  56. Paul, B.D., and Snyder, S.H. (2012). H<sub>2</sub>S signalling through protein sulfhydration and beyond. *Nat Rev Mol Cell Biol* 13, 499-507. 10.1038/nrm3391.
  57. Miller, D.L., and Roth, M.B. (2007). Hydrogen sulfide increases thermotolerance and lifespan in *Caenorhabditis elegans*. *Proc Natl Acad Sci U S A* 104, 20618-20622. 10.1073/pnas.0710191104.
  58. Blackstone, E., Morrison, M., and Roth, M.B. (2005). H<sub>2</sub>S induces a suspended animation-like state in mice. *Science* 308, 518. 10.1126/science.1108581.
  59. Shi, Y.X., Chen, Y., Zhu, Y.Z., Huang, G.Y., Moore, P.K., Huang, S.H., Yao, T., and Zhu, Y.C. (2007). Chronic sodium hydrosulfide treatment decreases medial thickening of intramyocardial coronary arterioles, interstitial fibrosis, and ROS production in spontaneously hypertensive rats. *Am J Physiol Heart Circ Physiol* 293, H2093-2100. 10.1152/ajpheart.00088.2007.
  60. Wang, Y., Zhao, X., Jin, H., Wei, H., Li, W., Bu, D., Tang, X., Ren, Y., Tang, C., and Du, J. (2009). Role of hydrogen sulfide in the development of atherosclerotic lesions in apolipoprotein E knockout mice. *Arterioscler Thromb Vasc Biol* 29, 173-179. 10.1161/ATVBAHA.108.179333.
  61. Zanardo, R.C., Brancaleone, V., Distrutti, E., Fiorucci, S., Cirino, G., and Wallace, J.L. (2006). Hydrogen sulfide is an endogenous modulator of leukocyte-mediated inflammation. *FASEB J* 20, 2118-2120. 10.1096/fj.06-6270fje.
  62. Elrod, J.W., Calvert, J.W., Morrison, J., Doeller, J.E., Kraus, D.W., Tao, L., Jiao, X., Scalia, R., Kiss, L., Szabo, C., et al. (2007). Hydrogen sulfide attenuates myocardial ischemia-reperfusion injury by preservation of mitochondrial function. *Proc Natl Acad Sci U S A* 104, 15560-15565. 10.1073/pnas.0705891104.



63. Das, A., Huang, G.X., Bonkowski, M.S., Longchamp, A., Li, C., Schultz, M.B., Kim, L.J., Osborne, B., Joshi, S., Lu, Y., et al. (2018). Impairment of an Endothelial NAD. *Cell* 173, 74-89.e20. 10.1016/j.cell.2018.02.008.
64. EM, B., R, W., PM, S., M, B., J, D., M, F., J, M., JL, H., RJ, P., G, Y., et al. (2013). Cystathionine  $\gamma$ -lyase protects against renal ischemia/reperfusion by modulating oxidative stress. *Journal of the American Society of Nephrology : JASN* 24. 10.1681/ASN.2012030268.
65. KR, O. (2009). Is hydrogen sulfide a circulating "gasotransmitter" in vertebrate blood? *Biochimica et biophysica acta* 1787. 10.1016/j.bbabi.2009.03.019.
66. Módis, K., Coletta, C., Erdélyi, K., Papapetropoulos, A., and Szabo, C. (2013). Intramitochondrial hydrogen sulfide production by 3-mercaptopyruvate sulfurtransferase maintains mitochondrial electron flow and supports cellular bioenergetics. *FASEB J* 27, 601-611. 10.1096/fj.12-216507.
67. Wallace, J.L., and Wang, R. (2015). Hydrogen sulfide-based therapeutics: exploiting a unique but ubiquitous gasotransmitter. *Nat Rev Drug Discov* 14, 329-345. 10.1038/nrd4433.
68. BD, P., and SH, S. (2018). Gasotransmitter hydrogen sulfide signaling in neuronal health and disease. *Biochemical pharmacology* 149. 10.1016/j.bcp.2017.11.019.
69. Lameire, N.H., Bagga, A., Cruz, D., De Maeseneer, J., Endre, Z., Kellum, J.A., Liu, K.D., Mehta, R.L., Pannu, N., Van Biesen, W., and Vanholder, R. (2013). Acute kidney injury: an increasing global concern. *Lancet* 382, 170-179. 10.1016/s0140-6736(13)60647-9.
70. Thomas, M.E., Blaine, C., Dawnay, A., Devonald, M.A., Ftouh, S., Laing, C., Latchem, S., Lewington, A., Milford, D.V., and Ostermann, M. (2015). The definition of acute kidney injury and its use in practice. *Kidney Int* 87, 62-73. 10.1038/ki.2014.328.
71. Murugan, R., Karajala-Subramanyam, V., Lee, M., Yende, S., Kong, L., Carter, M., Angus, D.C., and Kellum, J.A. (2010). Acute kidney injury in non-severe pneumonia is associated with an increased immune response and lower survival. *Kidney Int* 77, 527-535. 10.1038/ki.2009.502.
72. Sileanu, F.E., Murugan, R., Lucko, N., Clermont, G., Kane-Gill, S.L., Handler, S.M., and Kellum, J.A. (2015). AKI in low-risk versus high-risk patients in intensive care. *Clin J Am Soc Nephrol* 10, 187-196. 10.2215/cjn.03200314.
73. R, K. (2013). Risk factors for chronic kidney disease: an update. *Kidney international supplements* 3. 10.1038/kisup.2013.79.
74. CJ, W., JB, W., and AK, I. (2017). Old versus new: Progress in reaching the goals of the new kidney allocation system. *Human immunology* 78. 10.1016/j.humimm.2016.08.007.
75. Zens, T.J., Danobeitia, J.S., Leverson, G., Chlebeck, P.J., Zitur, L.J., Redfield, R.R., D'Alessandro, A.M., Odorico, S., Kaufman, D.B., and Fernandez, L.A. (2018). The impact of kidney donor profile index on delayed graft function and transplant outcomes: A single-center analysis. *Clin Transplant* 32, e13190. 10.1111/ctr.13190.
76. Siedlecki, A., Irish, W., and Brennan, D.C. (2011). Delayed graft function in the kidney transplant. *Am J Transplant* 11, 2279-2296. 10.1111/j.1600-6143.2011.03754.x.
77. PM, B., MA, S., D, A., PR, S., and KL, L. (2012). The clinical and financial burden of early dialysis after deceased donor kidney transplantation. *Journal of nephrology & therapeutics* 2012. 10.4172/2161-0959.s4-001.
78. RB, M. (2018). Delayed Graft Function: The AKI of Kidney Transplantation. *Nephron* 140. 10.1159/000491558.
79. Fenoglio, R., Sciascia, S., Baldovino, S., and Roccatello, D. (2019). Acute kidney injury associated with glomerular diseases. *Curr Opin Crit Care* 25, 573-579. 10.1097/MCC.0000000000000675.

80. Venkatachalam, M.A., Weinberg, J.M., Kriz, W., and Bidani, A.K. (2015). Failed Tubule Recovery, AKI-CKD Transition, and Kidney Disease Progression. *J Am Soc Nephrol* 26, 1765-1776. 10.1681/asn.2015010006.
81. Polichnowski, A.J., Lan, R., Geng, H., Griffin, K.A., Venkatachalam, M.A., and Bidani, A.K. (2014). Severe renal mass reduction impairs recovery and promotes fibrosis after AKI. *J Am Soc Nephrol* 25, 1496-1507. 10.1681/asn.2013040359.
82. Venkatachalam, M.A., Griffin, K.A., Lan, R., Geng, H., Saikumar, P., and Bidani, A.K. (2010). Acute kidney injury: a springboard for progression in chronic kidney disease. *Am J Physiol Renal Physiol* 298, F1078-1094. 10.1152/ajprenal.00017.2010.
83. Chawla, L.S., Eggers, P.W., Star, R.A., and Kimmel, P.L. (2014). Acute kidney injury and chronic kidney disease as interconnected syndromes. *N Engl J Med* 371, 58-66. 10.1056/NEJMra1214243.
84. Basile, D.P., Donohoe, D., Roethe, K., and Osborn, J.L. (2001). Renal ischemic injury results in permanent damage to peritubular capillaries and influences long-term function. *Am J Physiol Renal Physiol* 281, F887-899. 10.1152/ajprenal.2001.281.5.F887.
85. Zager, R.A. (2013). 'Biologic memory' in response to acute kidney injury: cytoresistance, toll-like receptor hyper-responsiveness and the onset of progressive renal disease. *Nephrol Dial Transplant* 28, 1985-1993. 10.1093/ndt/gft101.
86. Pickkers, P., Ostermann, M., Joannidis, M., Zarbock, A., Hoste, E., Bellomo, R., Prowle, J., Darmon, M., Bonventre, J.V., Forni, L., et al. (2017). The intensive care medicine agenda on acute kidney injury. *Intensive Care Med* 43, 1198-1209. 10.1007/s00134-017-4687-2.
87. Desborough, J.P. (2000). The stress response to trauma and surgery. *Br J Anaesth* 85, 109-117.
88. Vinten-Johansen, J., and Nakanishi, K. (1993). Postcardioplegia acute cardiac dysfunction and reperfusion injury. *J Cardiothorac Vasc Anesth* 7, 6-18.
89. Chambers, D.J., and Fallouh, H.B. (2010). Cardioplegia and cardiac surgery: pharmacological arrest and cardioprotection during global ischemia and reperfusion. *Pharmacol Ther* 127, 41-52. 10.1016/j.pharmthera.2010.04.001.
90. Wald, R., Waikar, S.S., Liangos, O., Pereira, B.J., Chertow, G.M., and Jaber, B.L. (2006). Acute renal failure after endovascular vs open repair of abdominal aortic aneurysm. *J Vasc Surg* 43, 460-466; discussion 466. 10.1016/j.jvs.2005.11.053.
91. Vajdová, K., Graf, R., and Clavien, P.A. (2002). ATP-supplies in the cold-preserved liver: A long-neglected factor of organ viability. *Hepatology* 36, 1543-1552. 10.1053/jhep.2002.37189.
92. Bruinsma, B.G., Sridharan, G.V., Weeder, P.D., Avruch, J.H., Saeidi, N., Özer, S., Geerts, S., Porte, R.J., Heger, M., van Gulik, T.M., et al. (2016). Metabolic profiling during ex vivo machine perfusion of the human liver. *Sci Rep* 6, 22415. 10.1038/srep22415.
93. Miyagi, S., Iwane, T., Akamatsu, Y., Nakamura, A., Sato, A., and Satomi, S. (2008). The significance of preserving the energy status and microcirculation in liver grafts from non-heart-beating donor. *Cell Transplant* 17, 173-178. 10.3727/000000008783906874.
94. van Golen, R.F., van Gulik, T.M., and Heger, M. (2012). Mechanistic overview of reactive species-induced degradation of the endothelial glycocalyx during hepatic ischemia/reperfusion injury. *Free Radic Biol Med* 52, 1382-1402. 10.1016/j.freeradbiomed.2012.01.013.
95. Nohl, H., Koltover, V., and Stolze, K. (1993). Ischemia/reperfusion impairs mitochondrial energy conservation and triggers O<sub>2</sub>- release as a byproduct of respiration. *Free Radic Res Commun* 18, 127-137.

96. Lanir, A., Jenkins, R.L., Caldwell, C., Lee, R.G., Khettry, U., and Clouse, M.E. (1988). Hepatic transplantation survival: correlation with adenine nucleotide level in donor liver. *Hepatology* 8, 471-475. 10.1002/hep.1840080306.
97. Kamiike, W., Burdelski, M., Steinhoff, G., Ringe, B., Lauchart, W., and Pichlmayr, R. (1988). Adenine nucleotide metabolism and its relation to organ viability in human liver transplantation. *Transplantation* 45, 138-143. 10.1097/00007890-198801000-00030.
98. Parsons, R.F., and Guarrera, J.V. (2014). Preservation solutions for static cold storage of abdominal allografts: which is best? *Curr Opin Organ Transplant* 19, 100-107. 10.1097/mot.0000000000000063.
99. Kayler, L.K., Magliocca, J., Zendejas, I., Srinivas, T.R., and Schold, J.D. (2011). Impact of cold ischemia time on graft survival among ECD transplant recipients: a paired kidney analysis. *Am J Transplant* 11, 2647-2656. 10.1111/j.1600-6143.2011.03741.x.
100. Lee, C.M., Carter, J.T., Alfrey, E.J., Ascher, N.L., Roberts, J.P., and Freise, C.E. (2000). Prolonged cold ischemia time obviates the benefits of 0 HLA mismatches in renal transplantation. *Arch Surg* 135, 1016-1019; discussion 1019-1020. 10.1001/archsurg.135.9.1016.
101. Quiroga, I., McShane, P., Koo, D.D., Gray, D., Friend, P.J., Fuggle, S., and Darby, C. (2006). Major effects of delayed graft function and cold ischaemia time on renal allograft survival. *Nephrol Dial Transplant* 21, 1689-1696. 10.1093/ndt/gfl042.
102. Salahudeen, A.K., Haider, N., and May, W. (2004). Cold ischemia and the reduced long-term survival of cadaveric renal allografts. *Kidney Int* 65, 713-718. 10.1111/j.1523-1755.2004.00416.x.
103. M, M., RG, C., P, B., and AJ, K. (2011). Enhanced recovery after surgery (ERAS) protocols: Time to change practice? *Canadian Urological Association journal = Journal de l'Association des urologues du Canada* 5. 10.5489/cuaj.11002.
104. SM, S., A, L., JL, R., JD, M., J, T., TJ, G., and E, B.-G. (2021). A U.S. survey of pre-operative carbohydrate-containing beverage use in colorectal enhanced recovery after surgery (ERAS) programs. *Perioperative medicine (London, England)* 10. 10.1186/s13741-021-00187-3.
105. Bilku, D.K., Dennison, A.R., Hall, T.C., Metcalfe, M.S., and Garcea, G. (2014). Role of preoperative carbohydrate loading: a systematic review. *Ann R Coll Surg Engl* 96, 15-22. 10.1308/003588414X13824511650614.
106. KK, V., KR, N., CH, D., KC, F., O, L., and DN, L. (2010). The enhanced recovery after surgery (ERAS) pathway for patients undergoing major elective open colorectal surgery: a meta-analysis of randomized controlled trials. *Clinical nutrition (Edinburgh, Scotland)* 29. 10.1016/j.clnu.2010.01.004.

## AIM OF THE STUDY

Each chapter is presented below and currently in the form of an original article or draft planned for publication.

Better preservation procedures for marginal kidney grafts could increase the number of viable kidneys and increase patient survival. Warm (22°C and 37°C) ex-vivo perfusion has been proposed to reduce preservation injury, but the underlying mechanism is unknown. We evaluated kidney quality, including adenosine triphosphate (ATP) production, during sub-normothermic (22 °C) versus hypothermic (4°C) ex-vivo kidney machine perfusion in a porcine autotransplantation model using magnetic resonance spectroscopic imaging (pMRSI) coupled with a fitting method using the Convolutional Neural Network. We have made promising progress toward demonstrating the potential of 22°C perfusion to improve kidney graft longevity and outcomes, necessitating further clinical trials (**Chapter 1**).

In rodents, H<sub>2</sub>S has been found to reduce IRI and improve renal graft function. This research sought to determine if these benefits extend to swine, which provides a more applicable clinical model for humans. Adult porcine kidneys were subjected to 60 minutes of mild ischemia (WI) and treated with 100 μM NaHS during hypothermic ex vivo perfusion, during WI, or both. Here, using MRI and pMRSI, we examined the effect of NaHS on a relevant porcine ex vivo HMP model and autotransplantation. To increase the translational value of our study, NaHS was given in relevant clinical situations, including ex vivo perfusion only or concomitant to heparin administration before WI (**Chapter 2**).

Dietary restriction promotes resistance to acute surgical stress in multiple organisms. Counterintuitively, current medical protocols recommend short-term carbohydrate loading before surgery, involving carbohydrate-rich drinks as part of a multimodal perioperative care pathway designed to enhance surgical recovery. Despite widespread clinical use, preclinical and mechanistic studies on carbohydrate loading in surgical contexts are lacking. In this study, our aims were to 1) Explore how ad-libitum access to carbohydrate loading drinks impacts food intake, 2) Evaluate the effects of short-term carbohydrate loading on IRI, a model of acute surgical stress, and 3) Identify the mechanisms that underlie the benefits of carbohydrate loading. We hypothesized that mice with access to carbohydrate loading drinks would consume less food, resulting in protein dilution. We further hypothesized that carbohydrate loading-induced short-term protein dilution would protect against acute surgical stress through conserved mechanisms of protein restriction (**Chapter 3**).

These data build up on the importance of optimal organ preservation in transplantation surgery and could have a meaningful impact on 1) kidney availability and 2) provides rationale for short-term preconditioning with carbohydrates or pharmacological DR mimetic, such as FGF21 agonists to protect against IRI and the stress associated with surgery and reduce the occurrence of potential postoperative complications.

# RESULTS

## Chapter 1: Subnormothermic Ex Vivo Porcine Kidney Perfusion Improves Energy Metabolism: Analysis Using 31P Magnetic Resonance Spectroscopic Imaging.

This work was published in 2022 in the journal Transplant Direct.

- Agius, T., Songeon, J., Klausner, A., Allagnat, F., Longchamp, G., Ruttimann, R., Lyon, A., Ivaniesevic, J., Meier, R., Déglise, S., et al. (2022). Subnormothermic Ex Vivo Porcine Kidney Perfusion Improves Energy Metabolism: Analysis Using 31P Magnetic Resonance Spectroscopic Imaging. *Transplant Direct* 8, e1354.
- DOI: [10.1097/TXD.0000000000001354](https://doi.org/10.1097/TXD.0000000000001354)

### Summary:

The preservation temperature for kidney grafts after circulatory death remains a point of contention. This study investigated the potential benefits of subnormothermic (22 °C) ex vivo kidney machine perfusion, specifically its ability to enhance kidney metabolism and reduce the effects of ischemia-reperfusion injuries. Using the kidneys of swine subjected to 60 minutes of warm ischemia, the study subjected these organs to a 4-hour perfusion at either 22 °C or the colder 4 °C. The adenosine triphosphate (ATP) content was increased by four at 22 °C relative to 4 °C perfusion, which was a significant finding. In addition, ATP levels initially increased during the first few hours of perfusion at 22 °C but subsequently decreased. Moreover, the presence of phosphomonoesters, which contain adenosine mono-phosphate, increased significantly at 22 °C but gradually decreased. Significantly, the kidneys perfused at 22 °C displayed superior cortical and medullary perfusion and significantly fewer histological lesions following transplantation. The promising findings demonstrate the potential of 22°C perfusion to improve kidney graft longevity and outcomes, necessitating further clinical trials.



OPEN

# Subnormothermic Ex Vivo Porcine Kidney Perfusion Improves Energy Metabolism: Analysis Using <sup>31</sup>P Magnetic Resonance Spectroscopic Imaging

Thomas Agius, MS,<sup>1</sup> Julien Songeon, MS,<sup>2</sup> Antoine Klausner, PhD,<sup>2,3</sup> Florent Allagnat, PhD,<sup>1</sup> Grégoire Longchamp, MD,<sup>4</sup> Raphael Ruttimann, BS,<sup>4</sup> Arnaud Lyon, MD,<sup>1</sup> Julijana Ivaniesevic, PhD,<sup>5</sup> Raphael Meier, MD, PhD,<sup>6</sup> Sébastien Déglise, MD,<sup>1</sup> James F. Markmann, MD, PhD,<sup>7</sup> Korkut Uygun, PhD,<sup>8</sup> Leo Buhler, MD,<sup>9</sup> Christian Toso, MD, PhD,<sup>4</sup> Jean-Marc Corpataux, MD,<sup>1</sup> Francois Lazeyras, PhD,<sup>2,3</sup> and Alban Longchamp, MD, PhD<sup>1</sup>

**Background.** The ideal preservation temperature for donation after circulatory death kidney grafts is unknown. We investigated whether subnormothermic (22 °C) ex vivo kidney machine perfusion could improve kidney metabolism and reduce ischemia-reperfusion injury. **Methods.** To mimic donation after circulatory death procurement, kidneys from 45-kg pigs underwent 60 min of warm ischemia. Kidneys were then perfused ex vivo for 4 h with Belzer machine perfusion solution UW at 22 °C or at 4 °C before transplantation. Magnetic resonance spectroscopic imaging coupled with LCModel fitting was used to assess energy metabolites. Kidney perfusion was evaluated with dynamic-contrast enhanced MRI. Renal biopsies were collected at various time points for histopathologic analysis. **Results.** Total adenosine triphosphate content was 4 times higher during ex vivo perfusion at 22 °C than at 4 °C perfusion. At 22 °C, adenosine triphosphate levels increased during the first hours of perfusion but declined afterward. Similarly, phosphomonoesters, containing adenosine monophosphate, were increased at 22 °C and then slowly consumed over time. Compared with 4 °C, ex vivo perfusion at 22 °C improved cortical and medullary perfusion. Finally, kidney perfusion at 22 °C reduced histological lesions after transplantation (injury score: 22 °C: 10.5±3.5; 4 °C: 18±2.25 over 30). **Conclusions.** Ex vivo kidney perfusion at 22°C improved graft metabolism and protected from ischemia-reperfusion injuries upon transplantation. Future clinical studies will need to define the benefits of subnormothermic perfusion in improving kidney graft function and patient's survival.

(*Transplantation Direct* 2022;8: e1354; doi: 10.1097/TXD.0000000000001354).

## INTRODUCTION

Transplantation is the preferred treatment for end-stage kidney disease, but it suffers from a severe shortage of

available organs. Approximately 100 000 patients are currently waiting for a donor kidney, with only 18 000 kidney transplants performed in the United States each year.<sup>1</sup> This

Received 23 May 2022.

Accepted 24 May 2022.

<sup>1</sup>Department of Vascular Surgery, Centre Hospitalier Universitaire Vaudois and University of Lausanne, Lausanne, Switzerland.

<sup>2</sup>Department of Radiology and Medical Informatics, University of Geneva, Geneva, Switzerland.

<sup>3</sup>Center for Biomedical Imaging (CIBM), Geneva, Switzerland.

<sup>4</sup>Visceral and Transplant Surgery, Department of Surgery, Geneva University Hospitals and Medical School, Geneva, Switzerland.

<sup>5</sup>Metabolomics Platform, Faculty of Biology and Medicine, University of Lausanne, Switzerland.

<sup>6</sup>Department of Surgery, University of Maryland School of Medicine, Baltimore, MD, USA.

<sup>7</sup>Department of Surgery, Transplant Center, Massachusetts General Hospital, Harvard Medical School, Boston, USA.

<sup>8</sup>Department of Surgery, Center for Engineering in Medicine, Massachusetts General Hospital, Harvard Medical School, Boston, USA.

<sup>9</sup>Faculty of Science and Medicine, Section of Medicine, University of Fribourg, Fribourg, Switzerland.

T.A., J.S., F.L., and A.L. have contributed equally to this work.

The authors declare no conflicts of interest.

This work was supported by the Swiss National Science Foundation to J.-M.C., F.L. (SNSF 320030\_182658), and A.L. (SNSF PZ00P3-185927), as

well as the Mendez National Institute of Transplantation and the Leenards Foundation to A.L.

A.L., A.K., J.S., T.A., L.B., J.-M.C., and F.L. participated in research design. A.L., A.K., R.M., K.U., J.F.M., and F.L. participated in the writing of the article. A.L., A.K., J.S., T.A., A.N., R.R., Ar.L., J.I., S.M., R.M., S.D., J.-M.C., and F.L. participated in the performance of the research. A.N., R.R., S.M., and F.L. contributed new reagents or analytic tools. A.L., A.K., J.S., T.A., S.M., R.M., L.B., J.-M.C., and F.L. participated in data analysis.

Supplemental digital content (SDC) is available for this article. Direct URL citations appear in the printed text, and links to the digital files are provided in the HTML text of this article on the journal's Web site ([www.transplantationdirect.com](http://www.transplantationdirect.com)).

Correspondence: Alban Longchamp, MD, PhD, Department of Vascular Surgery, Centre Hospitalier Universitaire Vaudois and University of Lausanne, Rue du Bugnon 46, 1011 Lausanne, Switzerland. ([alban.longchamp@chuv.ch](mailto:alban.longchamp@chuv.ch)).

Copyright © 2022 The Author(s). *Transplantation Direct*. Published by Wolters Kluwer Health, Inc. This is an open-access article distributed under the terms of the Creative Commons Attribution-Non Commercial-No Derivatives License 4.0 (CCBY-NC-ND), where it is permissible to download and share the work provided it is properly cited. The work cannot be changed in any way or used commercially without permission from the journal.

ISSN: 2373-8731

DOI: 10.1097/TXD.0000000000001354



scarcity led to the expansion of the donor pool beyond standard-criteria kidney donors, including extended criteria donors and donation after circulatory death (DCD).<sup>1,2</sup> Although organs from these donors allow a higher survival rate than dialysis, their use is complicated by an increased rate of delayed graft function (DGF)<sup>3</sup> and acute rejection.<sup>4</sup>

DCD grafts are particularly vulnerable to ischemia-reperfusion (IR) injury, an issue that is not addressed at all by current standard storage strategies, including static cold storage and nonoxygenated hypothermic machine perfusion (eg, LifePort).<sup>5,6</sup> With this approach, prolonged periods (>24h) of cold ischemia are associated with tubular necrosis, DGF, and poor graft survival.<sup>4,7,8</sup> Although static cold storage is the most prevalent method for renal allograft preservation, hypothermic machine perfusion without oxygen was shown to reduce DGF and to improve 1- and 3-y graft survival.<sup>9</sup> Hypothermic storage slows but does not entirely suspend cellular metabolism, resulting in a slow but inexorable consumption of cellular energy stores.<sup>10</sup> In a prior preclinical study, we found that, at 4 °C, oxygen supplementation was required to maintain adenosine triphosphate (ATP) levels.<sup>10</sup> In the COMPARE study, oxygen supplementation reduced biopsy-proven acute rejection but did not improve kidney graft survival or glomerular filtration rate at 12 mo.<sup>11</sup>

Although cold anoxic storage aims to arrest cell metabolism, ex vivo perfusion at physiologic normothermic temperature (37 °C) provides a continuous flow of warmed, oxygenated perfusate containing nutritional substrates, thereby maintaining the metabolic activity of the tissue.<sup>12</sup> Normothermic red cell-based-perfusion of porcine kidneys at 37 °C improved early postoperative creatinine and urea clearance in DCD grafts.<sup>13</sup> In addition, normothermic ex vivo perfusion allows graft assessment, reconditioning, and repair.<sup>14,15</sup> Using a red cell-based plasma-free solution, perfusion of marginal kidneys at 37 °C reduced DGF compared with static cold storage.<sup>16</sup> However, perfusion of organ at 37 °C is limited by the availability and cost of a blood perfusion system, complex heating system, tight pH and glucose control, red blood cell hemolysis, and risk of infection and immunization.<sup>17,18</sup> In addition, failure of the perfusion machine would rapidly lead to graft loss.

Subnormothermic (22 °C) ex vivo kidney perfusion was proposed as an alternative to perfusion at 37 °C.<sup>19</sup> Importantly, a previous study demonstrated that, compared with perfusion at 37 °C, kidney perfusion with blood:PlasmaLyte at 22 °C reduced acute tubular necrosis and improved kidney function in a DCD porcine model.<sup>20</sup> In liver grafts, perfusion of a cell-free, oxygenated perfusate at 22 °C promoted mitochondrial respiration and ATP stores before transplantation.<sup>21</sup> Overall, these studies suggest that 22 °C might be the optimal temperature to protect against kidney (IR) injuries, whereas avoiding complex normothermic perfusion machines.

Several tools are used to predict the suitability of kidney grafts. Although MRI is a well-established clinical diagnostic tool for assessing kidney graft function,<sup>22</sup> <sup>31</sup>P magnetic resonance spectroscopic imaging (pMRSI) enables the detection of high-energy phosphate metabolites such as ATP.<sup>22</sup> In fact, we previously reported that, in porcine kidneys, warm ischemia reduced energy stores, which correlated with kidney viability.<sup>10</sup>

## MATERIAL AND METHODS

### Ex Vivo Kidney Perfusion

Kidneys were assigned to the following ex vivo perfusion groups: (i) 4 °C with passive oxygenation of the perfusate (4 °C), (ii) 4 °C with active oxygenation (PO<sub>2</sub>>100kPa) of the perfusate (4 °C+O<sub>2</sub>), (iii) 22 °C ex vivo kidney perfusion with active oxygenation (PO<sub>2</sub>>100kPa) of the perfusate (22 °C+O<sub>2</sub>, Figure 1A). Passive oxygenation corresponded to ambient air oxygen diffusion.

Immediately after retrieval, kidneys were flushed with Belzer machine perfusion solution (MPS) UW Machine Perfusion Solution and immediately perfused for 4h (before autotransplantation) or 42h (time course experiment) using a homemade MRI-compatible pulsatile perfusion machine as published.<sup>10</sup> Belzer MPS UW solution can be stored between 2 °C and 25 °C and has a pH of 7.4 at 22 °C. Active oxygenation was achieved using a 0.15 m<sup>2</sup> membrane oxygenator (Biochrom Ltd, Cambridge, United Kingdom), maintaining the PO<sub>2</sub> levels at 100 kPa for the whole preservation time. The PO<sub>2</sub> levels during passive oxygenation were set at 20 kPa. The perfusion module was kept in an isolating box that passively kept the kidney at the desired temperature. Systolic and diastolic pressure were set at 40 and 20 mmHg, respectively.

### MRI Imaging

Measurements were performed on a 3 Tesla multinuclear Prisma-fit 3T whole-body MRI scanner (Siemens Healthineers, Erlangen, Germany). <sup>1</sup>H imaging was performed with the body coil using a T2-weighted sequence (turbo SE, TR 6530ms, TE 110ms, 2 mm slices) for kidney localization and structural imaging. Dynamic-contrast enhanced MRI with gadolinium (Gd-MRI) was used to determine the perfusion distribution between the cortex and the medulla and as an estimate of glomerular filtration rate as previously described.<sup>7,10</sup> Data were collected using a dynamic 2D saturation-prepared turbo flash sequence with the scanner body coil. This sequence has an inversion time of 255 ms, a flip angle of 12°, 1.3 mm × 1.3 mm resolution, and 6 slices of 4 mm (1 mm gap), TR 500ms, and a TE of 1.4ms. The perfusion-descending cortical slope was determined using the angle of the linear regression between the maximum signal value and the lowest intensity point after the initial peak.<sup>21</sup>

### <sup>31</sup>P Magnetic Resonance Imaging Spectroscopy

pMRSI was performed as described previously.<sup>7</sup> Briefly, a single loop <sup>31</sup>P-tuned coil fixed at the bottom of the perfusion tank allows the measurement of the signal. Scanner embedded body coil was used for <sup>1</sup>H imaging and for shimming to ensure field homogeneity. pMRSI consisted of 3D spatial encoding, with a field of view 250 × 250 × 160 mm<sup>3</sup>, matrix size 16 × 16 × 8, nominal spatial resolution 15.6 × 15.6 × 20 mm<sup>3</sup>, TR 1.0s, flip angle of 35°, echo delay 0.6ms, bandwidth 4000 Hz, and 2k sampling points. Elliptical encoding with 18 weighted averages resulted in an acquisition time of 45 min. The resonance of the inorganic phosphate (Pi, 5.2 ppm), which is uniformly present in the container and the kidney, was used as a reference for quantification of the pMRSI signal. Excitation pulse bandwidth has been adjusted to the ATP frequency range (Pi resonance—500 Hz). An exponential time filter with 20 Hz frequency width and zeroth and first order phase corrections were used to process the spectra. The metabolites (ATP, phosphomonoesters [PME], Pi, phosphocreatine/PCr) were fitted



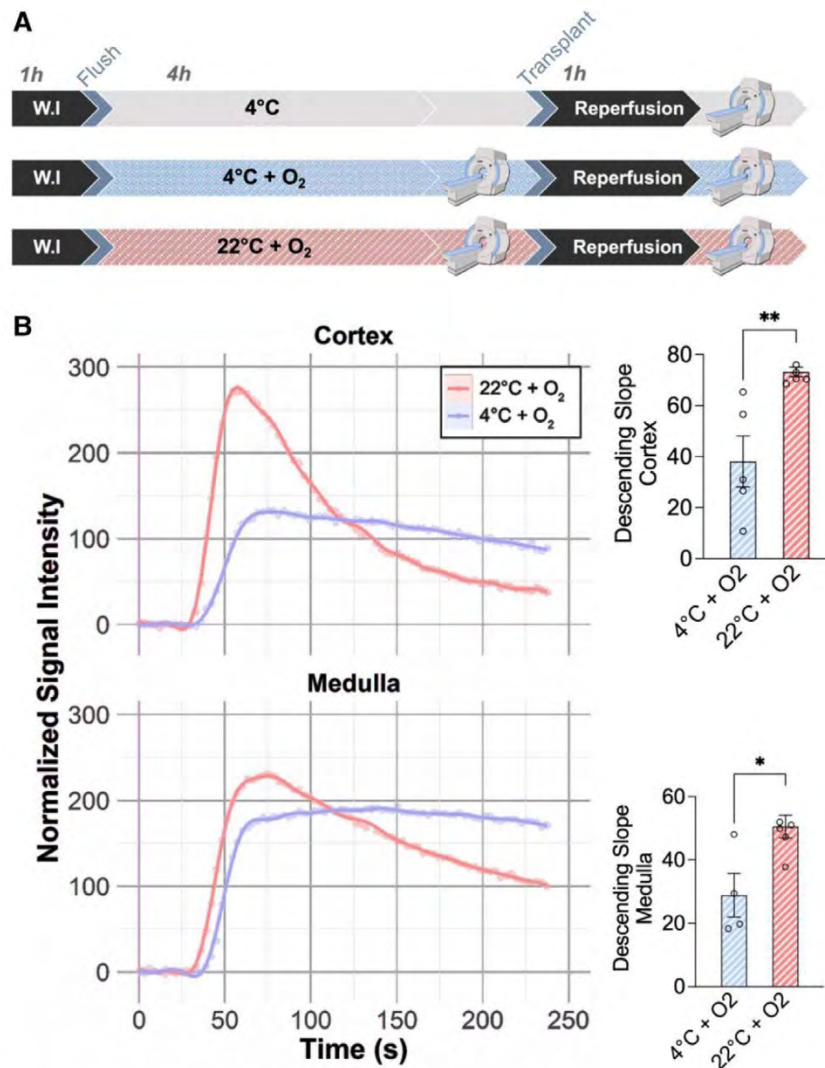


**FIGURE 1.** Ex vivo subnormothermic perfusion improves kidney perfusion. A, Experimental groups and design. Kidneys were retrieved after 60min warm ischemia and placed into a hypothermic+passive oxygenation ( $4^{\circ}\text{C}$ ), hypothermic+active oxygenation ( $4^{\circ}\text{C}+\text{O}_2$ ), or subnormothermic+active oxygenation ( $22^{\circ}\text{C}+\text{O}_2$ ) perfusion machine with or without oxygen for 4h. Kidney were autografted into the same pig. Dynamic-contrast enhanced MRI analysis was performed prior ( $4^{\circ}\text{C}+\text{O}_2$ ,  $22^{\circ}\text{C}+\text{O}_2$ ) and after transplantation ( $4^{\circ}\text{C}$ ,  $4^{\circ}\text{C}+\text{O}_2$ ,  $22^{\circ}\text{C}+\text{O}_2$ ). B, Pretransplant representative Gd uptake in cortex (top) and medulla (bottom) of kidneys during hypothermic (blue line) or subnormothermic (red) perfusion and Gd perfusion-DS quantification (right,  $n=5/\text{group}$ ). Bars indicate mean  $\pm$  SEM, and asterisks indicate the significance of the difference between perfusions methods by Student's *t* test or 1-way ANOVA and Tukey test. \* $P<0.05$ , \*\* $P<0.01$ .  $n=4$  to 6 per group. DS, descending slope.

with Gaussian peaks using the *syngo.via* software (SIEMENS, Erlangen, Germany) and were estimated over the whole kidneys by averaging pMRSI voxels containing graft tissue, resulting in a single spectrum. Quantification results provided by 3D  $^{31}\text{P}$ -MRSI at 3T were analyzed with LCMoDel for magnetic resonance spectroscopy fitting as previously described.<sup>23</sup> The 3 ATP peaks were quantified separately to prevent methodological bias because of excitation profile imperfection. In each condition, pMRSI allowed the detection of  $\alpha$ -,  $\beta$ -, and  $\gamma$ -ATP and PME composed by phosphocholine, phosphoethanolamine (PE), and adenosine monophosphate (AMP). ATP and PME concentration (mM) were quantified from the fitting

and using the concentration of the inorganic-phosphate buffer (Pi, 25 mmol/L) as reference.<sup>7</sup> As single ATP concentration was calculated by average of the  $\alpha$ -,  $\beta$ -, and  $\gamma$ -ATP values, ATP maps were generated using the spectroscopy software (Syngo MR Spectroscopy Evaluation, Siemens Healthineers, Erlangen, Germany). The colors represent the metabolite concentration normalized to the Pi for each voxel.

#### Animals and Surgery

The study was approved by the University of Geneva's animal ethics committee (protocol number: GE83/33556). Female pigs of 5 mo old were obtained from the animal facility

of Arare, Switzerland (n = 16). All pigs were maintained under standard conditions. Water and food were provided ad libitum. Animals were premedicated and anesthetized as previously described.<sup>24</sup> Animals were kept intubated and ventilated during the procedure. An arterial line was inserted in the internal carotid artery. Monitoring included heart rate, systemic blood pressure, pulse oximetry, and end-tidal CO<sub>2</sub>.

Kidneys were explanted and transplanted back into the same animal (autotransplantation).<sup>24</sup> To mimic circulatory arrest during DCD procurement, renal arteries were crossed clamped for 60 min before collection. Kidneys were then immediately flushed and perfused as described earlier in the ex vivo kidney perfusion section above. At the end of the perfusion, both kidneys were transplanted sequentially onto the vena cava and aorta using a 6-0 running suture. After 2 h of reperfusion, pigs were sacrificed using 100 mEq of potassium chloride intravenously.

### Histopathologic Analysis of Biopsies

Cortical kidney biopsies were obtained at baseline, after 60 min of warm ischemia, after 4 h of ex vivo perfusion, and at 2 h after autotransplantation. Biopsies were immediately flash frozen or formalin fixed and embedded in paraffin. Fixed kidney biopsies were cut into sections of 3 μm thickness and stained with silver Jones and Periodic Acid-Schiff. Slides were scanned using a Axio Scan z1 slide scanner (Zeiss). Histopathologic analysis score was performed based on those described by Goujon et al<sup>25,26</sup> using Zen software (Zeiss). Whole biopsies were assessed and blinded to group assignment. The following categories were assessed: glomerular integrity, tubular dilatation, brush border integrity, cellular debris in lumina of tubules, interstitial edema, and tubular cell vacuolization. Briefly, to assess glomerulus integrity, >10 glomeruli were randomly selected from the section and assigned a score of 0 to 3. The same procedure was followed in the remaining categories. After that, the score for each category was converted to a percentage. The final score was converted to a final scale from 0 to 5 according to the percentage of damage: 0% to 15% (0), 15% to 30% (1), 30% to 45% (2), 45% to 60% (3), 60% to 75% (4), and >75% (5) using the following formula:  $(\text{Category}_{\text{Final Score}}/3) * 100$ . The final score for each biopsy ranged from 0 to 30, with 30 the highest score corresponding to more severe damage. Scoring was performed blindly by 2 independent researchers.

### RT-qPCR Analysis

Kidney biopsy powder was homogenized in Tripure Isolation Reagent (Roche, Switzerland). Total RNA was extracted as previously described.<sup>27</sup> cDNA was synthesized by random hexamer priming with the Verso cDNA kit (Prime Script RT reagent, Takara). RT-qPCR was performed with Power SYBR Green Master Mix (Ref: 4367659, Applied Biosystems, Thermo Fisher Scientific AG, Switzerland) in a ViiA 7 Real-Time PCR System (Applied Biosystems, Thermo Fisher Scientific AG, Switzerland). Amplification data were analyzed using the QuantStudio 1.3 software (Thermo Fisher Scientific AG, Switzerland). Fold changes were calculated using relative standard curves methods, using ribosomal protein RPL27 genes as standards. Inflammatory gene expression was quantified 2 h after reperfusion and compared with their respective baseline. Primers' sequences are indicated in Table S1 (SDC, <http://links.lww.com/TXD/A437>).

### Metabolite Analysis

Tissue samples were preextracted and homogenized by the addition of 150 μL of MeOH:H<sub>2</sub>O (4:1) in the Cryolys Precellys 24 sample homogenizer (2 × 20 s at 10000 rpm, Bertin Technologies, Rockville, MD, United States) with ceramic beads. The bead beater was air-cooled down at a flow rate of 110 L/min at 6 bar. Homogenized extracts were centrifuged for 15 min at 4000 g at 4 °C (Hermle, Gosheim, Germany). The resulting supernatant was collected and analyzed by hydrophilic interaction liquid chromatography coupled to tandem mass spectrometry (HILIC-MS/MS). Proteins were extracted using 20 mmol/L Tris-HCl (pH 7.5), 4 M guanidine hydrochloride, 150 mmol/L NaCl, 1 mmol/L Na<sub>2</sub>EDTA, 1 mmol/L EGTA, 1% Triton, 2.5 mmol/L sodium pyrophosphate, 1 mmol/L betaglycerophosphate, 1 mmol/L Na<sub>3</sub>VO<sub>4</sub>, and 1 μg/mL leupeptin using the Cryolys Precellys 24 sample Homogenizer (2 × 20 s at 10000 rpm, Bertin Technologies, Rockville, MD, United States) with ceramic beads. BCA Protein Assay Kit (Thermo Scientific, Massachusetts, United States) was used to measure (A562 nm) total protein concentration (Hidex, Turku, Finland), and samples were normalized based on the tissue weight before the LC-MS/MS analysis by extracting with different volumes of MeOH:H<sub>2</sub>O (4:1, v/v). Extracted samples were analyzed by HILIC-MS/MS in both positive and negative ionization modes using a 6495 triple quadrupole system (QqQ) interfaced with a 1290 UHPLC system (Agilent Technologies). Raw LC-MS/MS data were processed using the Agilent Quantitative analysis software (version B.07.00, MassHunter Agilent technologies). Relative quantification of metabolites was based on extracted ion chromatogram areas for the monitored MRM transitions. Peak areas of detected metabolites were analyzed in "R" software, and signal intensity drift correction and noise filtering (if necessary, using CV [QC features] >30%) was done within the MRM PROBS software.

### Statistical Analysis

Data are presented as mean ± SEM, and differences are considered significant when *P* < 0.05. Comparisons between groups were analyzed using ANOVA and post hoc Tukey tests or Sidak's test when indicated. Tukey's and Sidak's test were used to test for differences between 22 °C + O<sub>2</sub> and 4 °C perfusions. Two-group comparisons were performed using Student *t* tests (Prism 9.2, GraphPad Softwares, San Diego, CA, United States). Fitting curves of the metabolites concentration over time were computed using R (version 4.1, <https://cran.r-project.org>).

## RESULTS

### Ex Vivo Kidney Perfusion Improves Kidney Perfusion and ATP Generation

To mimic DCD, kidneys underwent 60 min of warm ischemia before procurement. Kidney grafts were then perfused in a homemade MRI-compatible pulsatile perfusion machine at 22 °C with active oxygenation (22 °C + O<sub>2</sub>), at 4 °C with active oxygenation (4 °C + O<sub>2</sub>), or 4 °C without additional oxygen (4 °C, Figure 1A). After 4 h at 22 °C + O<sub>2</sub>, cortical and medullary flows were improved compared with 4 °C + O<sub>2</sub>. This was reflected by an increase in the perfusion-descending slope (+35% cortex +26% medulla, Figure 1B).



Next, mean ATP levels were measured by averaging pMRSI voxels containing graft tissue resulting in a single spectrum (Figure 2A). In fact, we previously demonstrated that mean ATP levels (average AUC of the  $\beta$ - and  $\gamma$ -ATP peaks) are reduced by warm ischemia and correlate with (IR) injuries.<sup>10</sup> Using pMRSI,  $\alpha$ -,  $\beta$ -, and  $\gamma$ -ATP and PME containing AMP were only detected during ex vivo perfusion with active oxygenation at 4 °C and 22 °C (Figure 2A). In kidneys perfused at 22 °C+O<sub>2</sub>, ATP and PME levels were 3 times higher than at 4 °C+O<sub>2</sub> perfusion (5.5 mmol/L versus 2.1 mmol/L and 0.79 mmol/L versus 0.26 mmol/L, Figure 2B). This increase of AMP and ATP levels at 22 °C+O<sub>2</sub> was confirmed by liquid chromatography-mass spectrometry (LC-MS, +59%, +36% and +45%, respectively; Figure 2C). Surprisingly, PME and ATP concentrations tended to be higher in the medulla independently of the perfusion conditions, as demonstrated by voxel mapping of the metabolites (Figure S1, SDC, <http://links.lww.com/TXD/A437>).

#### Kidney ATP Levels Increased up to 10h During Ex Vivo Subnormothermic Kidney Perfusion

In healthy kidneys perfused at 4 °C+O<sub>2</sub>,  $\alpha$ -,  $\beta$ -, and  $\gamma$ -ATP remained stable for up to 22h of perfusions.<sup>10</sup> To determine the effect of 22 °C perfusion on ATP production over time in DCD grafts, PME and  $\alpha$ -,  $\beta$ -, and  $\gamma$ -ATP concentrations were

monitored for 42h (time course experiment). Kidney  $\alpha$ -,  $\beta$ -, and  $\gamma$ -ATP concentrations were 2 times higher after 10h of perfusion compared with baseline (0.5 mmol/L to 1 mmol/L for  $\beta$ -ATP, 0.75 mmol/L to 1.5 mmol/L for  $\gamma$ -ATP; Figure 3A) and 4 °C+O<sub>2</sub>.<sup>10</sup> The PME concentration was 4 times higher than ATP at the beginning of the perfusion (4 mmol/L of PME versus 1 mmol/L of  $\alpha$ -,  $\beta$ -, and  $\gamma$ -ATP), and rapidly decreased to reach a plateau at 2 mmol/L. This is consistent with the hypothesis that the PME containing the AMP is consumed over time to generate ATP. Finally, after 10h of perfusion at 22 °C+O<sub>2</sub>, ATP levels gradually decline to ultimately reach 0 mmol/L after 42h of perfusion (Figure 3B). PME concentration remains stable for up to 42h (Figure 3B).

#### Ex Vivo Kidney Perfusion at 22 °C Reduces Kidney Ischemia and Reperfusion Injuries

To evaluate the benefit of 22 °C ex vivo perfusion before transplantation, we examined the histological damage using a modified Goujon score (described in the methods section), shown to reflect kidney function.<sup>10,25</sup> Kidney biopsies were analyzed at baseline, after 60min of warm ischemia, at the end of the ex vivo perfusion, and at 1h after transplantation. Surprisingly, no significant damage was observed after warm ischemia (Figure 4A,B). Consistent with previous findings, histological damages were significantly increased at the end of the

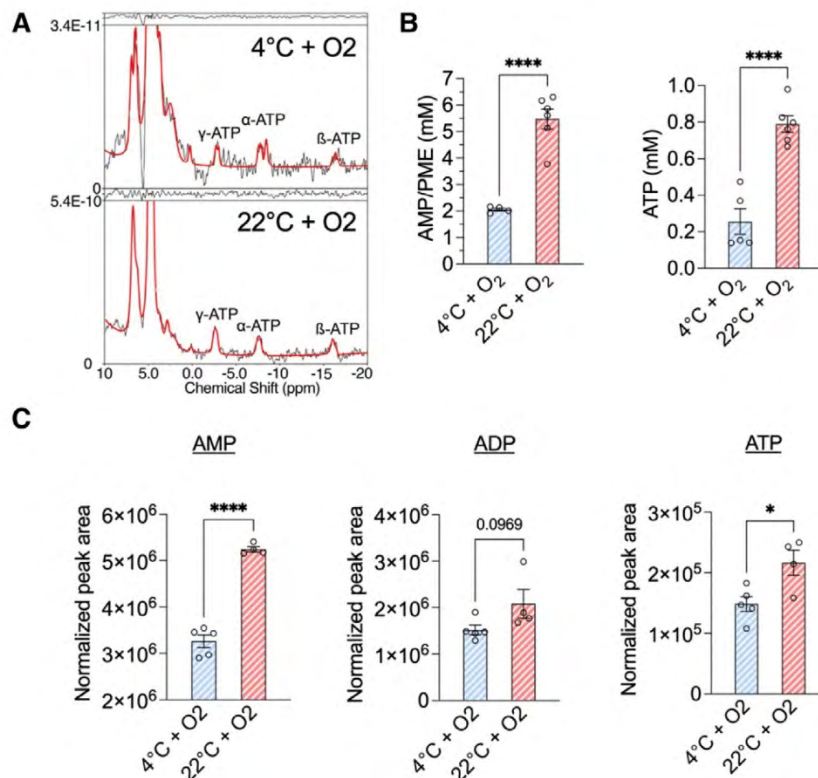


**FIGURE 2.** Energy metabolism is improved during subnormothermic perfusion. A and B, Representative of pMRSI spectra fitted with LCModel (A) and kidney PME and  $\beta$ ,  $\gamma$ -mean ATP levels (B) during 4 °C+O<sub>2</sub> and 22 °C+O<sub>2</sub> perfusion before transplantation. C, Kidney AMP, ADP, and ATP levels measured by LC-MS. Bars indicate mean  $\pm$  SEM, and asterisks indicate the significance of the difference between perfusions methods by Student's *t* test or 1-way ANOVA and Tukey test. \*\*\*\**P* < 0.0001. *n* = 4 to 5 per group. ADP, adenosine diphosphate; AMP, adenosine monophosphate; ATP, adenosine triphosphate; LC-MS, liquid chromatography-mass spectrometry; PME, phosphomonoesters; pMRSI, <sup>31</sup>P magnetic resonance spectroscopic imaging.

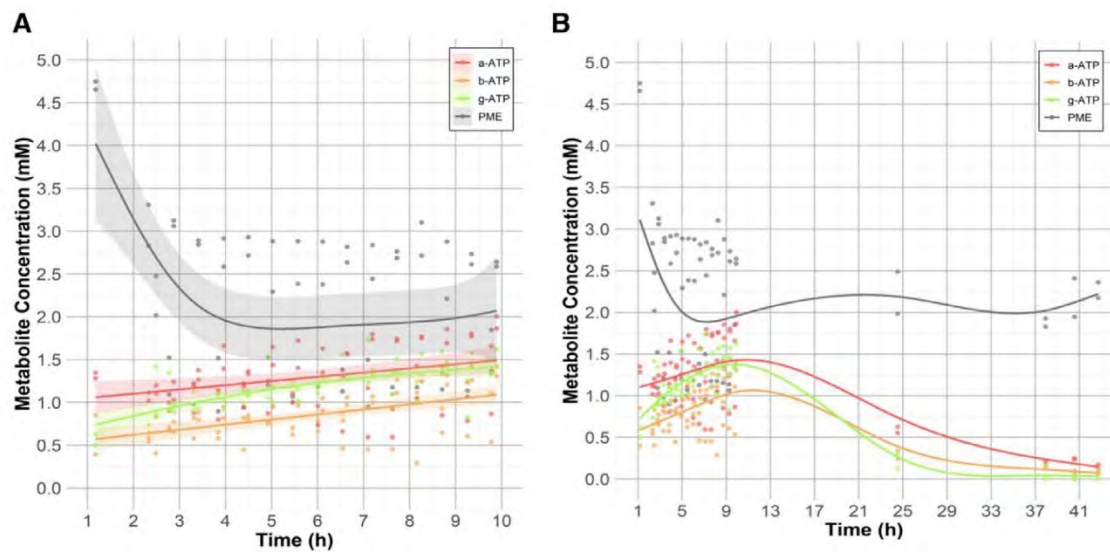


**FIGURE 3.** Kidney ATP levels increased up to 10h during ex vivo subnormothermic kidney perfusion. A, Monitoring of ATP levels during 22 °C+O<sub>2</sub> perfusion (A) up to 10h and (B) up to 42h. Concentration (mM) of the indicated metabolites over time, in kidney, during 22 °C+O<sub>2</sub> perfusion. n=4 per group. Fitting curves are generalized additive model (formula:  $y \sim s(x)$ ) with a basis size of k=15, n=3. ATP, adenosine triphosphate; PME, phosphomonoesters.

ex vivo perfusion and after reperfusion in vivo (Figure 4A,B; Table S2, SDC, <http://links.lww.com/TXD/A437>). Importantly, 22 °C perfusion led to the greatest protection from IR injury (score of 22 °C+O<sub>2</sub>, 4 °C+O<sub>2</sub>, and 4 °C: 10.5±2.3, 19.25±3.9, and 18.3±2.5,±SD, Figure 4A,B). Perfusion of 22 °C significantly reduced tubular dilatation and luminal cell debris and protected the brush border (Figure 4A; Figure S2, SDC, <http://links.lww.com/TXD/A437>). In the 22 °C ex vivo perfusion group, interleukin (IL)-6 and IL-10 gene expressions were upregulated after transplantation (log2 fold-change of 22 °C+O<sub>2</sub>, 4 °C+O<sub>2</sub>, and 4 °C: 6.5±0.8, 2.4±0.9, and 3.9±0.4 and 3.9±0.4, 1.4±0.9, 2.6±0.7, respectively), whereas the expression of TNFalpha and Arg1 remained unaffected (Figure 4C). In addition, 2h after kidney implantation, flow in the cortex and medulla improved at 22 °C+O<sub>2</sub> (+18% and +4% cortex, +17% and +11% medulla compared with 4 °C and 4 °C+O<sub>2</sub> respectively; Figure S2, SDC, <http://links.lww.com/TXD/A437>). Finally, ATP and, to a lesser extent, PME levels were significantly higher after transplantation in organs that were previously perfused 22 °C+O<sub>2</sub> (Figure 4D). Altogether, ex vivo perfusion at 22°C improved kidney metabolism and reduced (IR) injuries during transplantation.

## DISCUSSION

Here, we found that kidney graft perfusion at 22 °C with an oxygenated MP-Belzer solution, without oxygen carrier, increased ATP production and minimized IR injuries during transplantation compared with perfusion at 4 °C. Of interest, active oxygenation did not increase ATP production at 4 °C. In addition, the simplicity of subnormothermic perfusion machine, without the need for a heating unit or oxygen carrier, could be easily used in a clinical setting and lower the costs. Altogether, perfusion of kidney graft at 22 °C could translate into greater utilization of kidney allograft.

Previously, the benefits of normothermic perfusion (37 °C) were linked to an increase in fatty acid metabolism and oxidative phosphorylation.<sup>12</sup> Similarly, kidney perfusion at 22°C improved mitochondrial ATP production, consistent with our hypothesis that, at 22 °C, kidneys are metabolically active.<sup>22,28</sup> Interestingly, in cold-stored organs, it has also been shown that gradual rewarming from hypothermia to normothermia before transplantation improves kidney function,<sup>29,30</sup> highlighting the importance of restoring metabolism before implantation. At 22 °C, we observed an increase in PME and ATP levels during the first 10h of perfusion. After 10h of perfusion at 22 °C, ATP level gradually declined to reach 0 mmol/L at 42h of perfusion. We previously reported that, at 4 °C, in the absence of warm ischemia, ATP levels remained stable up to 22h of perfusion but at significantly lower levels (0.26 mmol/L).<sup>10</sup> Similarly, ATP levels decrease during cold storage in the kidney<sup>28</sup> and liver<sup>31</sup> and correlate with the degree of injury. In humans, ATP predicted immediate graft function,<sup>10,31</sup> and ATP is often used as a marker of viability during ischemia.<sup>27,32</sup> Although long-term perfusion at 22 °C using MP-Belzer solution might not be viable, it is a promising strategy to recondition organs and improve initial graft function. Future studies should investigate the advantages of short-term (<10h) reconditioning at 22 °C of previously cold-stored organs.

In this study, LC-MS/MS was used to validate the accurate quantification of nucleotides by pMRSI.<sup>27</sup> Indeed, the fitting of α-ATP with a broad Gaussian might include the NAD<sup>+</sup> and NADH signal.<sup>10,33</sup> Recent improvements using deep learning algorithms were used to reduce concentration estimation bias of metabolites with overlapping spectra.<sup>34</sup> pMRSI also suffers from a relative low sensitivity compared with liquid chromatography or 1H imaging at a constant magnetic field.<sup>10</sup> Thus, the acquisition is generally performed with higher voxel size to achieve enough signal to noise ratio while keeping an



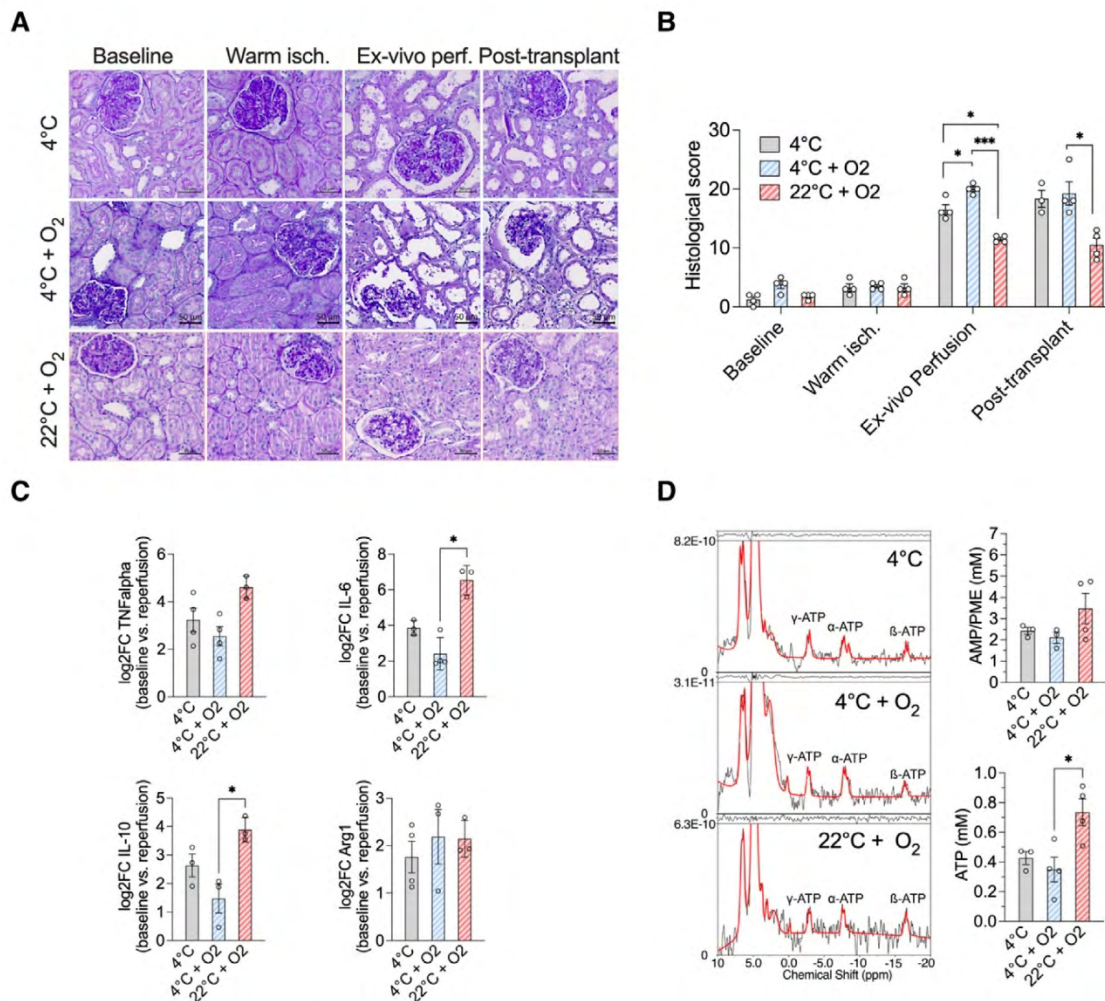


**FIGURE 4.** Subnormothermic perfusion reduces kidney damages. A and B, Representative cortical kidney sections (A) stained with PAS, and histological score (B) at the indicated time and conditions (4 °C, 4 °C + O<sub>2</sub>, 22 °C + O<sub>2</sub>). C, Expression of the indicated gene in kidney, analyzed by RT-PCR at baseline and after transplantation after 4 h of 4 °C, 4 °C + O<sub>2</sub>, or 22 °C + O<sub>2</sub> perfusion. D, Representative of pMRSI spectra (left), and quantification (right) of kidney AMP and ATP levels during 4 °C, 4 °C + O<sub>2</sub>, or 22 °C + O<sub>2</sub> perfusion after transplantation. The spectra are fitted using LCModel. Bars indicate mean ± SEM and median ± IQR. Asterisks indicate the significance of the difference between perfusions methods by 2-way ANOVA and Sidak post hoc test. \*P < 0.05, \*\*\*P < 0.001, n = 4 per group. AMP, adenosine monophosphate; ATP, adenosine triphosphate; IQR, interquartile range; PAS, periodic acid-Schiff; PME, phosphomonoesters; pMRSI, <sup>31</sup>P magnetic resonance spectroscopic imaging.

acceptable scan time. As an example, this lack of sensitivity limitation hinders the measurement of ATP at 4 °C without oxygen. The application of machine learning<sup>35</sup> and neural network can further improve pMRSI sensitivity, spatial resolution, and computing time.<sup>36</sup> Indeed, ongoing improvement in pMRSI spatial resolution, in combination with spatial phase encoding, can provide multivoxels acquisition of the kidney graft that enables metabolite mapping over the full field of view (Figure S1, SDC, <http://links.lww.com/TXD/A43737>). Overall pMRSI remains a powerful, noninvasive tool to quantify ATP.<sup>10</sup>

During ex vivo perfusion at 22 °C, we did not compare passive versus active oxygenation of Belzer MPS UW, perfusion with Hb-based oxygen carrier, or packed red blood cells. Importantly, oxygenated machine perfusion at 22 °C lowers

metabolic demand compared with organs perfused at 37 °C.<sup>38</sup> Thus, although still metabolically active, grafts maintained at 22 °C could be safely perfused with MP-Belzer without oxygen carriers. At 22 °C, Hb-based oxygen carrier achieved short-term kidney function equivalent to blood.<sup>39</sup> Similarly in human kidneys, compared with hemoglobin oxygen carrier, perfusion with packed red blood cells at 37 °C resulted in similar vascular flow, oxygen consumption, or ATP levels.<sup>40</sup> It is likely, that, although perfusion at 22 °C allows considerable recovery of energy metabolism compared with 4 °C, metabolism is significantly reduced (compared to 37 °C) so that passive oxygenation is sufficient for adequate oxygen delivery. Altogether, we hypothesize that adequate tissue oxygenation can be achieved at 22 °C without the use of packed red blood cells and complex blood perfusion machine.



Interestingly, we did not observe a benefit of active oxygenation at 4 °C, except for slightly improved graft perfusion. Consistently, the addition of oxygen to hypothermic machine perfusion did not significantly improve DCD porcine kidney function.<sup>41</sup> Similarly, a recent clinical trial failed to show 12-mo difference in eGFR between kidneys perfused at 4 °C with oxygen compared with hypothermic perfusion alone.<sup>11</sup> Previous studies comparing oxygenated perfusion used various flow rates (50–100 mL/min) and PO<sub>2</sub> levels (500–650 mmHg), complicating data interpretation.<sup>11,42–44</sup>

A potential disadvantage of normothermic preservation appears to be the generation of a proinflammatory milieu, with the accumulation of inflammatory mediators including cytokines and damage-associated molecular patterns.<sup>45,46</sup> Consistently, here both pro- and anti-inflammatory cytokines (IL-6 and IL-10, respectively) were increased after ex vivo perfusion at 22 °C. On the other hand, compared with 37 °C, ex vivo lung perfusion at 25 °C reduced the production of inflammatory mediators and was associated with reduced histologic graft injury after transplantation.<sup>47</sup> Altogether, cytokines profile and its relevance over time in kidney graft undergoing perfusion at 22 °C needs to be evaluated further.

Our study has several limitations that need to be acknowledged. First, the impact of perfusion at 22 °C and ATP levels on kidney function (serum creatinine, urea, and estimated glomerular filtration rate) or urine production after transplantation were not assessed. Consistent with previous reports, no urine output was recorded during the first hour following transplantation.<sup>48</sup> Interestingly, in human, urine production during normothermic ex vivo perfusion was not correlated with posttransplant kidney function.<sup>49</sup> Moreover, proper assessment of kidney function could not be performed because of local regulation, which did not allow survival surgery. Thus, the histological score, previously correlated with the degree of kidney injury,<sup>10,24–26</sup> was used as a surrogate endpoint of kidney function. Future clinical trials should help determine the benefits of perfusion at 22 °C on postoperative graft function. In addition, the benefits of subnormothermic perfusion should be tested in all forms of marginal donors, including kidneys from old donors, after acute kidney injury, and after prolonged cold preservation.

In conclusion, subnormothermic perfusion of porcine DCD kidneys improved ATP production and reduced IRI. Perfusion of DCD grafts at 22 °C should be tested in clinical trials to determine if it can improve posttransplant graft function and patient survival.

## ACKNOWLEDGMENTS

We thank Jean-Pierre Giliberto from the department of surgery, University Hospitals of Geneva, as well as Hector Gallart Ayala from the Metabolomics Platform, Faculty of Biology and Medicine, University of Lausanne, Switzerland, for the excellent technical assistance.

## REFERENCES

- Assis-Borba L, Cristelli MP, Paula MI, et al. Expanding the use of expanded criteria donors in kidney transplantation. *Int Urol Nephrol*. 2014;46:1663–1671.
- Summers DM, Watson CJ, Pettigrew GJ, et al. Kidney donation after circulatory death (DCD): state of the art. *Kidney Int*. 2015;88:241–249.
- Tennakore KK, Kim SJ, Alwayn IP, et al. Prolonged warm ischemia time is associated with graft failure and mortality after kidney transplantation. *Kidney Int*. 2016;89:648–658.
- Dragun D, Hoff U, Park JK, et al. Prolonged cold preservation augments vascular injury independent of renal transplant immunogenicity and function. *Kidney Int*. 2001;60:1173–1181.
- Zhao H, Alam A, Soo AP, et al. Ischemia-reperfusion injury reduces long term renal graft survival: mechanism and beyond. *Ebiomedicine*. 2018;28:31–42.
- Ponticelli C. Ischaemia-reperfusion injury: a major protagonist in kidney transplantation. *Nephrol Dial Transplant*. 2014;29:1134–1140.
- Lee CM, Carter JT, Randall HB, et al. The effect of age and prolonged cold ischemia times on the national allocation of cadaveric renal allografts. *J Surg Res*. 2000;91:83–88.
- Kayler LK, Magliocca J, Zendejas I, et al. Impact of cold ischemia time on graft survival among ECD transplant recipients: a paired kidney analysis. *Am J Transplant*. 2011;11:2647–2656.
- Moers C, Smits JM, Maathuis MH, et al. Machine perfusion or cold storage in deceased-donor kidney transplantation. *N Engl J Med*. 2009;360:7–19.
- Longchamp A, Klausner A, Songeon J, et al. Ex vivo analysis of kidney graft viability using 31p magnetic resonance imaging spectroscopy. *Transplantation*. 2020;104:1825–1831.
- Jochmans I, Brat A, Davies L, et al; COMPARE Trial Collaboration and Consortium for Organ Preservation in Europe (COPE). Oxygenated versus standard cold perfusion preservation in kidney transplantation (COMPARE): a randomised, double-blind, paired, phase 3 trial. *Lancet*. 2020;396:1653–1662.
- Urbanellis P, McEvoy CM, Skrtić M, et al. Transcriptome analysis of kidney grafts subjected to normothermic ex vivo perfusion demonstrates an enrichment of mitochondrial metabolism genes. *Transplant Direct*. 2021;7:e719.
- Urbanellis P, Hamar M, Kathis JM, et al. Normothermic ex vivo kidney perfusion improves early DCD graft function compared with hypothermic machine perfusion and static cold storage. *Transplantation*. 2020;104:947–955.
- Hosgood SA, Barlow AD, Hunter JP, et al. Ex vivo normothermic perfusion for quality assessment of marginal donor kidney transplants. *Br J Surg*. 2015;102:1433–1440.
- Kathis JM, Hamar M, Echeverri J, et al. Normothermic ex vivo kidney perfusion for graft quality assessment prior to transplantation. *Am J Transplant*. 2018;18:580–589.
- Nicholson ML, Hosgood SA. Renal transplantation after ex vivo normothermic perfusion: the first clinical study. *Am J Transplant*. 2013;13:1246–1252.
- Parente A, Osei-Bordom DC, Ronca V, et al. Organ restoration with normothermic machine perfusion and immune reaction. *Front Immunol*. 2020;11:565616.
- Eshmunin D, Becker D, Bautista Borrego L, et al. An integrated perfusion machine preserves injured human livers for 1 week. *Nat Biotechnol*. 2020;38:189–198.
- Kathis JM, Paul A, Robinson LA, et al. Ex vivo machine perfusion for renal graft preservation. *Transplant Rev (Orlando)*. 2018;32:1–9.
- Bhattacharjee RN, Ruthirakanthan A, Sun Q, et al. Subnormothermic oxygenated perfusion optimally preserves donor kidneys ex vivo. *Kidney Int Rep*. 2019;4:1323–1333.
- Bruinsma BG, Sridharan GV, Weeder PD, et al. Metabolic profiling during ex vivo machine perfusion of the human liver. *Sci Rep*. 2016;6:22415.
- Lazeyras F, Buhler L, Vallee JP, et al. Detection of ATP by “in line” 31P magnetic resonance spectroscopy during oxygenated hypothermic pulsatile perfusion of pigs’ kidneys. *MAGMA*. 2012;25:391–399.
- Provencher SW. Automatic quantitation of localized in vivo 1H spectra with LCModel. *NMR Biomed*. 2001;14:260–264.
- Longchamp A, Meier RPH, Colucci N, et al. Impact of an intra-abdominal cooling device during open kidney transplantation in pigs. *Swiss Med Wkly*. 2019;149:w20143.
- Meier RPH, Piller V, Hagen ME, et al. Intra-abdominal cooling system limits ischemia-reperfusion injury during robot-assisted renal transplantation. *Am J Transplant*. 2018;18:53–62.
- Goujon JM, Hauet T, Menet E, et al. Histological evaluation of proximal tubule cell injury in isolated perfused pig kidneys exposed to cold ischemia. *J Surg Res*. 1999;82:228–233.
- Longchamp A, Mirabella T, Arduini A, et al. Amino acid restriction triggers angiogenesis via GCN2/ATF4 regulation of VEGF and H2S production. *Cell*. 2018;173:117–129.e14.

28. Buchs JB, Lazeyras F, Bühler L, et al. [The viability of kidneys tested by gadolinium-perfusion MRI during ex vivo perfusion]. *Prog Urol*. 2009;19:307–312.
29. Bruinsma BG, Yeh H, Ozer S, et al. Subnormothermic machine perfusion for ex vivo preservation and recovery of the human liver for transplantation. *Am J Transplant*. 2014;14:1400–1409.
30. Mahboub P, Ottens P, Seelen M, et al. Gradual rewarming with gradual increase in pressure during machine perfusion after cold static preservation reduces kidney ischemia reperfusion injury. *PLoS One*. 2015;10:e0143859.
31. González FX, Rimola A, Grande L, et al. Predictive factors of early post-operative graft function in human liver transplantation. *Hepatology*. 1994;20:565–573.
32. de Rougemont O, Breitenstein S, Leskosek B, et al. One hour hypothermic oxygenated perfusion (HOPE) protects nonviable liver allografts donated after cardiac death. *Ann Surg*. 2009;250:674–683.
33. Graveron-Demilly D. Quantification in magnetic resonance spectroscopy based on semi-parametric approaches. *MAGMA*. 2014;27:113–130.
34. Iqbal Z, Nguyen D, Thomas MA, et al. Deep learning can accelerate and quantify simulated localized correlated spectroscopy. *Sci Rep*. 2021;11:8727.
35. Lam F, Li Y, Guo R, et al. Ultrafast magnetic resonance spectroscopic imaging using SPICE with learned subspaces. *Magn Reson Med*. 2020;83:377–390.
36. Lee HH, Kim H. Deep learning-based target metabolite isolation and big data-driven measurement uncertainty estimation in proton magnetic resonance spectroscopy of the brain. *Magn Reson Med*. 2020;84:1689–1706.
37. Klauser A, Klauser P, Grouiller F, et al. Whole-brain high-resolution metabolite mapping with 3D compressed-sensing SENSE low-rank. *NMR Biomed*. 2022;35:e4615.
38. Raigani S, Carroll C, Griffith S, et al. Improvement of steatotic rat liver function with a defatting cocktail during ex situ normothermic machine perfusion is not directly related to liver fat content. *PLoS One*. 2020;15:e0232886.
39. Bhattacharjee RN, Patel SVB, Sun Q, et al. Renal protection against ischemia reperfusion injury: hemoglobin-based oxygen carrier-201 versus blood as an oxygen carrier in ex vivo subnormothermic machine perfusion. *Transplantation*. 2020;104:482–489.
40. Aburawi MM, Fontan FM, Karimian N, et al. Synthetic hemoglobin-based oxygen carriers are an acceptable alternative for packed red blood cells in normothermic kidney perfusion. *Am J Transplant*. 2019;19:2814–2824.
41. Venema LH, Brat A, Moers C, et al. Effects of oxygen during long-term hypothermic machine perfusion in a porcine model of kidney donation after circulatory death. *Transplantation*. 2019;103:2057–2064.
42. De Beule J, Jochmans I. Kidney perfusion as an organ quality assessment tool—are we counting our chickens before they have hatched? *J Clin Med*. 2020;9:E879.
43. Jochmans I, Akhtar MZ, Nasralla D, et al. Past, present, and future of dynamic kidney and liver preservation and resuscitation. *Am J Transplant*. 2016;16:2545–2555.
44. Hoyer DP, Gallinat A, Swoboda S, et al. Subnormothermic machine perfusion for preservation of porcine kidneys in a donation after circulatory death model. *Transpl Int*. 2014;27:1097–1106.
45. Scheuermann U, Zhu M, Song M, et al. Damage-associated molecular patterns induce inflammatory injury during machine preservation of the liver: potential targets to enhance a promising technology. *Liver Transpl*. 2019;25:610–626.
46. Sadaria MR, Smith PD, Fullerton DA, et al. Cytokine expression profile in human lungs undergoing normothermic ex-vivo lung perfusion. *Ann Thorac Surg*. 2011;92:478–484.
47. Gloria JN, Yerxa J, Kessell SJ, et al. Subnormothermic ex vivo lung perfusion attenuates graft inflammation in a rat transplant model. *J Thorac Cardiovasc Surg*. 2021;164:e59–e70.
48. Juriasingani S, Ruthirakanthan A, Richard-Mohamed M, et al. Subnormothermic perfusion with H. *Biomolecules*. 2021;11:446.
49. Mazilescu LI, Urbanellis P, Kim SJ, et al. Normothermic ex vivo kidney perfusion for human kidney transplantation: first north American results [published online ahead of print, 2022 Mar 1]. *Transplantation*. 2022; doi:10.1097/TP.0000000000004098

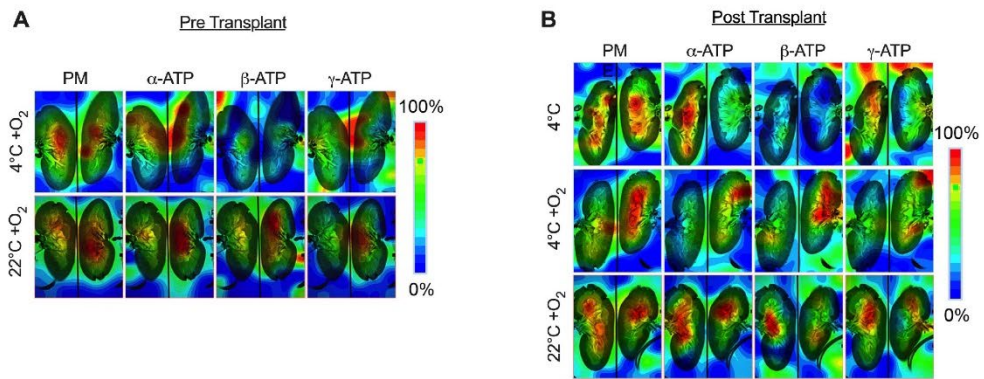


**FIGURE S1.**



Post transplant

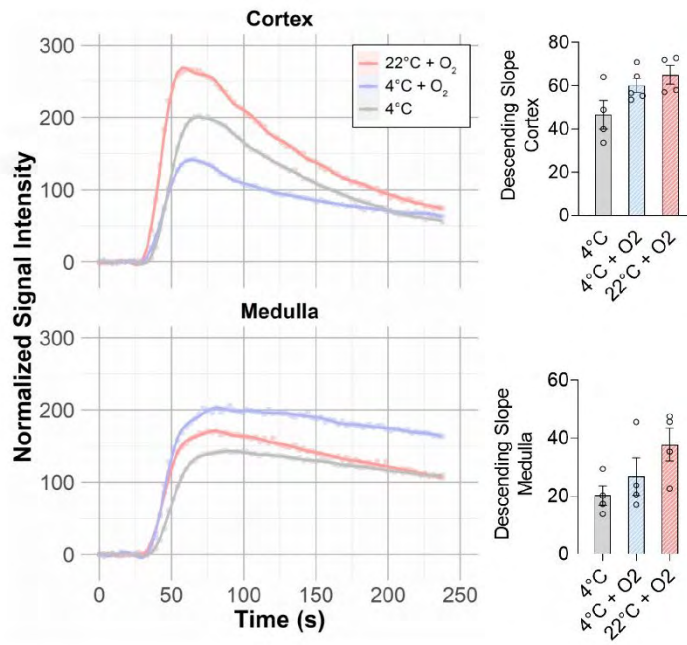


FIGURE S2.

| Oligonucleotides |                      |                         |
|------------------|----------------------|-------------------------|
| Gene             | Forward sequence     | Reverse sequence        |
| sus scrofa Agr1  | TACTGGGCGGAGACCACAGT | CCACCCAAATGACACAGAGATCT |
| sus scrofa IL10  | CTGGAAGACGTAATGCCGAA | GCTCTTGTTTTCACAGGGCA    |
| sus scrofa IL6   | CCCTGAGGCAAAGGAAAG   | ATCCACTGTTCTGTGACTGC    |
| sus scrofa TNF   | GGCCAAGGACTCAGATCAT  | CTGTCCCTCGGCTTTGACAT    |
| sus scrofa Rpl27 | CGCAAAGCGGTATCGTAA   | AATCCAGCCACCAGAGCAT     |

TABLE S1.

|                                     | Baseline     |                    |                     | Warm isch.      |                    |                     |                  | In-vivo Perfusion  |                     |                 |                    | Post-transplant     |  |  |
|-------------------------------------|--------------|--------------------|---------------------|-----------------|--------------------|---------------------|------------------|--------------------|---------------------|-----------------|--------------------|---------------------|--|--|
|                                     | 4°C          | 4°C O <sub>2</sub> | 22°C O <sub>2</sub> | 4°C             | 4°C O <sub>2</sub> | 22°C O <sub>2</sub> | 4°C              | 4°C O <sub>2</sub> | 22°C O <sub>2</sub> | 4°C             | 4°C O <sub>2</sub> | 22°C O <sub>2</sub> |  |  |
| Glomerular Integrity                | 0 (0-0)      | 1 (1-1.25)         | 0 (0-0.25)          | 1.5 (0.75-2.25) | 1 (1-1)            | 0.5 (0-1)           | 2.5 (1.75-3)     | 4 (3.75-4)         | 3 (2.75-3)          | 2.5 (0.75-4.25) | 3 (2-4.25)         | 1.5 (1-2)           |  |  |
| Tubular Distortion                  | 0 (0-0)      | 2 (1.75-3)         | 1 (0.75-1.25)       | 0 (0-0.25)      | 0 (0-0)            | 2 (1.5-2)           | 3 (2-3)          | 4 (3.75-4.25)      | 2 (2-2.25)          | 4 (3-5)         | 4.5 (3.75-5)       | 2.5 (1.75-3)        |  |  |
| Brush Border Integrity              | 0 (0-0)      | 3.2 (3-3)          | 0 (0-0)             | 0 (0-0.25)      | 0 (0-0)            | 3 (2-3)             | 3.5 (2.75-3)     | 4.5 (3.5-5)        | 2 (2-3)             | 3 (2.5-3.25)    | 4 (3.75-4.25)      | 1.5 (1-2.25)        |  |  |
| Cellular Debris in Lumen of Tubules | 0 (0-0)      | 0 (0-0.5)          | 0 (0-0.25)          | 0 (0-0)         | 0 (0-0)            | 2.5 (0-1.5)         | 3 (2.5-3.25)     | 4 (4-4.5)          | 1.5 (1.75-2.25)     | 3 (1.5-4.25)    | 4 (4-4.25)         | 3.5 (1.75-5)        |  |  |
| Interstitial Edema                  | 1.5 (0.75-2) | 2 (1-4)            | 0 (0-0.25)          | 1 (0-2)         | 2 (1-2)            | 0.5 (0-1)           | 2 (1.5-2.5)      | 2.5 (1.75-3)       | 3 (2.75-3.25)       | 2.5 (1.75-3.25) | 3.5 (1-2.25)       | 1.5 (1-2)           |  |  |
| Vasculization                       | 0 (0-0)      | 0 (0-0.25)         | 0 (0-0)             | 0 (0-0)         | 0 (0-0)            | 0 (0-0)             | 1 (0-2)          | 1.5 (0.75-2.25)    | 0 (0-0)             | 0.5 (0-1.25)    | 2 (1.5-2.25)       | 4.5 (0-3)           |  |  |
| Overall                             | 1.5 (0.75-2) | 4.5 (3.25-5)       | 2 (1.75-3)          | 3 (2.75-3.4)    | 3 (3-4)            | 3 (2.75-3.4)        | 16 (13.75-18.75) | 20 (16.75-20)      | 11.5 (11-12)        | 17 (13.5-18.75) | 18 (17-18.75)      | 16.5 (8.75-19.25)   |  |  |

TABLE S2.

## Chapter 2: Sodium Hydrosulfide Treatment During Porcine Kidney Ex Vivo Perfusion and Transplantation

This work was accepted and will be published in 2023 in the journal Transplant Direct.

- Agius, T., Songeon, J., Lyon, A., Justine, L., Ruttimann, R., Allagnat, F., Déglise, S., Corpataux, J.-M., Golshayan, D., Buhler, L., et al. (2023). Sodium Hydrosulfide Treatment During Porcine Kidney Ex Vivo Perfusion and Transplantation. Transplantation Direct XXX, e.
- DOI: [10.1097/TXD.0000000000001508](https://doi.org/10.1097/TXD.0000000000001508)

### Summary:

In rodents, hydrogen sulfide (H<sub>2</sub>S) has been found to reduce ischemia-reperfusion injuries and improve renal graft function. This research sought to determine if these benefits extend to swine, which provides a more applicable clinical model for humans. Adult porcine kidneys were subjected to 60 minutes of mild ischemia (WI) and treated with 100 μM sodium hydrosulfide (NaHS) during hypothermic ex vivo perfusion, during WI, or both. MRI spectroscopy for renal perfusion and ATP levels and histopathological evaluations of specimens did not reveal any significant improvements. Perfusion with NaHS resulted in renal perfusion, ATP levels, and histological outcomes comparable to those in the control group. While H<sub>2</sub>S appears promising in rodent models, treating pigs with NaHS did not substantially reduce ischemia-reperfusion damage or increase kidney metabolism. Further research on humans, potentially using alternative H<sub>2</sub>S donors, is recommended.



OPEN

# Sodium Hydrosulfide Treatment During Porcine Kidney Ex Vivo Perfusion and Transplantation

AQ1

AQ2

Thomas Agius, MS,<sup>1,2,3</sup> Julien Sonjeon, MS,<sup>4</sup> Arnaud Lyon, MD,<sup>1,5</sup> Justine Longchamp, MD,<sup>1</sup> Raphael Ruttimann, BS,<sup>6</sup> Florent Allagnat, PhD,<sup>1</sup> Sébastien Déglise, MD,<sup>1</sup> Jean-Marc Corpataux, MD,<sup>1</sup> Déla Golshayan, MD, PhD,<sup>5</sup> Leo Buhler, MD,<sup>7</sup> Raphael Meier, MD, PhD,<sup>8</sup> Heidi Yeh, MD,<sup>2,3</sup> James F. Markmann, MD, PhD,<sup>2,3</sup> Korkut Uygun, PhD,<sup>3</sup> Christian Toso, MD, PhD,<sup>6</sup> Antoine Klausner, PhD,<sup>4,9</sup> Francois Lazeyras, PhD,<sup>4,9</sup> and Alban Longchamp, MD, PhD<sup>1,2,3</sup>

**Background.** In rodents, hydrogen sulfide (H<sub>2</sub>S) reduces ischemia-reperfusion injury and improves renal graft function after transplantation. Here, we hypothesized that the benefits of H<sub>2</sub>S are conserved in pigs, a more clinically relevant model. **Methods.** Adult porcine kidneys retrieved immediately or after 60 min of warm ischemia (WI) were exposed to 100 μM sodium hydrosulfide (NaHS) (1) during the hypothermic ex vivo perfusion only, (2) during WI only, and (3) during both WI and ex vivo perfusion. Kidney perfusion was evaluated with dynamic contrast-enhanced MRI. MRI spectroscopy was further employed to assess energy metabolites including ATP. Renal biopsies were collected at various time points for histopathological analysis. **Results.** Perfusion for 4 h pig kidneys with Belzer MPS UW + NaHS resulted in similar renal perfusion and ATP levels than perfusion with UW alone. Similarly, no difference was observed when NaHS was administered in the renal artery before ischemia. After autotransplantation, no improvement in histologic lesions or cortical/medullary kidney perfusion was observed upon H<sub>2</sub>S administration. In addition, AMP and ATP levels were identical in both groups. **Conclusions.** In conclusion, treatment of porcine kidney grafts using NaHS did not result in a significant reduction of ischemia-reperfusion injury or improvement of kidney metabolism. Future studies will need to define the benefits of H<sub>2</sub>S in human, possibly using other molecules as H<sub>2</sub>S donors.

(*Transplantation Direct* 2023;XXX: e; doi: 10.1097/TXD.0000000000001508.)

One of the challenges in solid organ transplantation is improving the organ preservation method especially in the grafts with inferior quality. The current clinical standard for kidney preservation is hypothermic preservation/perfusion at +4°C for a typical storage duration of ~20h. Hypothermic noxygenated preservation results in a slow but inexorable deterioration of vital cellular functions, notably ATP

production and redox homeostasis, eventually leading to cell death. Hypothermic machine perfusion (HMP) has been developed as an alternative preservation method to static cold storage (SCS) with promising short-term results.<sup>1</sup> In a landmark study including 672 kidney transplant recipients, HMP reduced ischemia-reperfusion injury, clinically manifested as delayed graft function (DGF).<sup>2</sup> These results were confirmed

Received 14 April 2023. Revision received 1 May 2023.

Accepted 16 May 2023.

<sup>1</sup> Department of Vascular Surgery, Lausanne University Hospital, Lausanne, Switzerland.

<sup>2</sup> Department of Surgery, Transplant Center, Massachusetts General Hospital, Harvard Medical School, Boston, MA.

<sup>3</sup> Department of Surgery, Center for Engineering in Medicine, Massachusetts General Hospital, Harvard Medical School, Boston, MA.

<sup>4</sup> Department of Radiology and Medical Informatics, University of Geneva, Geneva, Switzerland.

<sup>5</sup> Department of Medicine, Transplantation Centre, Lausanne University Hospital, Lausanne, Switzerland.

<sup>6</sup> Visceral and Transplant Surgery, Department of Surgery, Geneva University Hospitals and Medical School, Geneva, Switzerland.

<sup>7</sup> Section of Medicine, Faculty of Science and Medicine, University of Fribourg, Switzerland.

<sup>8</sup> Department of Surgery, University of Maryland School of Medicine, Baltimore, MD.

<sup>9</sup> CIBM Center for Biomedical Imaging, Geneva, Switzerland.

The authors declare no conflicts of interest.

Supported by the Swiss National Science Foundation to J.M.C., FL (SNSF 320030\_182658), and AL (SNSF PZ00P3-185927) as well as the Mendez National Institute of Transplantation, and the Mercier Foundation to AL.

T.A., J.S., F.A., S.D., J.M.C., L.B., R.M., K.U., C.T., A.K., F.L., and A.L. participated in research design. T.A., J.S., Ar.L., J.L., R.R., F.A., S.D., J.M.C., D.G., L.B., R.M., H.Y., J.F.M., K.U., C.T., A.K., F.L., and A.L. participated in the writing of the article. T.A., J.S., Ar.L., J.L., R.R., J.M.C., R.M., A.K., F.L., and A.L. participated in the performance of the research. T.A., J.S., Ar.L., J.L., F.L., and A.L. participated in data analysis.

Correspondence: Alban Longchamp, MD, PhD, Division of Transplantation, Massachusetts General Hospital, Mass General Brigham, 55 Fruit Street, Boston, MA. (alongchamp@mgh.harvard.edu).

Copyright © 2023 The Author(s). *Transplantation Direct*. Published by Wolters Kluwer Health, Inc. This is an open-access article distributed under the terms of the Creative Commons Attribution-Non Commercial-No Derivatives License 4.0 (CCBY-NC-ND), where it is permissible to download and share the work provided it is properly cited. The work cannot be changed in any way or used commercially without permission from the journal.

ISSN: 2373-8731

DOI: 10.1097/TXD.0000000000001508

AQ4

AQ3



by later meta-analysis, demonstrating that HMP reduces the incidence of DGF in all types of donors: standard and extended criteria donors, in both donation after brainstem and donation after circulatory death (DCD).<sup>1</sup>

Hydrogen sulfide ( $H_2S$ ) is a small endogenous gaseous molecule produced mainly by cystathionine gamma-lyase (CGL) or cystathionine beta-synthase.<sup>3,4</sup> During ischemia-reperfusion injury, genetic deletion of CGL was shown to increase damage and mortality after renal ischemia-reperfusion injury in mice, which could be rescued by exogenous  $H_2S$  sodium hydrosulfide (NaHS).<sup>5</sup> Similarly, we demonstrated that administration of exogenous NaHS in wild-type mice reduced hepatic and renal ischemia-reperfusion injury.<sup>6</sup> Addition of NaHS to Belzer MPS UW preservation solution in SCS reduced necrosis apoptosis and improved early kidney function after transplantation in rats.<sup>7</sup> In porcine kidneys subjected to 2h of warm ischemia (WI), administration of  $H_2S$  systemically or into the renal artery before reperfusion improved creatine clearance, reduced apoptosis, and tubular injury.<sup>8</sup> Moreover, the addition of AP39 (a mitochondrial-targeted  $H_2S$  donor) during porcine kidneys subnormothermic perfusion (21°C) for 4h with an  $O_2$  carrier (Hemopure) improved urine output and graft oxygenation.<sup>9</sup>

Relevant to ischemia-reperfusion injury,  $H_2S$  was shown to have direct antioxidant properties,<sup>10</sup> can promote glutathione synthesis and induced stress response pathways (eg, Nrf2).<sup>11</sup> Of importance, we previously demonstrated that  $H_2S$  can reversibly inhibit the mitochondrial electron transport chain, thus reducing reactive oxygen species (ROS) formation during reperfusion.<sup>3,12</sup> In ischemic conditions,  $H_2S$  promotes glucose uptake and glycolytic ATP production.<sup>3</sup> The ATP depletion occurring during ischemia causes inhibition of mitochondrial  $Na^+/K^+$  ion channels, resulting in increased mitochondrial inner membrane permeability and cell death. In prior studies, we used MRI, and <sup>31</sup>P magnetic resonance spectroscopic imaging (pMRSI) for the detection of high-energy phosphate metabolites such as ATP during kidney transplantation.<sup>13</sup> In fact, recovery from ischemia-reperfusion injury is an ATP-dependent process,<sup>14</sup> and ATP level was shown to determine kidney graft function following transplantation.<sup>13</sup>

Here, using MRI and pMRSI, we examined the effect of exogenous  $H_2S$  (NaHS) in a relevant porcine ex vivo HMP model and autotransplantation. The effect of  $H_2S$  was evaluated in both kidneys that were retrieved immediately, as well as after 60min of warm ischemia to mimic circulatory arrest during DCD procurement. To increase the translational value of our study, NaHS was given in relevant clinical situations, including ex vivo perfusion only, or concomitant to heparin administration before WI.

## MATERIAL AND METHODS

### Animals and Surgery

The study was approved by the University of Geneva's animal ethics committee (protocol number: GE83/33556). Five-month-old female pigs were obtained from the animal facility of Arare, Switzerland. All pigs were maintained under standard conditions. Water and food were provided ad libitum. Animals were premedicated, anesthetized then kept intubated and ventilated during the procedure.<sup>15</sup> An arterial line was inserted in the internal carotid artery. Monitoring included heart rate, systemic blood pressure, pulse oximetry, and end-tidal  $CO_2$ .

All surgeries were performed by the same surgeon. After a midline incision, the peritoneal cavity was opened, and the bowels were retracted. Abdominal aorta, inferior vena cava, and renal vessels were dissected. The pigs received 300 IU/kg heparin intravenously. In some groups, 1 ml of 100  $\mu$ M NaHS was administered into the renal artery 10 min before clamping. The kidneys were either immediately explanted or after 60 min of WI (DCD model). During the WI, the arterial inflow was interrupted using an atraumatic clamp. Blood flow cessation was verified using a handheld Doppler. The model did not include an agonal phase. Kidneys were then instantly flushed with 1 L of Belzer MPS UW Machine Perfusion Solution on ice with or without 100  $\mu$ M NaHS. The renal artery was cannulated, and the kidneys were perfused for 3h (see later), as previously described using our MRI-compatible machine.<sup>13,16</sup> At the end of the perfusion, both kidneys were transplanted sequentially with anastomosis on the inferior vena cava and infrarenal aorta using a prolene 6-0 running suture. Of importance, the implantation of 2 kidneys in the same recipient precluded any blood-based analysis of kidney function. After 2h of in vivo reperfusion, pigs were sacrificed using 100 mEq of potassium chloride intravenously.

### Ex Vivo Kidney Perfusion

Flushed kidneys were perfused for a total of 4h (3h before the MRI, 45 min during the MRI, and 15 min transport to the MRI, see later) with Belzer MPS UW Machine Perfusion Solution in presence or absence of 100  $\mu$ M NaHS (as indicated in the figures and legends), active oxygenation was achieved using a 0.15 m<sup>2</sup> membrane oxygenator (Biochrom Ltd, Cambridge, UK), maintaining the  $pO_2$  levels at 100 kPa for the whole preservation time, and measured every 30min with a blood gas analyzer. The perfusion module was kept in an insulating box containing ice keeping the kidney at 4°C. Systolic and diastolic pressure were set at 40 and 20 mm Hg, respectively.

### MRI

MRI and pMRSI (see later) were performed during the ex vivo perfusion pretransplantation, and posttransplantation, as indicated in the figures and legends. Measurements were performed on a 3 Tesla multi-nuclear Prisma-fit 3T whole-body MRI scanner (Siemens Healthineers, Erlangen, Germany). <sup>1</sup>H imaging was performed with the body coil using a T2-weighted sequence (turbo SE, TR 6530ms, TE 110ms, 2mm slices) for kidney localization and structural imaging. Dynamic contrast-enhanced MRI with gadolinium was used to determine the perfusion distribution between the cortex and the medulla, a surrogate of glomerular filtration rate as previously described.<sup>13,16</sup> Data were collected using a dynamic 2D sequence with the scanner body coil. This sequence has an inversion time of 255ms, a flip angle of 12°, 1.3mm × 1.3mm resolution, 6 slices of 4mm (1mm gap), TR 500ms, and a TE of 1.4ms. The perfusion-descending cortical slope (DS) was determined for the cortex and the medulla using the angle of the linear regression between the maximum signal value and the lowest intensity point after the initial peak.<sup>13</sup>

### <sup>31</sup>P Magnetic Resonance Spectroscopic Imaging

pMRSI was performed as described previously.<sup>13,16,17</sup> Briefly, a single-loop <sup>31</sup>P-tuned coil fixed at the bottom of the perfusion tank allows the measurement of the signal. Scanner embedded body coil was used for <sup>1</sup>H imaging and for shimming

AQ5



to ensure field homogeneity. pMRSI consisted of 3D spatial encoding, with a field-of-view  $250 \times 250 \times 160 \text{ mm}^3$ , matrix size  $16 \times 16 \times 8$ , nominal spatial resolution  $15.6 \times 15.6 \times 20 \text{ mm}^3$ , TR 1.0s, flip angle 35 degrees, echo delay 0.6ms, bandwidth 4000 Hz, 2 k sampling points. Elliptical encoding with 18 weighted averages resulted in an acquisition time of 45 min. The resonance of the inorganic phosphate (Pi, 5.2 ppm), which is uniformly present in the container and the kidney, was used as a reference for quantification of the pMRSI signal. Excitation pulse bandwidth has been adjusted to the ATP frequency range (Pi resonance—500 Hz). An exponential time filter (apodization) with 20 Hz bandwidth, zeroth, and first-order phase corrections were used to process the spectra. The metabolites (ATP, phosphomonoesters, Pi, phosphocreatine) were fitted with Gaussian peaks using the syngo.via software (SIEMENS, Erlangen, Germany) and were estimated over the whole kidneys by averaging pMRSI voxels containing graft tissue, resulting in a single spectrum. The 3 ATP peaks were quantified separately to prevent methodological bias because of excitation profile imperfection. In each condition, pMRSI allowed the detection of Alpha ( $\alpha$ )-, beta ( $\beta$ )-, and gamma ( $\gamma$ )-ATP and phosphomonoesters composed of phosphocholine, phosphoethanolamine, and AMP. ATP and phosphomonoesters concentration (mM) were calculated using a known concentration of the Pi (25 mM) as reference.<sup>13</sup> As single ATP concentration was calculated by average of the  $\alpha$ -,  $\beta$ -, and  $\gamma$ -ATP values.

### Histopathological Analysis of Biopsies

Surgical kidney cortical biopsies were collected at baseline (before clamping), after WI, at the end of the ex vivo perfusion (pretransplantation), and after 2 h of reperfusion/transplantation (posttransplantation) which were formalin-fixed then embedded in paraffin. Fixed kidney biopsies were cut into sections of 3  $\mu\text{m}$  thickness and stained with silver Jones and periodic acid-Schiff. Slides were scanned using an Axio Scan z1 slide scanner (Zeiss). The histopathological analysis score was performed based on those described by Goujon et al<sup>16,18,19</sup> using Zen software (Zeiss) and previously demonstrated to reflect the degree of injury posttransplantation.<sup>13,16</sup> Whole biopsies were assessed and blinded to group assignment. The following categories were assessed: glomerular integrity, tubular dilatation, tubular brush border integrity, cellular debris in the lumen of tubules, interstitial edema, and tubular cell vacuolization. Each category was assigned a score of 0–3 (low to high degree of injury), which was then converted to a percentage of damage. This was converted to a final scale from 0 to 5 according to the percentage of damage: 0%–15% (0), 15%–30% (1), 30%–45% (2), 45%–60% (3), 60%–75% (4), and >75% (5) using the following formula:  $(\text{Category}_{\text{final}} / 3) * 100$ . The final score for each biopsy ranged from 0 to 30 with 30 the highest score corresponding to more severe damage. Scoring was performed blindly by 2 independent researchers.

### Statistical Analysis

Data are presented as mean  $\pm$  SEM, and differences are considered significant when  $P < 0.05$ . Comparisons between groups were analyzed using ANOVA and post hoc Tukey tests. Two-group comparisons were performed using Student *t* tests (Prism 9.2, GraphPad Softwares, San Diego, CA). Fitting curves of the concentration of metabolites over time were computed using R (4.1, <https://cran.r-project.org>).

## RESULTS

### H<sub>2</sub>S Treatment During Hypothermic Machine Perfusion

We first examined the effect of H<sub>2</sub>S administration during ex vivo perfusion (Figure 1A). Immediately after harvest, kidneys were flushed and perfused with 4°C Belzer MPS UW solution with or without (control) 100  $\mu\text{M}$  NaHS before autotransplantation. After 3 h of cold perfusion, cortical and medullary flow were similar in both the control- and the NaHS-treated kidneys (Figure 1B). This was reflected by the absence of significant differences in the DS ( $-78 \pm 1.32$  and  $P = 0.53$  cortex,  $-67 \pm 14.8$ ;  $P = 0.10$  medulla for control and NaHS, respectively, Figure 1B). Next, mean ATP levels were measured by averaging pMRSI voxels containing graft tissue.<sup>13,16</sup> Alpha ( $\alpha$ ), beta ( $\beta$ ), and gamma ( $\gamma$ ) ATP, and phosphomonoesters containing AMP, were similar in both groups (Figure 1C). Similarly, post-autotransplantation, cortical and medullary flow (Figure 1D), and ATP levels (Figure 1E) were similar in both control- and NaHS-treated kidneys. Finally, we examined the histologic damage using a modified Goujon score (described in the methods section), shown to reflect kidney function.<sup>13,16,18</sup> Kidney biopsies were analyzed at baseline, at the end of the ex vivo perfusion (pretransplantation), and 2 h posttransplantation. Consistent with previous findings, histologic damages, were significantly increased after transplantation/ reperfusion (Figure 1F). It is important to note that treatment with NaHS during ex vivo perfusion did not reduce histologic injuries, such as tubular dilatation, luminal cell debris, and brush border lesions before and after transplantation (Figure 1F).

### H<sub>2</sub>S Treatment During Hypothermic Machine Perfusion in DCD Grafts

Since we did not observe any benefits of H<sub>2</sub>S treatment in organs retrieved immediately, we next investigated the effect of NaHS in kidneys obtained after 60 min of WI. Immediately after procurement, kidneys were flushed and perfused for 3 h with 4°C Belzer MPS UW solution with 100  $\mu\text{M}$  NaHS or vehicle (control) before autotransplantation (Figure 2A). In DCD kidneys, at the end of 4°C ex vivo perfusion, cortical and medullary flow were similar in both the control- and the NaHS-treated kidneys (Figure 2B). Similarly, at the end of ex vivo perfusion, ATP levels were unaffected by NaHS administration (Figure 2C). In addition, after transplantation, kidney perfusion (Figure 2D), ATP levels (Figure 2E), and histologic injuries (Figure 2F) were not reduced by the administration of NaHS during the ex vivo perfusion.

### H<sub>2</sub>S Treatment Before Ischemia in DCD

The absence of significant differences observed between the control- and H<sub>2</sub>S-treated DCD kidneys might be related to the timing of NaHS administration. Thus, we investigated the effect of a single injection of 100  $\mu\text{M}$  NaHS, directly into the renal artery before the interruption of blood flow (WI, Figure 3A). In these conditions, kidney perfusion and descending slopes were similar in both the control and NaHS-treated kidney (Figure 3B) during ex vivo perfusion. Similarly, intrarterial NaHS administration before ischemia did not impact ATP production in perfused kidneys (Figure 3C). After transplantation, cortical and medullary perfusion were similar in both groups (Figure 3D). Similarly, we did not observe differences in ATP concentration (Figure 3E) or histologic injuries (Figure 3F).

F1

F2

F3



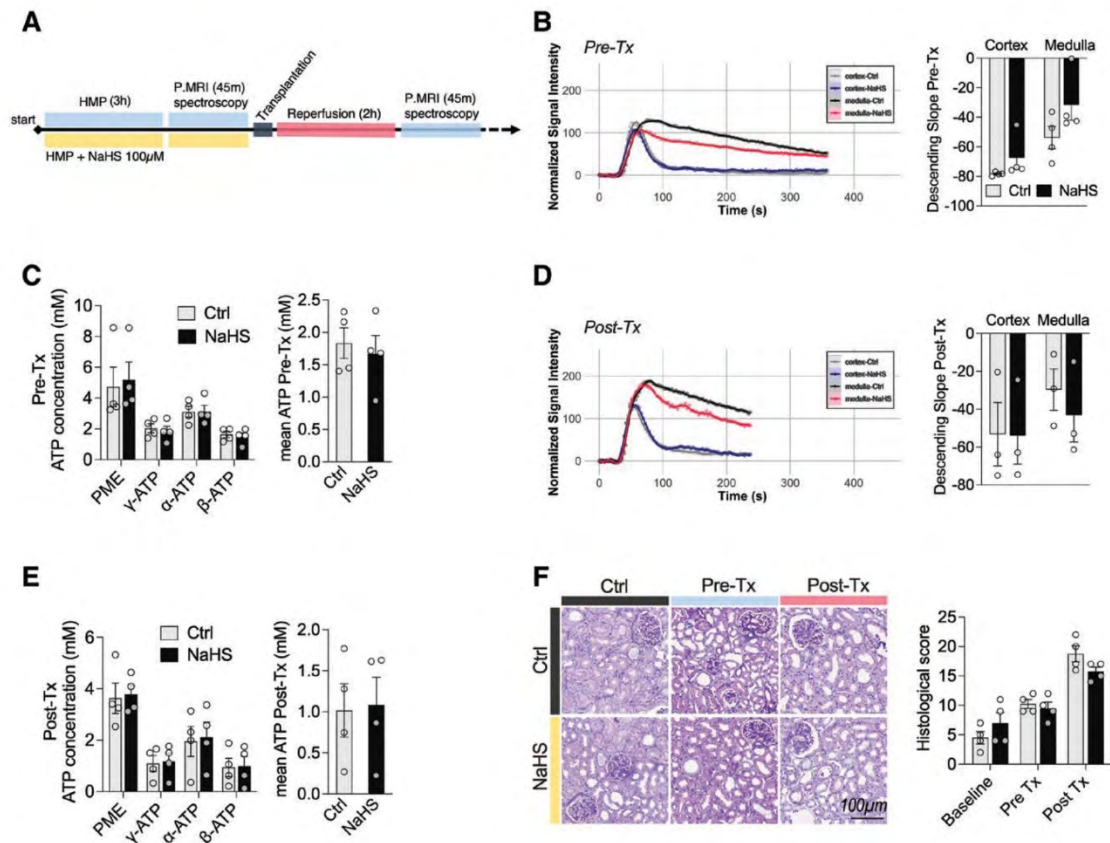


**FIGURE 1.** Effects of hydrogen sulfide supplementation during HMP. (A) Experimental design. Pig kidneys were perfused at 4°C with O<sub>2</sub> (HMP) with Belzer MPS UW with or without 100 μM NaHS for 3 h, during <sup>31</sup>P MRSI and before autotransplantation (reperfusion) and posttransplant <sup>31</sup>P MRSI during <sup>31</sup>P MRSI and before autotransplantation (reperfusion) and posttransplant <sup>31</sup>P MRSI (B) Pretransplant cortical and medullary Gd-normalized signal intensity over time (right) and quantification (descending slopes, left) in the indicated groups. (C) Pretransplant phosphomonoesters, α, β, and γ ATP levels (left) and mean ATP (right) in control- and NaHS-treated kidney. (D) Posttransplant cortical and medullary Gd-normalized signal intensity over time (right) and quantification (descending slopes, left) in the indicated groups. (E) Posttransplant phosphomonoesters, α, β, and γ ATP levels (left) and mean ATP (right) in control- and NaHS-treated kidney. (F) Representative transverse PAS-stained sections of kidneys at the indicated time in control and NaHS groups (left) and quantification of histologic damages (score, right). Data expressed as mean ± SEM, n = 4. Gd, gadolinium; HMP, hypothermic machine perfusion; NaHS, sodium hydrosulfide; PAS, periodic acid-Schiff; PMRSI, <sup>31</sup>P magnetic resonance spectroscopic imaging.

We reasoned that a single injection of NaHS before WI might be insufficient because of uncontrolled rapid delivery of H<sub>2</sub>S observed with NaHS. Therefore, 100 μM NaHS was administered into the renal artery, before WI as well as in the perfusate, during the entire ex vivo perfusion period (Figure 4A). Under this condition, cortical and medullary perfusion after transplantation were similar in the vehicle and NaHS-treated kidney (Figure 4B). α, β, and γ ATP, and phosphomonoesters containing AMP, were similar in both groups (Figure 4C). Finally, using the Goujon score, we did not detect significant differences in histologic damages in both groups (Figure 4D).

**DISCUSSION**

In this study, we found that 100 μM NaHS administration during ex vivo kidney perfusion in kidney porcine graft, and before WI in a DCD model, did not improve energy metabolism, kidney perfusion, or histologic damages upon transplantation.

Our group and others previously demonstrated that NaHS protects against renal ischemia-reperfusion injury in several models of warm tissue ischemia, as well as during cold preservation before transplantation in rodents.<sup>3,6,8,20</sup> However, we could not replicate these findings here in an adult pig model (approximately animal weight 35 kg) during cold storage followed by in vivo reperfusion/transplantation. Of interest, in mice, exposure to 20–80 ppm gaseous H<sub>2</sub>S dose-dependently decreased energy expenditure within a few minutes, as assessed by whole-body O<sub>2</sub> uptake and CO<sub>2</sub> production. This fall in metabolic activity was associated with bradypnea and consecutive hypothermia, with core temperature falling to levels close to ambient values.<sup>21</sup> Subsequent work has thus described and studied H<sub>2</sub>S-induced suspended animation—a hibernation-like state. Various other rodent models confirmed these observations: Inhaling gaseous H<sub>2</sub>S<sup>22</sup> and infusing the soluble sulfide salts (NaHS or Na<sub>2</sub>S) Na<sub>2</sub>S also induced a reversible reduction in energy expenditure with a subsequent fall in core temperature.<sup>23</sup> Of utmost importance, the metabolic

F4



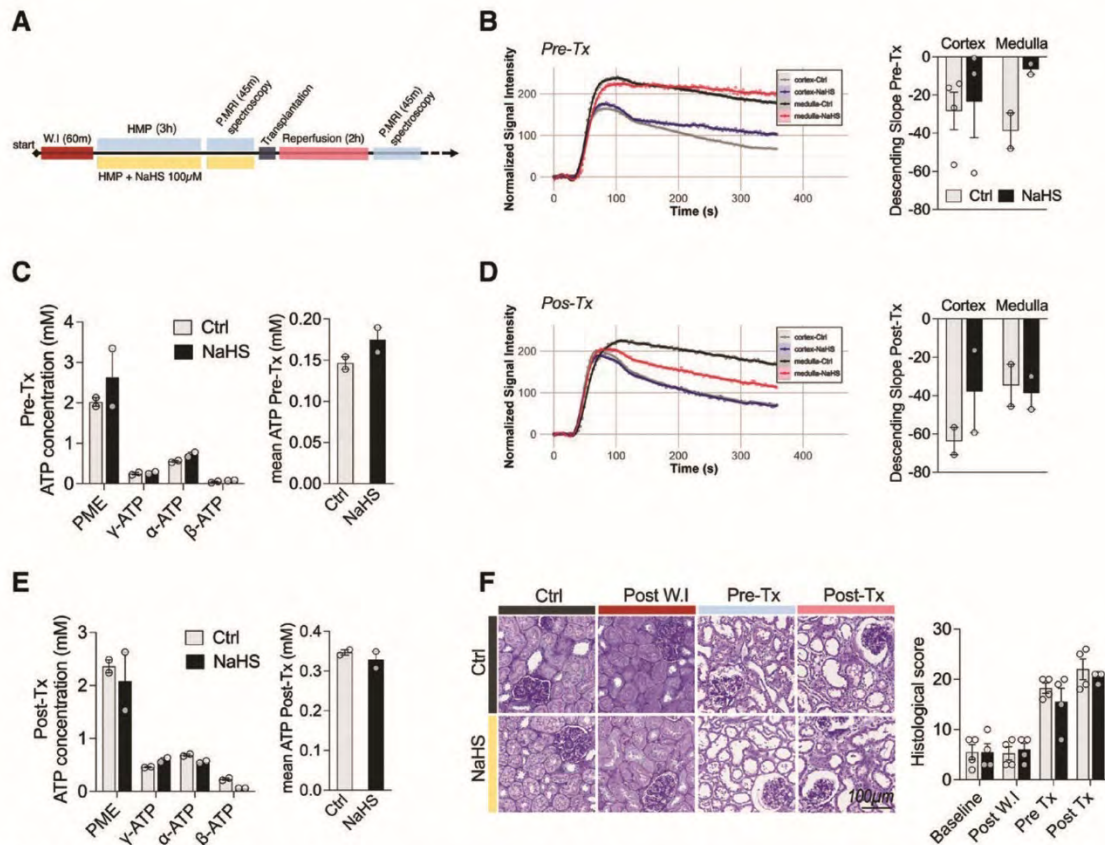


**FIGURE 2.** Effects of hydrogen sulfide supplementation during HMP in a DCD model. (A) Experimental design. Pig kidneys underwent 60 min of WI before 4°C oxygenated (HMP) with Belzer MPS UW with or without 100 μM NaHS for 3 h during <sup>31</sup>P MRSI and before autotransplantation (reperfusion) and posttransplant <sup>31</sup>P MRSI assessment. (B) Pretransplant cortical and medullar Gd-normalized signal intensity over time (right) and quantification (descending slopes, left) in the indicated groups. (C) Pretransplant phosphomonoesters, α, β, and γ ATP levels (left) and mean ATP (right) in control- and NaHS-treated kidney. (D) Posttransplant cortical and medullar Gd-normalized signal intensity over time (right) and quantification (descending slopes, left) in the indicated groups. (E) Posttransplant phosphomonoesters, α, β, and γ ATP levels (left) and mean ATP (right) in control- and NaHS-treated kidney. (F) Representative transverse PAS-stained sections of kidneys at the indicated time in control and NaHS groups (left) and quantification of histologic damages (score, right). Data expressed as mean ± SEM, n = 3. DCD, donation after circulatory death; HMP, hypothermic machine perfusion; NaHS, sodium hydrosulfide; PAS, periodic acid-Schiff; PMRSI, <sup>31</sup>P magnetic resonance spectroscopic imaging; WI, warm ischemia.

depressant property of H<sub>2</sub>S appears to depend on the animal size. In rats, the H<sub>2</sub>S-induced decrease in O<sub>2</sub> uptake was several-fold lower than in mice.<sup>24</sup> In larger species (swine, sheep), various authors failed to confirm any H<sub>2</sub>S-related reduction in metabolic activity at all, regardless of the administration route.<sup>25</sup> Similarly, in sheep, gaseous H<sub>2</sub>S administration had no impact on whole-body O<sub>2</sub> uptake, CO<sub>2</sub> production, and cardiac output.<sup>26</sup> The reduction in oxygen consumption induced by H<sub>2</sub>S is thought to occur via reversible inhibition of the mitochondrial electron transport complex I and IV.<sup>3</sup> Upon reperfusion, the accumulated succinate is rapidly re-oxidized, driving extensive ROS generation by reverse electron transport at mitochondrial complex I.<sup>27</sup> It is important to note that it remained to be tested if the inhibition of complex I is required to protect from ischemia-reperfusion injury upon H<sub>2</sub>S exposure. However, these data are consistent with our latest findings and suggest that achieving metabolic suppression (suspended animation-like status), and subsequent protection from warm and cold ischemia in larger animals, or

humans will be more difficult and would require more time because of the small surface area/mass ratio.<sup>28</sup> Alternatively, H<sub>2</sub>S can directly scavenge ROS, or at more relevant physiological concentration can stimulate antioxidant pathways (such as glutathione via the transsulfuration pathways).<sup>10</sup>

NaHS dissociates to Na<sup>+</sup> and HS<sup>-</sup>, and then binds partially to H<sup>+</sup> to form undissociated H<sub>2</sub>S. Although H<sub>2</sub>S levels were not measured in this study, NaHS rapidly releases H<sub>2</sub>S, the effect occurring within seconds.<sup>3</sup> Thus, NaHS rapid and uncontrolled delivery of H<sub>2</sub>S might contribute to the absence of effect observed in this study. diallyl trisulfide and diallyl disulfide are other H<sub>2</sub>S-releasing molecules that protect from ischemia-reperfusion injury but are also unstable and short-lived.<sup>29</sup> Morpholin-4-ium-4-methoxyphenyl phosphinodithioate (GYY4137) might be a more attractive alternative, as it releases H<sub>2</sub>S at a slow and steady rate at physiological pH and temperature.<sup>30</sup> GYY4137 was shown to mitigate renal acute kidney injury following ischemia-reperfusion in mice.<sup>31</sup> In vitro, the mitochondrial-targeted H<sub>2</sub>S prodrug AP39 was



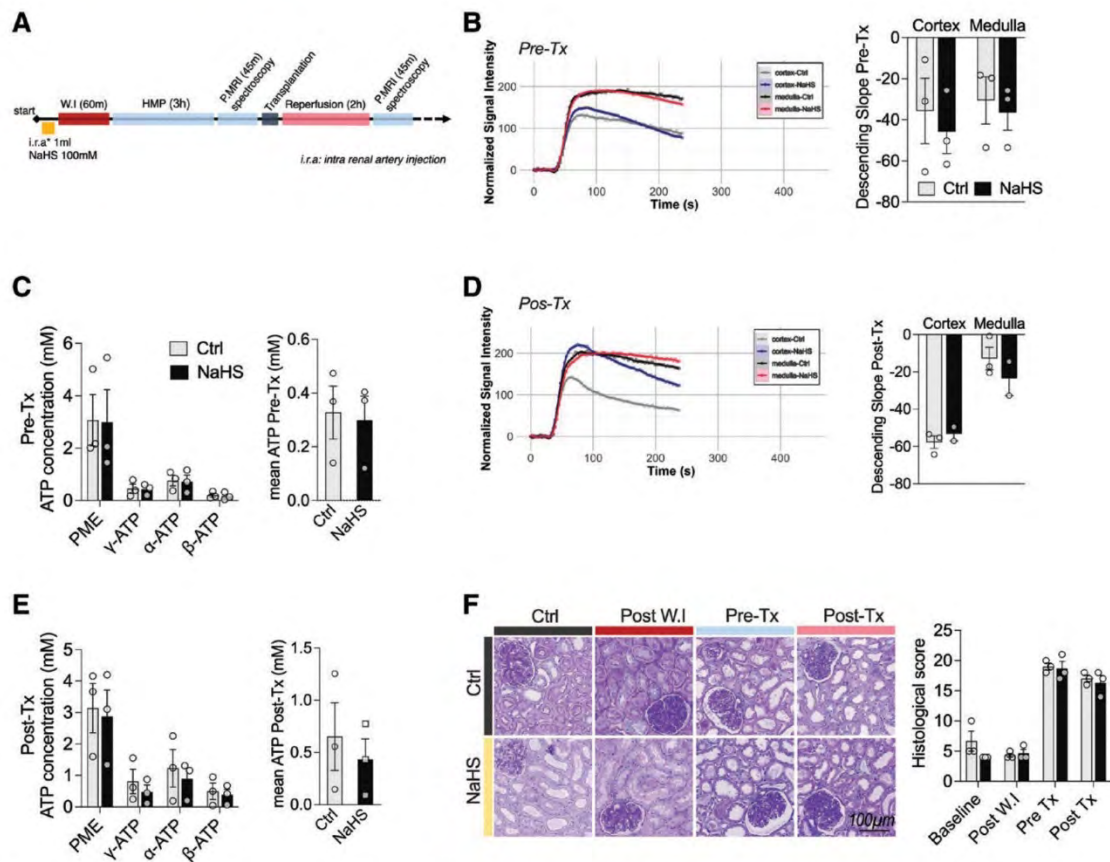


**FIGURE 3.** Administration of hydrogen sulfide before WI in a DCD model. (A) Experimental design: Administration of 100  $\mu$ M NaHS into the renal artery before 60 min WI. Immediately after procurement, kidneys were perfused at 4°C with  $O_2$  in Belzer MPSJ UW for 3 h and underwent  $^{31}P$  MRSI, before autotransplantation (reperfusion) and posttransplant  $^{31}P$  MRSI assessment. (B) Pretransplant cortical and medullar Gd-normalized signal intensity over time (right) and quantification (descending slopes, left) in the indicated groups. (C) Pretransplant phosphomonoesters,  $\alpha$ ,  $\beta$ , and  $\gamma$  ATP levels (left) and mean ATP (right) in control- and NaHS-treated kidney. (D) Posttransplant cortical and medullar Gd-normalized signal intensity over time (right) and quantification (descending slopes, left) in the indicated groups. (E) Posttransplant phosphomonoesters,  $\alpha$ ,  $\beta$ , and  $\gamma$  ATP levels (left) and mean ATP (right) in control- and NaHS-treated kidney. (F) Representative transverse PAS-stained sections of kidneys at the indicated time in control and NaHS groups (left) and quantification of histologic damages (score, right). Data expressed as mean  $\pm$  SEM,  $n = 3$ . DCD, donation after circulatory death; Gd, gadolinium; NaHS, sodium hydrosulfide; PAS, periodic acid-Schiff; PMRSI,  $^{31}P$  magnetic resonance spectroscopic imaging; WI, warm ischemia.

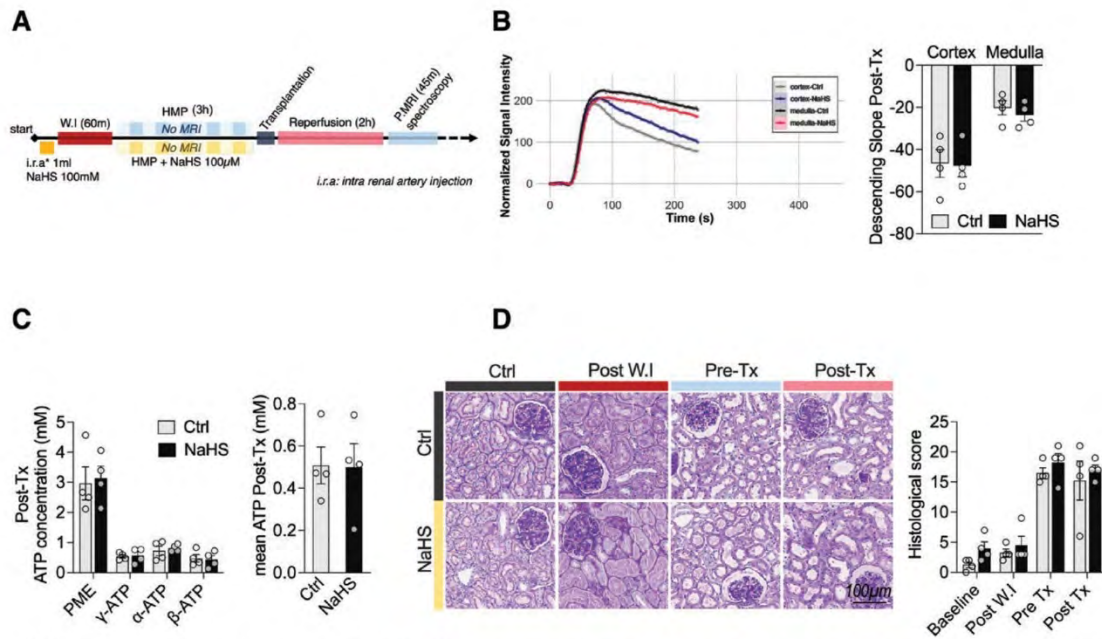
shown to be significantly more potent than GYY4137. In rats, AP39 improved renal allograft survival following 24h SCS and transplantation.<sup>32</sup> In DCD porcine kidneys, ex vivo sub-normothermic perfusion (SNMP, 21°C) with autologous blood and AP39 improved urine output and reduced apoptosis compared with SCS or SNMP alone for 4h.<sup>9</sup> Of note, reperfusion was assessed ex vivo with autologous blood at 37°C, and the kidneys were not transplanted in the latter study.<sup>9</sup> It is important to note that these  $H_2S$  donors remain to be tested in larger animals during cold preservation, which remains the easiest and most employed method during kidney preservation.

We did not compare the effect of NaHS at higher perfusion temperatures (SNMP at 21°C or NMP at 37°C). (S)NMP provides a continuous flow of warmed, oxygenated perfusate containing nutritional substrates, aiming to maintain the metabolic activity of the kidney.<sup>33</sup> Instead, the rationale here was to use  $H_2S$ -specific inhibition of the mitochondrial electron transport chain during cold preservation and reduce ROS

generation during reperfusion, rather than solely relying on passive temperature effects to depress metabolism.<sup>3</sup>

ATP measurement relied exclusively on pMRSI. However, we previously, demonstrated that nucleotide quantification with pMRSI was accurate.<sup>16</sup> pMRSI also suffers from a relatively low sensitivity compared with liquid chromatography or  $^1H$  imaging at a constant magnetic field.<sup>13</sup> Thus, the acquisition is generally performed with a higher voxel size to achieve enough signal-to-noise ratio while keeping an acceptable scan time. Of importance, this lack of sensitivity limitation hinders the measurement of ATP at 4°C without oxygen. The application of machine learning and neural network can further improve pMRSI sensitivity, spatial resolution, and computing time.<sup>34,35</sup> Overall pMRSI remains a powerful, noninvasive tool to quantify ATP.<sup>13</sup>

Our study has several limitations that need to be acknowledged. Kidney function (serum creatinine, urea, and estimated glomerular filtration rate) and urine production after transplantation were not assessed. Kidney function tests could



AQ6

**FIGURE 4.** Administration of hydrogen sulfide before WI and during HMP in a DCD model. (A) Experimental design. Administration of 100  $\mu$ M NaHS into the renal artery before 60 min WI. Immediately after procurement, kidneys were perfused at 4°C without  $O_2$  in Belzer MPS UW with or without NaHS as indicated for 3 h, before autotransplantation (reperfusion) and posttransplant  $^{31}P$  MRSI assessment. (B) Posttransplant cortical and medullary Gd-normalized signal intensity over time (right) and quantification (descending slopes, left) in the indicated groups. (C) Posttransplant phosphomonoesters,  $\alpha$ ,  $\beta$ , and  $\gamma$  ATP levels (left) and mean ATP (right) in control- and NaHS-treated kidney. (D) Representative transverse PAS-stained sections of kidneys at the indicated time in control and NaHS groups (left) and quantification of histologic damages (score, right). Data expressed as mean  $\pm$  SEM, n = 4. DCD, donation after circulatory death; Gd, gadolinium; HMP, hypothermic machine perfusion; NaHS, sodium hydrosulfide; PAS, periodic acid-Schiff; PMRSI,  $^{31}P$  magnetic resonance spectroscopic imaging; WI, warm ischemia.

not be performed because of local regulations, which did not allow survival surgery. In addition, follow-up beyond 2 h after transplantation would be required to truly assess longer-term graft injury and function. Thus, the histologic score, previously correlated with the degree of kidney injury was used as a surrogate endpoint of kidney function.<sup>13,15,18,19</sup> Similarly, the sample size was small, thus increasing the risk of type II errors. As discussed earlier, other  $H_2S$ -releasing molecules or gaseous  $H_2S$  should be evaluated in the (pre)clinical model of kidney transplantation. In addition, our study only included healthy adult pig kidneys. Similar studies should be performed using marginal (eg, old) kidney grafts.

In conclusion, perfusion of porcine kidneys with NaHS did not improve preservation nor reduced ischemia-reperfusion injury. Perfusion of organs with alternative  $H_2S$  donors, or at different temperatures should be tested to determine if  $H_2S$  can improve posttransplant graft function and patient survival.

#### ACKNOWLEDGMENTS

The authors thank Jean-Pierre Giliberto from the Department of Surgery, University Hospitals of Geneva for the excellent technical assistance. They thank the cellular imaging facility for access and training on the ZEISS Axioscan 7 Microscope Slide Scanner (<https://cif.unil.ch>). They thank the mouse pathology facility for assistance with paraffin embedding and cutting of the tissues (<https://www.unil.ch/mpf/home.html>).

#### REFERENCES

1. Tingle SJ, Figueiredo RS, Moir JA, et al. Machine perfusion preservation versus static cold storage for deceased donor kidney transplantation. *Cochrane Database Syst Rev.* 2019;3:CD011671.
2. Moers C, Smits JM, Maathuis MH, et al. Machine perfusion or cold storage in deceased-donor kidney transplantation. *N Engl J Med.* 2009;360:7–19.
3. Longchamp A, Mirabella T, Arduini A, et al. Amino acid restriction triggers angiogenesis via GDNF/ATF4 regulation of VEGF and H. *Cell.* 2018;173:117–129.e14.
4. Hine C, Kim HJ, Zhu Y, et al. Hypothalamic-pituitary axis regulates hydrogen sulfide production. *Cell Metab.* 2017;25:1320–1333.e5.
5. Bos EM, Wang R, Snijder PM, et al. Cystathionine  $\gamma$ -lyase protects against renal ischemia/reperfusion by modulating oxidative stress. *J Am Soc Nephrol.* 2013;24:759–770.
6. Hine C, Harputlugil E, Zhang Y, et al. Endogenous hydrogen sulfide production is essential for dietary restriction benefits. *Cell.* 2015;160:132–144.
7. Zhang MY, Dugbartey GJ, Juriasingani S, et al. Sodium thiosulfate-supplemented UW solution protects renal grafts against prolonged cold ischemia-reperfusion injury in a murine model of syngeneic kidney transplantation. *Biomed Pharmacother.* 2022;145:112435.
8. Sekijima M, Sahara H, Miki K, et al. Hydrogen sulfide prevents renal ischemia-reperfusion injury in CLAWN miniature swine. *J Surg Res.* 2017;219:165–172.
9. Juriasingani S, Jackson A, Zhang MY, et al. Evaluating the effects of subnormothermic perfusion with AP39 in a novel blood-free model of ex vivo kidney preservation and reperfusion. *Int J Mol Sci.* 2021;22:7180.
10. Macabrey D, Longchamp A, Dégliose S, et al. Clinical use of hydrogen sulfide to protect against intimal hyperplasia. *Front Cardiovasc Med.* 2022;9:876639.
11. Corsello T, Komaravelli N, Casola A. Role of hydrogen sulfide in NRF2- and sirtuin-dependent maintenance of cellular redox balance. *Antioxidants (Basel).* 2018;7:129.



12. Chouchani ET, Pell VR, James AM, et al. A unifying mechanism for mitochondrial superoxide production during ischemia-reperfusion injury. *Cell Metab.* 2016;23:254–263.
13. Longchamp A, Klausner A, Songeon J, et al. Ex vivo analysis of kidney graft viability using 31P magnetic resonance imaging spectroscopy. *Transplantation.* 2020;104:1825–1831.
14. Szeto HH, Liu S, Soong Y, et al. Mitochondria-targeted peptide accelerates ATP recovery and reduces ischemic kidney injury. *J Am Soc Nephrol.* 2011;22:1041–1052.
15. Longchamp A, Meier RPH, Colucci N, et al. Impact of an intra-abdominal cooling device during open kidney transplantation in pigs. *Swiss Med Wkly.* 2019;149:w20143.
16. Agius T, Songeon J, Klausner A, et al. Subnormothermic ex vivo porcine kidney perfusion improves energy metabolism: analysis using. *Transplant Direct.* 2022;8:e1354.
17. Songeon J, Courvoisier S, Xin L, et al. In vivo magnetic resonance P-spectral analysis with neural networks: 31P-SPAWN. *Magn Reson Med.* 2023;89:40–53.
18. Meier RPH, Piller V, Hagen ME, et al. Intra-abdominal cooling system limits ischemia-reperfusion injury during robot-assisted renal transplantation. *Am J Transplant.* 2018;18:53–62.
19. Goujon JM, Hauet T, Menet E, et al. Histological evaluation of proximal tubule cell injury in isolated perfused pig kidneys exposed to cold ischemia. *J Surg Res.* 1999;82:228–233.
20. Lobb I, Davison M, Carter D, et al. Hydrogen sulfide treatment mitigates renal allograft ischemia-reperfusion injury during cold storage and improves early transplant kidney function and survival following allogeneic renal transplantation. *J Urol.* 2015;194:1806–1815.
21. Blackstone E, Morrison M, Roth MB. H<sub>2</sub>S induces a suspended animation-like state in mice. *Science.* 2005;308:518.
22. Blackstone E, Roth MB. Suspended animation-like state protects mice from lethal hypoxia. *Shock.* 2007;27:370–372.
23. Morrison ML, Blackwood JE, Lockett SL, et al. Surviving blood loss using hydrogen sulfide. *J Trauma.* 2008;65:183–188.
24. Haouzi P, Bell HJ, Notet V, et al. Comparison of the metabolic and ventilatory response to hypoxia and H<sub>2</sub>S in unsedated mice and rats. *Respir Physiol Neurobiol.* 2009;167:316–322.
25. Drabek T, Kochanek PM, Stezoski J, et al. Intravenous hydrogen sulfide does not induce hypothermia or improve survival from hemorrhagic shock in pigs. *Shock.* 2011;35:67–73.
26. Derwall M, Francis RC, Kida K, et al. Administration of hydrogen sulfide via extracorporeal membrane lung ventilation in sheep with partial cardiopulmonary bypass perfusion: a proof of concept study on metabolic and vasomotor effects. *Crit Care.* 2011;15:R51.
27. Chouchani ET, Pell VR, Gaude E, et al. Ischaemic accumulation of succinate controls reperfusion injury through mitochondrial ROS. *Nature.* 2014;515:431–435.
28. Asfar P, Calzia E, Radermacher P. Is pharmacological, H<sub>2</sub>S-induced 'suspended animation' feasible in the ICU? *Crit Care.* 2014;18:215.
29. Yu L, Di W, Dong X, et al. Diallyl trisulfide exerts cardioprotection against myocardial ischemia-reperfusion injury in diabetic state, role of AMPK-mediated AKT/GSK-3 $\beta$ /HIF-1 $\alpha$  activation. *Oncotarget.* 2017;8:74791–74805.
30. Li L, Whiteman M, Guan YY, et al. Characterization of a novel, water-soluble hydrogen sulfide-releasing molecule (GYY4137): new insights into the biology of hydrogen sulfide. *Circulation.* 2008;117:2351–2360.
31. Zhao H, Qiu Y, Wu Y, et al. Protective effects of GYY4137 on renal ischaemia/reperfusion injury through Nrf2-mediated antioxidant defence. *Kidney Blood Press Res.* 2021;46:257–265.
32. Ahmad A, Olah G, Szczesny B, et al. AP39, a mitochondrially targeted hydrogen sulfide donor, exerts protective effects in renal epithelial cells subjected to oxidative stress in vitro and in acute renal injury in vivo. *Shock.* 2016;45:88–97.
33. Urbanellis P, McEvoy CM, Škrtić M, et al. Transcriptome analysis of kidney grafts subjected to normothermic ex vivo perfusion demonstrates an enrichment of mitochondrial metabolism genes. *Transplant Direct.* 2021;7:e719.
34. Lam F, Li Y, Guo R, et al. Ultrafast magnetic resonance spectroscopic imaging using SPICE with learned subspaces. *Magn Reson Med.* 2020;83:377–390.
35. Lee HH, Kim H. Deep learning-based target metabolite isolation and big data-driven measurement uncertainty estimation in proton magnetic resonance spectroscopy of the brain. *Magn Reson Med.* 2020;84:1689–1706.

## Chapter 3: Short-Term Hypercaloric Carbohydrate Loading Increases Surgical Stress Resilience by Inducing FGF21.

This work was submitted on 08/2023 in the journal *Cell Metabolism*.

### Summary:

Dietary restriction promotes resistance to acute surgical stress in multiple organisms. Counterintuitively, current medical protocols recommend short-term carbohydrate loading before surgery, involving carbohydrate-rich drinks as part of a multimodal perioperative care pathway designed to enhance surgical recovery. Despite widespread clinical use, preclinical and mechanistic studies on carbohydrate loading in surgical contexts are lacking. Here we demonstrated in ad libitum-fed mice that liquid carbohydrate loading for 1 week reduces solid food intake while nearly doubling total caloric intake. Similarly, simple carbohydrate intake was inversely correlated with dietary protein intake in humans. Carbohydrate loading-induced protein dilution increased expression of hepatic fibroblast growth factor 21 (FGF21) independent of caloric intake, resulting in protection in two models of surgical stress: renal and hepatic ischemia-reperfusion injury. The protection was consistent across male, female, and aged mice. In vivo, amino acid add-back or genetic FGF21 deletion blocked carbohydrate loading-mediated protection from ischemia-reperfusion injury. Finally, carbohydrate loading induction of FGF21 was associated with the induction of the canonical integrated stress response (ATF3/4, NFkB) and oxidative metabolism (PPAR $\gamma$ ). Together, these data support carbohydrate loading drinks prior to acute surgical stress, revealing an essential role of protein dilution via FGF21.





# Short-term hypercaloric carbohydrate loading increases surgical stress resilience by inducing FGF21

Received: 18 August 2023

Accepted: 8 January 2024

Published online: 05 February 2024



Thomas Agius<sup>1,2,3,12</sup>, Raffaella Emsley<sup>1,12</sup>, Arnaud Lyon<sup>1</sup>, Michael R. MacArthur<sup>4</sup>, Kevin Kiesworo<sup>1</sup>, Anna Faivre<sup>5,6</sup>, Louis Stavart<sup>7</sup>, Martine Lambelet<sup>1</sup>, David Legouis<sup>5,8</sup>, Sophie de Seigneux<sup>5,6</sup>, Déla Golshayan<sup>7</sup>, Francois Lazeyras<sup>9,10</sup>, Heidi Yeh<sup>2,3</sup>, James F. Markmann<sup>2,3</sup>, Korkut Uygun<sup>2,3</sup>, Alejandro Ocampo<sup>11</sup>, Sarah J. Mitchell<sup>4</sup>, Florent Allagnat<sup>1,11</sup>, Sébastien Déglise<sup>1</sup> & Alban Longchamp<sup>1,2,3</sup> ✉

Dietary restriction promotes resistance to surgical stress in multiple organisms. Counterintuitively, current medical protocols recommend short-term carbohydrate-rich drinks (carbohydrate loading) prior to surgery, part of a multimodal perioperative care pathway designed to enhance surgical recovery. Despite widespread clinical use, preclinical and mechanistic studies on carbohydrate loading in surgical contexts are lacking. Here we demonstrate in *ad libitum*-fed mice that liquid carbohydrate loading for one week drives reductions in solid food intake, while nearly doubling total caloric intake. Similarly, in humans, simple carbohydrate intake is inversely correlated with dietary protein intake. Carbohydrate loading-induced protein dilution increases expression of hepatic fibroblast growth factor 21 (FGF21) independent of caloric intake, resulting in protection in two models of surgical stress: renal and hepatic ischemia-reperfusion injury. The protection is consistent across male, female, and aged mice. In vivo, amino acid add-back or genetic FGF21 deletion blocks carbohydrate loading-mediated protection from ischemia-reperfusion injury. Finally, carbohydrate loading induction of FGF21 is associated with the induction of the canonical integrated stress response (ATF3/4, NF- $\kappa$ B), and oxidative metabolism (PPAR $\gamma$ ). Together, these data support carbohydrate loading drinks prior to surgery and reveal an essential role of protein dilution via FGF21.

Worldwide, 310 million surgeries are performed annually, with approximately 40 to 50 million taking place in the USA and 20 million in Europe. These surgeries carry a postoperative mortality rate of 1–4%, a morbidity rate of up to 15%, and a readmission rate within 30 days ranging from 5–15%. With an estimated global annual mortality of 8 million, the mortality associated with major surgery is comparable to that of cardiovascular disease (17.9 million), stroke (5 million), and

cancer (10 million)<sup>1</sup>. Ischemia-reperfusion injury (IRI) is an important component of surgical stress, involving the occlusion of blood flow to an organ or tissue for a certain period of time (ischemia) and subsequent restoration of blood supply (reperfusion)<sup>2</sup>. IRI represents a major clinical concern in controlled elective surgery, which requires temporary restriction of blood flow (e.g. solid organ transplantation, vascular surgery) and uncontrolled settings (stroke, heart attack, limb

A full list of affiliations appears at the end of the paper. ✉ e-mail: [alban.longchamp@chuv.ch](mailto:alban.longchamp@chuv.ch)

trauma). During the ischemic period, cells are deprived of oxygen and nutrients, resulting in ATP depletion, loss of membrane potential, and the accumulation of toxic byproducts. Subsequent reperfusion introduces additional damage via extensive ROS generation by the reverse electron transport at the mitochondria<sup>3</sup>. Together, there is a significant need for interventions that can reduce IRI and enhance resilience to surgical stress.

Currently, perioperative surgical care in humans includes enhanced-recovery protocols (ERAS<sup>®</sup>), which encourage the consumption of carbohydrate-loaded fluids before surgery<sup>4</sup>. Carbohydrate loading practices vary among institutions, encompassing both simple carbohydrates (e.g. Gatorade) and complex carbohydrates (e.g., maltodextrin), with multiple commercial preparations available<sup>5</sup>. In the context of surgery, carbohydrate loading may reduce insulin resistance and improve recovery<sup>6</sup>, although the exact mechanisms are unknown, and is confounded by numerous interventions (e.g. analgesia, early removal of catheters, thromboprophylaxis, etc.). Moreover, ERAS<sup>®</sup> pre-surgery drinks often contain high amounts of protein (up to 80 g/L). Interestingly, the benefit of high-protein diet before surgery has not been demonstrated. Inversely, high animal protein intake was positively associated with cardiovascular mortality<sup>7</sup>.

Counterintuitively, decades of research have demonstrated that short-term preconditioning with dietary restriction (DR) from two days to one week increases resilience against stress, including IRI to the kidney, liver, brain, heart, and vein grafts<sup>9–15</sup>. DR can include either restriction of total energy intake (calorie restriction) or dilution of specific macronutrients in the diet, such as total protein, or specific amino acids like methionine, cysteine, or tryptophan<sup>13,16,17</sup>. While DR has been extensively used in preclinical models, achieving voluntary food restriction in humans remains challenging, even for a short period of time<sup>18</sup>. Thus, one of the goals in this research area is to identify simple interventions that are feasible in humans and can replicate the benefits of DR without the burden of restricting food intake. Consequently, many studies have focused on alternative nutritional strategies or on the molecular effectors that mediate the benefits of dietary restriction<sup>19</sup>.

From a nutritional standpoint, many of the pleiotropic benefits of calorie restriction can be triggered by the restriction of dietary protein or single amino acids<sup>20</sup>. These benefits include resistance to hepatic IRI<sup>14</sup>, improved recovery upon limb ischemia<sup>13</sup>, increased energy expenditure<sup>21</sup>, and improved glucose and lipid homeostasis, even during short-term interventions<sup>22–24</sup>. Protein restriction also extends lifespan, while high-fat and high-protein diets may accelerate aging and reduce lifespan<sup>25</sup>. The interaction between protein and carbohydrate intake is also important, as the isocaloric replacement of dietary protein with carbohydrates drives greater benefit than isocaloric replacement with fat<sup>26,27</sup>. Interestingly, the type of carbohydrate used to replace protein seems to have relatively little effect on the overall protein restriction response<sup>28</sup>.

On a molecular level, protein and calorie restriction modulate pathways, including insulin/insulin-like growth factor-1 (IGF-1)<sup>29,30</sup>, the redox-sensing transcription factor Nuclear Factor Erythroid 2-Related Factor (NRF2)<sup>31</sup> and hydrogen sulfide (H<sub>2</sub>S) signaling<sup>14</sup>. One feature unique to protein restriction is increased fibroblast growth factor 21 (FGF21) production, which responds to starvation and protein/amino acid restriction, but not calorie restriction<sup>32,33</sup>. This is a conserved response, with circulating FGF21 increased 10-fold in rodents and approximately 2-fold in humans fed a low-protein (LP) diet for one month<sup>32</sup>. FGF21 signaling is associated with increased insulin sensitivity, improved glucose homeostasis, a reduction in circulating lipids, and an increased lifespan in mice<sup>34–37</sup>. FGF21 induces thermogenesis by increasing the expression of UCPI in adipose tissue<sup>38</sup>, which drives the browning of adipose tissue and increased energy expenditure<sup>39</sup>. During protein restriction, FGF21 signaling is essential to regulate adaptive homeostatic changes in metabolism and feeding behavior<sup>40</sup>.

In this study, our aims were to 1) explore how *ad-libitum* access to carbohydrate-loading drinks impacts food intake, 2) evaluate the effects of one-week carbohydrate loading on IRI, a model of surgical stress, and 3) identify the mechanisms that underlie the benefits of carbohydrate loading. We hypothesized that mice with access to carbohydrate-loading drinks would consume less food, resulting in protein dilution. We further hypothesized that carbohydrate loading-induced short-term protein dilution would protect against surgical stress through conserved mechanisms of protein restriction.

We find that one week of carbohydrate loading reduces food intake and induces voluntary protein dilution in mice. Consistent with the benefits of low-protein diets<sup>24,26</sup>, carbohydrate loading protects from surgical stress in two models: hepatic and renal IRI. In this context, FGF21 is required for protection from surgical stress, and FGF21 administration is sufficient to protect without any dietary intervention. Mechanistically, carbohydrate loading induction of FGF21 is associated with the induction of the canonical integrated stress response (ATF3/4, NF-κB), and oxidative metabolism (PPARγ).

## Results

### Short-term carbohydrate loading promotes resilience to surgical stress

Carbohydrate-loading drinks were modeled using a 50% (w/w) sucrose-water solution, hereafter referred to as “high carbohydrate - HC”. The choice of sucrose as the source of carbohydrate was based on the following rationale: 1) Dietary protein restriction benefits have been achieved by substituting protein with sucrose<sup>24,41</sup>. 2) Metabolic outcomes of low (10%)-protein, high (70%)-carbohydrate diets are worse when carbohydrates comprise a mixture of monosaccharides fructose and glucose<sup>28</sup>. 3) Sucrose is commonly employed in ERAS protocols<sup>5</sup>.

We began by examining the effects of HC prior to surgery by using a model of surgical stress that consisted of right nephrectomy and unilateral left kidney IRI (Supplementary Data Fig. 1a). Prior to IRI, 10-week-old C57BL/6J male mice were given *ad libitum* access to water (Ctrl) or HC for one week. All mice were fed the same standardized *ad libitum* diet. All mice were given regular water postoperatively (Supplementary Data Fig. 1a). Mice on HC showed improved renal function after IRI, with reduced postoperative serum urea (Fig. 1a and Supplementary Data Fig. 1b, 935 ± 322 versus 1426 ± 309 AUC), day 3 serum creatinine levels (Fig. 1b, 0.4 ± 0.3 versus 1.11 ± 0.6 ng/mL) and improved glomerular filtration rate (GFR) as estimated by clearance of FITC-sinistrin (Supplementary Data Fig. 1c). HC also alleviated IRI as measured by histological assessment of tissue necrosis (Fig. 1c, 3.9 ± 0.94 versus 6.16 ± 1.8% necrotic area), lipid peroxidation (Supplementary Data Fig. 1d; 4HNE staining), and *Krt20* gene expression (Fig. 1d), a marker of proximal tubule damage<sup>42</sup>.

Sex-specific differences have been observed in preclinical models of renal ischemic injury. In particular, females recover more readily from IRI than males<sup>43</sup>. Thus to substantiate our findings, we subjected C57BL/6J female mice to the same HC preconditioning for one week, followed by renal IRI (Supplementary Data Fig. 1a). In accordance with what was observed in males, HC preconditioning reduced IRI in female mice (Fig. 1e and Supplementary Data Fig. 1e, serum urea 318 ± 47 versus 536 ± 79 AUC). Similarly, serum creatinine levels (Fig. 1f, 0.28 ± 0.05 versus 0.49 ± 0.08 ng/mL), tissue necrosis (Fig. 1g, 0.92 ± 0.30 versus 2.63 ± 0.70% necrotic area), and *Krt20* expression (Fig. 1h) were reduced in HC female mice compared to Ctrl.

Some benefits of DR appear lost when started late-in-life<sup>44</sup>, but most surgical patients are older. Thus, we asked whether HC was similarly effective in aged male mice (22-months-old). As in young mice, HC preconditioning improved renal function upon IRI in old mice (Fig. 1i and Supplementary Data Fig. 1f, serum urea 593.3 ± 40.73 versus 733.8 ± 28.69 AUC), reduced renal necrosis (Figs. 1j, 4.6 ± 0.94 versus 7.69 ± 0.48%) and *Krt20* expression (Fig. 1k). Moreover, one



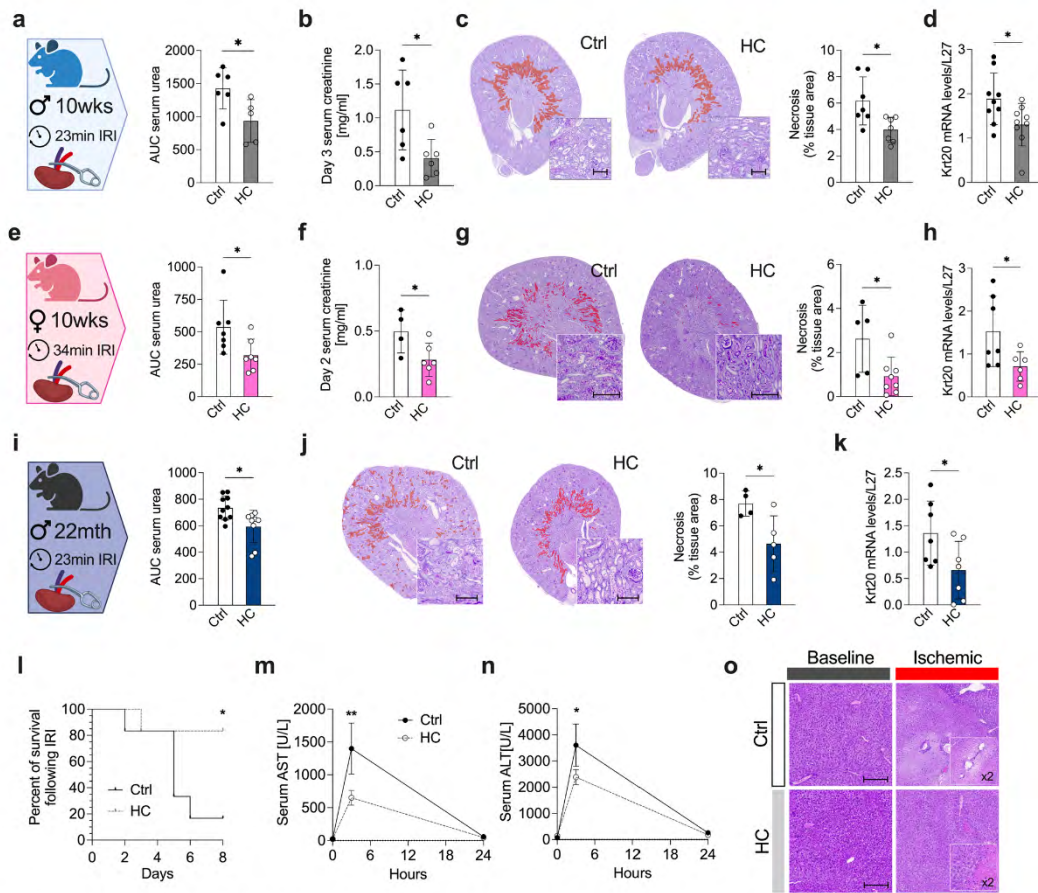


**Fig. 1 | Improved resistance to ischemia-reperfusion injury (IRI) following carbohydrate loading with 50% sucrose water.** **a** Experimental group (left) and serum urea levels (right; AUC) post-renal IRI after one week of preconditioning with Ctrl or HC. Created with BioRender.com. **b** Serum creatinine levels at day 3 post-renal IRI. **c** Representative cross sections of PAS-stained kidneys with necrotic area digitally highlighted in red (left;  $\times 10$  magnification; scale bar  $100\ \mu\text{m}$ ) and necrotic tissue area quantification (right) at day 2 post-renal IRI. **d** Relative Krt20 mRNA levels in kidney at day 2 post-renal IRI. **e** Experimental group (left) and serum urea levels (AUC) post-renal IRI after one week of preconditioning with Ctrl or HC. Created with BioRender.com. **f** Serum creatinine levels at day 2 post-renal IRI. **g** Representative cross sections of PAS-stained kidneys with necrotic area digitally highlighted in red (left;  $\times 10$  magnification; scale bar  $100\ \mu\text{m}$ ) and quantification of necrotic tissue area (right) at day 2 post-renal IRI. **h** Relative Krt20 mRNA levels in kidney at day 2 post-renal IRI. **i** Experimental group (left) and serum urea levels (AUC) post-renal IRI after one week of preconditioning with Ctrl or HC. Created with BioRender.com. **j** Representative cross sections of PAS-stained kidneys with necrotic area digitally highlighted in red (left;  $\times 10$  magnification; scale bar  $100\ \mu\text{m}$ ) and quantification of necrotic tissue area (right) at day 2 post-renal IRI. **k** Relative Krt20 mRNA levels in kidney at day 2 post-renal IRI. **l** Kaplan-Meier survival curve

post-renal IRI after one week of preconditioning with Ctrl or HC. **m** Serum aspartate aminotransferase (AST) and **(n)** alanine aminotransferase (ALT) enzyme levels at the indicated time post-hepatic IRI. **o** Representative cross sections of H&E-stained livers ( $\times 20$  magnification; scale bar  $30\ \mu\text{m}$ ) at baseline or at day 1 post-hepatic IRI. \**p* values for **a–k** were calculated with unpaired two-tailed T-test, and for **l** with two-way repeated measures (RM) ANOVA with Geisser-Greenhouse correction and **n, m** with two-way ANOVA followed by a Sidak's post hoc analysis, \**p* < 0.05 \*\**p* < 0.01. *p* values for **a** = 0.303, for **b** = 0.0234, for **c** = 0.0154, for **d** = 0.0345, for **e** = 0.0352, for **f** = 0.0467, for **g** = 0.0246, for **h** = 0.0445, for **i** = 0.0107, for **j** =, for **k** = 0.0427, for **l** = 0.0462, for **m** = 0.0346, for **n** = 0.0252. Images 1a, 1e and 1i were partly created with BioRender.com. ♂ indicates males, ♀ indicates females; In **a–d** and **l–o**, experiments were carried out in 10-weeks old male mice; in **e–h**, in 10-week-old female mice; in **i–k**, in 22-month-old male mice. Sample sizes: (**a–c**), *n* = 6–7, *n* = 7 for Ctrl diet, and *n* = 6 for HC diet; (**d**) *n* = 9 in all experimental groups; (**e–h**), *n* = 7 in all experimental groups; (**i**), *n* = 10 in all experimental groups (2 experiments pooled, experiment 1: *n* = 7 in all experimental groups, experiment 2: *n* = 3 in all experimental groups; (**j–k**) *n* = 7 in all experimental groups; (**l–o**), *n* = 6 for all conditions. Data shown as mean  $\pm$  SD. See also Supplementary Data Fig. 1.

week of pre-operative IIC caused a significant survival advantage after severe (35 min) renal ischemia, with only 20% mortality at 8 days post-surgery compared to 80% mortality in the Ctrl group (Fig. 1l).

Finally, we tested whether HC could also protect from surgical stress by using a mouse model of hepatic IRI, as previously described<sup>14</sup>. Here, 10-weeks-old male mice on HC had decreased liver damage

relative to Ctrl at 3 hours post-surgery, as measured by serum aspartate aminotransferase (AST, Fig. 1m,  $651 \pm 275$  versus  $1400 \pm 952$  U/L) and serum alanine transaminase (ALT, Fig. 1n,  $2384 \pm 706$  versus  $3608 \pm 1622$  U/L). Histological analysis of hemorrhagic necrosis in livers collected 24 hours after reperfusion was consistent with liver damage markers and a protective effect of the HC (Fig. 1o). Taken



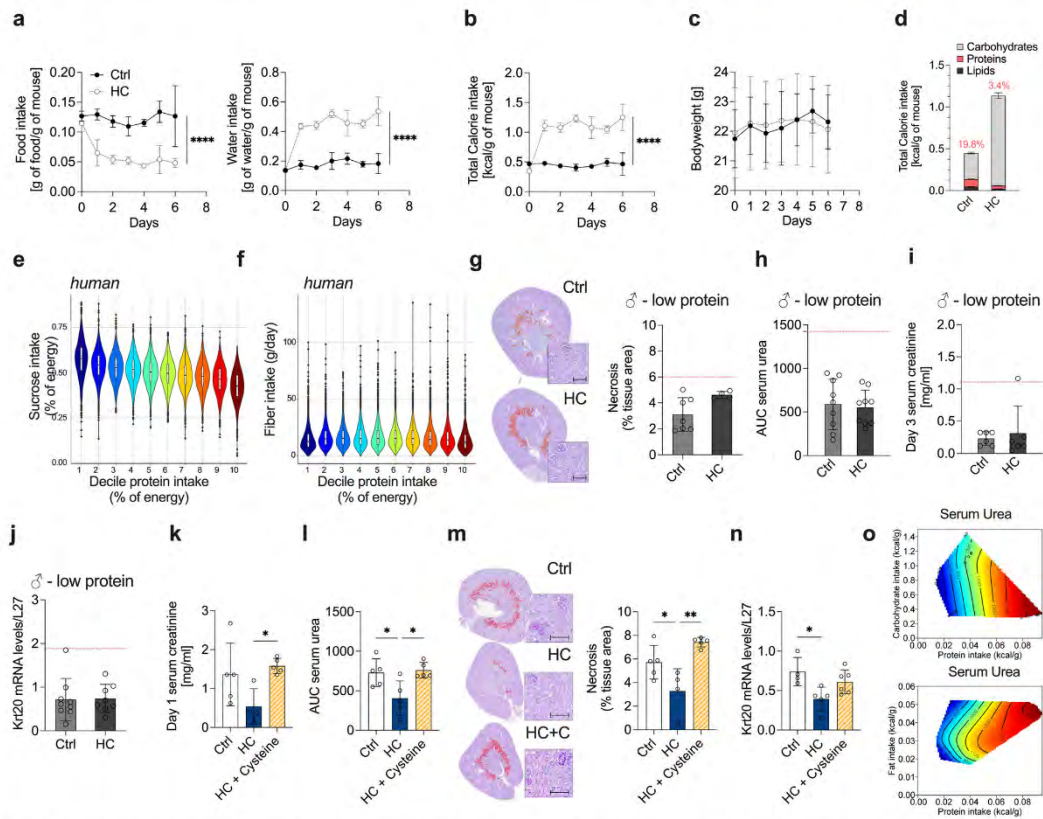


**Fig. 2 | Carbohydrate loading-induced protein dilution is required for protection against IRI.** **a** Food (left) and water (right) intake (normalized by body weight) of 10-week-old male mice given *ad libitum* access to water (Ctrl) or 50% sucrose-water (HC). **b** Total calorie intake normalized to body weight by day. **c** Body weight at the indicated time in mice given *ad libitum* access to Ctrl or HC. **d** Total calorie intake by macronutrient normalized to body weight by day. The % of protein intake is indicated on top of each bar. **e** Relationship between sucrose intake and protein intake, and **(f)** fiber intake and protein intake in humans from the US National Health and Nutrition Examination Survey (NHANES). Box plots represent median with 25th and 75th percentile. Whiskers plots represent hinge  $\pm$  1.5 IQR. **g** Representative cross sections of PAS-stained kidneys with necrotic area digitally highlighted in red (left;  $\times 10$  magnification; scale bar 100  $\mu$ m) and quantification of necrotic tissue area (right) at day 2 post-renal IRI after one week of preconditioning with low protein diet (LP) combined with Ctrl or HC. The red line indicates the level of the control group (Ctrl). **h** Serum urea levels (AUC) post-renal IRI after one week of preconditioning with the indicated diet. The red line indicates the level of the control group (Ctrl). **i** Serum creatinine levels at day 3 post-renal IRI. The red line indicates the level of the control group (Ctrl). **j** Relative Krt20 mRNA levels in kidneys at day 2 post-renal IRI after one week of preconditioning with the indicated diet. The red line indicates the level of the control group (Ctrl). **k** Serum creatinine

levels at day 1 post-renal IRI after one week of preconditioning with Ctrl, HC or HC with cysteine oral gavage (HC + cysteine). **l** Serum urea levels (AUC) post-renal IRI after one week of preconditioning with the indicated diet. **m** Representative cross sections of PAS-stained kidneys with necrotic area digitally highlighted in red (left;  $\times 10$  magnification; scale bar 100  $\mu$ m) and quantification of necrotic tissue area (right) at day 2 post-renal IRI after one week of preconditioning with the indicated diet. **n** Relative Krt20 mRNA levels in kidney at day 2 post-renal IRI after one week of preconditioning with the indicated diet. **o** Relationship between serum urea at day 2 post-renal IRI and dietary protein intake or carbohydrate or fat intake. In all surfaces, red indicates the highest value while blue indicates the lowest value, with the colors standardized across each slice. \**p* values for **a–c** were calculated with two-way repeated measures (RM) ANOVA with Geisser-Greenhouse correction, **k–n** with unpaired two-tailed T-test and **o**. with a generalized additive model (GAM; **k** = 6), \**p* < 0.05 \*\**p* < 0.01 \*\*\**p* < 0.0001. *p* values for **a** are respectively <0.0001 and <0.0001, for **b** < 0.0001, for **c** = 0.0411, for **l** = 0.0283 and 0.0171, for **m** = 0.0474 and 0.0019, for **n** = 0.0174. In **a–d** and **g–o**, experiments were carried out in 10-weeks old male mice. Sample sizes: (**a–d**), *n* = 8; (**e–f**), *n* = 11064 men, 12181 women (**g–j**), *n* = 8–9, *n* = 8 for low protein Ctrl, and *n* = 9 for HC; (**k–n**), *n* = 5 for all conditions; (**o**), *n* = 16 for all conditions. Data in all panels are shown as mean  $\pm$  SD. See also Supplementary Data Figs. 2 and 3.

together, these data suggest that pre-operative HC confers hepatic and renal protection against surgical stress, independent of sex or age.

### One-week of carbohydrate loading-induced voluntary protein restriction required for surgical stress resistance

Having demonstrated that one week of carbohydrate loading increased surgical stress resistance, we then sought to identify the underlying nutritional mechanism. Given the links between dietary restriction and protection from surgical stress<sup>4</sup>, we hypothesized that

carbohydrate loading would impact food intake. Indeed, HC induced a voluntary 2-fold reduction in solid food intake (Fig. 2a, 0.05 versus 0.12 g food/g body weight), with effects apparent within 24 hours. Strikingly, mice on HC doubled their water intake (Fig. 2a, 0.42 versus 0.18 g water/g body weight). Changes in the HC group drove a significant increase in total energy intake relative to body weight (Figs. 2b, 1.13  $\pm$  0.09 versus 0.45  $\pm$  0.03 kcal/g body weight). One week of HC did not affect bodyweight, lean or fat mass percentages compared to Ctrl (Fig. 2c and Supplementary Data Fig. 2a). Moreover, spontaneous

activity level was unchanged, as measured by average walk time over 72 hours (Supplementary Data Fig. 2b). When examining the contribution of each macronutrient to whole body energy intake, HC resulted in a significant increase in energy from carbohydrates (Figs. 2d,  $1.08 \pm 0.08$  versus  $0.31 \pm 0.02$  kcal/g body weight), and a decrease in energy from protein (Fig. 2d,  $0.04 \pm 0.005$  versus  $0.09 \pm 0.007$  kcal/g body weight) and fat (Fig. 2d,  $0.02 \pm 0.003$  versus  $0.05 \pm 0.004$  kcal/g body weight). In both sexes and aged male mice, HC induced a reduction in food intake, associated with a 2-fold increase in sucrose-water intake (Supplementary Data Figs. 2c and 2f). Similarly, body weight was unaffected (Supplementary Data Fig. 2d, g), and HC increased total energy intake relative to body weight (Supplementary Data Fig. 2e, f).

Given the robustness of these data, we asked whether similar effects could be observed in humans. Total carbohydrate and protein intake was analyzed from the National Health and Nutrition Examination Survey (NHANES) from 2005 to 2012 including two 24-h dietary recalls per person on a representative sample of the United States population every 2 years (four distinct cycles of data collection). Using this large dataset ( $n = 23,245$ ), we indeed found an inverse association between sucrose and protein intake (Fig. 2e), but not between fiber and protein intake (Fig. 2f), consistent with our observations in rodents (Fig. 2a–d).

Given the voluntary protein restriction observed during carbohydrate loading, and because restricting dietary protein has pronounced effects on glucose tolerance<sup>26</sup>, lipid metabolism<sup>24</sup> and resistance to IRI<sup>12</sup> in vivo, we hypothesized that HC might not have additional benefits in mice fed a low protein (LP) diet. To test this hypothesis, we fed an additional cohort of mice an LP diet (Supplementary Data Figs. 3a, 6.4 versus 19.8% of energy from protein in the standard diet), in the presence or absence of HC. Similar to mice on a standard diet, mice on an LP diet with access to HC decreased their food intake and increased their water and total energy intake (Supplementary Data Fig. 3B). Mice on an LP diet for one week lost weight (Supplementary Data Fig. 3c), but the LP diet did not affect total energy intake compared to a standard diet (Supplementary Data Fig. 3d). In line with our hypothesis that the benefits of carbohydrate loading are mediated by protein dilution, mice fed with an LP diet with access to HC had no additional protection from IRI, as assessed by tissue necrosis, serum urea, creatinine levels, and *Krt20* expression (Fig. 2g–j).

Next, we asked whether the reintroduction of protein would reverse the benefits of HC. To achieve this, we administered cysteine, a sulfur-containing amino acid previously shown to be relevant in the beneficial effects of DR<sup>14</sup>, via oral gavage to mice treated with HC. We estimated the amount of cysteine to be 5.58 mg/day per mouse, which corresponded to the cysteine intake deficit in HC versus Ctrl mice. Interestingly, food, water, total energy intake, and body weight were unaffected by cysteine add-back (Supplementary Data Fig. 3e, g, HC + C). On the other hand, consistent with our hypothesis, the addition of cysteine to the diet (HC + Cysteine) abrogated HC benefits on surgical stress. This was evident by increased serum creatinine at day 1 and serum urea levels after IRI (Fig. 2k, l and Supplementary Data Fig. 3h) in the HC + Cysteine group. In addition, tissue necrosis and *Krt20* expression in the HC + Cysteine mice were comparable to those observed in the Ctrl (Fig. 2m, n). Finally, we utilized the geometric framework<sup>26</sup> to evaluate the effects of *ad libitum*-fed diets varying in macronutrients on kidney function (serum urea). Resistance to surgical stress was most robustly associated with protein intake (Fig. 2o). In contrast, fat and carbohydrate intake had negligible influence. Interestingly, while HC induced a further reduction in protein energy intake in the LP diet group (LP + HC 1.7%, LP + Ctrl 6.4%), no additional benefits on IRI protection were observed, possibly associated with a specific threshold, rather than a “linear effect” as previously observed<sup>24,41</sup>. Overall, we found that one week of HC increased total caloric intake while reducing protein intake, which is required for resistance to surgical stress.

### Carbohydrate loading induces FGF21 signaling

Nutrient sensing pathways proposed to link dietary restriction with stress resistance include H<sub>2</sub>S production downstream of the integrated stress response (Activating Transcription Factor 4; ATF4) and oxidative stress responses (NRF2). We previously demonstrated that H<sub>2</sub>S was necessary and sufficient for increased stress resistance under certain DR paradigms<sup>33,34</sup>. Surprisingly, HC in both standard and LP diets did not induce the H<sub>2</sub>S-producing enzyme cystathionine-γ-lyase (CGL; *Cth* gene) in either the liver or kidney (Supplementary Data Fig. 4a). Similarly, H<sub>2</sub>S production capacity in the liver, kidney, and serum was unaffected by HC (Supplementary Data Fig. 4b, d). To experimentally validate a lack of involvement of H<sub>2</sub>S production in HC protection, mice were administered propargylglycine and aminooxyacetic acid (PAG + AOAA) to inhibit CGL-dependent H<sub>2</sub>S production (Supplementary Data Fig. 4e). We fed standard or LP diets to wild-type mice with access to Ctrl or HC drinks, and treated them with either vehicle or PAG + AOAA. Resistance to IRI, assessed by serum urea and creatinine levels, was significantly improved by HC, LP, and LP + HC in both vehicle- and PAG-treated mice (Supplementary Data Fig. 4f, g) compared to Ctrl mice, confirming that H<sub>2</sub>S production was not required for the protection induced by HC.

Fibroblast growth factor 21 (FGF21) is another key nutrient-sensing molecule<sup>32</sup>. In both rodents and humans, one month of protein restriction increases FGF21 and drives key physiologic adaptations, including thermogenesis and altered feeding behavior<sup>32,37,45</sup>. Here, one week of HC induced a 13-fold increase in serum FGF21 levels (Fig. 3a), which was already observed after 2 days on HC (Supplementary Data Fig. 5a). HC induced a similar increase in serum FGF21 levels in females (Supplementary Data Fig. 5b) and in old mice (Supplementary Data Fig. 5c). The LP diet increased serum FGF21 levels to a greater extent, but the combination of HC water and the LP diet did not result in an additional increase (Fig. 3a). FGF21 is a metabolic hormone predominantly produced in the liver<sup>32</sup>. Here Fgf21 mRNA expression was restricted to the liver, with low expression in the kidney, skeletal muscle, and adipose tissue (Supplementary Data Fig. 5d). Consistently, FGF21 induction was observed in the liver (Fig. 3b), but not in the kidney (Fig. 3c) of HC mice. In accordance with the activation of FGF21, HC increased whole-body metabolic rate, as shown by VO<sub>2</sub> consumption (Supplementary Data Fig. 5e) and VCO<sub>2</sub> production (Supplementary Data Fig. 5f), as well as energy expenditure (Supplementary Data Fig. 5g). Similarly, the effects of HC were driven by protein dilution, as no additive effect was observed in mice fed an LP diet (Supplementary Data Fig. 5e, g). Underlying these changes in metabolism, the HC diet-induced subcutaneous adipocyte browning with smaller multilocular adipocytes on H&E staining (Supplementary Data Fig. 5h) and a 2-fold increase of the thermogenesis-associated gene *Ucp1* in brown and white adipose tissue (Supplementary Data Fig. 5i, j). Serum FGF21 levels correlated negatively with dietary protein intake (Fig. 3d,  $r^2 = 0.43$ ,  $p = 0.0001$ ) and with kidney function at day 2 post-renal IRI as measured by serum urea AUC (Fig. 3e,  $r^2 = 0.30$ ,  $p = 0.0167$ ). Cysteine supplementation (HC + Cysteine) also reduced FGF21 (Fig. 3f), which is consistent with our hypothesis that protein dilution is required for the HC-mediated benefits.

To further explore the importance of HC-mediated induction of FGF21 signaling, we sought to compare the Fgf21 transcriptional signature to one week of HC. To do so, we examined the hepatic differentially expressed genes (DEGs) from a publicly available dataset of Fgf21-overexpressing mice (GSE39313)<sup>35</sup>. We identified 31 significant DEGs with an FDR  $p < 0.1$  and  $\log_2FC > 1$ , overlapping with the HC transcriptional signature (Fig. 3g). Of these 31 DEGs, the top 10 highest from the Fgf21-overexpression dataset were similarly upregulated in the livers of HC mice (Fig. 3h). Together, these data support the hypothesis that HC effects on stress resistance are mediated by FGF21 signaling induced downstream of dietary protein dilution.



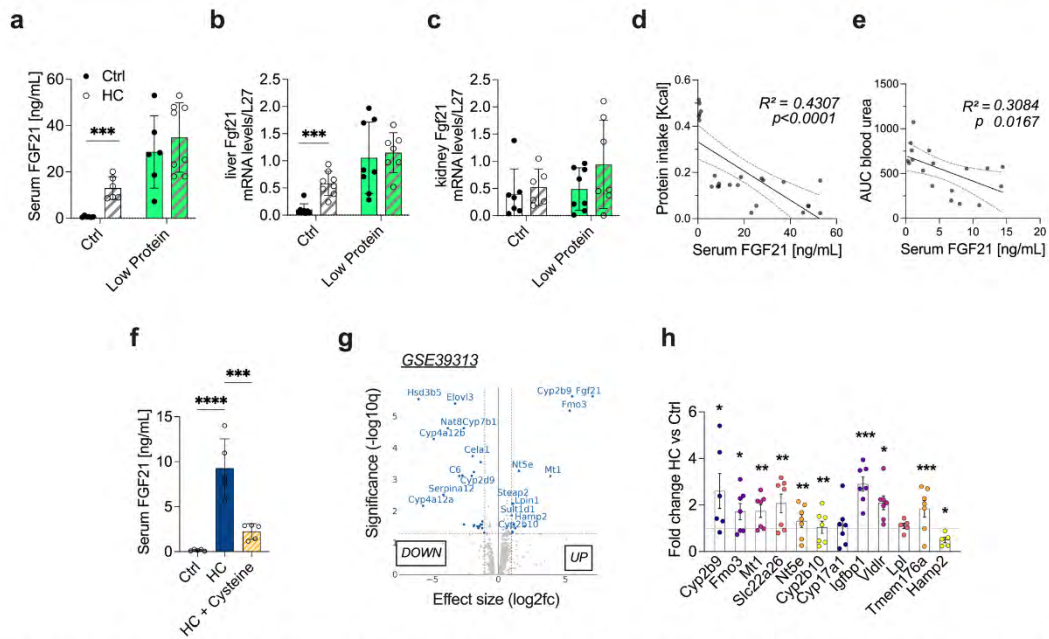


**Fig. 3 | Carbohydrate loading induces FGF21 expression.** **a** Serum FGF21 levels after one week of preconditioning with control or low protein diet (LP) with control (Ctrl) or 50% sucrose-water (HC). **b** Relative liver Fgf21 mRNA levels after one week of preconditioning with the indicated diet. **c** Relative kidney Fgf21 mRNA levels after one week of preconditioning with the indicated diet. **d** Linear regression showing the relationship between serum FGF21 levels versus protein intake and (e) serum urea (AUC).  $R^2$  coefficient was calculated using Pearson's method. **f** Serum FGF21 levels after one week of preconditioning with Ctrl, HC or HC with cysteine oral gavage (HC + Cysteine). **g** Volcano plot of liver differential expressed genes (DEG) with  $FDR < 0.05$  and  $\log_2FC > 2$  from FGF21 overexpressing male mice from

GSE39313. **h** Fold change of top DEGs from GSE39313 in liver after one week of preconditioning with HC compared to Ctrl. \* $p$  values of **a,b** were calculated with two-way ANOVA followed by a Tukey's post hoc analysis, **d,e** are linear regressions and  $r$  squared Pearson's coefficient, **f** with one-way ANOVA and **h** with unpaired two-tailed T-test with Bonferroni correction, \* $p < 0.05$  \*\* $p < 0.01$  \*\*\* $p < 0.001$  \*\*\*\* $p < 0.0001$ .  $p$ -values for **a** = 0.0001, for **b** = 0.0001, for **d** < 0.0001, for **f** < 0.0001, for **h** = 0.0003. In all panels, experiments were carried out in 10-weeks old male mice. Sample sizes: (**a-c**),  $n = 8$ ; (**d-e**),  $n = 32$ ; (**f**),  $n = 5$  for all conditions; (**h**),  $n = 8$  for all conditions. Data in all panels are shown as mean  $\pm$  SD. See also Supplementary Data Figs. 4 and 5.

### FGF21 is required for the protection from IRI

The necessity of FGF21 for HC-mediated benefits was tested with whole-body Fgf21 deletion (Fgf21<sup>KO</sup>) mice (Fig. 4a). HC-mediated changes in body weight (Supplementary Data Fig. 6a), total calorie intake (Supplementary Data Fig. 6b, c), food and water intake (Fig. 4b) were similar in both Fgf21<sup>WT</sup> and Fgf21<sup>KO</sup> mice. However, while the absence of FGF21 had no effect on renal IRI response in Ctrl mice, Fgf21<sup>KO</sup> mice failed to gain protection upon IIC, as demonstrated by serum urea (Fig. 4c and Supplementary Data Fig. 6d), creatinine levels (Fig. 4d), histological damage (Fig. 4e), tissue necrosis (Fig. 4f), and *Krt20* gene expression (Fig. 4g). Finally, we tested whether protection against general surgical stress conferred by HC required FGF21. Indeed, HC-mediated protection against hepatic IRI was also lost in Fgf21<sup>KO</sup> mice, as demonstrated by serum AST/ALT levels (Fig. 4h) and histological damage (Fig. 4i). In addition, *Hmgb1* mRNA expression, a biomarker of cellular stress responses and damage-associated molecular patterns<sup>46</sup>, was decreased in Fgf21<sup>WT</sup> mice on HC, but not in Fgf21<sup>KO</sup> mice (Fig. 4j). In conclusion, our findings demonstrate that FGF21 is required for surgical stress resistance via mechanisms that may be independent of diet-induced metabolic adaptations.

### Exogenous FGF21 is sufficient to promote stress resilience

Long-term treatment with FGF21 agonists improves circulating lipid profiles in humans<sup>47</sup>, but could negatively impact blood pressure with long-term use<sup>48</sup>. After showing that FGF21 was required for

protection against IRI, we tested whether short-term FGF21 treatment was sufficient to confer protection against surgical stress. Mouse FGF21 (mFGF21) at 1 mg/kg/day or sodium chloride vehicle (Veh) was administered continuously for one week via osmotic minipumps prior to renal IRI surgery (Fig. 5a). Serum FGF21 levels in mice treated with FGF21 were significantly higher than in mice given access to HC water (100 ng/mL versus 0.48 ng/mL, Fig. 5b). During the baseline period prior to surgery, and consistent with previous findings in Fgf21 transgenic mice<sup>35</sup>, total food intake and water intake doubled in mice treated with FGF21 (Fig. 5c). On day 7 of treatment, FGF21-treated mice had a lower body weight compared to the control group (Supplementary Data Fig. 6e), which can be likely attributed to increased energy expenditure. Similar trends were observed for protein, carbohydrate, and lipid intake (Supplementary Data Fig. 6f, g). Immediately following renal IRI, and despite osmotic minipump removal, serum FGF21 remained high in the treated mice, but began decreasing by 48 hours post-surgery (Fig. 5b). Serum urea was significantly decreased in FGF21-treated mice compared to Veh (Fig. 5d,  $530 \pm 319$  versus  $813 \pm 100$ , AUC). Serum creatinine at day 2 post-renal IRI was similarly reduced (Fig. 5e,  $1.2 \pm 1.3$  mg/mL versus  $3.5 \pm 0.93$  mg/mL). FGF21 preconditioning also decreased the expression of *Krt20* (Fig. 5f), decreased histological damage (Fig. 5g,  $9.1 \pm 3.4$  versus  $12.8 \pm 2.9$ ), and necrotic area (Fig. 5h). Together, these data are consistent with the hypothesis that FGF21 treatment for one week is sufficient to recapitulate HC-induced surgical stress protection.

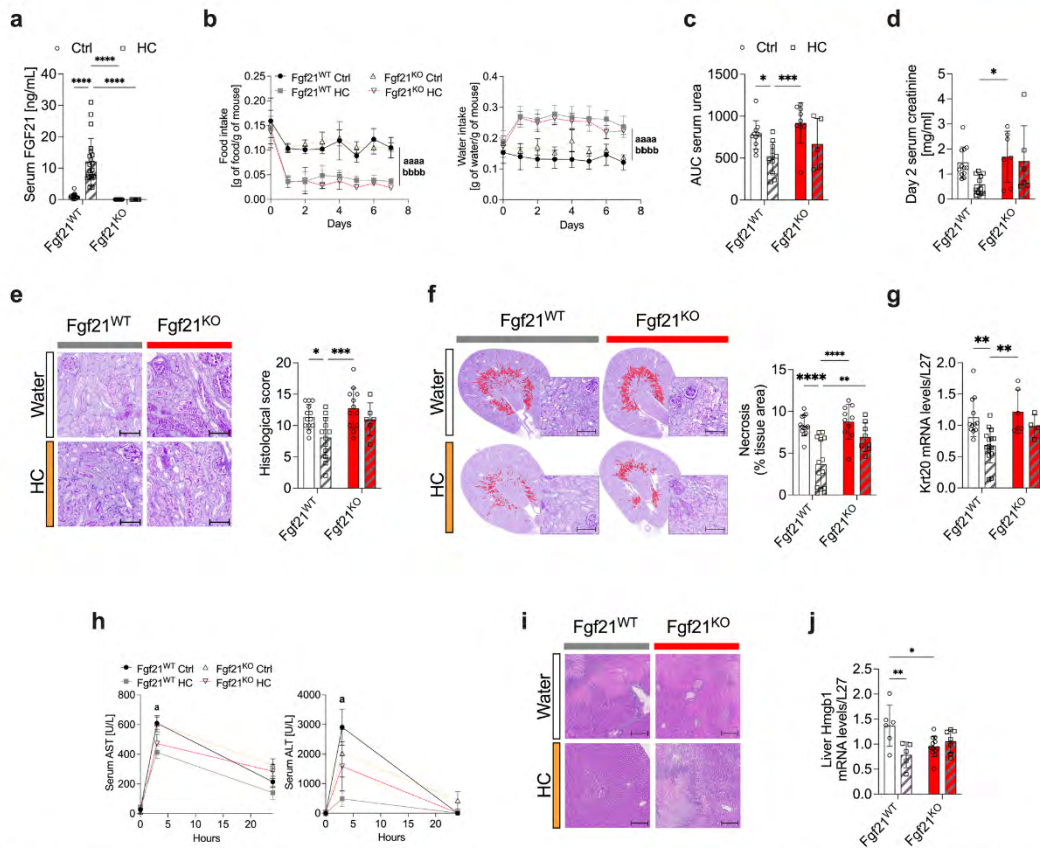


**Fig. 4 | FGF21 is required for the protective effects of carbohydrate loading.** **a** Serum FGF21 levels after one week of preconditioning with standard (Ctrl) or 50% sucrose-water (HC). **b** Food (left) and water (right) intake (normalized by body weight) after one week of preconditioning with the indicated diet. **c** Serum urea (AUC) and **(d)** serum creatinine levels at day 2 post-renal IRI after one week of preconditioning with the indicated diet. **e** Representative cross sections of PAS-stained kidneys (left;  $\times 10$  magnification; scale bar  $100\ \mu\text{m}$ ) and histological score (right) at day 2 post-renal IRI after one week of preconditioning with the indicated diet. **f** Representative cross sections of PAS-stained kidneys with necrotic area digitally highlighted in red (left;  $\times 10$  magnification; scale bar  $100\ \mu\text{m}$ ) and quantification of necrotic tissue area (right) at day 2 post-renal IRI after one week of preconditioning with the indicated diet. **g** Relative Krt20 mRNA levels in the kidney at day 2 post-renal IRI after one week of preconditioning with the indicated diet. **h** Serum aspartate aminotransferase (AST) and alanine aminotransferase (ALT) enzyme levels at the indicated time post-hepatic IRI. **i** Representative cross sections of H&E-stained livers ( $\times 20$  magnification; scale bar  $30\ \mu\text{m}$ ) at day 1 post-hepatic IRI.

Ischemic areas appearing in light pink. **j** Relative Hmgb1 mRNA levels in the liver at day 2 post-renal IRI after one week of preconditioning with the indicated diet. \**p* values for a,c,g,j were calculated with two-way ANOVA followed by a Tukey's post hoc analysis, b with two-way RM ANOVA with Geisser-Greenhouse correction and h with two-way ANOVA followed by a Sidak's post hoc analysis. \**p* < 0.05 \*\**p* < 0.01 \*\*\**p* < 0.001 \*\*\*\**p* < 0.0001 a *p* < 0.05 aaaa *p* < 0.0001 Fgf21<sup>WT</sup> HC vs. Fgf21<sup>WT</sup> Ctrl, bbbb *p* < 0.0001 Fgf21<sup>KO</sup> HC vs. Fgf21<sup>WT</sup> Ctrl. *p* values for a < 0.0001, < 0.0001 and < 0.0001, for b < 0.0001 and < 0.0001, for c = 0.0269 and 0.0008, for d = 0.0453, for e = 0.0236 and 0.001, for f < 0.0001, < 0.0001 and = 0.0074, for g = 0.0002 and 0.0031, for h = 0.0328 and 0.0351, for j = 0.007 and 0.022. In a-j, experiments were carried out in Fgf21<sup>WT</sup> and Fgf21<sup>KO</sup> 10-weeks old male mice. Sample sizes: (a-g), *n* = 10–15, *n* = 15 for Fgf21<sup>WT</sup> Ctrl, *n* = 15 for Fgf21<sup>WT</sup> HC, *n* = 15 Fgf21<sup>KO</sup> Ctrl, *n* = 10 for Fgf21<sup>KO</sup> HC; (h-j), *n* = 6–13, *n* = 6 Fgf21<sup>WT</sup> Ctrl and HC, *n* = 10 for Fgf21<sup>KO</sup> Ctrl, *n* = 13 for Fgf21<sup>KO</sup> HC. Data in all panels are shown as mean  $\pm$  SD. See also Supplementary Data Fig. 6.

**Identification of a carbohydrate loading and FGF21-dependant signature**

We finally sought to understand the changes in gene expression induced by FGF21 during HC, and how they underlie the protective effects on IRI. To do this, we identified gene expression modules associated with serum FGF21 expression in both kidney and liver transcriptomic datasets using weighted correlation network analysis (WGCNA). For the kidney, we performed bulk RNA-seq in mice preconditioned for one week with either Ctrl or HC on both standard and LP diets. For the liver, we used a public dataset (SRA accession PRJNA851959) of male mice receiving *ad libitum* access to diets

containing different protein levels (0%, 2%, 6%, 10%, 14%, and 18% protein intake) for 7 days<sup>41</sup>. To identify the genes associated with various kidney and liver phenotypes and traits, all expressed protein-coding genes were aggregated and analyzed using WGCNA, including 13106 genes for kidney and 11880 for liver. A total of 13 and 15 WGCNA modules were identified (Supplementary Data Fig. 7a, 8a), with each WGCNA module containing 24 to 4693 genes. The maroon, pale-turquoise, and darkseagreen modules in the kidney, and the darkred, salmon4, darkorange, indianred, and navajowhite modules in the liver, correlated (*p* < 0.05) with circulating FGF21 levels (Fig. 6a, b). Genes in these modules significantly associated with serum FGF21 levels



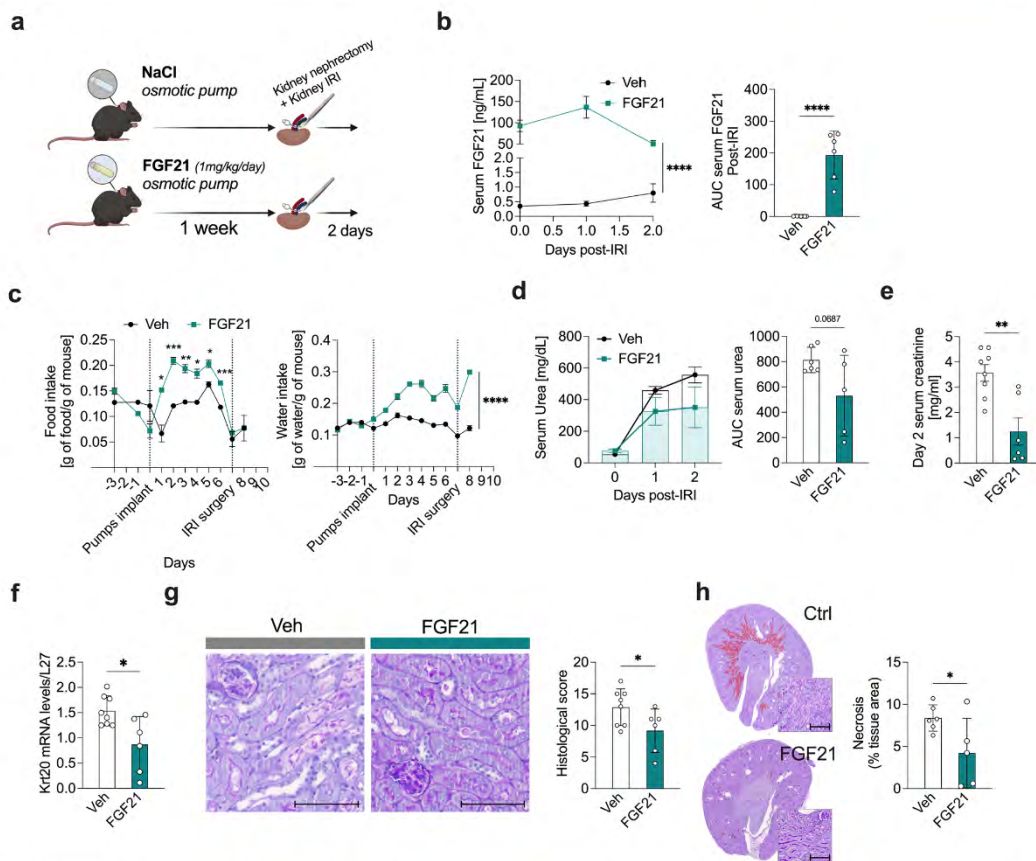


**Fig. 5 | FGF21 protects against kidney ischemia-reperfusion injury.**

**a** Experimental setup. Ad-libitum fed 10-week-old male mice were given free access to a standard diet (Ctrl) and implanted with osmotic pumps containing either NaCl (Veh) or human recombinant FGF21 (FGF21; 1 mg/kg/day) for 7 days prior to renal IRI surgery. Created with BioRender.com. **b** Serum FGF21 levels (left) and AUC (right) post-renal IRI after one week of preconditioning with the indicated treatment. **c** Food (left) and water (right) intake (normalized by body weight) after one week of preconditioning with the indicated treatment. **d** Serum urea levels (left) and AUC (right) at the indicated time post-renal IRI. **e** Serum creatinine levels at day 2 post-renal IRI after one week of preconditioning with the indicated treatment. **f** Relative Krt20 mRNA levels at day 2 post-renal IRI after one week of preconditioning with the indicated treatment. **g** Representative cross sections of PAS-stained kidneys (left;  $\times 10$  magnification; scale bar 100  $\mu\text{m}$ ) and histological score (right) after one week of preconditioning with the indicated

treatment. **h** Representative cross sections of PAS-stained kidneys with necrotic area digitally highlighted in red and quantification (left;  $\times 10$  magnification; scale bar 100  $\mu\text{m}$ ) and necrotic tissue area (right) at day 2 post-renal IRI after one week of preconditioning with the indicated treatment. \* $p$  values for **b**, **c** were calculated with two-way RM ANOVA with Geisser-Greenhouse correction, **c** with two-way ANOVA followed by a Sidak's post hoc analysis, and **b**, **d**, **e**, **f**, **g**, **h** with unpaired two-tailed T-tests. \* $p < 0.05$  \*\* $p < 0.01$  \*\*\* $p < 0.001$  \*\*\*\* $p < 0.0001$ .  $p$  values for **b**  $< 0.0001$  and  $< 0.0001$ , for **c** = 0.0120, 0.0002, 0.0028, 0.0121, 0.0129 and 0.0001, for **d** = 0.0667, for **e** = 0.0022, for **f** = 0.0129, for **g** = 0.0488, for **h** = 0.0471. Image1A was partially created with BioRender.com. In **b**–**h**, experiments were carried out in 10-week-old male mice. Sample sizes: (**a**–**h**),  $n = 6$ – $8$ ,  $n = 8$  Ctrl1 and  $n = 6$  FGF21 treated group. Data in all panels are shown as mean  $\pm$  SD. See also Supplementary Data Fig. 6.

( $R^2 > 0.5$ ,  $p < 0.05$  in both liver and kidney) were involved in “ribonucleoprotein complex biogenesis”, “ncRNA processing” and “regulation of apoptotic signaling pathway” (Fig. 6c). Genes inversely correlated with serum FGF21 levels were associated with metabolic processes, such as “regulation of cellular catabolic process” and “autophagy” (Fig. 6d and Supplementary Data Fig. 8b). Next, STRING (Search Tool for the Retrieval of Interacting Genes/Proteins) protein-protein interaction (PPI) network analysis was used to identify relevant transcription factors (TF) implicated in HC and FGF21-mediated benefits. E twenty-six (Ets), Nuclear factor kappa-light-chain-enhancer of activated B cells (Nf $\kappa$ b), ATF4, Peroxisome proliferator-activated receptor gamma (PPAR $\gamma$ ) and NRF2 (NES = 5.33, 10.26, 5.5, 9.4 and 6.78

respectively) were the most significant regulators associated with the binding motifs in the kidney module genes (Fig. 6e). Ets and Nf $\kappa$ b have been implicated in the regulation of immune and cell survival processes, while PPAR $\gamma$  has been identified as a key regulator of cellular metabolism. Interestingly, in the liver, we identified ATF3/4, UQCRB, and Sox9 (NES = 13.49, 7.92 and 5.8 respectively) as the most significant regulators associated with binding motifs in genes positively correlated with serum FGF21 levels (Fig. 6f). ATF3 and ATF4 are involved in cellular stress responses, including amino acid deprivation and oxidative stress, while UQCRB is a subunit of complex III in the mitochondrial electron transport chain, suggesting the induction of tissue regeneration or repair-like responses. To validate our analysis,

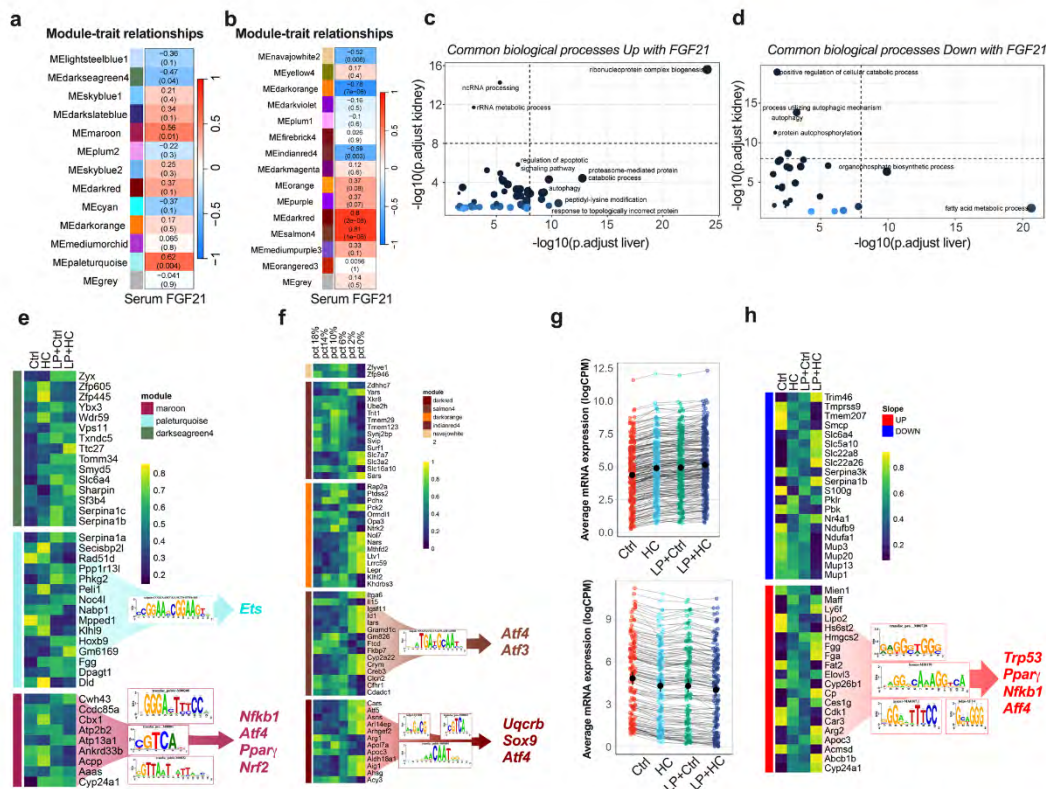


**Fig. 6 | Identification of FGF21-associated gene modules in kidney and liver induced by protein dilution.** **a** Module-Trait relationships with serum FGF21 levels identified through Weighted Gene Co-expression Network Analysis (WGCNA) from kidneys of male mice given access to *ad libitum* Ctrl, HC, LP and LPHC diet for one week. Top line corresponds to Pearson  $R^2$  and bottom line to adjusted  $p$  value. Color scales represent positive correlation (red) and negative correlation (blue). **b** Module-Trait relationships with serum FGF21 levels identified through WGCNA from livers of mice after one week on diets with 18%, 14%, 10%, 6%, 2% and 0% protein content. Top line corresponds to Pearson  $R^2$  and bottom line to adjusted  $p$  value. **c** Common biological processes (GO terms) enriched in kidney and liver modules with significant positive and **(d)** negative Module-Trait relationships with serum FGF21 identified through WGCNA. The dot size corresponds to the number of genes in the pathway. The color of the dots indicates the degree of significance of the pathway enrichment, with darker shades indicating higher significance. **e** Heatmap of percentile-transformed expression levels of the top 15 genes from kidney and liver **(f)** modules with significant Module-Trait relationships with serum

FGF21. Yellow indicating high expression and blue indicating low expression. The genes from each module with positive Module-Trait relationships with serum FGF21 were used in STRING and non-singleton were used for transcription factor analysis (TFA). The motifs picture shows the top NES motifs and their associated direct transcription factors. **g** Average mRNA expression levels of genes from kidney with slope  $> 10$  and  $R^2 > 0.70$  for each diet group (Ctrl, HC, LP, and LP+HC). Top panel shows genes with positive slopes, while bottom panel shows negative slopes, reflecting protein dilution intake. **h** Heatmap of percentile-transformed expression levels of the top 20 genes from kidney with slope  $> 10$  and  $R^2 > 0.70$  for each diet group (Ctrl, HC, LP, and LP+HC). Yellow indicates high expression and blue indicates low expression. Upregulated genes were used in STRING and non-singleton were used for transcription factor analysis (TFA). The motifs picture shows the top NES motifs and their associated direct transcription factors.  $p$  values for **a** and **b** were calculated with Pearson correlation, and **c** and **d** with Benjamin-Hochberg (BH) test with  $FDR < 0.05$ . Sample sizes: **(g)**,  $n = 3$  Ctrl,  $n = 3$  HC,  $n = 6$  LP,  $n = 5$  LP + HC. See also Supplementary Data Fig. 7 and 8.

we employed an alternative method, identifying 263 positively (Fig. 6g top panel and Supplementary Data Fig. 8e) and 146 negatively (Fig. 6g bottom panel and Supplementary Data Fig. 8e) correlated genes with protein intake. In addition, network and transcription factor analysis identified PPAR $\gamma$  and Nf $\kappa$ b, as well as Trp53 and ATF4 (Fig. 6h). Together, these results suggest that activation of stress responses and cell survival pathways is associated with FGF21 induction during HC.

**Discussion**

In this study, we demonstrate that one week of carbohydrate loading induces protein dilution in mice, which confers protection from surgical stress *in vivo* via FGF21. We not only found that short-term carbohydrate loading is sufficient to induce protein dilution, but also

demonstrated that these benefits can be achieved under hypercaloric conditions. In fact, we are among the first to demonstrate a dietary intervention that protects from surgical stress without inducing body weight reduction. A model is presented in Supplementary Data Fig. 9.

Voluntary adherence to a dietary restriction is difficult for most people. One potential benefit of carbohydrate loading is that it does not involve forced food restriction but instead promotes an alternative source of energy and spontaneous macronutrient dilution. The response to carbohydrate was consistent across sex and in older mice, supporting the general validity of our findings. Interestingly, this differs from previous work in which low protein diet does not induce FGF21 in C57BL/6J female mice<sup>19</sup>. Our carbohydrate loading protocol does induce greater protein restriction than diets used previously



(~3.5% vs 6% protein intake), so it is possible that females require greater protein restriction to induce FGF21. The observational human data from the USDA NHANES suggested an inverse association between sucrose and protein intake, indicating the potential for conserved appetitive mechanisms. However, the metabolic response and the extent to which carbohydrate loading may result in favorable outcomes in humans are still unknown. As with any epidemiologic study, the association of macronutrient intake can be confounded by any other variable (lifestyle, other dietary factors, comorbidities, medications, etc.). Although protein energy intake was treated as a single variable, it truly is a combination of amino acid ratios that cannot be fixed, even in mice which limit drawing conclusions about the effects of dietary protein in humans.

Here, carbohydrate loading consisted of an *ad libitum* solution of 50% sucrose in water for one week. This slightly differs from ERAS<sup>®</sup> protocols, classically recommending 100 g of carbohydrate the evening before surgery, and 50 g of carbohydrate until 2 hours before surgery<sup>50</sup>. Alternatively, healthy individuals have undergone 3–7 days of high carbohydrate loading diet (approximately 70% of calories from carbohydrate), at the expense of protein<sup>51</sup>. The latter is similar to most murine dietary protein restriction regimens, that replaced dietary protein with carbohydrates utilized complex carbohydrates derived from starch<sup>15,41</sup>. While we did not study the interactions between carbohydrate sources here, one of the few studies testing the effects of carbohydrate composition during protein dilution showed that a sucrose-rich diet improved metabolic parameters compared to a 50:50 mixture of glucose and fructose<sup>28</sup>. Of interest, carbohydrate loading resulted in an overconsumption of excess energy from sucrose and a voluntary reduction in protein intake. Rodents have a dominant protein appetite, which drives food intake to reach a protein target<sup>52</sup> via an FGF21-dependent mechanism<sup>37,40</sup>. Thus, protein-restricted diet typically results in the overconsumption of total energy. This response is called protein leverage<sup>52</sup>. A limited body of evidence also supports the protein leverage hypothesis in humans, at least down to 10% of protein energy<sup>53</sup>. While we do replicate the protein leverage hypothesis in mice fed low protein with normal water, we interestingly observe that mice given sucrose-water do not increase food intake on a low protein diet. This suggests the intriguing possibility that liquid carbohydrate intake may override protein leverage. Future studies may test the resulting hypothesis that FGF21 action on drinking behavior may override its action on feeding behavior, or that an FGF21-independent mechanism affects feeding behavior upon liquid carbohydrate intake.

Consistent with the latter hypothesis, carbohydrate loading-mediated changes in food and water intake were unaffected by the absence of FGF21. On the other hand, exogenous FGF21 administration, without any dietary intervention, was sufficient to increase both water and food intake. While protein restriction is required for the benefits of carbohydrate loading, this suggests that protein restriction might be dispensable for FGF21 benefits when given exogenously. These differences in the metabolic response to dietary protein restriction and protein dilution during carbohydrate loading will need to be further investigated. Additionally, liquid carbohydrate loading may be a previously unrecognized method to limit protein intake.

The response to dietary protein is also not linear. Previous work demonstrated that protein restriction has a threshold around 8–10% of dietary protein calories to produce the strongest improvements in body composition, insulin sensitivity<sup>41</sup> and induction of FGF21<sup>24</sup>. In our study, when comparing carbohydrate loading (3.4% dietary protein calories) versus a low protein diet (6.4% dietary protein calories), the protection from surgical stress was equivalent. This is consistent with the idea of a threshold and non-linear effects<sup>41,54</sup>. A study comparing a range of sucrose concentrations during carbohydrate loading would be of interest to better investigate the potential for dose response to carbohydrate loading.

The duration of carbohydrate loading required for the onset of stress resistance benefits is unknown. Here, we show that only one week of carbohydrate loading is sufficient for the observed benefits in mice with maximal FGF21 induction already achieved after two days, indicating that this relatively short duration of carbohydrate loading might be sufficient to yield the observed benefits. Whether or not longer periods of carbohydrate loading will further increase protection remains to be experimentally determined.

Our previous results demonstrated that CGL is required for the benefits of DR, including protection from ischemia<sup>13</sup> and IRI<sup>14</sup>. Surprisingly, H<sub>2</sub>S/CGL was not influenced by carbohydrate loading or protein restriction, nor required for surgical stress resistance. Protein restriction was associated with a decrease in CGL expression and cysteine level<sup>41</sup>, while caloric and methionine restriction were previously demonstrated to increase both CGL and H<sub>2</sub>S production. CGL expression was also increased in response to a high-protein diet<sup>55</sup>, but was not affected in long-lived mice overexpressing Fgf21<sup>35,56</sup>. Thus, our data demonstrate that, while CGL may be critical for the beneficial effects of caloric or methionine/cysteine restriction, it may be dispensable for the effects of carbohydrate loading/protein restriction in the liver and kidney.

Instead, FGF21 appears to be the molecular mediator of the benefits of carbohydrate loading. Additionally, we propose that HC-mediated protection from IRI functions as a para- and endocrine mechanism involving hepatic secretion of FGF21, consistent with a previous report<sup>32</sup>. This could serve as a basis for FGF21-based therapeutics during surgical stress or trauma, where there is currently no widely accepted risk mitigation strategy. FGF21 is a critical mediator of protein restriction<sup>32</sup>. In line with previous studies, we show that FGF21 signaling increases energy expenditure and thermogenesis<sup>34,38,57</sup>. During protein restriction, FGF21 signaling is essential to regulate adaptive, homeostatic changes in metabolism and feeding behavior<sup>32,37</sup>. Consistent with others<sup>45</sup>, we found that carbohydrate loading induction of FGF21 caused increased adipose UCP-1 and increased energy expenditure. The importance of FGF21 signaling during carbohydrate loading also emphasizes that protein restriction is a key driver of the observed benefits. By which mechanism could endogenous FGF21 mediate the benefits of carbohydrate loading/protein restriction in mitigating IRI? While this remains unclear, our investigations into the regulatory networks and transcription factors involved in FGF21 benefits during carbohydrate loading suggest the importance of the stress response proteins ATF3/4 and the antioxidant regulator NRF2. Of note, in mice lacking ATF3, IRI was increased after orthotopic liver transplantation, which was associated with inhibition of HO-1 signaling and increased TLR4 as well as NFκB signaling<sup>58</sup>. ATF4 can induce hepatic FGF21 in both ATF4-overexpressing mice and a model of endoplasmic reticulum stress through eIF2α and the unfolded protein response<sup>59</sup>. However, the role of ATF4 in dietary restriction is complicated, as it is not required for FGF21 induction upon methionine restriction<sup>60</sup>. Similarly, NRF2 was not required for caloric restriction-dependent protection from hepatic IRI<sup>14</sup>. However, activation of NRF2 reduced tubular damage upon renal IRI and was associated with FGF21-mediated protection against diabetic nephropathy<sup>61,62</sup>.

Current clinical recommendations for the clinical presurgical care are to 1) avoid fasting, 2) initiate nutritional support or supplementation without delay, and 3) reduce factors that exacerbate stress-related catabolism or impair gastrointestinal function<sup>4,5</sup>. Thus, our findings carry significant implications for the development of nutritional strategies during surgery. While our data suggest an inverse correlation between protein and sucrose intake in humans, the impact of short-term carbohydrate loading on caloric and protein intake in patients undergoing surgery remains to be established. Additionally, the impact of such interventions in humans with altered glucose metabolism (insulin resistance, metabolic syndrome, etc.) will need to be

carefully evaluated prior to initiating a clinical trial. On the other hand, FGF21 could be an alternative strategy for those who are not able to tolerate carbohydrate loading<sup>63</sup>. Counterintuitively, FGF21 levels are increased in patients with obesity and chronic kidney disease (CKD)<sup>64,65</sup>. This may be explained by FGF21 resistance, which is also associated with worse metabolic profiles, higher inflammatory markers, more comorbidities, and higher mortality in CKD patients<sup>66</sup>. Thus, these patients may require either larger doses of exogenous FGF21 or an alternative intervention that promotes FGF21 sensitivity, such as carbohydrate loading/protein dilution, to achieve protection against IRI. Interestingly, in our study in FGF21-sensitive mice, short-term FGF21 delivery was sufficient to recapitulate the benefits of HC drinks without the need for prolonged administration, thus highlighting the translational potential.

In conclusion, in *ad libitum*-fed mice, carbohydrate loading promotes dietary protein restriction, the adaptive stress response, and resilience to surgical stress. ERAS<sup>®</sup> approaches currently promote short-term carbohydrate loading drinks to improve postoperative recovery without clear mechanistic explanations. Here, we identified FGF21 as a key molecular mediator of carbohydrate loading. These findings have broad implications for our basic understanding of the impact of carbohydrate and protein-carbohydrate interactions on metabolic health. Finally, our results provide a rationale for short-term carbohydrate loading or FGF21-based therapeutics during surgery, for which there is now no widely accepted risk mitigation strategy.

## Methods

### Mice

All experiments were performed with the approval of the cantonal Veterinary Office (Service de la Consommation et des Affaires Vétérinaires SCAV-EXANIM, authorization number 3346, 3554b and 3768). All animal experimentation conformed to the *Guide for the Care and Use of Laboratory Animals*. All efforts were made to minimize animal suffering, including the use of anesthesia and analgesia during surgical procedures as well as humane endpoints to prevent undue distress. Animals were monitored daily. Mice with weigh loss > 10%, lethargy, muscle twitching, bleeding, infected or dehiscent wound were euthanized by exsanguination under general anesthesia in accordance with the “*Commission pour l'éthique dans les expérimentations animales*”. 10 to 12-week-old male and female, and 22-month-old male C57BL/6J mice (Janvier Labs, France) were used for all experiments. All mice were kept on *ad libitum* (AL) access to food and tap water, and kept under standard housing conditions, with 12 hr light/12 hr dark cycles, 30–70% humidity and a temperature of 20–23 °C unless specified otherwise. Fgf21 knockout (Fgf21<sup>KO</sup>) was generated by crossing Fgf21<sup>loxP</sup> mice (B6.129S6(SJL)-Fgf21<sup>tm1.209m</sup>/J, Jackson Labs #022361) with loxP sites flanking exons 1–3 of the Fgf21 gene with CMV-cre expressing mice (B6.C-Tg(CMV-cre)1Cgn/J, Jackson Labs #006054). The resulting offspring had a deletion in exons 1–3 of Fgf21 in all tissues. The line was subsequently maintained by breeding animals heterozygous for the Fgf21 deletion allele. Mouse ear biopsies were taken and digested in DirectPCR lysis reagent with proteinase K. Wild type (WT), heterozygous and knockout (KO) mice were identified by PCR using the forward primer 5′- ACC CCC TGA GCA TGG TAG A-3′ to detect the WT allele, and forward primer 5′- CAG ACC AAG GAG CAC AGA CC-3′ to detect the KO allele, and the common reverse primer 5′- GCA GAG GCA AGT GAT TTT GA-3′, using GoTaqR G2 Green Master Mix (M7822, Promega).

### Experimental diets

All experimental diets were based on diet 2125 from Granovit AG (Kaiseraugst, Switzerland), with 19.8% of calories from protein (hydrolyzed casein and individual crystalline amino acids), 10.4% from and 69.9% from carbohydrate. The low protein (LP) diet was custom prepared by Granovit AG based on diet 2125 with 6.4% protein/ 10.4%

fat/ 83.2% of carbohydrate (Granovit AG) and was provided *ad libitum*. The nutritional value of the control diet was 3.6 Kcal/gr, and 3.35 Kcal/gr for the LP diet. The high sucrose (HC) drink was prepared by adding 50% sucrose (w/w) in the drinking water, giving 2 Kcal of carbohydrate/g of HC drink. HC drink was changed every two days. Food pellets and bottles were weighed daily in every cage of mice. The delta weight of food and drink was calculated, divided by the number of mice, and normalized by the weight of each individual mouse in the cage. Total calorie intake was measured by calculating the sum of each macronutrient and their calories per gram (carbohydrates, proteins 4 kcal/gram, and fat 9 kcal/gram).

### Cysteine addback

C57BL/6J 10 to 12 weeks-old male mice were gavaged with soft plastic oral 20 G gavage needles (Instech Laboratories). The cysteine solution concentration was calculated from the difference of daily food intake, in weight of food, between mice given *ad libitum* access to water (Ctrl) and HC. According to the diet composition, cysteine constitutes 0.30% of the food weight (diet 2125 from Granovit AG), resulting in a daily intake of cysteine of 0.00558 g/day. A stock solution containing a concentration of 27.9 mg/mL of L-Cysteine in drinkable water (#168149, Sigma) was prepared and stored at 4 °C. The prepared solution was administered via oral gavage (10 µL/g of body weight) once daily (5.58 mg/day of L-Cysteine). Daily oral gavage of an equivalent volume of drinkable water (10 µL/g body weight) was given as vehicle control.

### Nephrectomy and renal ischemia-reperfusion injury

Mice were anesthetized with 3% isoflurane in 2 L O<sub>2</sub> and kept at 37 °C with an electrical heating pad. Following a 2-cm abdominal incision, the vascular pedicles of the right and left kidneys were identified under a microscope. First, the right renal artery, vein, and ureter were ligated and cauterized. Immediately after, the right kidney was dissected and flash-frozen in liquid nitrogen. Second, the left pedicle was clamped for either 23 minutes for young male and old male mice or 34 min for young female mice with S&T vascular micro-clamps (FST 18055-03, Fine Science Tools). Of note, the survival experiment was performed as a bilateral clamping of both pedicles for 35 minutes. A darkening of the kidney was observed to ensure that the pedicle had been successfully clamped.

### Hepatic ischemia-reperfusion injury

Liver IRI was performed as described previously<sup>14</sup>. Briefly, mice were anesthetized with 3% isoflurane in 2 L O<sub>2</sub> and kept at 37 °C with an electrical heating pad. Following a 2-cm abdominal incision, the vascular pedicles of the median lobe and left lateral lobe were identified under a microscope. An atraumatic S&T vascular micro-clamp (FST 18055-03, Fine Science Tools) was placed across the portal vein, hepatic artery, and bile duct just above the branching to the right lateral lobe for 35 minutes. Blanching of the lobes was observed to ensure that the artery had been successfully clamped. After 35 minutes of ischemia, the clamp was removed.

### Postoperative management

The abdominal incision was sutured with 6-0 Prolene, and surgical staples were used to close the skin (427631, Aichele Medico AG). All mice received subcutaneous buprenorphine (0.05 mg/kg Temgesic, Reckitt Benckiser AG, Switzerland) 15 minutes before surgery and –6–8 hours following surgery. During the night, mice received paracetamol (2 mg/ml Dafalgan, UPSA) and buprenorphine (0.009 mg/ml Temgesic, Reckitt Benckiser AG, Switzerland) in the drinking water for 48 hours postoperatively. During the day, mice received subcutaneous buprenorphine injection in the morning and evening for 48 hours postoperatively. Blood samples from the tail vein were taken preoperatively, and at 3 h and 24 h postoperatively using a capillary tube.



Serum was separated by centrifugation (2000g for 20 minutes at 4 °C) and flash-frozen in liquid nitrogen before being stored at -80 °C. On the second- or third-day following surgery for renal IRI and 24 h following surgery for hepatic IRI, mice were euthanized under anesthesia via cervical dislocation, followed by exsanguination, and perfused with PBS. Of note, the surviving mice involved in the survival experiment were euthanized after 8 days. The remaining kidney was collected and cut in half transversally. One half was flash-frozen in liquid nitrogen, and the other was fixed in 10% neutral buffered formalin and paraffin-embedded for histology.

#### FGF21 treatment

Mouse recombinant FGF21 (Cat# 450-56, Peprotech) was dissolved and diluted in sterile distilled water to a final dosage of 1 mg/kg/day. The filled 1007D Alzet osmotic minipump was presoaked for 24 hours in NaCl at 37 °C in a dry incubator. Mice were anesthetized with 3% isoflurane in 2 L O<sub>2</sub> and kept at 37 °C with an electrical heating pad. A 1-cm incision was made in the skin of the upper back/neck to implant the sterile, preloaded minipump. 5-0 Prolene surgical thread was used to stitch the wound. Mice received paracetamol (2 mg/ml Dafalgan, UPSA) in the drinking water for 48 hours postoperatively.

#### In-vivo inhibition of endogenous H<sub>2</sub>S production

Inhibition of endogenous H<sub>2</sub>S production was achieved by injecting the mice with 100 µL of a stock solution of 1 mg/mL propargylglycine (PAG) and 1 mg/mL amino-oxyacetic acid (AOAA) in physiologic saline, or saline vehicle, as previously described<sup>14</sup>. Mice were injected intraperitoneally (i.p.) once a day for three days prior to the kidney IRI surgery.

#### Metabolic cages

Throughout the calorimetry studies, a standard 12-hour light/dark cycle was maintained. Prior to data collection, all animals were weighed and acclimated to either normal chow or a low protein diet (LP) for the first three days, with or without a 50% sucrose drink. After 24 hours of acclimatization, mice were placed in metabolic cages, and measurements began for two consecutive days. At the conclusion of the measurements, the mice were weighed again. Energy expenditure was determined using a computer-controlled indirect calorimetry system (PromethionH, Sable Systems, Las Vegas, NV) as published<sup>67</sup>. Animals had unlimited access to food and water throughout the study. XYZ beam arrays (BXYZ-R, Sable Systems, Las Vegas, NV) were used to record ambulatory activity and position, and respiratory gases were measured using an integrated fuel cell oxygen analyzer, a spectrophotometric CO<sub>2</sub> analyzer, and a capacitive water vapor partial pressure analyzer (GA3, Sable Systems, Las Vegas, NV). Oxygen consumption and CO<sub>2</sub> production were monitored for 1-minute at 5-minute intervals. The respiratory quotient (RQ) was determined by dividing CO<sub>2</sub> production by O<sub>2</sub> consumption. The Weir equation was used to calculate energy expenditure:  $\text{Kcal/hr} = 60 \times (0.003941 \times \text{VO}_2 + 0.001106 \times \text{VCO}_2)$ <sup>68</sup>. MetaScreen v. 2.5 was used to coordinate data acquisition and instrument control, and raw data was processed using ExpeData v. 1.8.5 (Sable Systems, Las Vegas, NV) via an analysis macro that detailed all aspects of data transformation (available on request from the corresponding author).

#### Glomerular filtration rate measurement

FITC-sinistrin clearance was utilized to determine the glomerular filtration rate. Mice were anesthetized with isoflurane and subsequently had their right flanks shaved. After 2 minutes of basal recording, a mini-camera was connected to the flank, and a 0.35 g/kg solution of FITC-sinistrin (Fresenius-Kebi) was injected intravenously into the tail vein. The mice were anesthetized again with isoflurane, and the camera was removed after 90 minutes of recording. MP&D lab software (Mannheim Pharma & Diagnostics) was used to analyze the FITC-sinistrin

data, and GFR was estimated as published<sup>69</sup>. The GFR was then normalized to control and represented in mL/min/kg of body weight.

#### Body composition (EchoMRI)

Body composition (EchoMRI-100H, Echo Medical System, Houston, TX) was obtained on awake mice contained in a thin-walled plastic cylinder with a cylindrical plastic insert to restrict their movement. Mice were exposed to a low-intensity electromagnetic field for a brief period, and their fat and lean mass were determined.

#### Histological analysis

3-micron sections from paraffin-embedded half kidneys were stained with PAS (Periodic Acid Schiff) and paraffin-embedded livers with H&E. The kidneys were scored histologically using a modified Goujon scoring method<sup>70-72</sup>. This score was created to limit the observer's subjectivity and to evaluate the entire section containing heterogeneous damage. The kidneys were imaged at a magnification of 20x using a Zeiss Axioscan Z.1 slide scanner (Carl Zeiss). The entire scanned section was analyzed using Zen Blue 3.4 software (Carl Zeiss) and scored on five parameters: 1) glomeruli integrity, 2) tubule dilatation, 3) brush border integrity, 4) debris in the tubules, and 5) medulla integrity in the cortico-medullary area. Within each category, each item was graded on a scale of 0 to 3, with 0 representing "no damage" and 3 representing "extremely damaged." Briefly, to assess glomerulus integrity, more than ten glomeruli were randomly selected from the section and assigned a score of 0 to 3 on a scale of 0 to 3. The same procedure was followed in the remaining categories. After that, the score for each category was converted to a percentage of damage. A final score between 0 and 5 was assigned based on this percentage of damage: 0 represents a percentage of damage between 0% and 15%; 1 represents a percentage of damage between 15% and 30%; 2 represents a percentage of damage between 30% and 45 percent; 3 represents a percentage of damage between 45 percent and 60%; 4 represents a percentage of damage greater than 60%; and 5 represents a percentage of damage greater than 75%. On a scale of 0 to 25, the final score was the sum of the scores for each category.

#### Necrosis quantification

PAS-stained entire scanned sections of kidneys were exported (50%) using Zen Blue 3.4 software (Carl Zeiss). Necrotic areas were identified using the following criteria: tubules with large debris, large dilation, and tubular cell loss; tubules with cast formation; and tubule loss. The pelvis region has been excluded from quantification.

The necrotic area of digitally highlighted images was measured by calculating the highlighted area fraction using ImageJ (v1.54r) and defined as the necrotic area divided by the total kidney area.

#### Immunohistochemistry staining

4HNE (MAB3249, R&D Systems) immunohistochemistry was performed on paraffin sections<sup>73</sup>. After rehydration and antigen retrieval (TRIS-EDTA buffer, pH 9, 1 minute in an electric pressure cooker autocuiseur Instant Pot duo 60 under high pressure), immunostaining was performed using the EnVision<sup>®</sup>+ Dual Link System-HRP (DAB+) according to the manufacturer's instructions. Slides were further counterstained with hematoxylin. The positive immunostaining area was quantified using the Fiji (ImageJ 1.54r) software and normalized to the total area of the tissue by two independent observers blinded to the conditions.

#### Reverse transcription-quantitative polymerase chain reaction (RT-qPCR)

Mouse RNA was isolated using the TriPure<sup>™</sup> method (Roche, Switzerland) from 30-50 mg of kidney, liver, and muscle powder, followed by complementary DNA (cDNA) synthesis using the Prime Script RT reagent kit (Takara). cDNA samples were loaded into a 384-well plate

format (Applied Biosystems, ThermoFischer Scientific AG, Switzerland) using SYBR Green reagent-based PCR chemistry (10- $\mu$ l reaction volume containing specific forward and reverse primers). The quantitative PCR program was run on a ViiA 7 Real-Time PCR System, according to the manufacturer's recommendations (Applied Biosystems, ThermoFischer Scientific AG, Switzerland). RPL27 was chosen as the housekeeping gene<sup>74</sup>. Ct values for candidate and housekeeping genes were determined, and standard curves for each gene were calculated using serial dilutions. The relative standard curve method was used to determine the relative level of expression of genes. For gene encoding, the primers listed in supplementary Table S1 were used, and analysis was performed using the QuantStudioTM 1.3 software (ThermoFischer Scientific AG, Switzerland).

#### Blood analysis

Serum was isolated from blood taken from the tail vein pre-operatively and on days 1, 2, and 3 postoperatively by centrifugation (2000g for 20 minutes at 4 °C). Triglyceride concentration was determined using a Sigma kit (Cat# TR0100). Urea was measured as published<sup>12</sup> and using the Jung colorimetric method using a reactive solution containing 100 mg/l o-Phthalaldehyde (32800, Serva), 300 mg/l N-(1-naphthyl) ethylenediamine dihydrochloride (222488, Sigma), 2.5 mol/l sulfuric acid, 2.5 g/l boric acid, and 0.003 % Brij 35. After 30 minutes in the dark and at room temperature, the response was measured at 505 nm with a Synergy Mx micro-plate reader (BioTek Instruments (Switzerland) GmbH). The serum creatinine level was determined using the mouse Creatinine Assay Kit (80350, Crystal Chem INC). Mouse FGF-21 (MF2100, R&D Systems) levels were determined using commercial ELISA kits using the manufacturer's recommended protocol. The concentrations of AST (TR70121) and ALT (TR71121) were determined according to the manufacturer's instructions (Thermo-Scientific, Middletown, VA).

#### Lead acetate assay

H<sub>2</sub>S production was quantified in the kidney and liver, as previously published<sup>13,14</sup>. Briefly, tissue powder was homogenized in passive lysis buffer (PLB E1941, Promega) and the protein concentration was determined using the ThermoFisher Pierce™ BCA Protein Assay Kit (Cat# 23227). In a 96-well plate covered with Whatmann paper soaked in 20 mM lead acetate, samples were diluted (80  $\mu$ g of protein in 80 L of PBS) and combined with 20 L of reaction mix containing PBS, 1 mM Pyridoxal 5'-phosphate (PLP) (82870, Sigma), and 10 mM Cysteine (c7352, Sigma). The plate was then incubated in a dry incubator at 37 °C for 2–4 hours until lead sulfide darkening of the paper occurred.

#### Response surfaces analysis

All data were analyzed in R v.4.2.2. Data involving response surfaces were analyzed using Generalized Additive Model (GAM) and previously described<sup>26</sup>. Briefly, GAMs with thin-plate splines were used to model the responses to the macronutrient composition of the diet. GAMs were fitted using the mgcv tool of the R programming language (v1.9.0). The effects of macronutrients were divided into main effects and interactions. The response included post-renal IRI serum urea levels.

#### NHANES analysis

Data from the US Department of Agriculture National Health and Nutrition Examination Survey were analyzed as previously described<sup>75</sup>. Briefly, NHANES XPT data files were downloaded from the CDC NHANES website for surveys carried out from 2005–2012. The data were imported into R using the sasxport.get function from the Hmisc package. Individuals who were not pregnant, over the age of 18 years, and had two complete 24-hour dietary recalls were included. As no gender-differences were observed, genders were pooled for the final

analysis presented in the manuscript. For nutrient analyses, values from each individual's two 24-hour recalls were averaged.

#### RNA-sequencing processing and computation

Data preprocessing, statistical computation, and visualization were performed using the Omics Playground version v2.8.10<sup>76</sup>. Data preprocessing included filtering genes based on variance, expression across the samples, and missing values. Only protein-coding genes on non-sexual chromosomes were included in the analysis. Batch effects were identified by an F-test for the first three principal components. Batch correction was performed for explicit batch variables or unwanted covariates. Parameters with a correlation  $r > 0.3$  with any of the variables of interest (i.e., the model parameters) were omitted from the regression. Correction was performed by regressing the covariates using the 'removeBatchEffect' function in the limma R/Bioconductor package. For gene-level testing and identification of differentially expressed genes (DEG), statistical significance was assessed using two independent statistical methods: voom and limma-no-trend. Only genes that were significant using both methods were included. Gene expression was normalized using logCPM normalization in the edgeR R/Bioconductor package. For slope analysis, normalized genes were correlated with the mean protein intake of each group (Ctrl, HC in both regular and low protein diets) to identify protein dilution-driven genes. 409 genes with a correlation  $r_2 > 0.6$  and a slope  $> 9$  were selected. Bonferroni corrections were applied to multiple Pearson correlations.

#### WGCNA analysis

Raw counts were normalized by performing a variance-stabilizing transformation using the DESeq2 package in R (v1.40.2.). Genes with counts  $< 15$  in more than 75% of samples were filtered out. The variance-stabilizing transformed gene expressions were subjected to WGCNA based on the WGCNA package in R (v1.72-1)<sup>77</sup>. WGCNA parameters were set as: no missing data expression; soft threshold = 7 (estimate value); adjacency = "signed hybrid"; TOMtype = "signed"; merge cut height = 0.4. Function annotations of the genes were obtained using the org.Mm.eg.db package in R (v3.15). The correlation of eigengenes with external traits (FGF21 levels) was performed using 'bicor' biweight midcorrelation to obtain the most significant and robust associations. Intramodular analysis identified genes with high gene-module membership and gene-trait significance. The ClusterProfiler package in R (v4.8.2) and STRING v11.5 (Search Tool for the Retrieval of Interacting Genes) was used for functional enrichment. Protein-Protein Interactions network was performed with the module/cluster analysis using the Markov Cluster Algorithm (MCL) in Cytoscape<sup>78</sup>. 16,377 detected genes were used as the enrichment background. Terms with a False Discovery Rate (FDR)  $< 0.05$  were included.

#### Transcription factor analysis

Transcription factor binding motifs, which are enriched in the genomic regions of a query gene set, were determined using the iRegulon plugin (version 1.3) in Cytoscape. The cis-regulatory control elements of genes from each module associated with serum FGF21 were used in the iRegulon analysis. We set: identity between orthologous genes  $\geq 0.01$ , FDR on motif similarity  $\leq 0.001$ , and TF motifs with a normalized enrichment score (NES)  $> 3.5$ , ranking option for Motif collection :10 K (9713 PWMs), and a putative regulatory region of 20 kb centered around TSS (7 species). For gene expression analysis the logCPM normalized genes with non-missing values and a gene-module significance  $> 0.6$  or  $< -0.6$  with serum FGF21 levels, as well as the top positive and negative slopes from the gene expression-protein intake association, were selected. Gene expression of selected genes underwent a z-transformation, and the top genes from each module were

used for the heatmaps using pheatmap in R (v1.0.12). RNA sequencing publicly available data of liver of the Fgf21 transgenic mice (GSE39313)<sup>35</sup> and protein restriction diet (SRA accession PRJNA851959)<sup>41</sup> were analyzed following the same pipeline.

#### Quantification, statistical analysis and artwork

All experiments adhered to the ARRIVE guidelines and followed strict randomization. All experiments and data analysis were conducted in a blind manner using coded tags rather than the actual group name. A power analysis was performed prior to the study to estimate sample-size. We hypothesized that HC would reduce IR injury by 50%. Using an SD at  $\pm 30\%$  for the surgery and considering a power at 0.8, we calculated that  $n = 6$  animals/group was necessary to validate a significant effect of the carbo-loading. Animals with pre-existing conditions (malocclusion, injury, abnormal weight) were not operated or excluded from the experiments upon discovery during dissection (kidney disease, tumor etc.). All experiments were analyzed using Prism 9.5.1 (GraphPad Software, USA). Data were presented as mean  $\pm$  SD and statistical significance was evaluated using Student's *t* test, one- or two-way ANOVA and multiple comparisons were analyzed using Tukey's and Sidak's post-hoc test. Correlation analyses were determined using Linear Regression Test. A *P* value inferior or equal to 0.05 was defined as statistically significant. Correlation analysis were determined using Linear Regression Test. A *P* value inferior or equal to 0.05 was defined as statistically significant. Artworks in figures S1A and S9 were created with BioRender.com (Academic License Terms, [www.biorender.com](http://www.biorender.com)).

#### Reporting summary

Further information on research design is available in the Nature Portfolio Reporting Summary linked to this article.

#### Data availability

All custom scripts are available on Figshare or at <https://github.com/Longchamp-Lab/agus-et-al-nature-comm-2023>. All other relevant data are available from the corresponding author on request. All data from Department of Agriculture National Health and Nutrition Examination Survey are available at <https://www.cdc.gov/nchs/nhanes/>.

The publicly available sequencing data generated in this study have been deposited in the National Center for Biotechnology Information Gene Expression Omnibus (GEO) and are accessible through the GEO Series accession number GSE39313 and through SRA accession PRJNA851959.

#### References

- Dobson, G. P. Trauma of major surgery: A global problem that is not going away. *Int. J. Surg.* **81**, 47–54 (2020).
- Jaeschke, H. Molecular mechanisms of hepatic ischemia-reperfusion injury and preconditioning. *Am. J. Physiol. Gastrointest. Liver Physiol.* **284**, G15–G26 (2003).
- Chouchani, E. T. et al. Ischaemic accumulation of succinate controls reperfusion injury through mitochondrial ROS. *Nature* **515**, 431–435 (2014).
- Gustafsson, U. O. et al. Guidelines for perioperative care in elective colonic surgery: Enhanced Recovery After Surgery (ERAS(R)) Society recommendations. *World J. Surg.* **37**, 259–284 (2013).
- Singh, S. M. et al. A U.S. survey of pre-operative carbohydrate-containing beverage use in colorectal enhanced recovery after surgery (ERAS) programs. *Perioper. Med. (Lond)* **10**, 19 (2021).
- Bilku, D. K., Dennison, A. R., Hall, T. C., Metcalfe, M. S. & Garcea, G. Role of preoperative carbohydrate loading: a systematic review. *Ann. R. Coll. Surg. Engl.* **96**, 15–22 (2014).
- Varadhan, K. K. et al. The enhanced recovery after surgery (ERAS) pathway for patients undergoing major elective open colorectal surgery: a meta-analysis of randomized controlled trials. *Clin. Nutr.* **29**, 434–440 (2010).
- Budhathoki, S. et al. Association of Animal and Plant Protein Intake With All-Cause and Cause-Specific Mortality in a Japanese Cohort. *JAMA Intern. Med.* **179**, 1509–1518 (2019).
- Mitchell, J. R. et al. Short-term dietary restriction and fasting preconditioning against ischemia reperfusion injury in mice. *Aging Cell* **9**, 40–53 (2010).
- Verweij, M. et al. Preoperative fasting protects mice against hepatic ischemia/reperfusion injury: mechanisms and effects on liver regeneration. *Liver Transpl.* **17**, 695–704 (2011).
- Harputlugil, E. et al. The TSC complex is required for the benefits of dietary protein restriction on stress resistance in vivo. *Cell Rep.* **8**, 1160–1170 (2014).
- Robertson, L. T. et al. Protein and Calorie Restriction Contribute Additively to Protection from Renal Ischemia Reperfusion Injury Partly via Leptin Reduction in Male Mice. *J. Nutr.* **145**, 1717–1727 (2015).
- Longchamp, A. et al. Amino Acid Restriction Triggers Angiogenesis via GCN2/ATF4 Regulation of VEGF and H2S Production. *Cell* **173**, 117–129.e114 (2018).
- Hine, C. et al. Endogenous hydrogen sulfide production is essential for dietary restriction benefits. *Cell* **160**, 132–144 (2015).
- Trocha, K. M. et al. Short-term preoperative protein restriction attenuates vein graft disease via induction of cystathionine gamma-lyase. *Cardiovasc. Res.* **116**, 416–428 (2020).
- Orentreich, N., Matias, J. R., DeFelice, A. & Zimmerman, J. A. Low methionine ingestion by rats extends life span. *J. Nutr.* **123**, 269–274 (1993).
- Peng, W. et al. Surgical stress resistance induced by single amino acid deprivation requires Gcn2 in mice. *Sci. Transl. Med.* **4**, 118ra111 (2012).
- Kip, P. et al. Insights From a Short-Term Protein-Calorie Restriction Exploratory Trial in Elective Carotid Endarterectomy Patients. *Vasc. Endovascular Surg.* **53**, 470–476 (2019).
- Partridge, L., Fuentealba, M. & Kennedy, B. K. The quest to slow ageing through drug discovery. *Nat. Rev. Drug Discov.* **19**, 513–532 (2020).
- Green, C. L., Lamming, D. W. & Fontana, L. Molecular mechanisms of dietary restriction promoting health and longevity. *Nat. Rev. Mol. Cell Biol.* **23**, 56–73 (2022).
- Maida, A. et al. A liver stress-endocrine nexus promotes metabolic integrity during dietary protein dilution. *J. Clin. Invest.* **126**, 3263–3278 (2016).
- Malloy, V. L. et al. Methionine restriction decreases visceral fat mass and preserves insulin action in aging male Fischer 344 rats independent of energy restriction. *Aging Cell* **5**, 305–314 (2006).
- Yu, D. et al. The adverse metabolic effects of branched-chain amino acids are mediated by isoleucine and valine. *Cell Metab.* **33**, 905–922.e906 (2021).
- Treviño-Villarreal, J. H. et al. Dietary protein restriction reduces circulating VLDL triglyceride levels via CREBH-APOA5-dependent and -independent mechanisms. *JCI Insight* **3**, e99470 (2018).
- Simpson, S. J. et al. Dietary protein, aging and nutritional geometry. *Ageing Res. Rev.* **39**, 78–86 (2017).
- Solon-Biet, S. M. et al. The ratio of macronutrients, not caloric intake, dictates cardiometabolic health, aging, and longevity in ad libitum-fed mice. *Cell Metab.* **19**, 418–430 (2014).
- Le Couteur, D. G. et al. The impact of low-protein high-carbohydrate diets on aging and lifespan. *Cell Mol. Life Sci.* **73**, 1237–1252 (2016).
- Wali, J. A. et al. Impact of dietary carbohydrate type and protein-carbohydrate interaction on metabolic health. *Nat. Metab.* **3**, 810–828 (2021).
- Madeo, F., Carmona-Gutierrez, D., Hofer, S. J. & Kroemer, G. Caloric Restriction Mimetics against Age-Associated Disease: Targets,

- Mechanisms, and Therapeutic Potential. *Cell Metab.* **29**, 592–610 (2019).
30. Holzenberger, M. et al. IGF-1 receptor regulates lifespan and resistance to oxidative stress in mice. *Nature* **421**, 182–187 (2003).
  31. Hine, C. M. & Mitchell, J. R. NRF2 and the Phase II Response in Acute Stress Resistance Induced by Dietary Restriction. *J Clin Exp Pathol.* **S4**, 7329 (2012).
  32. Laeger, T. et al. FGF21 is an endocrine signal of protein restriction. *J. Clin. Invest.* **124**, 3913–3922 (2014).
  33. Calubag, M. F. et al. FGF21 has a sex-specific role in calorie-restriction-induced beiging of white adipose tissue in mice. *Aging Biol.* **1**, 3 (2022).
  34. Chau, M. D., Gao, J., Yang, Q., Wu, Z. & Gromada, J. Fibroblast growth factor 21 regulates energy metabolism by activating the AMPK-SIRT1-PGC-1 $\alpha$  pathway. *Proc. Natl. Acad. Sci. USA* **107**, 12553–12558 (2010).
  35. Zhang, Y. et al. The starvation hormone, fibroblast growth factor-21, extends lifespan in mice. *Elife* **1**, e00065 (2012).
  36. Laeger, T. et al. Metabolic Responses to Dietary Protein Restriction Require an Increase in FGF21 that Is Delayed by the Absence of GCN2. *Cell Rep.* **16**, 707–716 (2016).
  37. Hill, C. M. et al. FGF21 is required for protein restriction to extend lifespan and improve metabolic health in male mice. *Nat. Commun.* **13**, 1897 (2022).
  38. Fisher, F. M. et al. FGF21 regulates PGC-1 $\alpha$  and browning of white adipose tissues in adaptive thermogenesis. *Genes Dev.* **26**, 271–281 (2012).
  39. BonDurant, L. D. et al. FGF21 Regulates Metabolism Through Adipose-Dependent and -Independent Mechanisms. *Cell Metab.* **25**, 935–944.e934 (2017).
  40. Hill, C. M. et al. FGF21 Signals Protein Status to the Brain and Adaptively Regulates Food Choice and Metabolism. *Cell Rep.* **27**, 2934–2947.e2933 (2019).
  41. MacArthur, M. R. et al. Multiomics assessment of dietary protein titration reveals altered hepatic glucose utilization. *Cell Rep.* **40**, 111187 (2022).
  42. Chen, J., Chen, Y., Olivero, A. & Chen, X. Identification and Validation of Potential Biomarkers and Their Functions in Acute Kidney Injury. *Front Genet* **11**, 411 (2020).
  43. Auffhauser, D. D. Jr et al. Improved renal ischemia tolerance in females influences kidney transplantation outcomes. *J. Clin. Invest.* **126**, 1968–1977 (2016).
  44. Hahn, O. et al. A nutritional memory effect counteracts benefits of dietary restriction in old mice. *Nat. Metab.* **1**, 1059–1073 (2019).
  45. Hill, C. M. et al. Low protein-induced increases in FGF21 drive UCP1-dependent metabolic but not thermoregulatory endpoints. *Sci Rep* **7**, 8209 (2017).
  46. Đurašević, S. et al. The Effects of Meldonium on the Renal Acute Ischemia/Reperfusion Injury in Rats. *Int. J. Mol. Sci.* **20**, 5747 (2019).
  47. Talukdar, S. et al. A Long-Acting FGF21 Molecule, PF-05231023, Decreases Body Weight and Improves Lipid Profile in Non-human Primates and Type 2 Diabetic Subjects. *Cell Metab.* **23**, 427–440 (2016).
  48. Kim, A. M. et al. Once-weekly administration of a long-acting fibroblast growth factor 21 analogue modulates lipids, bone turnover markers, blood pressure and body weight differently in obese people with hypertriglyceridaemia and in non-human primates. *Diabetes Obes Metab.* **19**, 1762–1772 (2017).
  49. Green, C. L. et al. Sex and genetic background define the metabolic, physiologic, and molecular response to protein restriction. *Cell Metab.* **34**, 209–226.e205 (2022).
  50. Son, K. H. et al. Preoperative Oral Carbohydrate Loading in Pancreaticoduodenectomy. *Clin. Nutr. Res.* **5**, 213–218 (2016).
  51. Michalczyk, M. M. et al. Anaerobic Performance after a Low-Carbohydrate Diet (LCD) Followed by 7 Days of Carbohydrate Loading in Male Basketball Players. *Nutrients* **11**, 778 (2019).
  52. Raubenheimer, D. & Simpson, S. J. Protein Leverage: Theoretical Foundations and Ten Points of Clarification. *Obesity (Silver Spring)* **27**, 1225–1238 (2019).
  53. Gosby, A. K. et al. Raised FGF-21 and Triglycerides Accompany Increased Energy Intake Driven by Protein Leverage in Lean, Healthy Individuals: A Randomised Trial. *PLoS One* **11**, e0161003 (2016).
  54. Wu, Y. et al. Very-low-protein diets lead to reduced food intake and weight loss, linked to inhibition of hypothalamic mTOR signaling, in mice. *Cell Metab.* **33**, 1264–1266 (2021).
  55. Gokarn, R. et al. Long-term Dietary Macronutrients and Hepatic Gene Expression in Aging Mice. *J. Gerontol. A Biol. Sci. Med. Sci.* **73**, 1618–1625 (2018).
  56. Tyshkovskiy, A. et al. Identification and Application of Gene Expression Signatures Associated with Lifespan Extension. *Cell Metab.* **30**, 573–593.e578 (2019).
  57. Badman, M. K. et al. Hepatic fibroblast growth factor 21 is regulated by PPAR $\alpha$  and is a key mediator of hepatic lipid metabolism in ketotic states. *Cell Metab.* **5**, 426–437 (2007).
  58. Rao, J. et al. ATF3-mediated NRF2/HO-1 signaling regulates TLR4 innate immune responses in mouse liver ischemia/reperfusion injury. *Am. J. Transplant.* **15**, 76–87 (2015).
  59. Gomez-Samano, M. A. et al. Fibroblast growth factor 21 and its novel association with oxidative stress. *Redox. Biol.* **11**, 335–341 (2017).
  60. Jonsson, W. O. et al. Physiologic Responses to Dietary Sulfur Amino Acid Restriction in Mice Are Influenced by Atf4 Status and Biological Sex. *J. Nutr.* **151**, 785–799 (2021).
  61. Nezu, M. & Suzuki, N. Roles of Nrf2 in Protecting the Kidney from Oxidative Damage. *Int. J. Mol. Sci.* **21**, 2951 (2020).
  62. Cheng, Y. et al. Up-regulation of Nrf2 is involved in FGF21-mediated fenofibrate protection against type 1 diabetic nephropathy. *Free Radic. Biol. Med.* **93**, 94–109 (2016).
  63. Loomba, R. et al. Randomized, Controlled Trial of the FGF21 Analogue Pegozafermin in NASH. *N. Engl. J. Med.* **389**, 998–1008 (2023).
  64. Suassuna, P. G. A., de Paula, R. B., Sanders-Pinheiro, H., Moe, O. W. & Hu, M. C. Fibroblast growth factor 21 in chronic kidney disease. *J. Nephrol.* **32**, 365–377 (2019).
  65. Kohara, M. et al. Association between circulating fibroblast growth factor 21 and mortality in end-stage renal disease. *PLoS One* **12**, e0178971 (2017).
  66. Hindricks, J. et al. Serum levels of fibroblast growth factor-21 are increased in chronic and acute renal dysfunction. *Clin. Endocrinol (Oxf)* **80**, 918–924 (2014).
  67. Brace, L. E. et al. Increased oxidative phosphorylation in response to acute and chronic DNA damage. *NPJ Aging Mech. Dis.* **2**, 16022 (2016).
  68. Weir, J. B. New methods for calculating metabolic rate with special reference to protein metabolism. *J. Physiol.* **109**, 1–9 (1949).
  69. Faivre, A. et al. Differential role of nicotinamide adenine dinucleotide deficiency in acute and chronic kidney disease. *Nephrol. Dial. Transplant* **36**, 60–68 (2021).
  70. Goujon, J. M. et al. Histological evaluation of proximal tubule cell injury in isolated perfused pig kidneys exposed to cold ischemia. *J. Surg. Res.* **82**, 228–233 (1999).
  71. Agius, T. et al. Subnormothermic Ex Vivo Porcine Kidney Perfusion Improves Energy Metabolism: Analysis Using <sup>31</sup>P Magnetic Resonance Spectroscopic Imaging. *Transplant Direct* **8**, e1354 (2022).
  72. Longchamp, A. et al. Ex Vivo Analysis of Kidney Graft Viability Using <sup>31</sup>P Magnetic Resonance Imaging Spectroscopy. *Transplantation* **104**, 1825–1831 (2020).



73. Allagnat, F. et al. Nitric Oxide Deficit Drives Intimal Hyperplasia in Mouse Models of Hypertension. *Eur. J. Vasc. Endovasc. Surg.* **51**, 733–742 (2016).
74. de Jonge, H. J. et al. Evidence based selection of housekeeping genes. *PLoS One* **2**, e898 (2007).
75. MacArthur, M. R. et al. Total protein, not amino acid composition, differs in plant-based versus omnivorous dietary patterns and determines metabolic health effects in mice. *Cell Metab.* **33**, 1808–1819.e1802 (2021).
76. Akhmedov, M., Martinelli, A., Geiger, R. & Kwee, I. Omics Playground: a comprehensive self-service platform for visualization, analytics and exploration of Big Omics Data. *NAR Genom. Bioinform.* **2**, lqz019 (2020).
77. Langfelder, P. & Horvath, S. WGCNA: an R package for weighted correlation network analysis. *BMC Bioinform.* **9**, 559 (2008).
78. Shannon, P. et al. Cytoscape: a software environment for integrated models of biomolecular interaction networks. *Genome Res* **13**, 2498–2504 (2003).

### Acknowledgements

We thank our deeply regretted friend and mentor James R. Mitchell. This work was supported by the Swiss National Science Foundation to FL (SNSF 320030\_182658) to FA and SD (SNSF-310030\_176158), and AL (SNSF PZ00P3-185927), the Mercier Foundation to AL, the Mendez National Institute of Transplantation Foundation to AL, the Novartis foundation to AL and FA, the Leenaards Foundation to AL, the University of Lausanne (projet de recherche interdisciplinaire) to DG and AL, the Fondation pour la recherche en chirurgie thoracique et vasculaire to FA, SD and AL, the Union des Sociétés Suisses des Maladies Vasculaires to SD. We are grateful to the Mouse Pathology Facility (MPF) and the Cellular Imaging Facility (CIF) of the University of Lausanne for their support and expertise.

### Author contributions

T.A., R.E., A.ly, M.R.M., K.K., A.F., M.L., D.L., S.S., D.G., F.L., H.Y., J.F.M., K.U., A.O., S.J.M., F.A., S.D. and A.L. participated in research design. T.A., R.E., A.ly, M.R.M., K.K., A.F., L.S., M.L., D.L., S.S., D.G., F.L., H.Y., J.F.M., K.U., A.O., S.J.M., F.A., S.D. and A.L. participated in the writing of the paper. T.A., R.E., A.ly, M.R.M., K.K., A.F., L.S., M.L., D.L., S.J.M., F.A., S.D. and A.L. participated in the performance of the research. S.S., D.G., F.L., H.Y., J.F.M., K.U., A.O., S.J.M., F.A., S.D. and A.L. contributed new

reagents or analytic tools. T.A., R.E., A.ly, M.R.M., K.K., A.F., M.L., D.L., S.J.M., F.A., S.D. and A.L. participated in data analysis. D.G., F.L., F.A., S.D., and A.L. obtained funding.

### Competing interests

The authors declare no competing interests.

### Additional information

**Supplementary information** The online version contains supplementary material available at <https://doi.org/10.1038/s41467-024-44866-3>.

**Correspondence** and requests for materials should be addressed to Alban Longchamp.

**Peer review information** *Nature Communications* thanks the anonymous reviewer(s) for their contribution to the peer review of this work. A peer review file is available.

**Reprints and permissions information** is available at <http://www.nature.com/reprints>

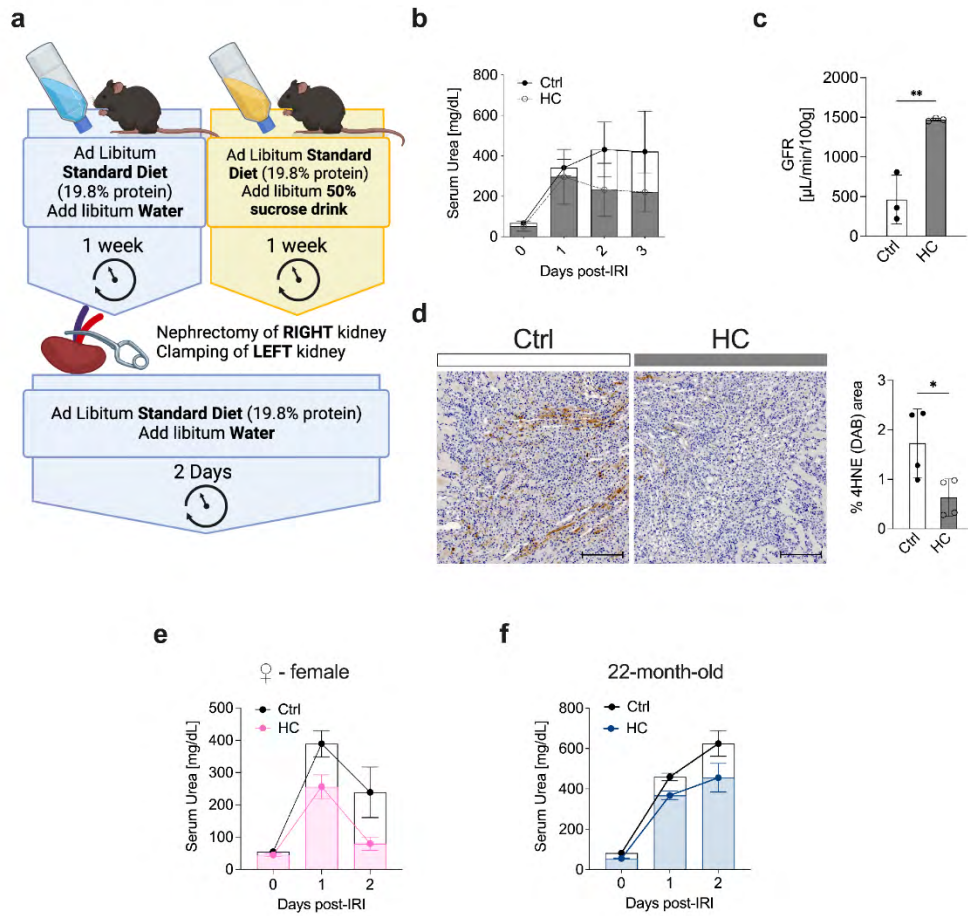
**Publisher's note** Springer Nature remains neutral with regard to jurisdictional claims in published maps and institutional affiliations.

**Open Access** This article is licensed under a Creative Commons Attribution 4.0 International License, which permits use, sharing, adaptation, distribution and reproduction in any medium or format, as long as you give appropriate credit to the original author(s) and the source, provide a link to the Creative Commons license, and indicate if changes were made. The images or other third party material in this article are included in the article's Creative Commons license, unless indicated otherwise in a credit line to the material. If material is not included in the article's Creative Commons license and your intended use is not permitted by statutory regulation or exceeds the permitted use, you will need to obtain permission directly from the copyright holder. To view a copy of this license, visit <http://creativecommons.org/licenses/by/4.0/>.

© The Author(s) 2024

<sup>1</sup>Department of Vascular Surgery, University Hospital of Lausanne (CHUV), Lausanne, Switzerland. <sup>2</sup>Transplant Center, Department of Surgery, Massachusetts General Hospital, Harvard Medical School, Boston, MA, USA. <sup>3</sup>Center for Engineering in Medicine, Department of Surgery, Massachusetts General Hospital, Harvard Medical School, Boston, MA, USA. <sup>4</sup>Lewis-Sigler Institute for Integrative Genomics, Princeton University, Princeton, NJ, USA. <sup>5</sup>Laboratory of Nephrology, Department of Internal Medicine Specialties and Department of Cell Physiology and Metabolism, University of Geneva, Geneva, Switzerland. <sup>6</sup>Service of Nephrology, Department of Internal Medicine Specialties, University Hospital of Geneva, Geneva, Switzerland. <sup>7</sup>Transplantation Center, Lausanne University Hospital (CHUV), University of Lausanne (UNIL), Lausanne, Switzerland. <sup>8</sup>Division of Intensive Care, Department of Acute Medicine, University Hospital of Geneva, Geneva, Switzerland. <sup>9</sup>Department of Radiology and Medical Informatics, University of Geneva, Geneva, Switzerland. <sup>10</sup>Center for Biomedical Imaging (CIBM), Geneva, Switzerland. <sup>11</sup>Department of Biomedical Sciences, University of Lausanne, Lausanne, Switzerland. <sup>12</sup>These authors contributed equally: Thomas Agius, Raffaella Emsley. ✉ e-mail: [alban.longchamp@chuv.ch](mailto:alban.longchamp@chuv.ch)

## Supplementary information

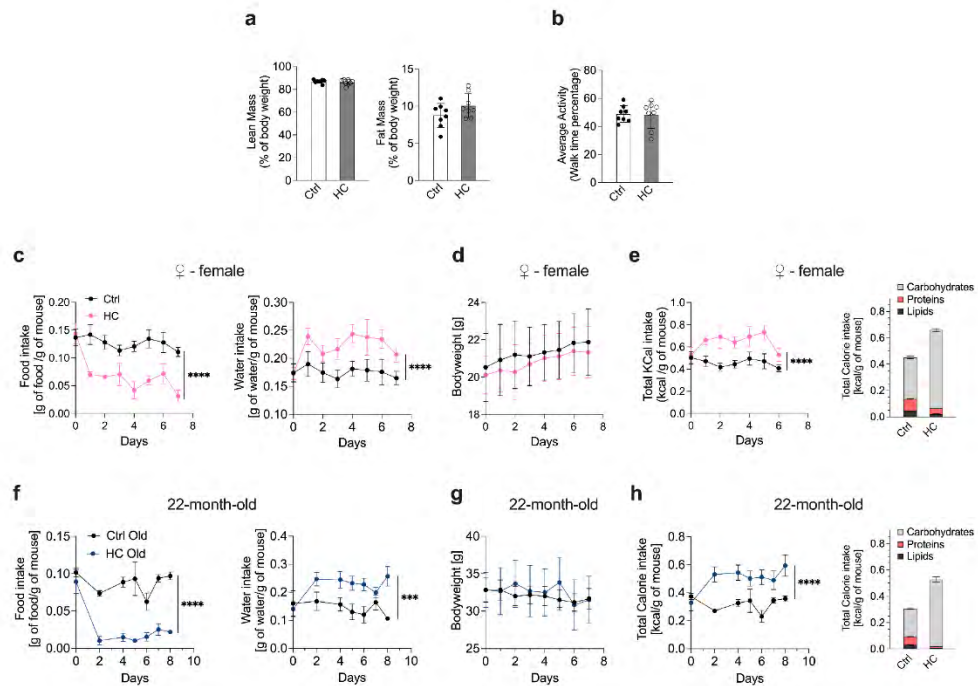


**Supplementary Data Fig.1. Additional data for the protective effect induced by the high-sucrose diet.**

- Experimental setup. Ad-libitum fed C57BL/6 mice were given free access to water (Ctrl) or to a 50% sucrose water solution (HC) for one week prior to renal IRI surgery. Created with [BioRender.com](https://www.biorender.com).
- Serum urea levels at the indicated time post-renal IRI after one week of preconditioning with control (Ctrl) or 50% sucrose drink (HC).
- Glomerular filtration rate (GFR) at day 2 post-renal IRI.

- d. Representative cross sections of 4HNE-stained kidneys (left; DAB; scale bar 100 $\mu$ m) and percentage area of reactive oxygen species 4HNE staining (right) in kidney at day 2 post-renal IRI.
- e. Serum urea levels at the indicated time post-renal IRI after one week of preconditioning with control (Ctrl) or 50% sucrose drink (HC).
- f. Serum urea levels at the indicated time post-renal IRI after one week of preconditioning with control (Ctrl) or 50% sucrose drink (HC).

\*p values for a. were calculated with unpaired two-tailed T-test, \*\*p < 0.01. In b-d, experiments were carried out in 10-weeks old male mice; in e, in 10-weeks old female mice ; in f, in 22-months old male mice. Sample sizes: (a-d), n = 8 for all conditions. Data in all panels are shown as mean  $\pm$  SD. See also Fig. 1



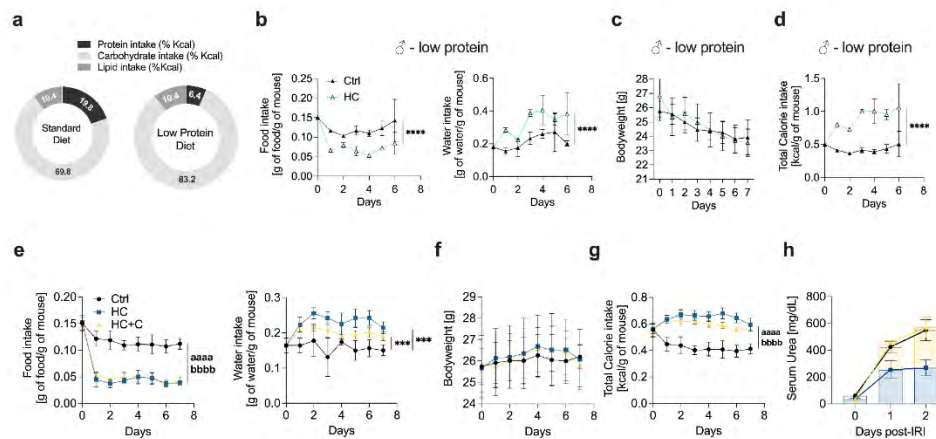
**Supplementary Data Fig. 2. Additional data for the high-sucrose diet-induced protective effects.**

- Percentage of lean (left) and fat mass (right) after one week of preconditioning with water (Ctrl) or 50% sucrose drink (HC).
- Average spontaneous activity after one week of preconditioning with water (Ctrl) or 50% sucrose drink (HC).
- Food (left) and water (right) intake (normalized by body weight) in mice given *ad libitum* access to water (Ctrl) or 50% sucrose drink (HC).
- Body weight at the indicated time of mice given *ad libitum* access to indicated diet.
- Total calorie intake (normalized by body weight) at the indicated time in mice and per macronutrient (right; protein, carbohydrate, fat).
- Food (left) and water (right) intake (normalized by body weight) of mice given *ad libitum* access to water (Ctrl) or 50% sucrose drink (HC).



- g. Body weight at the indicated time of mice given *ad libitum* access to water (Ctrl) or 50% sucrose drink (HC).
- h. Total calorie intake (normalized by body weight) at the indicated time of mice and per macronutrient (right; protein, carbohydrate, fat).

\*p values for c, e, f, h were calculated with two-way repeated measures (RM) ANOVA with Geisser-Greenhouse correction, \*\*\*p < 0.001 \*\*\*\*p < 0.0001. In a-b, experiments were carried out in 10-weeks old male mice; in c-e, in 10-weeks old female mice ; in f-h, in 22-months old male mice. Sample sizes: (a), n = 6-7 for 10-week-old female mice; (b), n = 6-7 for 22-month-old male mice; (c-e), n = 6-7 for 10-week-old; (f-h), n = 8 for 22-month-old male mice in all conditions. Data in all panels are shown as mean ± SD. See also Fig. 2 and 2 and Supplementary Data Fig.3.

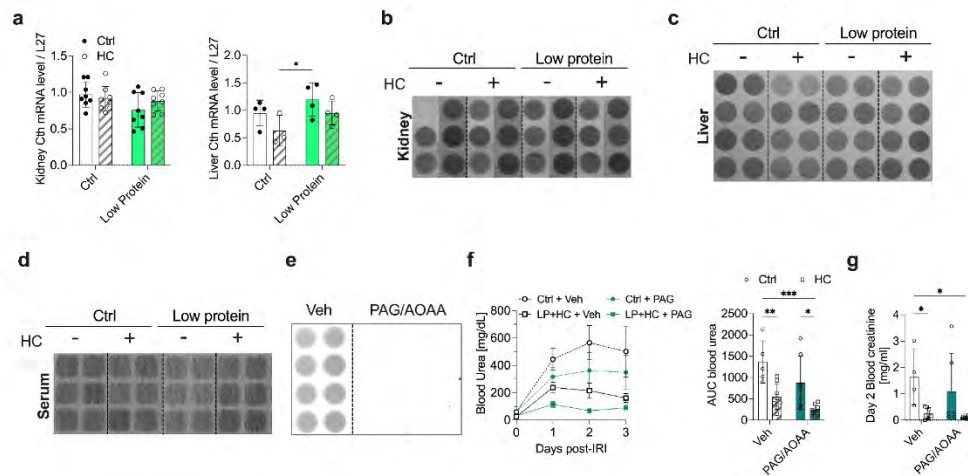


**Supplementary Data Fig. 3. Additional data for the high-sucrose diet-induced metabolic effects of the low protein diet.**

- Ratio of each macronutrient in the preconditioning control diet and low protein diet.
- Food (left) and water (right) intake (normalized by body weight) in mice given *ad libitum* access to low protein diet (LP) with water (Ctrl) or 50% sucrose drink (HC).
- Body weight in mice given *ad libitum* access to the indicated low protein diet.
- Total calorie intake (normalized by body weight) at the indicated time given *ad libitum* access to the indicated low protein diet.
- Food (left) and water (right) intake (normalized by body weight) in mice given *ad libitum* access to control (Ctrl), 50% sucrose drink (HC) or 50% sucrose drink with cysteine oral gavage (HC + cysteine).
- Body weight in mice given *ad libitum* access to the indicated diet.
- Total calorie intake (normalized by body weight) at the indicated time in mice given *ad libitum* access to the indicated low protein diet.
- Serum urea levels at the indicated time post-renal IRI in mice preconditioned for 1 week with the indicated diet.

\*p values of b, d, e, g were calculated with two-way RM ANOVA with Geisser-Greenhouse correction, \*\*\*p < 0.001 \*\*\*\*p < 0.0001 aaaa p < 0.0001 HC vs. Ctrl bbbb p < 0.0001 HC+C vs. Ctrl. In all panels, experiments were carried out in 10-week old male

mice. Sample sizes: (b–d),  $n = 6$  in all conditions; (e–h),  $n = 8$  in all conditions. Data in all panels are shown as mean  $\pm$  SD. See also Fig.2 and Supplementary Data Fig.2.



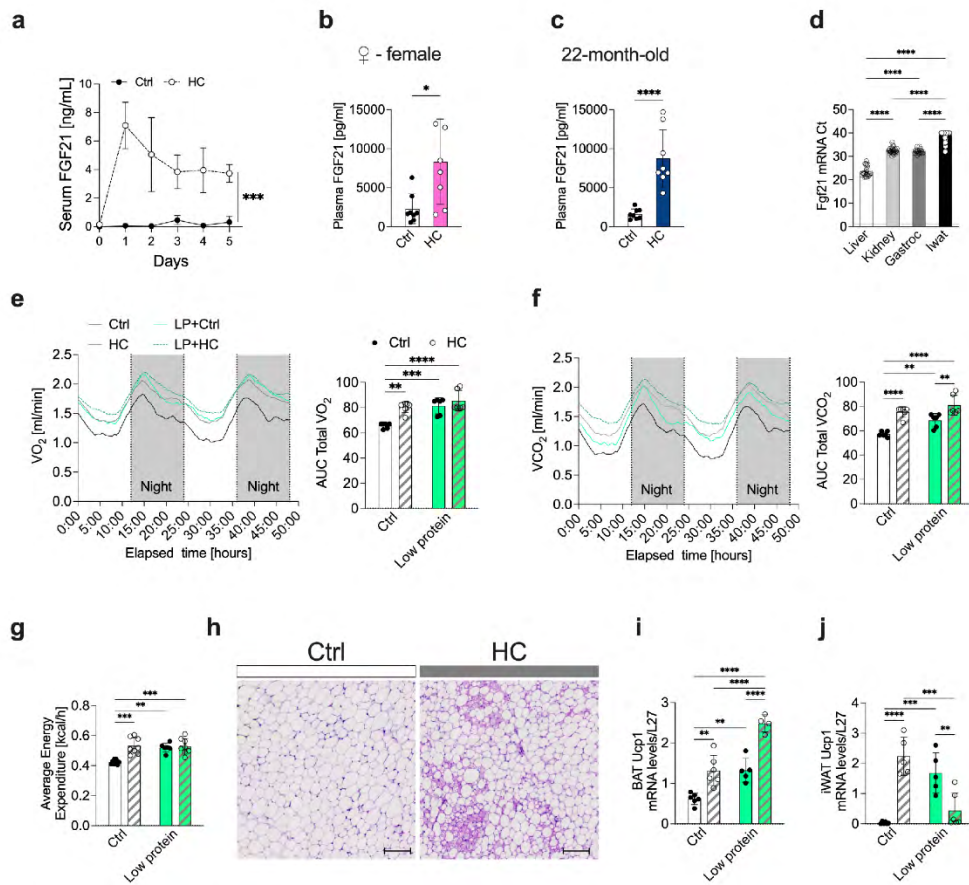
**Supplementary Data Fig.4. Additional data for the high-sucrose diet-induced protective effects.**

- Relative Cth (cystathionine gamma-lyase) mRNA levels after one week of preconditioning with control or low protein diet (LP) with control (Ctrl) or 50% sucrose drink (HC).
- Representative images of lead acetate assay in the kidney, (c) liver and (d) serum after one week of preconditioning on the indicated diet.
- Representative images of lead acetate assay in the liver of mice treated with Vehicle (Veh) or the H<sub>2</sub>S inhibitor propargylglycine (PAG) + amino-oxyacetic acid (AOAA) for one week.
- Serum urea levels (left) and AUC (right) at the indicated time post-renal IRI after one week of preconditioning with the indicated diet and treatment.
- Serum creatinine levels at day 2 post-renal IRI after one week of preconditioning with the indicated diet and treatment.

\*p values of a,f,g were calculated with two-way ANOVA followed by a Tukey's post hoc analysis, \*p < 0.05 \*\*p < 0.01 \*\*\*p < 0.001. In all panels, experiments were carried out in 10-week old male mice. Sample sizes: (a), n=8 for the kidney and n= 4 for the liver. (b), n=3 for all conditions with 2 technical replicates; (c), n=4 for all conditions with 2 technical



replicates; (d), n=3 for all conditions with 2 technical replicates; (c), n=4 for all conditions with 2 technical replicates; (f–g), n=8 for all conditions. Data in all panels are shown as mean  $\pm$  SD. See also Fig. 3 and3 and Supplementary Data Fig.5.

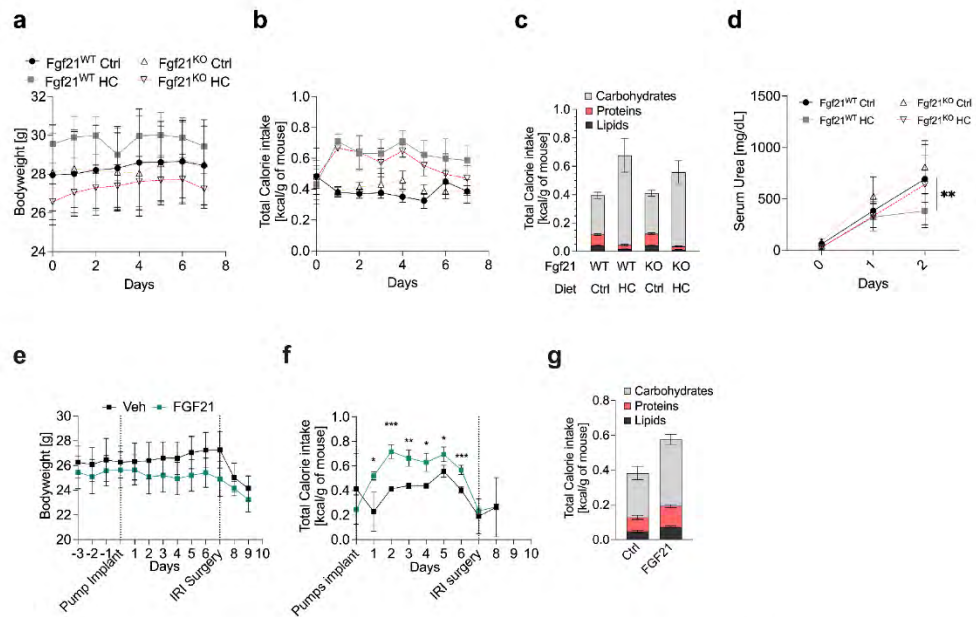


**Supplementary Data Fig.5. Metabolic and adipose tissue-related effects of the high-sucrose diet.**

- Serum FGF21 levels over time of mice given *ad libitum* access to water (Ctrl) or 50% sucrose drink (HC).
- Serum FGF21 levels after one week of preconditioning with control (Ctrl) or 50% sucrose water (HC).
- Serum FGF21 after one week of preconditioning with control (Ctrl) or 50% sucrose water (HC).
- FGF21 mRNA levels (cycle threshold; Ct) in the indicated tissue after one week of preconditioning with 50% sucrose drink (HC).

- e.  $VO_2$  consumption over time (left),  $VO_2$  (AUC; right) and (f)  $VCO_2$  consumption over time (left),  $VCO_2$  (AUC; right) after 6-7 days of preconditioning with control or low protein diet (LP) with control (Ctrl) or 50% sucrose drink (HC). Each light/dark bar represents a 12-hour duration.
- g. Energy expenditure after one week of preconditioning with the indicated diet.
- h. Representative sections of H&E-stained inguinal white adipose tissue (iWAT; scale bar 100 $\mu$ m) after one week of preconditioning with the indicated diet.
- i. Relative Ucp1 mRNA levels in the brown adipose tissue (BAT) and (j) in the iWAT after one week of preconditioning with the indicated diet.

\*p values of a-c were calculated with one-way ANOVA, d with two-way RM ANOVA with Geisser-Greenhouse correction and e-j with two-way ANOVA followed by a Tukey's post hoc analysis, \*\*p < 0.01 \*\*\*p < 0.001 \*\*\*\*p < 0.0001. In a and d-i, experiments were carried out in 10-weeks old male mice; in b, in 10-weeks old female mice ; in c, in 22-months old male mice. Sample sizes: (a-b), n=8, (c); n=32 for the kidney, n= 24 for the liver, n=22 for the gastrocnemius, n=48 for the iWAT; (d), n=4 for all conditions; (e-j), n=6 for all conditions. Data in all panels are shown as mean  $\pm$  SD. See also Fig.3 and Supplementary Data Fig.4

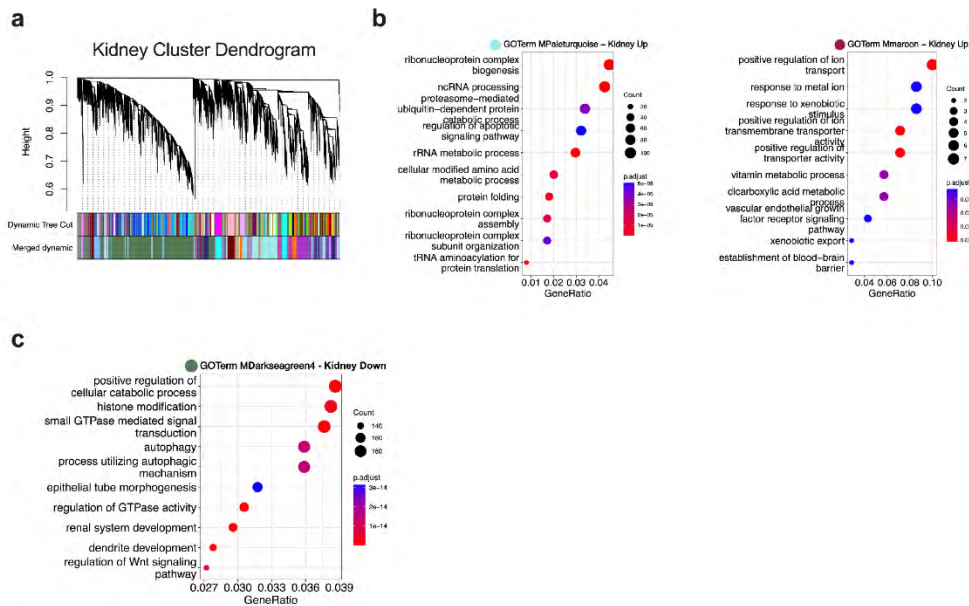


**Supplementary Data Fig. 6. Metabolic effects of carbohydrate loading in FGF21<sup>KO</sup> mice.**

- Body weight of Fgf21<sup>WT</sup> and Fgf21<sup>KO</sup> mice given *ad libitum* access to water (Ctrl) or 50% sucrose drink (HC).
- Total calorie intake (normalized by body weight) at the indicated time and (c) per macronutrients (protein, carbohydrate, fat) of Fgf21<sup>WT</sup> and Fgf21<sup>KO</sup> mice preconditioned with the indicated diet.
- Serum urea levels at the indicated time post-renal IRI of Fgf21<sup>WT</sup> and Fgf21<sup>KO</sup> mice preconditioned for one week with the indicated diet.
- Body weight of mice given *ad libitum* access to a control diet (Ctrl) and implanted with osmotic pumps containing either NaCl (Ctrl) or human recombinant FGF21 (FGF21; 1mg/kg/day) for 7 days prior to renal IRI surgery.
- Total calorie intake (normalized by body weight) at the indicated time and (g) per macronutrients (protein, carbohydrate, fat) of mice treated for one week with the indicated treatment.



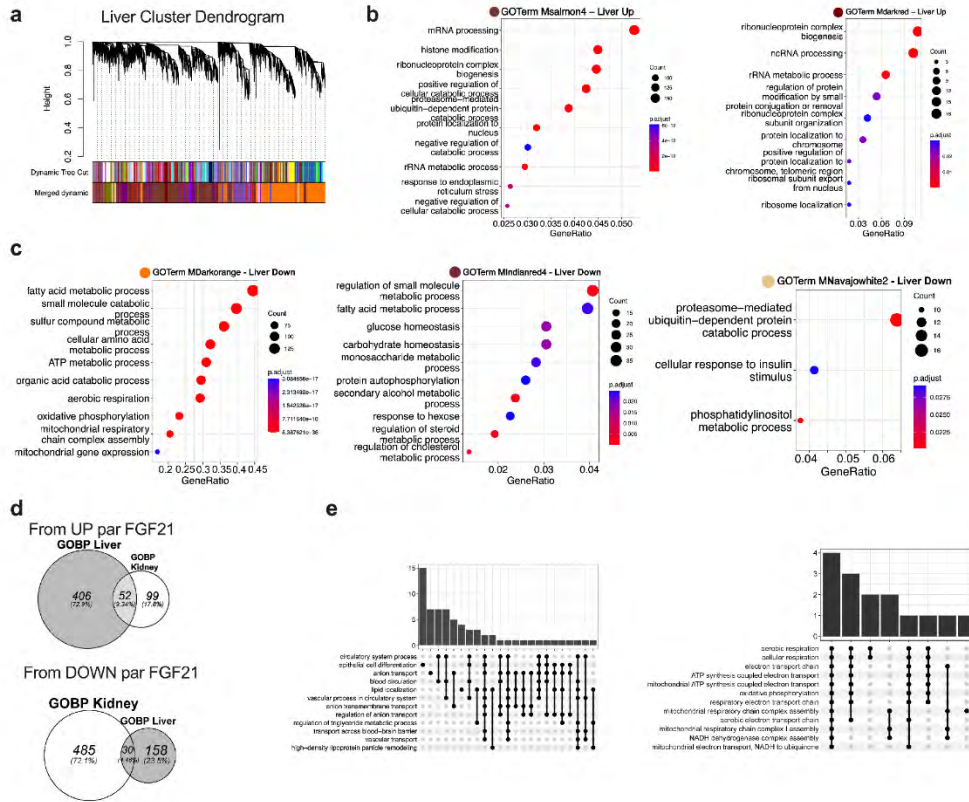
\*p values for d. were calculated with two-way RM ANOVA with Geisser-Greenhouse correction and f. with two-way ANOVA followed by a Sidak's post hoc analysis, \*p < 0.05 \*\*p < 0.01 \*\*\*p < 0.001. In all panels, experiments were carried out in 10-weeks old male mice. Sample sizes: (a-d), n = 8-22, n=18 for FGF21<sup>WT</sup> Ctrl, n= 12 for FGF21<sup>WT</sup> HC, n= 22 FGF21<sup>KO</sup> Ctrl, n= 8 for FGF21<sup>KO</sup> HC; (e-g), n= 6-8, n= 8 Ctrl and n= 6 FGF21 treated group. Data in all panels are shown as mean ± SD. See also Fig.4 and 5.



**Supplementary Data Fig. 7.**

- Dendrogram of kidney clusters displaying gene expression similarities among samples of 10-week-old male mice. Merge cluster dynamic tree cut algorithm identifies distinct color-coded modules at the bottom.
- Gene Set Enrichment Analysis (GSEA) of significantly positively correlated module MPaleturquoise and MMaroon color with serum FGF21. Size of dots corresponds to the number of genes in the pathway, while color represents the significance level, with red indicating a low significance and blue a high significance.
- Dotplot of GSEA of modules with negative correlation with serum FGF21 Darkseagreen4 color.

See also Fig. 6 and Supplementary Data Fig. 8.



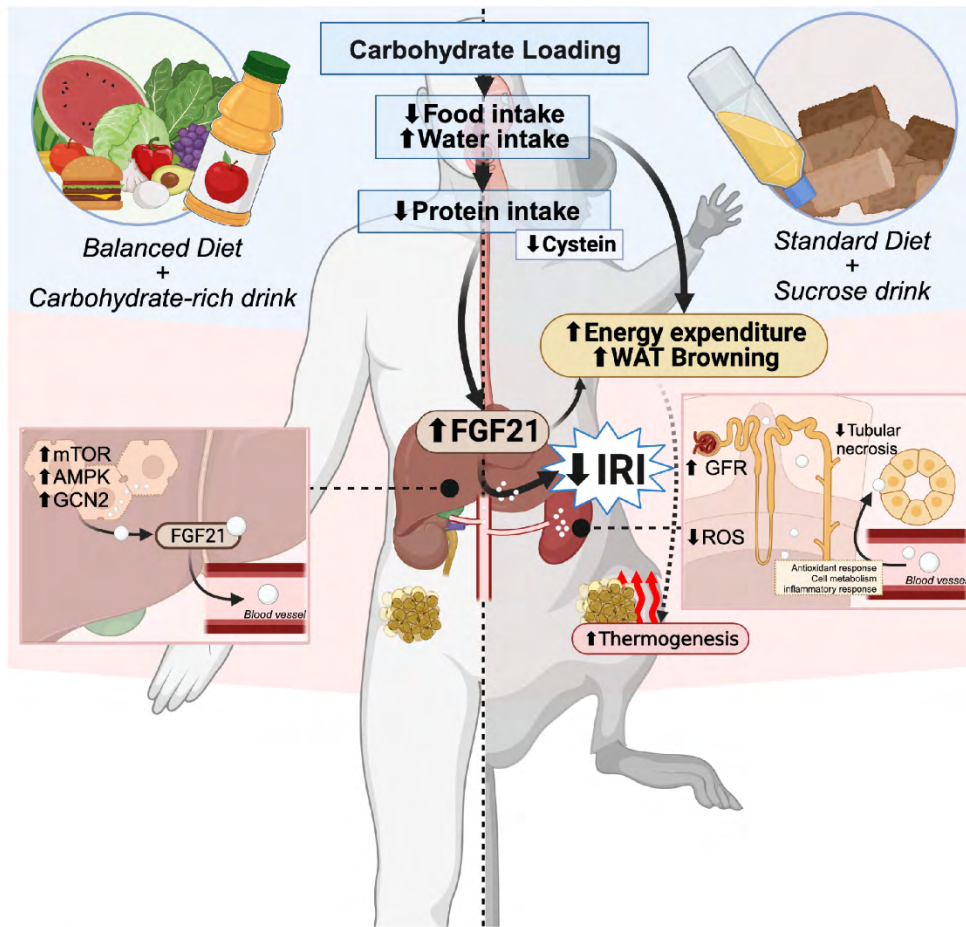
**Supplementary Data Fig. 8.**

- Dendrogram of liver Cluster displaying gene expression similarity among samples. Merge cluster dynamic tree cut algorithm identifies distinct color-coded modules at the bottom.
- Dotplot of GSEA of modules with positive correlation with serum FGF21 in Salmon4 and Darkred color.
- Dotplot of GSEA of modules with negative correlation with serum FGF21 in Darkorange, Indianred4 and Navajowhite2 color.
- Venn diagram of up-regulated (top) and down-regulated (bottom) correlated modules with serum FGF21 between liver and kidney. The diagram shows the number of shared and unique modules across the two tissues.

- e. Upset plot of significant genes positively (left) and negatively (right) correlated with protein dilution intake, identified from the slope  $> 9$  and  $r^2 > 0.7$ . The plot displays the distribution of the significant GOBP term in the different intersecting sets.

See also Fig.6 and Supplementary Data Fig.7





Supplementary Data Fig.9. Proposed Model. Created with [BioRender.com](https://www.biorender.com).

| Target   | Specie       | Forward Sequence 5'-3'   | Reverse Sequence 5'-3' | product size |
|----------|--------------|--------------------------|------------------------|--------------|
| Krt20    | mus musculus | ACAGTTCGAGAGACAGAGTCAA   | CTGAGGTGGGACTGCAACTC   | 138          |
| Rpl27a   | mus musculus | TGATGTTGTTTCGATCAGGCT    | ATTTGGCCTTCACGATGACA   | 80           |
| Cth      | mus musculus | TCCCTTCATCATGCTGAGACC    | GTCATGATTGCCGGAAGCTC   | 104          |
| Fgf21    | mus musculus | CACCGCAGTCCAGAAAGTCT     | AGAGCTCCATCTGGCTGTTG   | 110          |
| Cyp2b9   | mus musculus | CTGCCCTTCTCCACAGGAAA     | CTTTGGAGCAACAGGGCTTG   | 120          |
| Fmo3     | mus musculus | GCCATGTAGCTCAGAAGGTCA    | AGATGGCGGTGGGTAAGTTG   | 144          |
| Mt1      | mus musculus | CTCCGTAGCTCCAGCTTAC      | AGGAGCAGCAGCTCTTCTTG   | 137          |
| Nt5e     | mus musculus | GCAGCATTCTGAAGATGCG      | CTCCCGAGTTCCTGGGTAGA   | 88           |
| Cyp2b10  | mus musculus | GTACACAGACCGTCAGTTCTT    | AGAGAAGAGCTCAAACATCTGG | 97           |
| Cyp17a1  | mus musculus | GGAGAGTTTGCCATCCCGAA     | TCTAAGAAGCGCTCAGGCAT   | 113          |
| Igfbp1   | mus musculus | TTTATCACAGCAAACAGTGTGAGA | CATGGGTAGACACACCAGCAG  | 70           |
| Vldlr    | mus musculus | GGCTGGATTCCAAGTTGCAC     | TCCAGTAGACGCGATCCTCA   | 132          |
| Lpl      | mus musculus | GCGTAGTTCACAGCAGCAAAG    | AGAAATCTTCCC GCGTCTG   | 142          |
| Tmem176a | mus musculus | TGCCTCCAGGGACAGACGAT     | AGTTTGGCCAGAGCAGACTC   | 125          |
| Hamp2    | mus musculus | AGGGCAGACATTGCGATCC      | ACAGCACTGACAGCAGAATC   | 84           |
| Ucp1     | mus musculus | CGGGCATT CAGAGGCAAATC    | CCGAGAGAGGCAGGTGTTTC   | 103          |
| Hmgb1    | mus musculus | ACCTATATCCCTCCCAAAGGG    | GAGGAAGAAGGCCGAAGGAG   | 84           |
| Slc22a26 | mus musculus | CTTATACCCACAAGGTGGCTGA   | ACAACCTCCATGGTTAGGACAT | 143          |

**Supplementary Data Table 1. Primers for qPCR.**

## CONCLUSIONS

This work investigated translational nutritional and pharmacological strategies to limit IRI during transplantation and surgical stress.

We used *in vivo* models such as IRI in mice, *ex vivo* organ perfusion, and clinical data set. We demonstrated that 1) SNMP improves energy metabolism by increasing ATP production and minimizes IRI; 2) ATP predicts immediate graft function<sup>1,2</sup> and can be used as a biomarker of viability during *ex-vivo* perfusion. pMRSI allows great sensitivity, spatial resolution, and short computing time; 3) SNMP does not necessitate a Hb-based oxygen carrier, reducing the cost and logistics by allowing passive oxygenation and simpler machine perfusion; 4) H<sub>2</sub>S administration before and during HMP do not improve IRI in a translational porcine model of DCD; 5) Carbohydrate loading protects from acute surgical stress in mice models of IRI, through protein dilution; 6) FGF21 is a key mediator for surgical stress resistance given by carbohydrate loading.

In **Chapter 1**, we tested a new clinical approach, using non-invasive pMRSI, to evaluate energy metabolism in DCD grafts during oxygenated and non-oxygenated hypothermic *ex-vivo* perfusion (HMP) and SNMP using a porcine model of auto-transplantation. We have used pMRSI to measure ATP production and graft perfusion quality. In this study, we found that kidney graft perfusion at 22 °C with an oxygenated MP-Belzer solution, without oxygen carrier, increased ATP production and minimized IRI during transplantation compared with perfusion at 4 °C. Similarly to normothermic perfusion (37°C), the benefits of SNMP were linked to an increase in fatty acid metabolism and oxidative phosphorylation<sup>3</sup>. Consistent with others, SNMP is also shown to raise reduced glutathione levels and glutathione reductase activity, improving antioxidant mechanisms<sup>4</sup>. We found that kidneys perfused at 22°C have an improved mitochondrial ATP production, consistent with our hypothesis that at 22°C, kidneys are metabolically active<sup>5,6</sup>. We also observed an increase in PME and ATP levels during the first 10 h of perfusion. However, after 10 h of perfusion at 22 °C, the ATP level gradually declined to reach 0 mmol/L at 42 h of perfusion. ATP levels decreased during cold storage in the kidney<sup>6</sup> and liver<sup>7</sup> and correlated with the degree of injury. In humans, ATP predicted immediate graft function<sup>1,7</sup>, and ATP is often used as a viability marker during ischemia<sup>8,9</sup>. Consequently, long-term perfusion at 22 °C using MP-Belzer solution might not be viable. Interestingly, in cold-stored organs, it has also been shown that gradual rewarming from hypothermia to normothermia before transplantation improves kidney function<sup>10,11</sup> highlighting the importance of restoring metabolism before

implantation. In addition, the simplicity of SNMP, without the need for a heating unit or oxygen carrier, could be easily used in a clinical setting and lower the costs. Thus, SNMP at 22°C could translate into greater utilization of kidney allograft, which should be tested in clinical trials.

**Chapter 2** investigates the use of H<sub>2</sub>S to limit IRI in a translational porcine ex vivo HMP model and autotransplantation. The effect of H<sub>2</sub>S was evaluated in both kidneys that were retrieved immediately and after 60 min of WI to mimic circulatory arrest during DCD procurement. To increase the translational value of our study, NaHS was given in relevant clinical situations, including ex vivo perfusion only or concomitant to heparin administration before WI. We found that 100 μM NaHS administration HMP in kidney porcine graft did not improve energy metabolism, kidney perfusion, or histologic damages upon transplantation. These results could be due to different reasons. 1) The metabolic depressant property of H<sub>2</sub>S appears to depend on the animal size. Our group and others previously demonstrated that NaHS protects against IRI in several models of warm tissue ischemia and during cold preservation before transplantation in rodents<sup>8,12-14</sup>. However, we could not replicate these findings here in an adult pig model (approximately animal weight 35 kg) during cold storage, followed by in vivo reperfusion or transplantation. In fact, in larger species (swine, sheep), numerous authors, including us, failed to confirm any H<sub>2</sub>S-related reduction in metabolic activity, regardless of the administration protocol<sup>15</sup>. 2) NaHS rapidly releases H<sub>2</sub>S, the effect occurring within seconds<sup>8</sup>. Indeed, NaHS dissociates to Na<sup>+</sup> and HS<sup>-</sup> and then binds partially to H<sup>+</sup> to form undissociated H<sub>2</sub>S. Although H<sub>2</sub>S levels were not measured in this study, NaHS rapid and uncontrolled delivery of H<sub>2</sub>S could contribute to the absence of an effect. Morpholin-4-ium-4-methoxyphenyl phosphinodithioate (GYY4137) or the prodrug AP39 might be more attractive alternatives, as it releases H<sub>2</sub>S slowly and steadily at physiological pH and temperature<sup>16-18</sup>. Importantly, in DCD porcine kidneys, SNMP (21°C) with autologous blood and AP39 improved urine output and reduced apoptosis compared with SCS or SNMP alone for 4 h<sup>19</sup>. 3) HMP at 4°C is responsible for decreasing cellular metabolism to approximately 5% of its physiological level<sup>20</sup>. Additionally, the preservation solution reduces cellular metabolism and provides cytoprotection. As the cellular respiration rate is proportional to the surrounding temperature<sup>21</sup>, the suppressing effects of H<sub>2</sub>S on mitochondrial respiration and OxPhos might be confounded with the effect of the cold temperature<sup>22</sup>. In conclusion, perfusion of porcine kidneys with NaHS did not improve preservation nor reduced ischemia-reperfusion injury. Perfusion of organs with alternative



H<sub>2</sub>S donors, or at different temperatures, should be tested to determine if H<sub>2</sub>S can improve post-transplant graft function and patient survival.

In **Chapter 3**, we examined the effects of ad-libitum access to carbohydrate loading drinks on food intake and IRI and the mechanisms underlying the benefits. We demonstrate that 1 week of carbohydrate loading before surgery induces protein dilution in mice, which confers consistent protection from acute surgical stress via FGF21. We not only found that short-term carbohydrate loading is sufficient to induce protein dilution but also demonstrated that these benefits can be achieved under hypercaloric conditions. We are among the first to establish a dietary intervention that protects from surgical stress without inducing body weight reduction. One potential benefit of carbohydrate loading is that it does not involve forced food restriction but promotes an alternative energy source and spontaneous macronutrient dilution. Recent studies indicated that if taken in liquid form, carbohydrate promotes total daily calorie intake by approximately 20% in humans, which can be used to counteract malnutrition in elderly patients<sup>23</sup>. The type of carbohydrate is an additional significant determinant. Here, carbohydrate loading consisted of an ad libitum solution of 50% sucrose in water. Most murine dietary studies that replaced protein with carbohydrates utilized complex carbohydrates derived from starch<sup>24,25</sup>. While we did not study the interactions between carbohydrate sources here, one of the few studies testing the effects of carbohydrate composition during protein dilution showed that a sucrose-rich diet improved metabolic parameters compared to a 50:50 mixture of glucose and fructose<sup>26</sup>. Interestingly, studies assessing the effects of starch in the diet demonstrated that a corn-based diet lower insulin and glucose concentrations, caloric intake, and weight gain compared with a rice-based diet<sup>27</sup>.

Additionally, our data supports that FGF21 is the major molecular mediator of these benefits. We propose that HC-mediated protection from IRI functions as a para- and endocrine mechanism involving hepatic secretion of FGF21, consistent with a previous report<sup>28</sup>. In line with previous studies, we showed that FGF21 signaling increases energy expenditure and thermogenesis<sup>29-31</sup> and regulates adaptive, homeostatic changes in metabolism and feeding behavior<sup>28,32</sup>. While mechanisms by which FGF21 mediates the benefits of carbohydrate loading/protein restriction in mitigating IRI remain unclear, our investigations into regulatory networks and transcription factors suggest the importance of the stress response proteins ATF3/4 and the antioxidant regulator NRF2. Additionally, regulatory network analysis revealed that genes involved in cell catabolic, autophagic, and renal development processes were downregulated. In contrast, protein synthesis and maturation and cell

responsiveness to external stimuli increased after 1 week of carbohydrate loading. Like most physiological responses, the injury response is a dynamic process that follows a specific, balancing pro- and anti-signaling process. For instance, although interleukin 6 functions as a pro-inflammatory cytokine in the early postoperative period, it can also exert anti-inflammatory effects by attenuating TNF- $\alpha$  and IL-1 activity while promoting the release of IL-1Ra and soluble TNF receptors<sup>33,34</sup>. Moreover, carbohydrate loading appears to inhibit catabolism processes. From an evolutionary standpoint, promoting catabolism in response to stress was developed as a survival mechanism, allowing injured animals to sustain themselves until their injuries were healed<sup>35</sup>. Therefore, inhibiting canonical cell stress response and promoting alternative signaling cascade may play a significant role in carbohydrate loading protection against IRI, even though additional research is necessary to elucidate these mechanisms. In conclusion, in ad libitum-fed mice, carbohydrate loading promotes dietary protein restriction, the adaptive stress response, and resilience to surgical stress. ERAS approaches currently promote short-term carbohydrate loading drinks to improve postoperative recovery without clear mechanistic explanations. Here, we identified FGF21 as a key molecular mediator of carbohydrate loading. These findings have broad implications for our fundamental understanding of the impact of carbohydrate and protein-carbohydrate interactions on metabolic health. Finally, our results provide a rationale for short-term carbohydrate loading or FGF21-based therapeutics during acute stress, including major surgery, for which there is now no widely accepted risk mitigation strategy.

## FUTURE DIRECTIONS

### Biomarkers of organ viability prior to transplantation

Since the increased usage of DCD organs, machine perfusions strategies have emerged to prove organ quality and viability assessment. Several tools are used to predict graft viability before transplantation. These include stratification of donors according to clinical parameters, risk scores, or histological donor biopsy scores, but we lack quantitative and objective markers<sup>36</sup>. In the last decade, much effort, including ours, has been made to find non-invasive biomarkers capable of predicting short- and long-term outcomes<sup>37</sup>. To that extent, the increasing use of machine perfusion has provided a new platform for assessing graft viability. Various markers present in the perfusate, such as glutathione-S-transferase (GST), N-acetyl- $\beta$ -D-glucosaminidase (NAG), and heart-type fatty acid binding protein (H-FABP), were described as predictors of delayed graft function but not of primary nonfunction and graft survival<sup>37</sup>. Importantly, evidence from our lab and others shows that NMP is a promising approach for recovering cadaveric organs, especially livers that would otherwise be rejected from the donor pool<sup>38</sup>. The ability to repair these livers would significantly expand the donor pool of organs available for transplantation, alleviating the majority of the shortage within a few years. However, there is a significant knowledge gap in the pathophysiology of untransplantable livers. Recent data showed that aerobic metabolism and ATP content were direct predictors of hepatocyte viability, which can aid the quantitative assessment of donor organs<sup>39</sup>. We aim to develop and test algorithms for assessing organ viability for transplantation quantitatively and objectively. We hypothesize that the identification prior to transplant or during normothermic *ex-vivo* perfusion (NMP) of the (non)functional liver will create a unique “multi-omics liver viability signature” which can be used to 1) Assess the condition of the donor organs prior to transplantation surgery, and 2) design new and effective therapeutic molecules to repair marginal organs with high clinical translational value. The heterogeneity of cells released in the perfusion media could be biomarkers of graft viability and indicators of specific injury mechanisms during organ handling and transplantation. Using a metabolomic dataset from 40 human livers undergoing NMP before transplantation, we have identified trans-urocanate as a strong predictor of early allograft dysfunction (EAD, [Figure 6](#)).

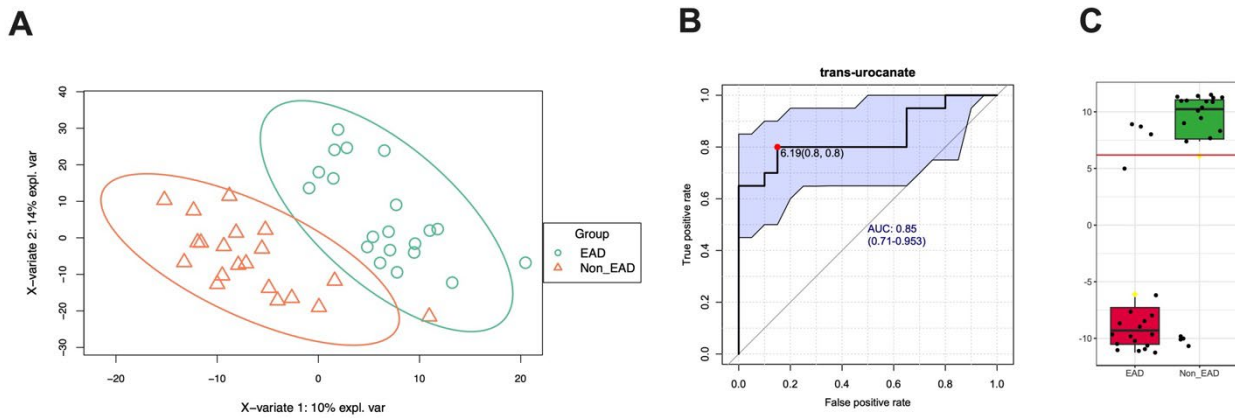


**Figure 7.** Identification of a metabolic signature of EAD. (A-B) Volcano plot of log<sub>2</sub> fold changes in hepatic metabolites versus non-EAD of EAD prior (A) and after transplantation (B). (C), trans-urocanate receiver operating characteristic curve (ROC). (D), trans-urocanate level in EAD versus non-EAD liver.

In this project, we propose to combine 1) metabolomics analysis including glycolytic, TCA, and PPP intermediate using UHPLC-MS/MS analysis, 2) bulk RNA-sequencing and 3) DNA methylation profiling in available liver biopsies taken during clinical liver transplant, prior and after NMP, to map the signaling networks and pathways that govern metabolism and determine its predictive value for EAD. Also, we will perform single-cell RNA sequencing of cells released from human liver graft during NMP prior to transplantation to identify biomarkers. We expect to unravel the composition of different cell types and functions of the cell released during NMP to predict EAD and one-year liver function.

## Improving organ preservation

Beyond short term perfusion and organ assessment, extending and enhancing organ preservation could potentially improve organ sharing, reduce the need for emergent surgeries, and improve allocation. Recently, organ preservation at sub-zero temperatures in the absence of ice, termed supercooling, resulted in a tripling of the preservation duration of mammalian livers (3 days in rodents and 27 h in humans)<sup>40-42</sup>. Despite the long-standing challenges cryopreservation scientists face in managing phase changes in water, the preservation media's ability to remain in a liquid state has proven to be an effective solution<sup>43,44</sup>. However, it is essential to note that the ice-free supercooled state is inherently thermodynamically unstable and susceptible to spontaneous ice formation, which poses a greater risk of harm than equilibrium freezing. Indeed, ice formation is proven to cause extensive structural damage that prevents revascularization and diminishes the attachment and integrity of constituent cells<sup>45</sup>. The limitation of supercooling is intrinsically linked to the



extent of metabolic stasis that can be achieved, as the risk of ice formation rises with decreasing storage temperature. Taken together, alternative strategies will be required to reach lower storage temperatures and longer preservation durations. The largely empirical approach to organ cryopreservation that has dominated for several decades were cryoprotective agent (CPA) cocktails, storage conditions, and pre- and post-thaw perfusion protocols. Freeze tolerance is an effective strategy utilized by multiple organisms in nature<sup>46</sup>. Inspired by the wood frogs (*Rana sylvatica*) that can survive in a frozen state at  $-6^{\circ}\text{C}$  to  $-16^{\circ}\text{C}$  for weeks<sup>47,48</sup>, freeze tolerance capitalizes on both ice nucleating agents (INA) and endogenous CPAs to orchestrate freezing and prevent injurious intracellular ice formation. Adopting some of these learnings, recent protocols for freezing whole organs (from rat to pig, livers, kidneys, heart or limbs)<sup>45</sup> that enter high subzero temperatures ranging from  $-10^{\circ}\text{C}$  to  $-15^{\circ}\text{C}$  for durations of up to 5 days in the presence of ice, termed as Partial Freezing (PF) emerged<sup>49</sup>. Here, we will aim to compare the storage efficiency of kidneys of PF to SCS for durations up to 30 days. Inspired by the wood frogs and other research done on liver<sup>49</sup>, we propose to fine-tune a cocktail of CPAs to optimize the storage solution for kidney preservation. Our preliminary data already suggests that 10 days of PF improves post-reperfusion/transplantation perfusion quality, as well as tissue function and metabolism compared to SCS, as evidenced by arterial flow and resistance, as well as oxygen consumption and lactate concentrations closer to those of a fresh kidney than SCS (Figure 7).

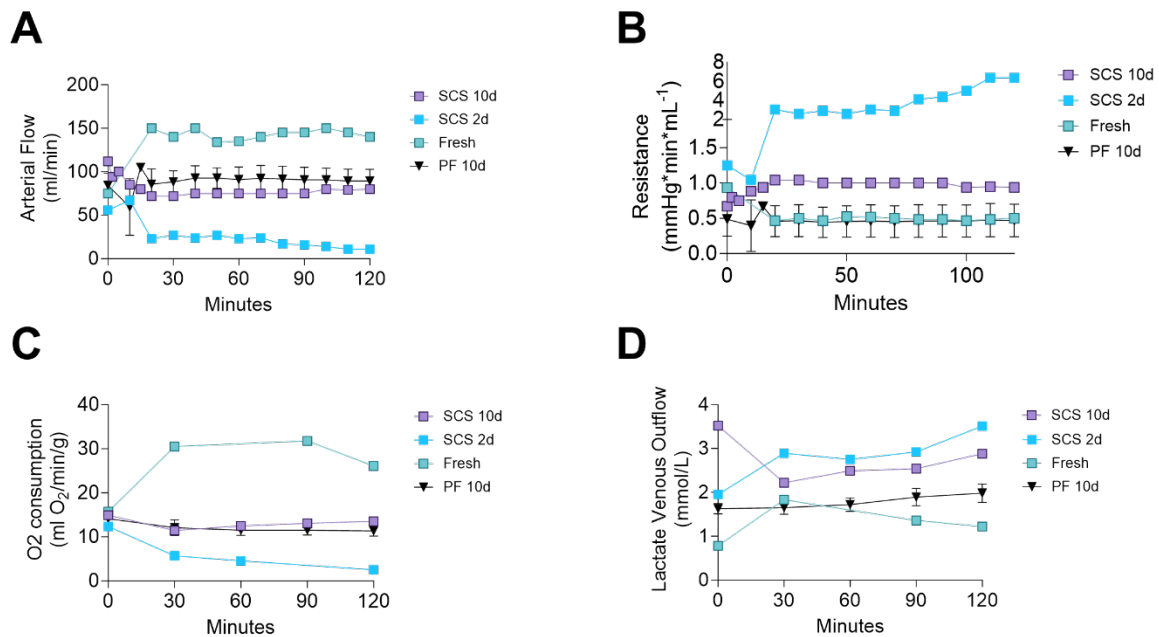


**Figure 8.** Partial Freezing tends to improve kidney quality. (A) Arterial flow during NMP of kidney stored 2 days SCS, 10 days SCS, 10 days PF and fresh organ. (B) Arterial resistance during NMP of kidney stored in the indicated conditions. (C) Oxygen consumption resistance during NMP of kidney stored in the indicated conditions. (D) Lactate production during NMP of kidney stored in the indicated conditions.  $n = 1-3$  per group, Data in all panels are shown as mean  $\pm$  SD.

## Target IGF-1 to reduce IRI

Experimental and epidemiological studies indicate that insulin-like growth factor (IGF1) and its binding proteins play a crucial role in the biology of aging<sup>50</sup>. Data from various studies have shown increased maximal lifespan and stress resistance in several genetic models of IGF1 deficiency or deletion<sup>50-52</sup>. Importantly, DR, by decreasing protein intake, significantly reduces serum IGF1 concentration while increasing serum corticosteroid levels<sup>50</sup>. Our lab and others have found that IGF1 supplementation abrogates DR's protective effect and worsens IRI independently of the metabolic benefits (Figure 8)<sup>53</sup>. Interestingly, inhibition of postreperfusion insulin signaling either pharmacologically, using the PI3K inhibitor or genetically, with liver-specific Tsc1 KO mice (leading to chronic mTORC1 activation) partially abrogated PR-mediated protection of liver IRI<sup>54</sup>. This contrasts with previous studies showing beneficial effects against myocardial IRI and infarcts when IGF1 was administered post-operatively<sup>55</sup> or in transgenic mouse hearts overexpressing IGF1<sup>55</sup>. IGF1 is a potent mitogenic growth factor that promotes cell proliferation and differentiation and inhibits apoptosis<sup>56</sup>. The inhibition of the IGF1 pathway causes several cellular and metabolic adaptations, including downregulation of growth pathways, upregulation of autophagic and apoptotic pathways, increased resistance to stress, and increased genome stability<sup>50</sup>. Here, we

propose to explore IGF1 as a target to reduce IRI. We aim to study the effects of IGF1 blockade prior to surgery and IGF1 supplementation post-operatively in mice models of IRI. We will define IGF1's therapeutic relevance in preventing and treating surgical stress.

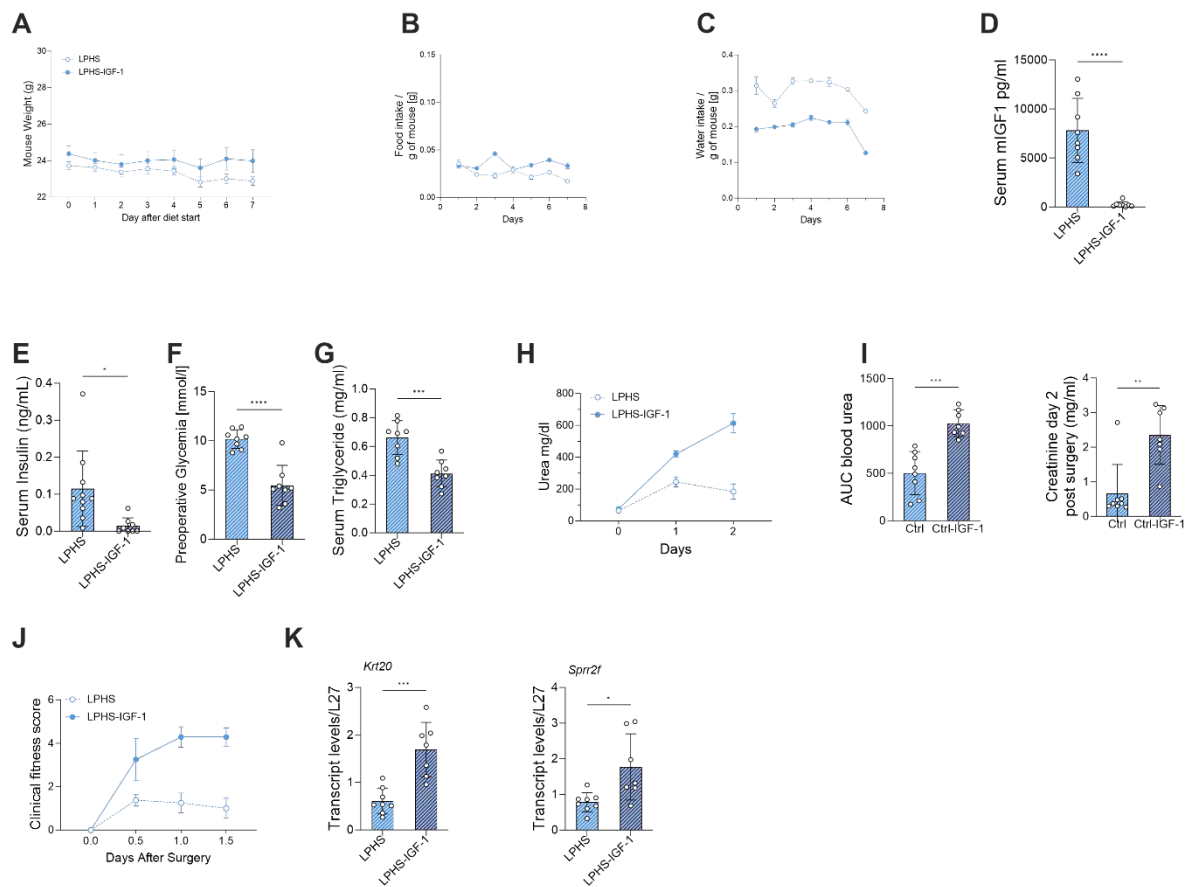


**Figure 9.** IGF1 supplementation prior to surgery worsens IRI. (A) Body weight at the indicated time of mice given ad libitum access to low protein (LP) with sucrose 50% solution drink (HC) treated intraperitoneally with a NaCl (Veh) or rhIGF1 (IGF1, 4mg/kg/day). (B) Food and water (C) intake (normalized by body weight) of mice in the indicated group. (D) Serum mIGF1 levels and serum insulin (E) of mice preconditioned for 1 week with Veh or IGF1. (F) Glycemia of mice 2h prior to surgery. (G) Serum triglyceride levels of mice in the indicated group. (H) Serum urea levels and AUC (I) at the indicated time post-renal IRI. (J) Clinical fitness score at the indicated time post-renal IRI. (K) Relative *Krt20* and *Spr2f* mRNA levels at day 2 post-renal IRI of mice treated for 1 week with the indicated treatment, \*p values for D,E,F,G,I,K were calculated with unpaired two-tailed T-tests, \*p < 0.05 \*\*\*p < 0.001 \*\*\*\*p < 0.0001. n = 6 per group, Data in all panels are shown as mean ± SD.

## Understand IRI in the context of aging.

Age is a significant predictor of kidney transplant outcome. Elderly recipients had significantly lower graft and patient survival rates, as well as a significantly higher risk of graft loss and patient death<sup>57</sup>. Furthermore, AKI has been shown to increase the risk of ESRD in elderly patients<sup>58,59</sup>. Immunosenescence, or the age-related decline in immune functions, has

been linked to an increase in the prevalence and severity of infectious diseases and post-operative complications in the elderly<sup>60</sup>. Immunosenescence is defined by reduced cell-mediated immune function and humoral immune responses. Age-related changes in the innate immune system coexist with age-dependent defects in T- and B-cell function<sup>60</sup>. Neutrophils, which are major effector cells of the innate immune system, are known to play a role in the pathogenesis of renal IRI<sup>61,62</sup>. Recent research found that IL6 expression was higher in aged mice's post-ischemic kidneys than in young mice, while TNF alpha and VEGF expression were lower<sup>63</sup>. Importantly, our data and several epidemiological studies have shown that old mice have a higher sensitivity to IRI (Figure 8) and a higher prevalence of AKI in elderly dialysis patients, increasing their risk of progression to CKD<sup>64,65</sup>. In aged kidneys, changes in hemodynamics, tissue metabolism, and structural changes all contribute to the development of this sensitivity. Indeed, recent research has revealed that aged kidneys exhibit altered transcriptomic, hemodynamic, and physiologic behavior both at rest and in response to renal injuries<sup>66</sup>. Furthermore, numerous studies show that late-onset DR has a limited potential efficacy. Late-onset DR only partially restored age-related declines in superoxide dismutase, catalase, glutathione peroxidase, glutathione, and elevated levels of lipid peroxidation in brain and peripheral organs, as well as increased HSP70 expression<sup>67</sup>.

In future research, we intend to validate carbohydrate loading benefits and identify the mechanisms underlying IRI sensitivity in aged mice, utilizing multimodal omics techniques such as spatial transcriptome analysis. This knowledge will help determine the influence of surgical stress on older organisms compared to juvenile organisms and provide the first hints for developing therapeutic approaches for the elderly population.



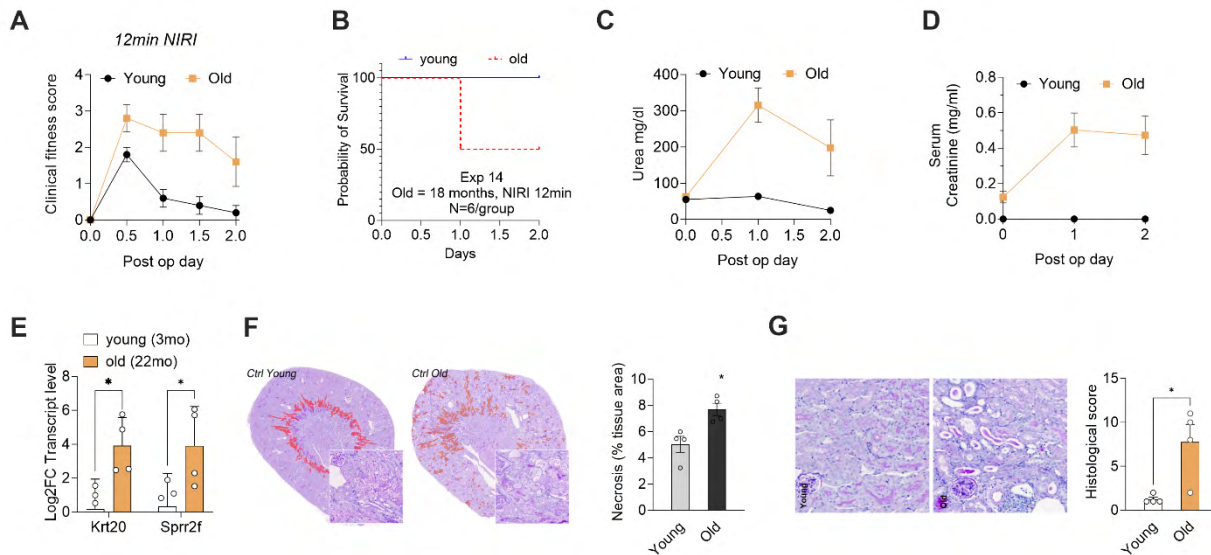


**Figure 10.** Increased sensitivity to IRI in aged compared to young mice. (A) Clinical fitness score post IRI of 8-week-old young and 22-month-old mice after post-renal IRI consisting in 12 minutes clamping of kidney pedicle. (B) Survival proportion of young and old mice post-renal IRI. (C) Serum urea and (D) creatinine levels in young and old mice post-renal IRI. (E) Relative Krt20 and Sprr2f, 2 biomarkers of kidney tubular injuries, in young and old mice post-renal IRI. (F) Representative cross sections of PAS-stained kidneys with necrotic area digitally highlighted in red (left; x10 magnification; scale bar 100 $\mu$ m) and necrotic tissue area quantification (right) at day 2 post-renal IRI. (G) Representative cross sections of PAS-stained kidneys (left; x10 magnification; scale bar 100 $\mu$ m) and histological score (right) at day 2 post-renal IRI. n = 4 per group, \*p values for A,F,G were calculated with two-way ANOVA followed by a Tukey's post hoc analysis, \*p < 0.05. Data in all panels are shown as mean  $\pm$  SD.

1. Longchamp, A., Klauser, A., Songeon, J., Agius, T., Nastasi, A., Ruttiman, R., Moll, S., Meier, R., Buhler, L., Corpataux, J.M., and Lazeyras, F. (2020). Ex Vivo Analysis of Kidney Graft Viability Using 31P Magnetic Resonance Imaging Spectroscopy. *Transplantation*. 10.1097/TP.0000000000003323.
2. Graveron-Demilly, D. (2014). Quantification in magnetic resonance spectroscopy based on semi-parametric approaches. *MAGMA* 27, 113-130. 10.1007/s10334-013-0393-4.
3. Urbanellis, P., McEvoy, C.M., Škrtić, M., Kathis, J.M., Kollmann, D., Linares, I., Ganesh, S., Oquendo, F., Sharma, M., Mazilescu, L., et al. (2021). Transcriptome Analysis of Kidney Grafts Subjected to Normothermic Ex Vivo Perfusion Demonstrates an Enrichment of Mitochondrial Metabolism Genes. *Transplant Direct* 7, e719. 10.1097/TXD.0000000000001157.
4. T, C., N, A., S, S.-N., S, D., and AV, G. (2016). Subnormothermic Perfusion in the Isolated Rat Liver Preserves the Antioxidant Glutathione and Enhances the Function of the Ubiquitin Proteasome System. *Oxidative medicine and cellular longevity* 2016. 10.1155/2016/9324692.
5. Lazeyras, F., Buhler, L., Vallee, J.P., Hergt, M., Nastasi, A., Ruttimann, R., Morel, P., and Buchs, J.B. (2012). Detection of ATP by "in line" 31P magnetic resonance spectroscopy during oxygenated hypothermic pulsatile perfusion of pigs' kidneys. *MAGMA* 25, 391-399. 10.1007/s10334-012-0319-6.
6. Buchs, J.B., Lazeyras, F., Bühler, L., Vallee, J.P., Nastasi, A., Ruttimann, R., and Morel, P. (2009). [The viability of kidneys tested by gadolinium-perfusion MRI during ex vivo perfusion]. *Prog Urol* 19, 307-312. 10.1016/j.purol.2009.01.004.
7. González, F.X., Rimola, A., Grande, L., Antolin, M., Garcia-Valdecasas, J.C., Fuster, J., Lacy, A.M., Cugat, E., Visa, J., and Rodés, J. (1994). Predictive factors of early postoperative graft function in human liver transplantation. *Hepatology* 20, 565-573. 10.1002/hep.1840200304.
8. Longchamp, A., Mirabella, T., Arduini, A., MacArthur, M.R., Das, A., Treviño-Villarreal, J.H., Hine, C., Ben-Sahra, I., Knudsen, N.H., Brace, L.E., et al. (2018). Amino Acid Restriction Triggers Angiogenesis via GCN2/ATF4 Regulation of VEGF and H. *Cell* 173, 117-129.e114. 10.1016/j.cell.2018.03.001.
9. de Rougemont, O., Breitenstein, S., Leskosek, B., Weber, A., Graf, R., Clavien, P.A., and Dutkowski, P. (2009). One hour hypothermic oxygenated perfusion (HOPE) protects nonviable liver allografts donated after cardiac death. *Ann Surg* 250, 674-683. 10.1097/SLA.0b013e3181bcb1ee.
10. Bruinsma, B.G., Yeh, H., Ozer, S., Martins, P.N., Farmer, A., Wu, W., Saeidi, N., Op den Dries, S., Berendsen, T.A., Smith, R.N., et al. (2014). Subnormothermic machine perfusion for ex vivo preservation and recovery of the human liver for transplantation. *Am J Transplant* 14, 1400-1409. 10.1111/ajt.12727.
11. Mahboub, P., Ottens, P., Seelen, M., 't Hart, N., t Hart, N., Van Goor, H., Ploeg, R., Martins, P.N., Martins, P., and Leuvenink, H. (2015). Gradual Rewarming with Gradual Increase in Pressure during Machine Perfusion after Cold Static Preservation Reduces Kidney Ischemia Reperfusion Injury. *PLoS One* 10, e0143859. 10.1371/journal.pone.0143859.
12. Hine, C., Harputlugil, E., Zhang, Y., Ruckenstuhl, C., Lee, B.C., Brace, L., Longchamp, A., Treviño-Villarreal, J.H., Mejia, P., Ozaki, C.K., et al. (2015). Endogenous hydrogen sulfide production is essential for dietary restriction benefits. *Cell* 160, 132-144. 10.1016/j.cell.2014.11.048.
13. Sekijima, M., Sahara, H., Miki, K., Villani, V., Ariyoshi, Y., Iwanaga, T., Tomita, Y., and Yamada, K. (2017). Hydrogen sulfide prevents renal ischemia-reperfusion injury in CLAWN miniature swine. *J Surg Res* 219, 165-172. 10.1016/j.jss.2017.05.123.
14. Lobb, I., Davison, M., Carter, D., Liu, W., Haig, A., Gunaratnam, L., and Sener, A. (2015). Hydrogen Sulfide Treatment Mitigates Renal Allograft Ischemia-Reperfusion Injury

- during Cold Storage and Improves Early Transplant Kidney Function and Survival Following Allogeneic Renal Transplantation. *J Urol* 194, 1806-1815. 10.1016/j.juro.2015.07.096.
15. Drabek, T., Kochanek, P.M., Stezoski, J., Wu, X., Bayir, H., Morhard, R.C., Stezoski, S.W., and Tisherman, S.A. (2011). Intravenous hydrogen sulfide does not induce hypothermia or improve survival from hemorrhagic shock in pigs. *Shock* 35, 67-73. 10.1097/SHK.0b013e3181e86f49.
  16. Li, L., Whiteman, M., Guan, Y.Y., Neo, K.L., Cheng, Y., Lee, S.W., Zhao, Y., Baskar, R., Tan, C.H., and Moore, P.K. (2008). Characterization of a novel, water-soluble hydrogen sulfide-releasing molecule (GYY4137): new insights into the biology of hydrogen sulfide. *Circulation* 117, 2351-2360. 10.1161/CIRCULATIONAHA.107.753467.
  17. Zhao, H., Qiu, Y., Wu, Y., Sun, H., and Gao, S. (2021). Protective Effects of GYY4137 on Renal Ischaemia/Reperfusion Injury through Nrf2-Mediated Antioxidant Defence. *Kidney Blood Press Res* 46, 257-265. 10.1159/000509933.
  18. Ahmad, A., Olah, G., Szczesny, B., Wood, M.E., Whiteman, M., and Szabo, C. (2016). AP39, A Mitochondrially Targeted Hydrogen Sulfide Donor, Exerts Protective Effects in Renal Epithelial Cells Subjected to Oxidative Stress in Vitro and in Acute Renal Injury in Vivo. *Shock* 45, 88-97. 10.1097/SHK.0000000000000478.
  19. Juriasingani, S., Jackson, A., Zhang, M.Y., Ruthirakanthan, A., Dugbartey, G.J., Sogutdelen, E., Levine, M., Mandurah, M., Whiteman, M., Luke, P., and Sener, A. (2021). Evaluating the Effects of Subnormothermic Perfusion with AP39 in a Novel Blood-Free Model of Ex Vivo Kidney Preservation and Reperfusion. *Int J Mol Sci* 22. 10.3390/ijms22137180.
  20. L, J., L, Y., M, Z., LP, P., and M, L. (2018). Organ preservation: from the past to the future. *Acta pharmacologica Sinica* 39. 10.1038/aps.2017.182.
  21. Robinson, W.R., Peters, R.H., and Zimmermann, J. (2011). The effects of body size and temperature on metabolic rate of organisms. <https://doi.org/10.1139/z83-037>. 10.1139/z83-037.
  22. Y, O., and T, K. (2009). Preservation solution for lung transplantation. *General thoracic and cardiovascular surgery* 57. 10.1007/s11748-009-0492-3.
  23. DP, D., and RD, M. (2000). Liquid versus solid carbohydrate: effects on food intake and body weight. *International journal of obesity and related metabolic disorders : journal of the International Association for the Study of Obesity* 24. 10.1038/sj.ijo.0801229.
  24. Solon-Biet, S.M., Mitchell, S.J., Coogan, S.C.P., Cogger, V.C., Gokarn, R., McMahon, A.C., Raubenheimer, D., de Cabo, R., Simpson, S.J., and Le Couteur, D.G. (2015). Dietary Protein to Carbohydrate Ratio and Caloric Restriction: Comparing Metabolic Outcomes in Mice. *Cell Reports* 11, 1529-1534. 10.1016/j.celrep.2015.05.007.
  25. Le Couteur, D.G., Solon-Biet, S., Cogger, V.C., Mitchell, S.J., Senior, A., De Cabo, R., Raubenheimer, D., and Simpson, S.J. (2016). The impact of low-protein high-carbohydrate diets on aging and lifespan. *Cellular and Molecular Life Sciences* 73, 1237-1252. 10.1007/s00018-015-2120-y.
  26. Wali, J.A., Milner, A.J., Luk, A.W.S., Pulpitel, T.J., Dodgson, T., Facey, H.J.W., Wahl, D., Kebede, M.A., Senior, A.M., Sullivan, M.A., et al. (2021). Impact of dietary carbohydrate type and protein-carbohydrate interaction on metabolic health. *Nat Metab* 3, 810-828. 10.1038/s42255-021-00393-9.
  27. S, Z., Y, R., Y, H., Y, W., H, D., and T, S. (2023). Effects of five carbohydrate sources on cat diet digestibility, postprandial glucose, insulin response, and gut microbiomes. *Journal of animal science* 101. 10.1093/jas/skad049.
  28. Laeger, T., Henagan, T.M., Albarado, D.C., Redman, L.M., Bray, G.A., Noland, R.C., Münzberg, H., Hutson, S.M., Gettys, T.W., Schwartz, M.W., and Morrison, C.D. (2014). FGF21 is an endocrine signal of protein restriction. *J Clin Invest* 124, 3913-3922. 10.1172/JCI74915.

29. Chau, M.D., Gao, J., Yang, Q., Wu, Z., and Gromada, J. (2010). Fibroblast growth factor 21 regulates energy metabolism by activating the AMPK-SIRT1-PGC-1 $\alpha$  pathway. *Proc Natl Acad Sci U S A* *107*, 12553-12558. 10.1073/pnas.1006962107.
30. Fisher, F.M., Kleiner, S., Douris, N., Fox, E.C., Mepani, R.J., Verdeguer, F., Wu, J., Kharitonov, A., Flier, J.S., Maratos-Flier, E., and Spiegelman, B.M. (2012). FGF21 regulates PGC-1 $\alpha$  and browning of white adipose tissues in adaptive thermogenesis. *Genes Dev* *26*, 271-281. 10.1101/gad.177857.111.
31. MK, B., P, P., AR, K., G, K., JS, F., and E, M.-F. (2007). Hepatic fibroblast growth factor 21 is regulated by PPAR $\alpha$  and is a key mediator of hepatic lipid metabolism in ketotic states. *Cell metabolism* *5*. 10.1016/j.cmet.2007.05.002.
32. Hill, C.M., Albarado, D.C., Coco, L.G., Spann, R.A., Khan, M.S., Qualls-Creekmore, E., Burk, D.H., Burke, S.J., Collier, J.J., Yu, S., et al. (2022). FGF21 is required for protein restriction to extend lifespan and improve metabolic health in male mice. *Nat Commun* *13*, 1897. 10.1038/s41467-022-29499-8.
33. H, T., E, T., MB, A., CA, D., and JW, M. (1994). Interleukin-6 (IL-6) as an anti-inflammatory cytokine: induction of circulating IL-1 receptor antagonist and soluble tumor necrosis factor receptor p55. *Blood* *83*.
34. N, N.C., and HP, R. (2006). Cell response to surgery. *Archives of surgery (Chicago, Ill. : 1960)* *141*. 10.1001/archsurg.141.11.1132.
35. JP, D. (2000). The stress response to trauma and surgery. *British journal of anaesthesia* *85*. 10.1093/bja/85.1.109.
36. Sung, R.S., Christensen, L.L., Leichtman, A.B., Greenstein, S.M., Distant, D.A., Wynn, J.J., Stegall, M.D., Delmonico, F.L., and Port, F.K. (2008). Determinants of discard of expanded criteria donor kidneys: impact of biopsy and machine perfusion. *Am J Transplant* *8*, 783-792. 10.1111/j.1600-6143.2008.02157.x.
37. C, M., OC, V., E, v.H., I, J., GR, K., A, R., HG, L., JP, S., A, P., J, P., et al. (2010). The value of machine perfusion perfusate biomarkers for predicting kidney transplant outcome. *Transplantation* *90*. 10.1097/TP.0b013e3181f5c40c.
38. Kwong, A.J., Ebel, N.H., Kim, W.R., Lake, J.R., Smith, J.M., Schladt, D.P., Skeans, M.A., Foutz, J., Gauntt, K., Cafarella, M., et al. (2022). OPTN/SRTR 2020 Annual Data Report: Liver. *Am J Transplant* *22 Suppl 2*, 204-309. 10.1111/ajt.16978.
39. Berendsen, T.A., Izamis, M.L., Xu, H., Liu, Q., Hertl, M., Berthiaume, F., Yarmush, M.L., and Uygun, K. (2011). Hepatocyte viability and adenosine triphosphate content decrease linearly over time during conventional cold storage of rat liver grafts. *Transplant Proc* *43*, 1484-1488. 10.1016/j.transproceed.2010.12.066.
40. de Vries, R.J., Tessier, S.N., Banik, P.D., Nagpal, S., Cronin, S.E.J., Ozer, S., Hafiz, E.O.A., van Gulik, T.M., Yarmush, M.L., Markmann, J.F., et al. (2019). Supercooling extends preservation time of human livers. *Nat Biotechnol* *37*, 1131-1136. 10.1038/s41587-019-0223-y.
41. Berendsen, T.A., Bruinsma, B.G., Puts, C.F., Saeidi, N., Usta, O.B., Uygun, B.E., Izamis, M.L., Toner, M., Yarmush, M.L., and Uygun, K. (2014). Supercooling enables long-term transplantation survival following 4 days of liver preservation. *Nat Med* *20*, 790-793. 10.1038/nm.3588.
42. BG, B., TA, B., ML, I., H, Y., ML, Y., and K, U. (2015). Supercooling preservation and transplantation of the rat liver. *Nature protocols* *10*. 10.1038/nprot.2015.011.
43. N, I., B, R., and CY, L. (2000). Transplantation of mammalian livers following freezing: vascular damage and functional recovery. *Cryobiology* *40*. 10.1006/cryo.1999.2225.
44. N, I., B, R., and CY, L. (1999). A histological analysis of liver injury in freezing storage. *Cryobiology* *39*. 10.1006/cryo.1999.2205.
45. N, W., and JP, A. (2021). High sub-zero organ preservation: A paradigm of nature-inspired strategies. *Cryobiology* *102*. 10.1016/j.cryobiol.2021.04.002.

46. BE, L., and KB, S. (2018). Solving Donor Organ Shortage with Insights from Freeze Tolerance in Nature: Activating endogenous antioxidant systems with non-coding RNA to precondition donor organs. *BioEssays : news and reviews in molecular, cellular and developmental biology* 40. 10.1002/bies.201800092.
47. JP, C., MC, d.A., AJ, R., and RE, L. (2013). Hibernation physiology, freezing adaptation and extreme freeze tolerance in a northern population of the wood frog. *The Journal of experimental biology* 216. 10.1242/jeb.089342.
48. JP, W., KB, S., and JG, B. (1990). Ice nucleating activity in the blood of the freeze-tolerant frog, *Rana sylvatica*. *Cryobiology* 27. 10.1016/0011-2240(90)90032-y.
49. Tessier, S.N., de Vries, R.J., Pendexter, C.A., Cronin, S.E.J., Ozer, S., Hafiz, E.O.A., Raigani, S., Oliveira-Costa, J.P., Wilks, B.T., Lopera Higueta, M., et al. (2022). Partial freezing of rat livers extends preservation time by 5-fold. *Nat Commun* 13, 4008. 10.1038/s41467-022-31490-2.
50. Fontana, L., Partridge, L., and Longo, V.D. (2010). Extending healthy life span--from yeast to humans. *Science* 328, 321-326. 10.1126/science.1172539.
51. Fontana, L., Weiss, E.P., Villareal, D.T., Klein, S., and Holloszy, J.O. (2008). Long-term effects of calorie or protein restriction on serum IGF-1 and IGFBP-3 concentration in humans. *Aging Cell* 7, 681-687.
52. L, F., DT, V., SK, D., SR, S., SN, M., AG, P., S, K., M, B., J, R., E, R., and JO, H. (2016). Effects of 2-year calorie restriction on circulating levels of IGF-1, IGF-binding proteins and cortisol in nonobese men and women: a randomized clinical trial. *Aging cell* 15. 10.1111/accel.12400.
53. LL, P., and AG, S. (1992). Reversal of food restriction-induced inhibition of mouse skin tumor promotion by adrenalectomy. *Carcinogenesis* 13. 10.1093/carcin/13.10.1925.
54. Harputlugil, E., Hine, C., Vargas, D., Robertson, L., Manning, B.D., and Mitchell, J.R. (2014). The TSC complex is required for the benefits of dietary protein restriction on stress resistance in vivo. *Cell Rep* 8, 1160-1170. 10.1016/j.celrep.2014.07.018.
55. Yamashita, K., Kajstura, J., Discher, D.J., Wasserlauf, B.J., Bishopric, N.H., Anversa, P., and Webster, K.A. (2001). Reperfusion-activated Akt kinase prevents apoptosis in transgenic mouse hearts overexpressing insulin-like growth factor-1. *Circ Res* 88, 609-614. 10.1161/01.res.88.6.609.
56. S, Y., D, L., and P, B. (2005). The role of the growth hormone/insulin-like growth factor axis in tumor growth and progression: Lessons from animal models. *Cytokine & growth factor reviews* 16. 10.1016/j.cytogfr.2005.01.010.
57. M, V., G, G., D, C., A, M., A, G., G, G., N, S., and P, V. (2012). Age is an important predictor of kidney transplantation outcome. *Nephrology, dialysis, transplantation : official publication of the European Dialysis and Transplant Association - European Renal Association* 27. 10.1093/ndt/gfr524.
58. United States Renal Data System 2022 USRDS Annual Data Report: Epidemiology of kidney disease in the United States. , 2022. <https://adr.usrds.org/2022>.
59. DC, J., SR, Y., SW, L., SW, H., W, K., J, P., and YK, K. (2015). Lessons from 30 years' data of Korean end-stage renal disease registry, 1985-2015. *Kidney research and clinical practice* 34. 10.1016/j.krcp.2015.08.004.
60. D, W., B, W., and B, G.-L. (2009). The aging of the immune system. *Transplant international : official journal of the European Society for Organ Transplantation* 22. 10.1111/j.1432-2277.2009.00927.x.
61. HR, J., and H, R. (2009). The innate immune response in ischemic acute kidney injury. *Clinical immunology (Orlando, Fla.)* 130. 10.1016/j.clim.2008.08.016.
62. SK, J., SA, S., WY, C., KJ, G., and HK, K. (2006). Macrophages contribute to the initiation of ischaemic acute renal failure in rats. *Nephrology, dialysis, transplantation : official*



publication of the European Dialysis and Transplant Association - European Renal Association 21. 10.1093/ndt/gfk047.

63. KK, D., X, M., A, A., MP, C., AH, H., and DR, M. (1999). Early kidney TNF-alpha expression mediates neutrophil infiltration and injury after renal ischemia-reperfusion. *The American journal of physiology* 277. 10.1152/ajpregu.1999.277.3.R922.
64. S, G., S, N., Z, L., C, C., Y, Z., J, Q., B, L., S, T., A, X., W, B., et al. (2016). Epidemiology and outcomes of acute kidney injury in elderly chinese patients: a subgroup analysis from the EACH study. *BMC nephrology* 17. 10.1186/s12882-016-0351-2.
65. CY, H., CE, M., D, F., JD, O., GM, C., and AS, G. (2007). Community-based incidence of acute renal failure. *Kidney international* 72. 10.1038/sj.ki.5002297.
66. MG, K., J, Y., YS, K., HY, L., SW, O., WY, C., and SK, J. (2019). Impact of aging on transition of acute kidney injury to chronic kidney disease. *Scientific reports* 9. 10.1038/s41598-019-54585-1.
67. S, S., R, S., M, K., and G, K. (2010). Late-onset dietary restriction compensates for age-related increase in oxidative stress and alterations of HSP 70 and synapsin 1 protein levels in male Wistar rats. *Biogerontology* 11. 10.1007/s10522-009-9240-4.

## APPENDIXES

- **Appendix 1**

- Longchamp, A., Klauser, A., Songeon, J., Agius, T., Nastasi, A., Ruttiman, R., Moll, S., Meier, R.P.H., Buhler, L., Corpataux, J.M., et al. (2020). Ex Vivo Analysis of Kidney Graft Viability Using 31P Magnetic Resonance Imaging Spectroscopy. *Transplantation* 104, 1825-1831.

- **Appendix 2**

- Songeon, J., Courvoisier, S., Xin, L., Agius, T., Dabrowski, O., Longchamp, A., Lazeyras, F., and Klauser, A. (2023). In vivo magnetic resonance 31 P-Spectral Analysis With Neural Networks: 31P-SPAWNN. *Magn Reson Med* 89, 40-53.

- **Appendix 3**

- Kiesworo, K., MacArthur, M.R., Kip, P., Agius, T., Macabrey, D., Lambelet, M., Hamard, L., Ozaki, C.K., Mitchell, J.R., Déglise, S., et al. (2023). Cystathionine- $\gamma$ -lyase overexpression modulates oxidized nicotinamide adenine dinucleotide biosynthesis and enhances neovascularization. *JVS Vasc Sci* 4, 100095.

- **Appendix 4**

- Halfon, M., Emsley, R., Agius, T., Lyon, A., Déglise, S., Pascual, M., Uygun, K., Markmann, J.F., Bochud, P.-Y., Golshayan, D., et al. (Year of publication). Association of Kidney Graft 10-Year Outcome with Recipient Cystathionine Gamma-Lyase 1 Polymorphisms and Hydrogen Sulfide Levels: A Cohort Study.



# Ex Vivo Analysis of Kidney Graft Viability Using <sup>31</sup>P Magnetic Resonance Imaging Spectroscopy

Alban Longchamp, MD, PhD,<sup>1</sup> Antoine Klausner, PhD,<sup>2,3</sup> Julien Songeon, MS,<sup>2</sup> Thomas Agius, MS,<sup>1</sup> Antonio Nastasi, BS,<sup>4</sup> Raphael Ruttiman, BS,<sup>4</sup> Solange Moll, MD,<sup>5</sup> Raphael P. H. Meier, MD, PhD,<sup>4,6</sup> Leo Buhler, MD,<sup>7</sup> Jean-Marc Corpataux, MD,<sup>1</sup> and Francois Lazeyras, PhD<sup>2,3</sup>

**Background.** The lack of organs for kidney transplantation is a growing concern. Expansion in organ supply has been proposed through the use of organs after circulatory death (donation after circulatory death [DCD]). However, many DCD grafts are discarded because of long warm ischemia times, and the absence of reliable measure of kidney viability. <sup>31</sup>P magnetic resonance imaging (pMRI) spectroscopy is a noninvasive method to detect high-energy phosphate metabolites, such as ATP. Thus, pMRI could predict kidney energy state, and its viability before transplantation. **Methods.** To mimic DCD, pig kidneys underwent 0, 30, or 60 min of warm ischemia, before hypothermic machine perfusion. During the ex vivo perfusion, we assessed energy metabolites using pMRI. In addition, we performed Gadolinium perfusion sequences. Each sample underwent histopathological analyzing and scoring. Energy status and kidney perfusion were correlated with kidney injury. **Results.** Using pMRI, we found that in pig kidney, ATP was rapidly generated in presence of oxygen (100 kPa), which remained stable up to 22 h. Warm ischemia (30 and 60 min) induced significant histological damages, delayed cortical and medullary Gadolinium elimination (perfusion), and reduced ATP levels, but not its precursors (AMP). Finally, ATP levels and kidney perfusion both inversely correlated with the severity of kidney histological injury. **Conclusions.** ATP levels, and kidney perfusion measurements using pMRI, are biomarkers of kidney injury after warm ischemia. Future work will define the role of pMRI in predicting kidney graft and patient's survival.

(*Transplantation* 2020;104: 1825–1831).

## INTRODUCTION

The lack of available kidneys for transplantation is a major concern, responsible for excess in morbimortality, and cost to healthcare systems.<sup>1</sup> Thus, to expand the organ supply, a variety of efforts have been made, such as accepting organs from donors after circulatory death (DCD), or with comorbidities (extended criteria donors [ECDs]). However, their usage is limited, due mainly to the fact that there is no reliable, noninvasive means to assess graft viability ex vivo. Shockingly, in the United States, 18% of all donated kidneys and 45% of ECD kidneys were not allocated for transplantation, despite that such kidneys could have been transplanted with good outcomes.<sup>1,2</sup> In addition, the

introduction of policies that penalize centers with poor outcomes resulted in an increase in the number discarded marginal kidneys,<sup>3</sup> a practice called “risk-averse transplant behavior.”<sup>4</sup>

A number of tools are used to predict the suitability of kidneys before transplantation. These include stratification of donors according to clinical parameters, risk scores, histological donor biopsy scores, machine perfusion characteristics, biomarkers, and so on.<sup>5</sup> Besides the dichotomous ECD classification,<sup>6</sup> none of the scoring tools are clinically used.<sup>7</sup> Consequently, transplant outcome remains difficult to predict based on current

Received 12 February 2020. Revision received 9 March 2020.

Accepted 24 March 2020.

<sup>1</sup> Department of Vascular Surgery, Centre Hospitalier Universitaire Vaudois and University of Lausanne, Lausanne, Switzerland.

<sup>2</sup> Department of Radiology and Medical Informatics, University of Geneva, Geneva, Switzerland.

<sup>3</sup> Center for Biomedical Imaging (CIBM), Geneva, Switzerland.

<sup>4</sup> Visceral and Transplant Surgery, Department of Surgery, Geneva University Hospitals and Medical School, Geneva, Switzerland.

<sup>5</sup> Division of Clinical Pathology, Department of Pathology and Immunology, Geneva University Hospital and Medical School, Geneva, Switzerland.

<sup>6</sup> Department of Surgery, University of Maryland School of Medicine, Baltimore, MD, USA.

<sup>7</sup> Faculty of Science and Medicine, Section of Medicine, University of Fribourg, Switzerland.

This work was supported by the Swiss National Science Foundation to J.-M.C., F.L. (SNSF 320030-182658), and A.L. (SNSF PZ00P3-185927) as well as the Mendez National Institute of Transplantation, and the Leenards Foundation to A.L.

The authors declare no conflicts of interest.

A.L., A.K., J.S., T.A., L.B., J.-M.C., and F.L. participated in research design. A.L., A.K., R.M., and F.L. participated in the writing of the article. A.L., A.K., J.S., T.A., A.N., R.R., S.M., R.M., J.-M.C., and F.L. participated in the performance of the research. A.N., R.R., S.M., and F.L. contributed new reagents or analytic tools. A.L., A.K., J.S., T.A., S.M., R.M., L.B., J.-M.C., and F.L. participated in data analysis.

Correspondence: François Lazeyras, PhD, Hôpitaux Universitaires de Genève, Service de Radiologie, CIBM Rue Gabrielle-Perret-Gentil 4, CH, 1211 Genève 14, Switzerland. (francois.lazeyras@unige.ch).

Copyright © 2020 Wolters Kluwer Health, Inc. All rights reserved.

ISSN: 0041-1337/20/1049-1825

DOI: 10.1097/TP.00000000000003323



methods, and useful predictors of outcome that incorporate tissue viability are urgently needed.

The importance of energy metabolism, by which living cells acquire, and use the energy needed to stay alive, during organ transplantation has been duly acknowledged.<sup>8</sup> Consequently, current methods of organ preservation aim to preserve the energy machinery<sup>9</sup> and reduce the rate energy depletion.<sup>10</sup> The consensus is that a period of warm ischemia (>30 min in human kidney<sup>11</sup>), primes the tissue for subsequent damage upon reperfusion. During ischemia, ATP depletion disrupts mitochondrial Na<sup>+</sup>/K<sup>+</sup> ion channels, which reduce mitochondrial membrane potential and increase mitochondrial inner membrane permeability, influx of calcium ions, and subsequent swelling of mitochondria.<sup>12</sup> Once energy levels have fallen beyond a critical point, the resulting injury is irreversible.<sup>13</sup> Respiratory defects were identified as early events of injury during preservation<sup>13</sup> and after ischemia-reperfusion.<sup>14</sup> In livers, ATP content correlated with transplant outcome.<sup>15,16</sup> Unfortunately, clinical applicability of ATP measurement has been limited by time-consuming, invasive, and costly methods of ATP analysis.<sup>9</sup>

Magnetic resonance imaging (MRI) is well established as a clinical diagnostic modality. Kidney perfusion can be assessed by dynamic MRI using the first passage of Gadolinium (Gd)-chelate bolus.<sup>17</sup> Abnormal Gd uptake may also reflect arterial stenosis, glomerular filtration dysfunction,<sup>18</sup> and ischemia.<sup>19</sup> In addition to imaging the hydrogen nucleus, MRI enables detection of high-energy phosphate metabolites (<sup>31</sup>P MRI [pMRI] spectroscopy), such as ATP, phosphomonoesters (PMEs, that contain the ATP precursor AMP), phosphodiester, and phosphocreatine. Therefore, this method could be particularly suitable for monitoring tissue function and graft viability during transplantation.

Here, we demonstrate that using pMRI, ATP can be quantified ex vivo in kidney graft. Importantly, kidney ATP levels significantly correlated with graft Gd perfusion, and tissue injuries after warm ischemia. Thus, pMRI could facilitate rapid, and accurate assessment of kidney viability, with the hope to predict survival of kidney recipients.

## MATERIALS AND METHODS

### Ex Vivo Hypothermic Oxygenated Pulsatile Perfusion

Kidneys were perfused by a homemade MRI-compatible machine with Belzer MPS UW Machine Perfusion Solution, and kept at 4°C for up to 22 h. All of the experiments were performed in presence of oxygen (100 kPa), as we previously demonstrated that the ability of the kidney to generate ATP relies on sufficient oxygenation.<sup>20</sup> The perfusion module, and its cooling box were MRI compatible. During the MRI acquisition, the control module was kept outside of the Faraday cage and was connected through the wall with an “umbilical cord,” that ensured adequate kidney oxygenation (Figure 1) and pulsatile perfusion. Systolic and diastolic pressure were set at 50 and 15 mmHg, respectively. Measurements were performed on a multi-nuclear Prisma-fit 3T whole-body MRI scanner (Siemens, Erlangen, Germany). Kidney localization was performed with a T2-weighted sequence (turbo spin echo, repetition time (TR) 5000 ms, echo time (TE) 108 ms, 3-mm slices).

### Gadolinium Perfusion

Gd perfusion enables the observation of the internal distribution of the flow between the cortex and the medulla. Low molecular weight Gd has a predominant renal elimination by glomerular filtration without any tubular secretion or reabsorption. Having a similar pharmacokinetics as tracer, they allow glomerular filtration rate assessment with MRI. The perfusion-descending cortical slope (DS) is evaluated with the elimination of the Gd using the angle between the maximum signal value in the cortex and the lowest intensity point at the end of the flushing (around 200s).<sup>21</sup> In this study, 5 mL (0.025 mmol/mL) Gd-diethylenetriaminepentaacetic acid bolus injection was used for the renal perfusion (at 4°C), followed by a 20-mL flush of MP Belzer. The perfusion is a fast sequence, as data were collected using a dynamic 2D saturation-prepared turbo flash sequence with the scanner body coil. This sequence has an inversion time of 240 ms, a flip angle of 12°, 1.0 mm × 1.3 mm resolution, 5 slices of 5 mm (1-mm gap), TR 460 ms, and a TE of 1.3 ms.

### <sup>31</sup>P Magnetic Resonance Imaging Spectroscopy

pMRI was performed with a single-loop coil tuned at 49.5 MHz, which was part of the perfusion machine, as it was fixed at the bottom of the perfusion tank. The coil was interfaced with a specially designed transceiver that allows both <sup>1</sup>H imaging and <sup>31</sup>P spectroscopy (Clinical MR Solutions, Brookfield, WI). The field homogeneity was optimized with automatic shimming over the kidneys. pMRI consisted of 3D spatial encoding, with a field of view 250 mm × 250 mm × 160 mm, matrix size 16 × 16 × 8, nominal spatial resolution 15.6 mm × 15.6 mm × 20 mm, TR 1.0 s, flip-angle 45°, echo delay 0.6 ms, bandwidth 4000 Hz, 2k sampling points. Elliptical encoding with 32 weighted averages, resulted in an acquisition time of 45 min. Chemical shift signal was referenced to the inorganic phosphate (Pi) resonance at 5.2 ppm, which can be considered homogeneously distributed over the surface of the coil. A frequency offset of -500 Hz was used to center excitation pulse bandwidth over ATP frequency range. Afterward, the spectrum was processed with a 20-Hz exponential time filter, and order 0 and 1 phase corrections. The metabolites (ATP,

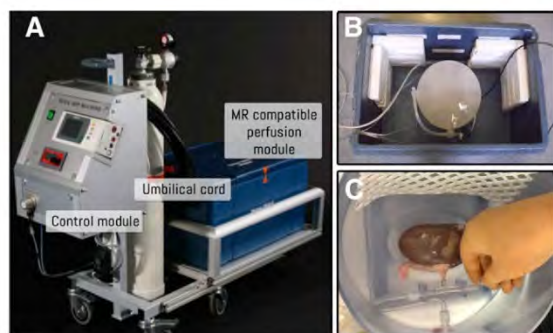


**FIGURE 1.** The homemade MR-compatible kidney ex vivo perfusion system. (A) The system is made of a control module to drive the pulsating pump and regulate the oxygenator, a perfusion tank containing the kidney graft, and linked through the umbilical cord. Compatible perfusion module fits in the MRI bore with a maximum size of 40 cm. (B, C) Inside view of the perfusion tank (B) with the kidney artery connected to a cannula (C). MRI, magnetic resonance imaging.



PME, Pi, phosphocreatine) were fitted with Gaussian peaks using the syngo software (SIEMENS, Erlangen, Germany) and were estimated over all the kidneys by averaging pMRI voxels containing kidney tissue (combined voxels resulting in a single spectrum).  $\alpha$ ,  $\beta$ , and  $\gamma$  ATP correspond to the resonances of the  $^3\text{P}$  nuclei contained in ATP. All 3 peak amplitudes are proportional to the ATP concentration but were quantified separately to prevent methodological bias. Indeed the excitation pulse profile might vary over the large frequency range spanned by the 3 peaks, and their quantification might be influenced by overlaps with other metabolite like nicotinamide adenine dinucleotide (NAD) (discussed further in the text). The metabolite concentrations were obtained as previously described.<sup>20</sup> Briefly,  $[\text{}^3\text{P}_m]$ , expressed as mmol/L (mM), was calculated using the following formula:  $[\text{}^3\text{P}_m] = (S_m/S_{\text{bPi}}) \times [\text{}^3\text{P}_{\text{buffer}}] \times C_{\text{sens}}$ , where  $S_m$  and  $S_{\text{bPi}}$  are the mean metabolite and buffer Pi signals (area), respectively.  $[\text{}^3\text{P}_{\text{buffer}}]$  is the buffer phosphate concentration (2.5 mmol/L).  $C_{\text{sens}}$  is the sensitivity correction factor.

### Animals

The study was approved by the University of Geneva animal ethics committee (protocol number: GE/53/14/22826). Five-month-old female pigs were obtained from the animal facility of Arare, Switzerland. All pigs were maintained under standard conditions. Water and food were provided ad libitum. Animals were first premedicated using azaperone (2.2 mg/kg IM), midazolam (1.6 mg/kg IM), and atropine (0.02 mg/kg IM) and anesthetized with ketamine (2–6 mg/kg/h), fentanyl (4–6  $\mu\text{g}/\text{kg}/\text{h}$ ), midazolam (0.2–0.4 mg/kg/h), and atracurium (1 mg/kg/h). Animals were then intubated and ventilated before a nasogastric tube was placed. The arterial line was placed in the internal carotid artery. Monitoring included heart rate, systemic blood pressure, pulse oximetry, and end-tidal  $\text{CO}_2$ . Following a midline incision, the peritoneal cavity was opened, and the bowels were retracted. First, the aorta, vena cava, and renal vessels were prepared. The pigs received 300 UI/kg heparin intravenous injections. Renal arteries and veins were clamped, and the kidneys were either immediately explanted or explanted after 30 and 60 min of warm ischemia (to mimic circulatory arrest during DCD procurement). Kidneys were then instantly flushed with 4°C Institut Georges Lopez-1 preservation solution on ice. Surgical kidney biopsies, including the cortex and the medulla, were formalin fixed and embedded in paraffin. The renal artery was cannulated, and the kidneys were cold perfused using our MR-compatible machine (Figure 1) before imaging. Pigs were sacrificed using 100 mEq of potassium chloride intravenous injections.

### Histopathological Analysis of Biopsies

Sections of 3- $\mu\text{m}$  thickness were prepared from formalin-fixed kidney biopsies and stained with silver Jones and Periodic Acid-Schiff. Histopathological analysis score was performed based on those described by Goujon et al<sup>22,23</sup> using Osirix software (www.osirix-viewer.com) and modified as previously described.<sup>22,24</sup> Four different representative fields were assessed and blinded to group assignment. Lesion severity was graded 0–5 according to the following criteria: no abnormality (0), mild lesions affecting, respectively, 1%–10% (1), 10%–25% (2), 25%–50% (3),

50%–75% (4), and >75% (5) of the sample surface. The final score for each biopsy ranges from 0 to 30. A higher score corresponding to the more severe ischemic damage.

### Statistical Analysis

The statistical tests used are defined for each figure in the appropriate legend. A  $P$  value <0.05 was considered statistically significant. Computations were performed using Prism 7 (GraphPad Softwares, San Diego, CA).

## RESULTS

### Kidney ATP Is Rapidly Generated During Ex Vivo Perfusion

Kidneys were perfused using a homemade MRI-compatible, hypothermic-oxygenated pulsatile perfusion machine (Figure 1). During the ex vivo perfusion, kidney metabolites were estimated by averaging pMRI voxels, resulting in a single spectrum (Figure 2A and B). In healthy kidneys (0 min of warm ischemia), pMRI allowed the detection of  $\alpha$ -,  $\beta$ -, and  $\gamma$ -ATP, PME and inorganic phosphate (Pi, Figure 2B). ADP was below the detection threshold. ATP and PME concentration (mM) were extrapolated from their spectra peak area and the buffer phosphate concentration (Pi, 2.5 mmol/L). In absence of warm ischemia, kidney  $\alpha$ -,  $\beta$ -, and  $\gamma$ -ATP, PME remained stable up to 22 h of perfusions (Figure 2C). On the other hand, PME concentration was 4 times higher than ATP at the initiation of the perfusion but gradually declined over time (Figure 2C). This is consistent with the hypothesis that the PME containing AMP signal is utilized over time to generate ATP.

### Warm Ischemia Reduces Kidney ATP Levels

To determine the effect of warm ischemia and to ensure sufficient sensibility of ATP measurement using pMRI in injured grafts, kidneys underwent 0 (control), 30 or 60 min of warm ischemia before retrieval. There was a significant reduction in the amount of  $\beta$ -ATP after 30 min (–48.4%;  $P=0.04$ ) and 60 min (–66.4%;  $P=0.007$ ) of warm ischemia (compared with no warm ischemia, Figure 3A). Similarly,  $\gamma$ -ATP was significantly decreased after 60 min of ischemia (–45.5%;  $P=0.05$ ; Figure 3A).  $\alpha$ -ATP did not significantly decrease, which could be explained by the presence of NAD overlapping at –8.3 ppm (Figure 3A). Since the peak of  $\alpha$ -ATP appears to be “contaminated” by NAD signal, ATP concentration was estimated by averaging  $\beta$ - and  $\gamma$ -ATP only. Compared with control, 60 min of warm ischemia induced a 58.5% fold reduction in total ATP (Student  $t$  test;  $P=0.03$ ). On the other hand, PME concentrations were not altered by warm ischemia (Figure 3B).

### ATP Levels and Kidney Perfusion Correlate With Histological Damage

To establish the relevance of ATP quantification using pMRI, we next examined the correlation with histological damage, as assessed by the Goujon score, which is thought to reflect kidney function.<sup>22</sup> As expected, 30 and 60 min of warm ischemia induced significant histological injuries (Figure 4A). Histological damages were quantified based on the number of tubules lumina with cellular debris, the loss of brush border, tubular dilatation, the percentage of flocculus in Bowman’s capsule, vacuolization, and



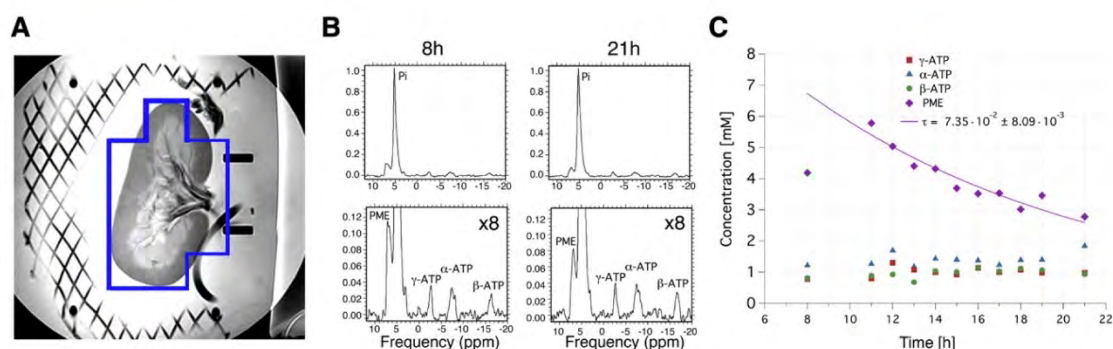


**FIGURE 2.** Representative pMRI spectra, and kidney ATP levels over time. (A) T2 image of a kidney, with the blue border representing the area of combined voxels that are analyzed for metabolite concentration. (B) Representative spectrum of kidney after 8 h (left) and 21 h (right) of hypothermic pulsatile perfusion. (C) Concentration (mM) of the indicated metabolites over time, in pig kidney, after 0 min of warm ischemia, during hypothermic pulsatile perfusion with a fixed  $pO_2$  of 110 kPa. pMRI,  $^{31}P$  magnetic resonance imaging; PME, phosphomonoester.

interstitial edema (Figure 4B), which were all increased by warm ischemia (except for vacuolization, Figure 4B). Of importance, the ability to produce ATP (Figure 4C and D) was tightly correlated with the degree of kidney injury (Figure 4D, Pearson's  $R^2=0.52$ ;  $P<0.001$ ). Histological injury did not correlate with PME levels (data not shown).

Gd perfusion enables the observation of flow between the cortex and the medulla, which was suggested to be altered during injury.<sup>21</sup> Consistent with our previous findings, kidney Gd cortex, and medulla perfusion were altered after 60 min of warm ischemia. This was reflected by a decrease in the DS (Figure 5A). Interestingly, kidney injury assessed using the cortex DS was significantly correlated with kidney ATP and with histological damage (Figure 5B and C; Pearson's  $R^2=0.64$  and  $0.43$ , respectively;  $P<0.001$ ). Thus, combining both ATP and DS measurements might allow the accurate prediction of kidney damage before transplantation.

## DISCUSSION

This study provides a noninvasive method to assess viability of kidneys ex vivo during hypothermic machine perfusion. In particular, the objective assessment of graft damage (eg, resulting from prolonged circulatory arrest,

DCD) could translate into greater utilization of kidney allograft.

Besides being used to reduce the risk of delayed graft function and improved graft survival after kidney transplantation,<sup>25</sup> machine perfusion enables viability testing by offering a dynamic environment. Various parameters have been proposed as predictive biomarkers, ranging from intrarenal resistance, markers of acid-base homeostasis, or lactate production.<sup>26</sup> Interestingly, we observed an exponential decrease of PME during the ex vivo perfusion, suggesting that AMP reserve contained in the PME metabolites is consumed to produce ATP. This is consistent with the idea that the kidneys are functionally and metabolically active in presence of oxygen.<sup>20,21</sup> In addition, there is emerging evidence that oxygenation is an important advantage during hypothermic machine perfusion.<sup>27,28</sup> Oxygen supplementation during organ preservation may drive ATP production through oxidative phosphorylation. Thus, cells can use ATP to sustain metabolic processes that protect from ischemic damage.<sup>29</sup> These further suggest the importance of functional mitochondria and the dependence on oxidative metabolism in healthy kidney. In addition, this suggests that kidney viability depends on the ability to generate ATP and not only the remaining

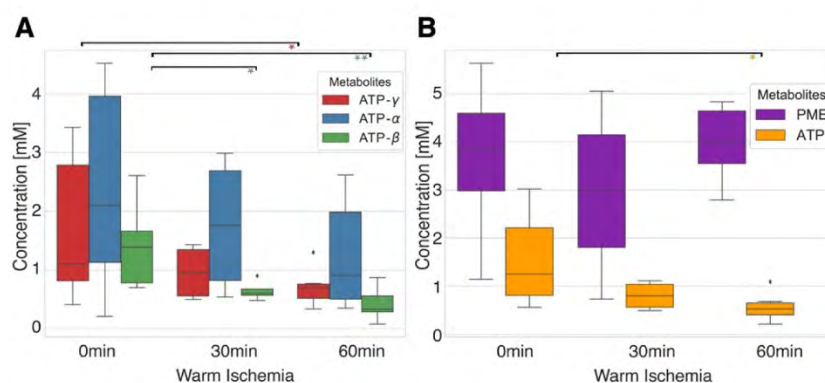


**FIGURE 3.** Kidney metabolite levels after 0, 30, and 60 min of warm ischemia. (A, B)  $\alpha$ -,  $\beta$ -, and  $\gamma$ -ATP expressed individually (A), and  $\beta$ - and  $\gamma$ -ATP combined and PME (B) following 0, 30, or 60 min of warm ischemia.  $n=4-9$  per group. Metabolites levels represent an average throughout perfusion. Error bars indicate SD \* $P<0.05$ , \*\* $P<0.01$ , by 2-way ANOVA. PME, phosphomonoesters.

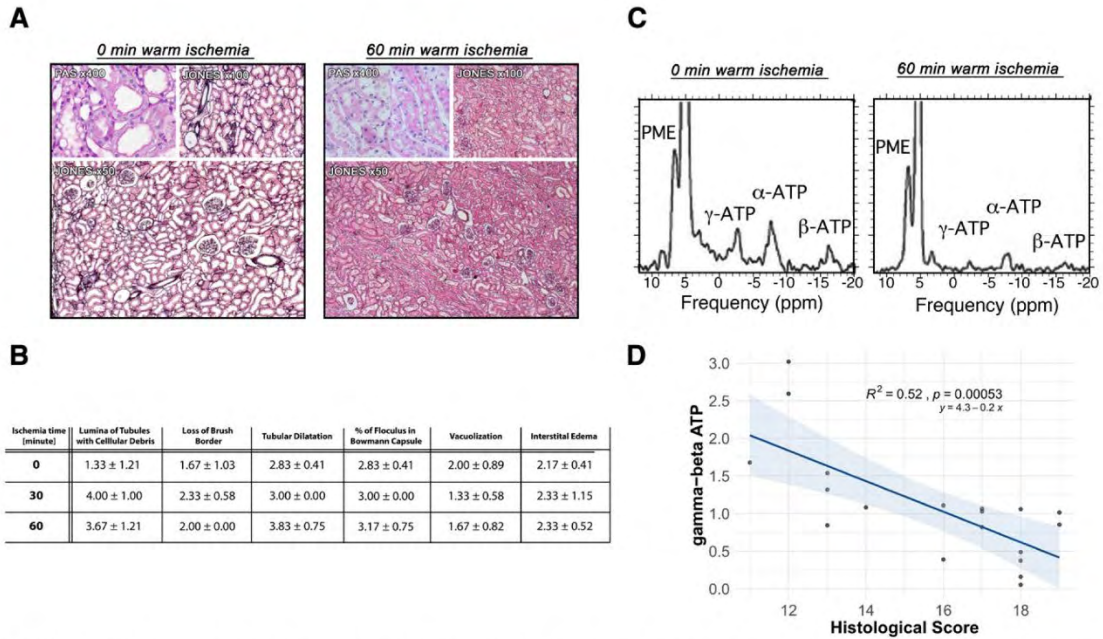


**FIGURE 4.** ATP levels correlate with histological damage. (A) Representative kidney sections stained with PAS or Jones after no (left) or 60 min (right) of warm ischemia. (B) Details of histological scoring after various warm ischemia time as indicated. Data are expressed as mean ± SD. (C) Representative MRI fitting spectra after no (left) or 60 min (right) of warm ischemia. (D) Nonparametric Spearman's correlation between  $\gamma$ - and  $\beta$ -ATP and histological score after 0–60 min of warm ischemia with the coefficient of determination  $R^2$  and  $P$  value. Metabolites levels represent an average throughout perfusion.  $n = 27$ . MRI, magnetic resonance imaging; PAS, Periodic Acid-Schiff; PME, phosphomonoester.

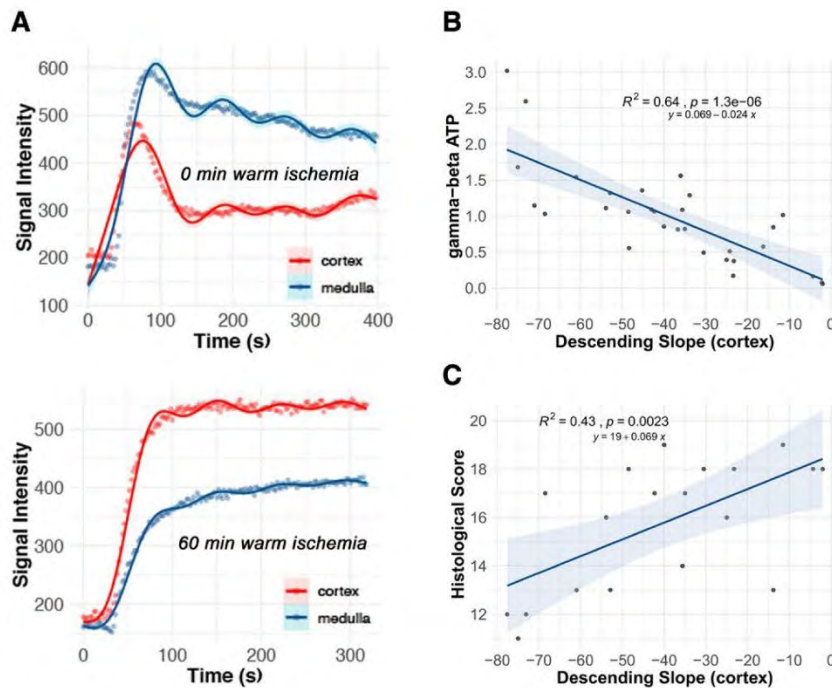


**FIGURE 5.** The perfusion-descending slope (DS) correlates with kidney ATP levels and histological damage. (A) Representative kidney Gd cortex (red line) and medulla (blue line) perfusion after no (top) or 60 min (bottom) of warm ischemia. (B, C) Unparametric Spearman's correlation between kidney cortex perfusion-descending slope, and  $\gamma/\beta$ -ATP (B) and with histological score (C) with their coefficient of determination  $R^2$  and  $P$  value,  $n = 27$ .

Downloaded from http://journals.lww.com/transplantjournal by BMDWFSEPHKAVI2E0UM10N4+KLIHEZGSIH04 XM0h0yMOX1AVWY0pH10H3I3D00DRY7TYSF4C3V1Y0abg9Zx9dGj2MwZLrE= on 08/11/2023



ATP store. Several studies demonstrated that ATP levels correlate with ischemic injury of the kidney<sup>30</sup> and liver.<sup>29</sup> Moreover, ATP is often used as a marker of viability during ischemia.<sup>31,32</sup> In humans, ATP level in liver tissue is an independent predictor of initial graft function.<sup>33</sup> Interestingly, ATP levels measured after transplantation were inversely related to warm ischemia time.<sup>16</sup> Similarly, low ATP levels were significantly associated with primary graft nonfunction.<sup>34</sup> Of importance, the inadequate recovery might be different in various marginal organs. For instance, ATP levels were lower in the DCD and steatotic livers.<sup>9</sup> Despite good correlation with outcome, energy status is difficult to measure, and yet to be used routinely for clinical testing. ATP measurements would be a precious addition to the pretransplant assessment of suboptimal organs, particularly in the setting of uncontrolled DCD procurement, where in the exact maximal donor warm ischemia duration is unknown, which is responsible for a large variation of acceptance criteria between centers.<sup>35</sup>

Our study has several limitations that need to be acknowledged. First, the broader utility of this methodology in determining graft viability should be tested in all form of marginal donor, including kidney from old donor, after acute kidney injury, and after prolonged cold preservation. In addition, we did not correlate ATP levels with kidney function in vivo, or after transplantation, mostly because of local regulation, that did not allow survival surgery. All of the above will hopefully be tested in a future human clinical trial. Although the histological score was not validated in a prospective human cohort, it was previously correlated with the degree of kidney injury.<sup>22-24</sup> The clinical use of pMRI might be limited by the time of acquisition (45 min). However, the acquisition was performed during the hypothermic ex vivo perfusion,<sup>27</sup> and the imaging time could be reduced either by reducing spatial encoding resolution or by using advanced method for fast spatial encoding.<sup>36</sup> In addition, the fitting of  $\alpha$ -ATP with a broad Gaussian probably includes the NAD<sup>+</sup> and NADH signal at  $-8.3$  ppm. Thus, the quantification of the pMRI spectra could be improved for overlapping metabolites, using a model that comprises each metabolite spectrum with multiplet structures. This could for instance allow for the specific detection of NAD<sup>+</sup>/H signal that is weak and overlaps with alpha-ATP peak.<sup>37</sup> Altogether, it is likely that the pMRI process can be integrated within the “normal” cold ischemia period.

In conclusion, pMRI performed on a kidney graft held in an ex vivo perfusion system produced excellent quality spectra. ATP levels and kidney perfusion measurements could accurately predict kidney damage caused by warm ischemia. In an era when up to 45% of ECD kidneys are discarded, this study provides a timely and innovative noninvasive tool to assess kidney viability before transplantation.

## ACKNOWLEDGMENTS

We thank Jean-Pierre Gilberto for his excellent technical assistance.

## REFERENCES

- Hart A, Smith JM, Skeans MA, et al. OPTN/SRTR 2017 annual data report: kidney. *Am J Transplant*. 2019;19(Suppl 2):19–123. doi:10.1111/ajt.15274
- Aubert O, Reese PP, Audry B, et al. Disparities in acceptance of deceased donor kidneys between the United States and France and estimated effects of increased US acceptance. *JAMA Intern Med*. 2019;179:1365–1374. doi:10.1001/jamainternmed.2019.2322.
- Rege A, Leraas H, Vikraman D, et al. Could the use of an enhanced recovery protocol in laparoscopic donor nephrectomy be an incentive for live kidney donation? *Cureus*. 2016;8:e889. doi:10.7759/cureus.889
- Heilman RL, Green EP, Reddy KS, et al. Potential impact of risk and loss aversion on the process of accepting kidneys for transplantation. *Transplantation*. 2017;101:1514–1517. doi:10.1097/TP.0000000000001715
- Sung RS, Christensen LL, Leichtman AB, et al. Determinants of discard of expanded criteria donor kidneys: impact of biopsy and machine perfusion. *Am J Transplant*. 2008;8:783–792. doi:10.1111/j.1600-6143.2008.02157.x
- Port FK, Bragg-Gresham JL, Metzger RA, et al. Donor characteristics associated with reduced graft survival: an approach to expanding the pool of kidney donors. *Transplantation*. 2002;74:1281–1286. doi:10.1097/00007890-200211150-00014
- Dare AJ, Pettigrew GJ, Saeb-Parsy K. Preoperative assessment of the deceased-donor kidney: from macroscopic appearance to molecular biomarkers. *Transplantation*. 2014;97:797–807. doi:10.1097/01.TP.0000441361.34103.53
- Vajdová K, Graf R, Clavien P-A. ATP-supplies in the cold-preserved liver: a long-neglected factor of organ viability. *Hepatology*. 2002;36:1543–1552. doi:10.1053/jhep.2002.37189
- Bruinsma BG, Sricharan GV, Weeder PD, et al. Metabolic profiling during ex vivo machine perfusion of the human liver. *Sci Rep*. 2016;6:22415. doi:10.1038/srep22415
- Miyagi S, Iwane T, Akamatsu Y, et al. The significance of preserving the energy status and microcirculation in liver grafts from non-heart-beating donor. *Cell Transplant*. 2008;17:173–178. doi:10.3727/000000008783906874
- Tennankore KK, Kim SJ, Alwayn IP, et al. Prolonged warm ischemia time is associated with graft failure and mortality after kidney transplantation. *Kidney Int*. 2016;89:648–658. doi:10.1016/j.kint.2015.09.002
- Chouchani ET, PellVR, James AM, et al. A unifying mechanism for mitochondrial superoxide production during ischemia-reperfusion injury. *Cell Metab*. 2016;23:254–263. doi:10.1016/j.cmet.2015.12.009
- van Golen RF, van Gulik TM, Heger M. Mechanistic overview of reactive species-induced degradation of the endothelial glycocalyx during hepatic ischemia/reperfusion injury. *Free Radic Biol Med*. 2012;52:1382–1402. doi:10.1016/j.freeradbiomed.2012.01.013
- Nohl H, Koltover V, Stolze K. Ischemia/reperfusion impairs mitochondrial energy conservation and triggers O<sub>2</sub>• release as a byproduct of respiration. *Free Radic Res Commun*. 1993;18:127–137. doi:10.3109/10715769309147486
- Lanir A, Jenkins RL, Caldwell C, et al. Hepatic transplantation survival: correlation with adenine nucleotide level in donor liver. *Hepatology*. 1988;8:471–475. doi:10.1002/hep.1840080306
- Kamiike W, Burdelski M, Steinhoff G, et al. Adenine nucleotide metabolism and its relation to organ viability in human liver transplantation. *Transplantation*. 1988;45:138–143. doi:10.1097/00007890-198801000-00030
- Grenier N, Pedersen M, Hauger O. Contrast agents for functional and cellular MRI of the kidney. *Eur J Radiol*. 2006;60:341–352. doi:10.1016/j.ejrad.2006.06.024
- Rusinek H, Kaur M, Lee VS. Renal magnetic resonance imaging. *Curr Opin Nephrol Hypertens*. 2004;13:667–673. doi:10.1097/00041552-200411000-00014
- Laiassy JP, Faraggi M, Lebtahi R, et al. Functional evaluation of normal and ischemic kidney by means of gadolinium-DOTA enhanced TurboFLASH MR imaging: a preliminary comparison with 99Tc-MAG3 dynamic scintigraphy. *Magn Reson Imaging*. 1994;12:413–419. doi:10.1016/0730-725x(94)92534-8
- Lazeyras F, Bühler L, Vallee J-P, et al. Detection of ATP by “in line” 31P magnetic resonance spectroscopy during oxygenated hypothermic pulsatile perfusion of pigs’ kidneys. *MAGMA*. 2012;25:391–399. doi:10.1007/s10334-012-0319-6
- Buchs JB, Lazeyras F, Bühler L, et al. The viability of kidneys tested by gadolinium-perfusion MRI during ex vivo perfusion. *Prog Urol*. 2009;19:307–312. doi:10.1016/j.purol.2009.01.004
- Meier RPH, Piller V, Hagen ME, et al. Intra-abdominal cooling system limits ischemia-reperfusion injury during robot-assisted renal transplantation. *Am J Transplant*. 2018;18:53–62. doi:10.1111/ajt.14399

23. Goujon JM, Hauet T, Menet E, et al. Histological evaluation of proximal tubule cell injury in isolated perfused pig kidneys exposed to cold ischemia. *J Surg Res.* 1999;82:228–233. doi:10.1006/jsre.1998.5526
24. Longchamp A, Meier RPH, Colucci N, et al. Impact of an intra-abdominal cooling device during open kidney transplantation in pigs. *Swiss Med Wkly.* 2019;149:w20143. doi:10.4414/smw.2019.20143
25. Moers C, Smits JM, Maathuis MH, et al. Machine perfusion or cold storage in deceased-donor kidney transplantation. *N Engl J Med.* 2009;360:7–19.
26. Kathis JM, Echeverri J, Chun YM, et al. Continuous normothermic ex vivo kidney perfusion improves graft function in donation after circulatory death pig kidney transplantation. *Transplantation.* 2017;101:754–763.
27. Kron P, Schlegel A, de Rougemont O, et al. Short, cool, and well oxygenated—HOPE for kidney transplantation in a rodent model. *Ann Surg.* 2016;264:815–822.
28. Venema LH, Brat A, Nijkamp DM, et al. Factors that complicated the implementation of a program of donation after unexpected circulatory death of lungs and kidneys. lessons learned from a regional trial in the Netherlands. *Transplantation.* 2019;103:e256–e262.
29. Berendsen TA, Izamis ML, Xu H, et al. Hepatocyte viability and adenosine triphosphate content decrease linearly over time during conventional cold storage of rat liver grafts. *Transplant Proc.* 2011;43:1484–1488.
30. Malek M, Nematbakhsh M. Renal ischemia/reperfusion injury; from pathophysiology to treatment. *J Renal Inj Prev.* 2015;4:20–27.
31. de Rougemont O, Breitenstein S, Leskosek B, et al. One hour hypothermic oxygenated perfusion (HOPE) protects nonviable liver allografts donated after cardiac death. *Ann Surg.* 2009;250:674–683.
32. Longchamp A, Mirabella T, Arduini A, et al. Amino acid restriction triggers angiogenesis via GCN2/ATF4 regulation of VEGF and H2S production. *Cell.* 2018;173:117–129.e14.
33. González FX, Rimola A, Grande L, et al. Predictive factors of early post-operative graft function in human liver transplantation. *Hepatology.* 1994;20:565–573.
34. Hamamoto I, Takaya S, Todo S, et al. Can adenine nucleotides predict primary nonfunction of the human liver homograft? *Transpl Int.* 1994;7:89–95.
35. Suntharalingam C, Sharples L, Dudley C, et al. Time to cardiac death after withdrawal of life-sustaining treatment in potential organ donors. *Am J Transplant.* 2009;9:2157–2165.
36. Vidya Shankar R, Kodibagkar VD. A faster PISTOL for 1 H MR-based quantitative tissue oximetry. *NMR Biomed.* 2019;32:e4076.
37. Graveron-Demilly D. Quantification in magnetic resonance spectroscopy based on semi-parametric approaches. *MAGMA.* 2014;27:113–130.



# In vivo magnetic resonance $^{31}\text{P}$ -Spectral Analysis With Neural Networks: 31P-SPAWNN

Julien Songeon<sup>1</sup> | Sébastien Courvoisier<sup>1,2</sup> | Lijing Xin<sup>2,3</sup> | Thomas Agius<sup>4</sup> | Oscar Dabrowski<sup>1</sup> | Alban Longchamp<sup>4</sup> | François Lazeyras<sup>1,2</sup> | Antoine Klausner<sup>1,2</sup>

<sup>1</sup>Department of Radiology and Medical Informatics, University of Geneva, Geneva, Switzerland

<sup>2</sup>CIBM Center for Biomedical Imaging, Geneva, Switzerland

<sup>3</sup>Animal Imaging and Technology, Ecole Polytechnique Fédérale de Lausanne (EPFL), Lausanne, Switzerland

<sup>4</sup>Department of Vascular Surgery, Centre Hospitalier Universitaire Vaudois and University of Lausanne, Lausanne, Switzerland

## Correspondence

Julien Songeon, Département De Radiologie Et Informatique Médicale, University Hospitals Geneva, Rue Gabrielle-Perret-Gentil 4, 1211 Geneva, Switzerland.  
Email: julien.songeon@unige.ch

## Funding information

Schweizerischer Nationalfonds zur Förderung der Wissenschaftlichen Forschung, Grant/Award Number: 320030\_182658

**Purpose:** We have introduced an artificial intelligence framework, 31P-SPAWNN, in order to fully analyze phosphorus-31 ( $^{31}\text{P}$ ) magnetic resonance spectra. The flexibility and speed of the technique rival traditional least-square fitting methods, with the performance of the two approaches, are compared in this work.

**Theory and Methods:** Convolutional neural network architectures have been proposed for the analysis and quantification of  $^{31}\text{P}$ -spectroscopy. The generation of training and test data using a fully parameterized model is presented herein. In vivo unlocalized free induction decay and three-dimensional  $^{31}\text{P}$ -magnetic resonance spectroscopy imaging data were acquired from healthy volunteers before being quantified using either 31P-SPAWNN or traditional least-square fitting techniques.

**Results:** The presented experiment has demonstrated both the reliability and accuracy of 31P-SPAWNN for estimating metabolite concentrations and spectral parameters. Simulated test data showed improved quantification using 31P-SPAWNN compared with LCMoDel. In vivo data analysis revealed higher accuracy at low signal-to-noise ratio using 31P-SPAWNN, yet with equivalent precision. Processing time using 31P-SPAWNN can be further shortened up to two orders of magnitude.

**Conclusion:** The accuracy, reliability, and computational speed of the method open new perspectives for integrating these applications in a clinical setting.

## KEYWORDS

convolutional neural network, deep learning, in vivo, LCMoDel, phosphorus magnetic resonance spectroscopy

This is an open access article under the terms of the Creative Commons Attribution-NonCommercial License, which permits use, distribution and reproduction in any medium, provided the original work is properly cited and is not used for commercial purposes.

© 2022 The Authors. *Magnetic Resonance in Medicine* published by Wiley Periodicals LLC on behalf of International Society for Magnetic Resonance in Medicine.

## 1 | INTRODUCTION

Phosphorus-31 magnetic resonance spectroscopy ( $^{31}\text{P}$ -MRS) is a noninvasive technique that is widely used to probe cellular metabolism *in vivo*.<sup>1,2</sup>  $^{31}\text{P}$ -MRS notably allows to measure high-energy phosphate metabolites that are associated with the metabolic activity of the cell, and represents an alternative method for estimating the intracellular pH.<sup>3-5</sup>  $^{31}\text{P}$ -MRS acquisition displays a lower relative sensitivity than hydrogen-1 ( $^1\text{H}$ ) at a constant magnetic field.<sup>6</sup> Thus, acquisition is usually performed using larger voxel sizes to achieve a sufficient signal-to-noise ratio (SNR), while maintaining an acceptable scan time for the patient. When performed in combination with spatial phase encoding,  $^{31}\text{P}$ -MRS imaging (MRSI) provides a multi-voxels acquisition that maps metabolites across the entire field-of-view (FOV).<sup>7</sup> As the current resolution is still a limitation for clinical applications, there has been increasing interest in achieving efficient quantification, while improving the spatial resolution.<sup>8-10</sup>

In recent decades, advances in computing power and parallelization capability have resulted in the rapid development of a wide variety of machine learning algorithms. These performance improvements along with the renewed interest in the field have broadened its scope of application.<sup>11</sup> One popular deep learning (DL) technique has so far been the convolutional neural network (CNN). CNNs are employed to detect and extract structural relationship features from data samples. This general characteristic is used for many applications, including visual and speech recognition, localization, segmentation, and general regression analysis, as well as classification.<sup>12</sup> The method requires a labeled training dataset that must be representative of the actual data to be analyzed. For some applications, the labeled dataset can be generated by simulation so as to create a training set of arbitrary size. Once trained, the CNN model is able to process large datasets within a short time without further adjustments.<sup>13</sup>

The widely used method of reference in this field, LCModel, is an a priori knowledge software for MRS fitting and quantification. The software performs a nonlinear optimization in order to fit the data with a linear combination of reference basis spectra, as well as to estimate spectral parameters, including line shape, phase, and chemical shift of the metabolites. However, the method requires non-negligible computing time and may thus be limited in quantifying low SNR spectra.<sup>14</sup> While the software has been originally developed to fit  $^1\text{H}$ <sup>15</sup> spectra, researchers were able to extend its use further in order to analyze carbon-13 ( $^{13}\text{C}$ )<sup>16</sup> and  $^{31}\text{P}$ <sup>17</sup> spectra.

CNNs are increasingly employed for medical image analysis such as MRI.<sup>18-21</sup> Preliminary application of machine learning<sup>14,22</sup> and CNN<sup>23-26</sup> in proton MRSI

revealed high robustness to noise. In addition, CNNs can be applied in order to perform concentration quantification.<sup>23</sup> Application of CNN to  $^1\text{H}$ -MRS has demonstrated this method to display equal or better level of performance, while having a faster computational time than current standard MRS metabolites quantification methods like LCModel.<sup>24</sup>

Whereas current methods for estimating metabolite concentration in MRS primarily rely on spectral fitting with residual least-square minimization, we have herein proposed an alternative approach using 31P-SPAWNN. Its objective function is based on residual minimization of the spectra parameters (i.e., metabolite concentrations). A spectrum can be reconstructed based on these estimates, which must, however, not be confused with a spectrum fitting.

Using our proposed 31P-SPAWNN method, we have demonstrated its feasibility and reliability in accurately quantifying  $^{31}\text{P}$ -MRS related metabolite concentrations and spectral parameters, even at low SNR, obtained on both simulated and *in vivo* data. The current study describes SPAWNN's architecture, and the generation of simulated datasets for supervised learning, as well as the reconstruction based on the physical model for comparison with fitted spectra. A performance evaluation is provided based on a comparison of our model with LCModel using simulated datasets. Lastly, we present the results using our proposed technique on the  $^{31}\text{P}$ -MRS *in vivo* and brain data acquired on a 3 tesla (T) clinical MRI.

## 2 | THEORY

### 2.1 | Generation of simulated spectra

The simulation of spectra must incorporate an extensive set of parameters in order to faithfully mimic the measured MRS spectra. The signal of a metabolite is the combination of multiple resonance modes,  $M_m(t)$ , based on the NMR parameters observed *in vitro*.<sup>27</sup> The complex magnetization of a molecule of metabolite  $m$  at time  $t$  after an excitation RF pulse can be calculated based on the expected value of the spin-raising operator for the corresponding coupled-spin system<sup>28(p. 158-165)</sup>

$$M_m(t) = \sum_n^{\text{modes}} A_{m,n} \cdot e^{i\phi_{m,n}} e^{2\pi i \psi_{m,n}}, \quad (1)$$

where  $n$  is the transition index between energy states within the density matrix formalism, which we refer to as "mode".  $A_{m,n}$  is the transition amplitude,  $\phi_{m,n}$  the phase modulation (e.g., due to J-coupling),  $\psi_{m,n}$  the transition frequency (chemical shift) of the  $n^{\text{th}}$  mode, and  $i$  is the



imaginary unit. A mode corresponds to a singlet resonance or one of the multiplet resonances observed in the frequency domain, such as the phosphocreatine (PCr) singlet, the  $\alpha$ -adenosine triphosphate (ATP) doublet, or the  $\beta$ -ATP triplet. The spectroscopic signal (FID)  $S_j(t)$  of a sample is a linear combination of all the metabolite time domain signals. A spectrum of index  $j$  versus time can be written as follows

$$S_j(t) = e^{i\Phi_j^0} \sum_m^{\text{metabolites}} C_{m,j} M_m(t + \Delta t_j) \cdot e^{2\pi i \Psi_{m,j}} e^{-(L_{m,j} + i^2 G_{m,j}^2)} + B_j(\Delta t_j) + c_j(t), \quad (2)$$

where  $\Phi_j^0$  is the zeroth-order phase and  $C_{m,j}$  is the concentration of the  $m^{\text{th}}$  metabolite, which multiplies the corresponding  $M_m(t)$  metabolite time series signal.  $\Psi_{m,j}$  corresponds to the chemical shift variation specific to the  $m^{\text{th}}$  metabolite. In the context of an excite-acquire acquisition scheme (FID-MRS, FID-MRST),  $\Delta t_j$  represents the acquisition delay time between the RF pulse and the beginning of the signal acquisition. This delay is associated with the first-order phase of the spectrum.  $L_{m,j}$  and  $G_{m,j}$  correspond to the Lorentzian and Gaussian parameters that combine into a Voigt linewidth  $V_{m,j}$ .  $c_j(t)$  is the noise, while  $B_j(t)$  is a baseline created by the sum of multiple Gaussian components, computed as follows

$$B_j(t) = \sum_k^{\text{no. of Gaussian components}} \xi_k \cdot e^{i\alpha_k} e^{2\pi i t \beta_k} e^{-t^2 \gamma_k^2}, \quad (3)$$

where  $\xi_k$  is the amplitude,  $\alpha_k$  is the zero-order phase,  $\beta_k$  is the frequency shift, and  $\gamma_k$  is the width of one component. The time domain signal  $S_j(t)$  is finally Fourier transformed in order to obtain the simulated spectrum used as input for either the SPAWNN or LCMModel approaches that are described below.

## 2.2 | Convolutional neural networks architectures

For our proposed SPAWNN method, we have combined two different CNN models, one being a variant of a LeNet-5 model<sup>29</sup> and the other being based on a U-Net model.<sup>30</sup>

LeNet-5, which is one of the most common neural network models, is widely used for classification and regression.<sup>31</sup> LeNet-based CNNs have been applied in the spectroscopy field.<sup>25,32,33</sup> The model consists of consecutive convolution layers that encode the data into features, and it is terminated by fully connected layers. Each convolution layer convolves the output of the previous layer using different filters, while extracting at each step higher-level

features and patterns.<sup>34</sup> Fully connected layers enable nonlinear relationships between features and extraction of targeted information. This SPAWNN-Quantification (SPAWNN-Q) model takes the Fourier transform of  $S_j(t)$  from Equation (2) as input, and it returns a finite number of target values. Our proposed approach uses the SPAWNN-Q model in order to estimate the metabolite concentrations, as well as the values of spectral parameters like  $\Phi_j^0$  or  $\Delta t_j$  from Equation (2).

The U-Net combines both low-level detail information and high-level semantic information.<sup>35</sup> This type of model that is mainly used for segmentation purposes<sup>30</sup> finds applications in MRS.<sup>36,37</sup> The model has been successfully applied to medical image classification, segmentation, and detection tasks.<sup>38</sup> The U-Net type model's architecture is first composed of an encoding part, and then of a decoding part. The contracting part uses a series of convolutional and down-sampling layers to extract information in features, while the expanding part then performs a series of up-sampling in order to recover the initial input's dimension.<sup>30</sup> At each up-scaling step, the U-Net performs a concatenation between the upscaled layer and the corresponding layer of the contracting part, allowing for higher resolution and less encoded information to be mixed in the subsequent decoding. Our SPAWNN-Baseline (SPAWNN-BL) U-Net model estimates the baseline, taking as input the Fourier transform of  $S_j(t)$  from Equation (2) and returning the estimated baseline  $B_j(t)$  from Equation (3).

## 3 | METHODS

### 3.1 | Spectra simulation and training dataset

The following metabolites have been included in the simulated spectra: phosphocreatine (PCr), inorganic phosphate (Pi), membrane phospholipids (MP), adenosine triphosphate ( $\alpha$ -ATP,  $\beta$ -ATP, and  $\gamma$ -ATP), and nicotinamide adenine dinucleotide (NAD+ and NADH). In addition, the phosphomonoesters (PME), composed of phosphocholine (PC) and phosphoethanolamine (PE), and the phosphodiester (PDE), composed of glycerophosphocholine (GPC) and glycerophosphoethanolamine (GPE), were also included. Spectra were simulated with this 12-metabolite set, as previously described in the theory section. The resulting dataset consisted of  $10^6$  simulated spectra for training,  $10^4$  simulated spectra for validation, and  $10^4$  simulated spectra for testing. Generating the training dataset took 1.5 h. The generated spectra were set to reproduce the experimental conditions at a 3T field strength, using spectra made from discrete time series of 2048 points with a dwell time of 0.25 ms, corresponding to a 4000 Hz

bandwidth ranging from  $-40$  to  $40$  ppm centered at the PCr resonance.

The structural modes of each metabolite multiplet were calculated by means of a density matrix simulation using GAMMA software library, including  $^{31}\text{P}$ - $^{31}\text{P}$  J-coupling ( $J_{pp}$ ) as appropriate, while yielding the mode amplitude, the resonance frequency and the phase according to Equation (1).<sup>39</sup> Homonuclear values of  $J_{pp}$  were found using the previously reported values of chemical shift and J-coupling.<sup>17</sup> Each metabolite time series was then multiplied by a concentration value  $C_m$  chosen following a normal distribution with a mean value of 1 and a standard deviation of 5, and taking account of its absolute value so as to impose positive concentration values.

Each Fourier transform  $S_j(t)$  of the Equation (2) was generated from randomly chosen parameters. The following parameters were chosen using a uniform probability distribution:  $\Phi^0 \in [0, 2\pi]$  rad,  $\Delta t \in [0, 0.6]$  ms, and  $\Psi \in [-20, 20]$  Hz. Each of the metabolites was chemically shifted within a range of  $\pm 16$  Hz, in addition to the chemical shift  $\Psi$  of the spectrum. The Voigt linewidth was set between 1 and 80 Hz, before being decomposed into a Lorentzian  $L$  coefficient and a Gaussian  $G$  coefficient. Given that the  $B_0$  inhomogeneity was the same for all metabolites, the linewidth was assumed to reflect a T2 effect, so PCh, PE, GPE, and GPC were grouped with the same linewidth coefficients values. ATPs were grouped together, as were NAD+ and NADH, while Pi, PCr, and MP all displayed their independent T2 values. The value of  $\phi_{m,n}$  turned out to be negligible and was thus set to zero as our data were acquired with an excite-acquire sequence.

The baseline  $B$  was a sum of 30 Gaussian components. Each Gaussian function exhibited four random parameters, chosen with a uniform probability distribution. The amplitude ranged from 0 to the spectrum's maximum amplitude. The Gaussian displayed the zero-order phase between 0 rad and  $2\pi$  rad, along with a frequency shift to cover the spectrum's 80 ppm range, and a linewidth with

a minimum value of 300 Hz. The noise  $e$  was simulated as a complex white noise, exhibiting a normal distribution centered around zero, and with a scaled deviation to the metabolite spectrum's energy so as to reach SNR values between 0.5 and 20. SNR was therefore defined as the ratio metabolite signals' mean value to the standard deviation of the noise. As all metabolites contributed to the SNR in our definition, we labeled  $\text{SNR}_{\text{mean}}$  for SPAWNN. This definition was useful upon developing the neural network for generating noise in the simulated dataset with the broad metabolite concentration variation.

The neural network was trained using a generated data set with specific parameter ranges, including spectrum frequency shift, metabolite chemical shifts, and linewidth. A trained network was then able to accurately estimate these parameters within the simulation ranges. For example, given that the range of metabolite chemical shifts was between  $-16$  and  $+16$  Hz, the neural network's estimation in an in vivo spectrum is anticipated to be accurate, provided that the actual metabolite chemical shifts are within this range.

### 3.2 | Convolutional neural network

All the networks were trained on  $10^6$  simulated spectra. The regression loss function was calculated based on the mean squared error (MSE) function, and we used Adam as an optimized gradient descent algorithm.<sup>40</sup> Figure 1 illustrates the flowchart of our method with the input data preparation and the different neural networks. The CNNs were trained on spectra ranging from 10 to  $-25$  ppm, corresponding to the in vivo metabolites chemical shifts range. With a resolution of 25.6 points/ppm, the frequency windowing of the spectrum corresponded to an array of 899 complex points. Prior to the input, each spectrum was normalized with respect to its energy, following which complex values were represented by two-channel arrays of 899 points.

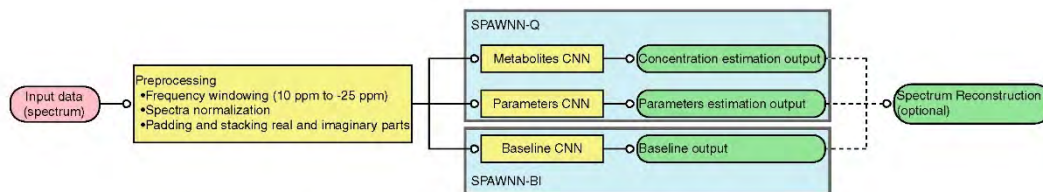


**FIGURE 1** Data analysis flowchart illustrating the different steps of the Spectral Analysis With Neural Networks (SPAWNN) pipeline. The method uses three convolutional neural networks (CNN) to estimate the metabolite concentrations, spectrum parameters, and baseline. Data preparation consists of spectrum normalization, with windowing over the range of 10 to  $-25$  ppm. Padding (mirror replication of the first and last 5 points of the array) and stacking of the real and imaginary parts (switch from a complex array of  $1 \times 899$  points to a real array of  $2 \times 909$  points by separating the real and complex part of each point) were then applied.



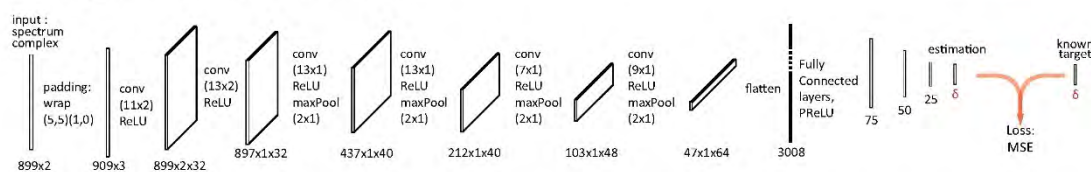


FIGURE 2 SPAWNN-Quantification (SPAWNN-Q) model architecture for metabolite concentration and parameter estimation. The convolutional neural network takes the spectrum as an input layer and performs six successive steps of convolution, ReLU activation, and pooling. Then, the five final steps are fully connected layers with PReLU activation.  $\delta$  is equal to 20 for the parameters, and 14 for the metabolite concentration estimations.

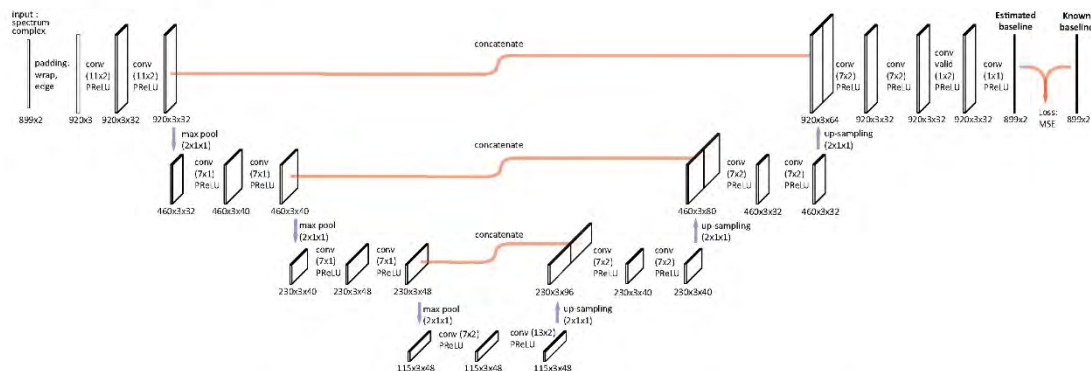


FIGURE 3 SPAWNN-Baseline (SPAWNN-BI) model architecture for baseline estimation. The U-Net takes the spectrum as an input layer and performs three down-sampling steps with convolution and PReLU activation. Then, it performs three up-scaling steps with convolution and PReLU activation. At each up-scaling, the new layer is concatenated with the corresponding down-sampling layer. The output is the estimation of the baseline and has the same dimension as the input.

The first two CNNs, which were inspired by a LeNet-5 model, were designed to assess metabolite concentration quantification and parameter estimation, as shown in Figure 2, with a network's output represented by  $\delta$ , as the number of targeted values returned by SPAWNN. For the metabolite concentration estimation, SPAWNN was trained to estimate the concentration of the 12 metabolites listed in section (III.A), along with adding the sum of PME and PDEs, whereby the metabolite concentration estimation returned 14 values. The second CNN was trained to estimate the values of 28 spectral parameters, including zero-order phase, time delay, spectrum frequency shift, metabolite chemical shifts, Voigt linewidths, Gaussian linewidths, and  $\text{SNR}_{\text{mean}}$ . The Lorentzian linewidths were then calculated with the Voigt and Gaussian values using the pseudo-Voigt approximation.<sup>41</sup> The CNNs were implemented in Python (3.6.9) using the libraries TensorFlow (2.2.2) and Keras (2.4.3). The networks were trained on 80 epochs with 800 spectra per mini-batch. There were about  $3 \cdot 10^5$  parameters to

train, with the training time taking less than 2 h on the GPU (NVIDIA Titan V).

The third network was a U-Net model, as shown in Figure 3. The network was able to estimate the input spectrum's baseline, returning an array of the same size (899 complex points). The U-Net was trained on 50 epochs with 500 spectra per mini-batch. There were about  $4 \cdot 10^5$  parameters to train, with the training time taking around 6 h.

### 3.3 | LCModel

As reference for comparison, we have analyzed all <sup>31</sup>P-spectra using LCModel (Version 6.3-1L).<sup>42</sup> The basis spectra were simulated using the GAMMA software library<sup>39</sup> using the same physical model as for the simulated data for SPAWNN. The metabolites included in the basis were the 12 metabolites described above. Since phosphorus spectra were centered on the PCr peak at 0 ppm,

the reference peak was set at 15 ppm (PPMK = -15) for generating the basis set. The basis was created using a fixed linewidth of 5 Hz, with the LCMoDel parameters: DEEXT2 = 15 and DESDT2 = 10. For LCMoDel fitting, Pi and  $\gamma$ -ATP were chosen as reference metabolites, resulting in the following parameters: CHUSE1 = 'Pi', 'gATP' and PPMREF(1,2) = 5. We set SDDEGP = 50 and SDDEGZ = 50 to enable LCMoDel to find the correct zero- and first-order phases. The other parameters used were the same as those reported by Deelchand et al.<sup>17</sup>

### 3.4 | Magnetic resonance spectroscopy protocol

In vivo measurements were performed on a clinical Prisma-fit 3T MRI scanner (Siemens Healthineers, Erlangen, Germany) equipped with multinuclear capabilities. Data were obtained from 10 healthy volunteers. Written informed consent was given by all the volunteers before participation and the study protocol was approved by the institutional ethics committee. No decoupling was applied during the phosphorus acquisition. Anatomical reference <sup>1</sup>H images were obtained with T1-weighted MP-RAGE acquisition. The volunteers were scanned using a dual-tuned <sup>1</sup>H and <sup>31</sup>P head coil (Clinical MR solutions, Brookfield, WI.)

The unlocalized FID sequence consisted of a rectangular excitation pulse of 0.25 ms with a flip angle of 45°. The repetition time (TR) was set at 1500 ms, and the echo time (TE) was 0.35 ms with 32 averages. The bandwidth was 4000 Hz for 2048 sampling points. The acquisition took about 1 min. For three volunteers out of 10, another unlocalized FID was obtained using the same parameters, yet with 600 averages.

The 3D <sup>31</sup>P-MRSI was acquired on the whole brain with a 10 × 10 × 10 matrix. The FOV dimension was 250 mm isotropic for a nominal spatial resolution of 25 mm isotropic. The sequence consisted of a rectangular excitation pulse of 0.25 ms with a flip angle of 45°. The repetition time (TR) was set at 1500 ms, and the echo time (TE) was 0.5 ms with 24 weighted averages.<sup>43</sup> The bandwidth was 4000 Hz for 2048 sampling points. The acquisition took 37 min.

### 3.5 | Spectrum processing

The in vivo FID data were extracted from the MRI raw data format. Averages and Fourier transforms were calculated using a Python script (Python Software Foundation, version 3.6.9), and the data were converted to Hierarchical Data Format (HDF5). No

preprocessing was applied to the spectra prior to analysis.

### 3.6 | Data analysis and statistic

The results estimated on the simulated dataset were analyzed using the coefficient of determination  $R^2$ .<sup>44</sup> To compute the variability of the coefficient of determination, bootstrap statistics was performed on the data.<sup>45</sup> The bootstrapping was performed by selecting randomly spectrum subsets with replacement and repeated computation of  $R^2$  on these subsets. This evaluation was repeated 2000 times in order to compute the probability distribution of  $R^2$ .

Concerning volunteer data, no reference measurement was available to correct for variation of B1 and signal intensity, allowing absolute concentration estimation. Both methods, LCMoDel and SPAWNN, returned normalized concentration values that were within a constant, yet unknown, factor of the actual concentration value. The results were presented and analyzed as metabolite concentration ratios, since the ratio of two metabolites is independent of the scaling factor.<sup>46</sup>

The computational analysis was performed using Python.

## 4 | RESULTS

Results of simulated data are shown in Figure 4. An example of a simulated spectrum with three decreasing SNR<sub>mean</sub> (no noise added, 4, 2) is presented in panel (A). For illustration purposes, the simulated spectra shown in the figure do not contain baselines, phase or frequency shifts, and significant linewidth. Panel (B) illustrates the performance of SPAWNN and LCMoDel with the coefficient of determination  $R^2$  and bootstrapping. The performance was assessed on another test set of 10<sup>4</sup> spectra that were independent of the training dataset and never evaluated by the model before. The bootstrap statistics was computed using random spectra subset selection with replacement and repetition of the analysis 2000 times. The results showed similar to slightly better performance of SPAWNN compared with LCMoDel for the quantifying Pi, ATPs, PCr, PE, PCh, and GPE, with similar or higher  $R^2$  values and smaller variance. Since LCMoDel displayed strong pairwise correlations between NAD<sup>+</sup> and NADH, the total NAD (tNAD) concentration was computed for both methods for comparison purposes. The performance of SPAWNN in quantifying tNAD ( $R^2 = 0.813 [\pm 0.005]$ ) was comparable to that of other metabolites, whereas the results of LCMoDel were less accurate ( $R^2 = 0.771 [\pm 0.006]$ ). GPC concentration was



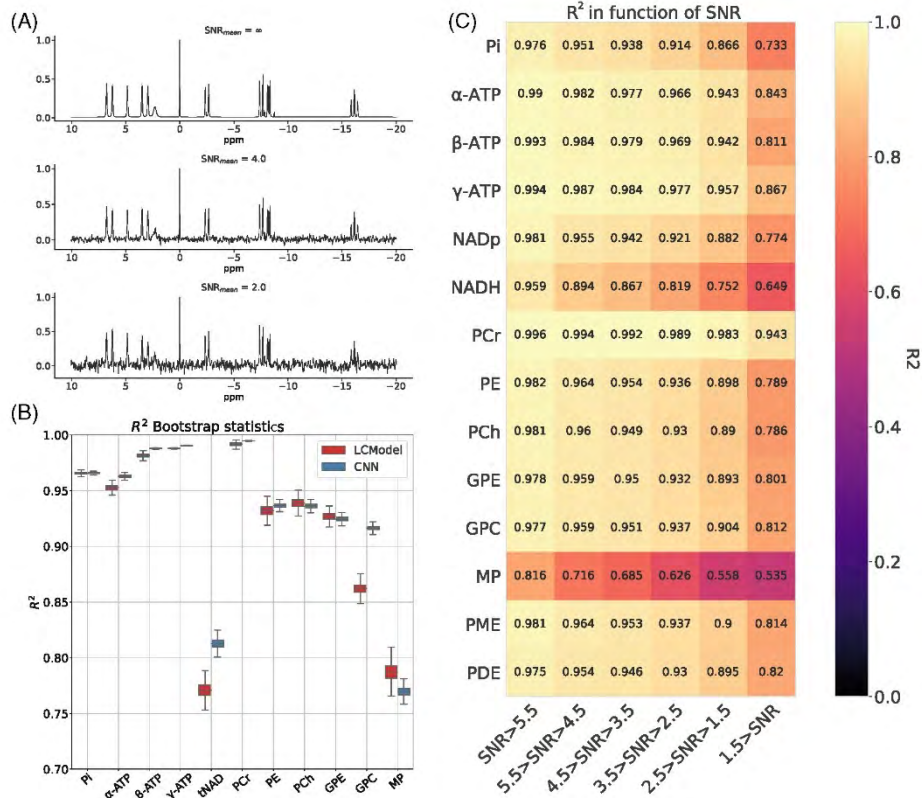


**FIGURE 4** Results on simulated data. (A) Examples of  $\text{SNR}_{\text{mean}}$  for a simulated spectrum with no noise (top),  $\text{SNR}_{\text{mean}}$  of 4 (middle), and  $\text{SNR}_{\text{mean}}$  of 2 (bottom). (B) Comparison of the coefficient of determination  $R^2$  with bootstrapping between SPAWNN and LCMoDel for each metabolite. A new dataset of  $10^4$  spectra was created to compare the two methods. (C) SPAWNN's coefficient of determination  $R^2$  for each metabolite concentration estimation as a function of the  $\text{SNR}_{\text{mean}}$  range.

better estimated with SPAWNN ( $R^2 = 0.916 [\pm 0.002]$ ) than LCMoDel ( $R^2 = 0.862 [\pm 0.005]$ ). Regarding MP estimation, both SPAWNN ( $R^2 = 0.770 [\pm 0.004]$ ) and LCMoDel ( $R^2 = 0.787 [\pm 0.008]$ ) exhibited a low performance compared with all other metabolites, regardless of SNR bins (Figure 4C). Figure 4C shows the SPAWNN's coefficient of determination  $R^2$  for each metabolite concentration estimation as a function of SNR range. The evaluation was performed on the simulated test dataset of  $10^4$  spectra, separated in SNR bins with increment of 1. The coefficient of determination  $R^2$  was computed on the entire test dataset between the model evaluation concentration and the ground truth. For all the metabolites, the value of the coefficient of determination decreased with SNR. Most metabolites had an  $R^2$  value greater than 0.8 for all SNR bins. SPAWNN-BI evaluation of the test set baseline yielded a coefficient of determination of  $R^2 = 0.97$  calculated between the pairwise correlation of the true baseline and the estimated baseline.

Analyzed  $^{31}\text{P}$ -MRSI in vivo data are shown in Figure 5 for SPAWNN (left) and LCMoDel (right). The data displayed are the sum of 8 voxels from the occipital cortex of one of the volunteers. The top plots are the spectra with either the reconstruction or the fit from each model. The middle plots are the residuals and the bottom plots show the signals for each metabolite separately. For SPAWNN, reconstruction of a spectrum was performed by using the estimated baseline, parameters, and concentration values, and by recreating the spectrum after Fourier transform of equation (2). The reconstructed spectrum is shown in red overlapping the in vivo data.

Comparative analysis of the metabolite concentration ratio between LCMoDel and SPAWNN is displayed in Figure 6. The results were derived from the sum of 8 MRSI voxels located in the occipital region for each of the 10 volunteers. The mean value of  $\alpha$ -ATP,  $\beta$ -ATP, and  $\gamma$ -ATP was computed and reported as ATP. The concentration of PCr

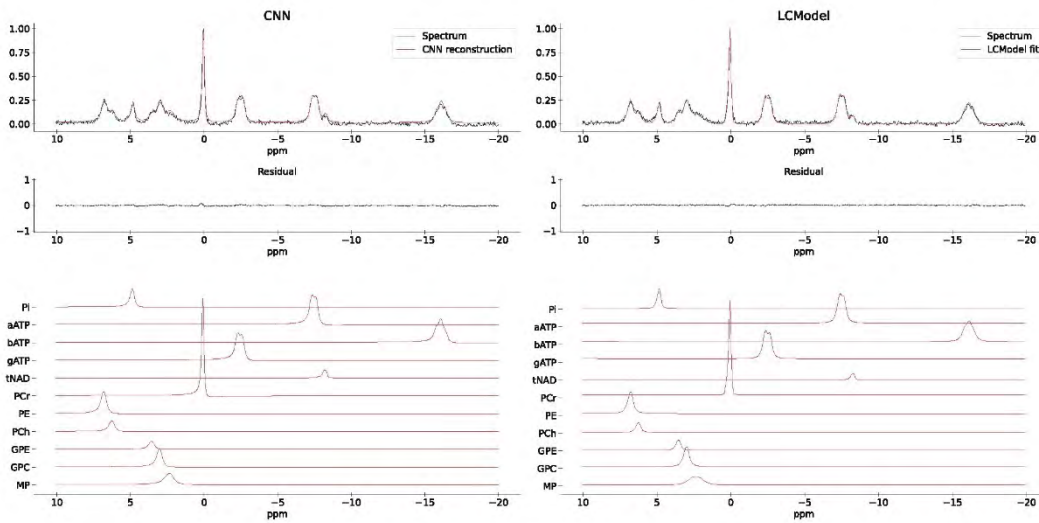


FIGURE 5 Comparison of in vivo  $^{31}\text{P}$ -MRSI spectrum (TR = 1.5 s, TE = 0.5 ms, sum of 8 voxels with 24 weighted averages each) evaluated and reconstructed with SPAWNN (left) and fitted with LCMoDel (right). The figure displays SPAWNN reconstruction and the LCMoDel fit (top), the residuals (middle), and the contribution of each metabolite (bottom). No correction was applied before analysis.

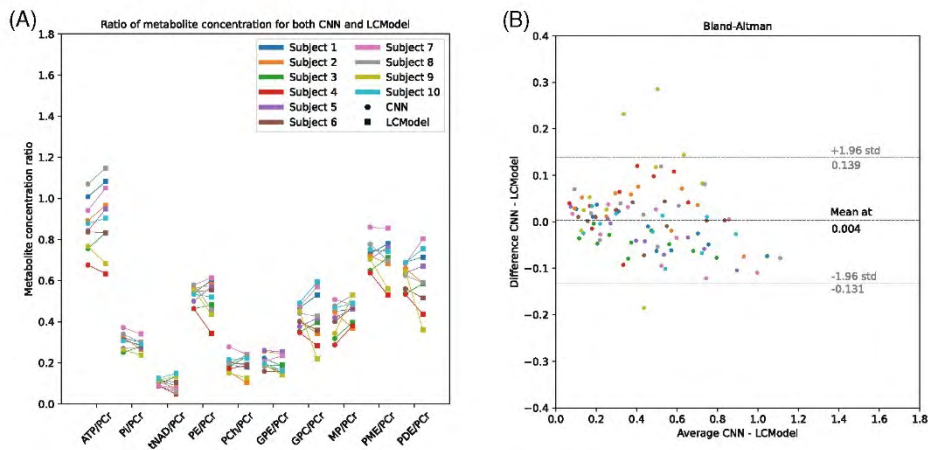


FIGURE 6 Results on  $^{31}\text{P}$ -MRSI data, with the sum on 8 voxels. (A) Comparison of metabolite concentration ratios for the 10 volunteers with SPAWNN (circles) and LCMoDel (squares). ATP concentration is computed by averaging the concentration of the three resonances. (B) Bland-Altman plot of the difference between estimated values by SPAWNN and LCMoDel versus the average of the estimated values across all metabolite ratios and subjects.

was used as denominator for the ratios. Figure 6A shows a plot of the metabolite concentration ratio estimated by SPAWNN and LCMoDel, with a line connecting the data of the same subject. Figure 6B shows a Bland-Altman plot of the data from Figure 6C, with the difference between the SPAWNN and LCMoDel estimations versus the average of the two values. The mean difference between the

two methods is  $4.0 \cdot 10^{-3}$ , and the limits of agreements ( $\pm 1.96\sigma$ ) are +0.139 and -0.131. The Bland-Altman plot shows few outliers, but no systematic bias. Relative differences and relative standard deviations are presented in Table 1. A statistical  $t$ -test with Bonferroni correction was performed, and the  $p$ -values are reported in the table as well. The Bonferroni correction took into account the



TABLE 1 Statistics of the comparison of the metabolic concentration ratio for the 10 volunteers with SPAWNN and LCMoel from Figure 6

| Metabolite ratio | Relative difference (%) | Relative standard deviation (%) | <i>p</i> -value (uncorrected) |
|------------------|-------------------------|---------------------------------|-------------------------------|
| ATP/PCr          | -4.69                   | 6.93                            | 0.073                         |
| Pi/PCr           | 7.37                    | 7.68                            | 0.018                         |
| tNAD/PCr         | 14.8                    | 31.1                            | 0.19                          |
| PE/PCr           | 3.0                     | 13.6                            | 0.53                          |
| PCh/PCr          | 2.16                    | 15.5                            | 0.68                          |
| GPE/PCr          | 8.36                    | 11.4                            | 0.055                         |
| GPC/PCr          | 1.63                    | 11.3                            | 0.83                          |
| MP/PCr           | -10.4                   | 15.5                            | 0.075                         |
| PME/PCr          | 3.0                     | 9.4                             | 0.36                          |
| PDE/PCr          | 3.9                     | 17.6                            | 0.52                          |

Note: Statistical *t*-test was performed with Bonferroni correction for multiple comparisons resulting in a lower threshold for rejecting the null hypothesis to  $\alpha = 0.0056$ . No difference in metabolite ratios was found to be significant.

repeated *t*-tests (10 metabolites) and reduced the threshold for rejecting the null hypothesis to  $\alpha = 0.0056$ . The metabolite ratios showed relative differences lower than 10% for most of the ratios, except for tNAD/PCr and MP/PCr. All metabolite ratios had a relative standard deviation higher than the relative differences, with none found to be significant.

Figure 7 illustrates the quantification performance of SPAWNN and LCMoel with respect to noise. The data used were unlocalized FIDs with 600 averages acquired on three volunteers. The 600 spectra acquired were randomly selected retrospectively and averaged in groups ranging from 1 to 600 spectra. We considered the reference values to be the values estimated with 600 averages. The convergence was then defined as the difference between the mean value of the estimations and the reference value, with precision representing the standard deviation of the reference value. Figure 7 presents the results for the  $\gamma$ -ATP, PCr, PE, PCh, GPC, and GPE. The two spikes in Subject #3 originate from an LCMoel fatal error where the model failed to converge.

Analysis of single voxels from in vivo  $^{31}\text{P}$ -MRSI with the two methods is shown in Figure 8. The SPAWNN spectrum reconstruction from two distinct brain voxels is displayed. The T1 MP-RAGE  $^1\text{H}$  image is presented on the left; the grid shows the voxel locations in the sagittal view (top) and the corresponding axial slice (bottom) centered on the blue box location. The analysis of voxel A and B with SPAWNN and LCMoel is shown on the right. Each

spectrum is presented with either the reconstruction or the fit, with the residual underneath. The estimated  $\text{SNR}_{\text{mean}}$  for the spectra were 1.56 and 1.63, and the LCMoel SNRs were 16 and 20 for voxels A and B, respectively.

## 5 | DISCUSSION

This study demonstrated the ability of SPAWNN to evaluate, quantify, and reconstruct  $^{31}\text{P}$ -MRS data. We focused on two network architectures specifically developed to fully identify spectral features of MRS data. SPAWNN-Q, displayed in Figure 2, was used to extract the metabolite concentrations and spectral parameters. We used two separate networks running in parallel for efficiency and flexibility, which also allowed for a better control of the training phase during model development. However, a single LeNet for both concentration and parameters estimation was tested and yielded similar results. SPAWNN-Q parameter network can be applied to MRSI data for phases and frequency shift correction in order to sum individual spectra before complete quantification. SPAWNN-BI (Figure 3) was used for spectral baseline estimation.

Our synthetic dataset was simulated by summing independent metabolite signals. However, ATP was simulated as three independent resonances for  $\gamma$ -,  $\alpha$ -, and  $\beta$ -ATP, thereby rendering the network more flexible in estimating concentration as well as chemical shift. The reason for this choice was that other metabolites, such as adenosine diphosphate (ADP), may overlap with  $\gamma$ - and  $\alpha$ -ATP and influence the estimated concentration. In addition, three ATP resonances were shown to exhibit different chemical shifts with varying concentrations of  $\text{Mg}^{2+}$ .<sup>47</sup> However, our physical model assumed the same linewidth for the three ATP resonances because of their identical T2 relaxation times. SPAWNN results demonstrated a high performance on simulated datasets as well as on in vivo data (Figures 4 and 6). This indicates that our simulation model (equation (2)) is a good emulation of the physical NMR signal and faithfully represents the measured spectra using excite-acquire sequences. The SPAWNN evaluations presented in Figures 5 and 8 show the reconstruction of the spectra and illustrate the ability of SPAWNN to provide a good estimation of the spectral parameters, concentrations, and baseline, as the reconstructions matched the spectra. Artificial intelligence (AI) approaches, such as CNN, perform accurately if the measured parameters are in the range of the training set. For specific applications, it might be possible to train the network with a smaller range of concentrations to possibly achieve better performance. One could imagine having a specialized model for each organ, with the concentration distribution centered on the values reported in the literature. However, training

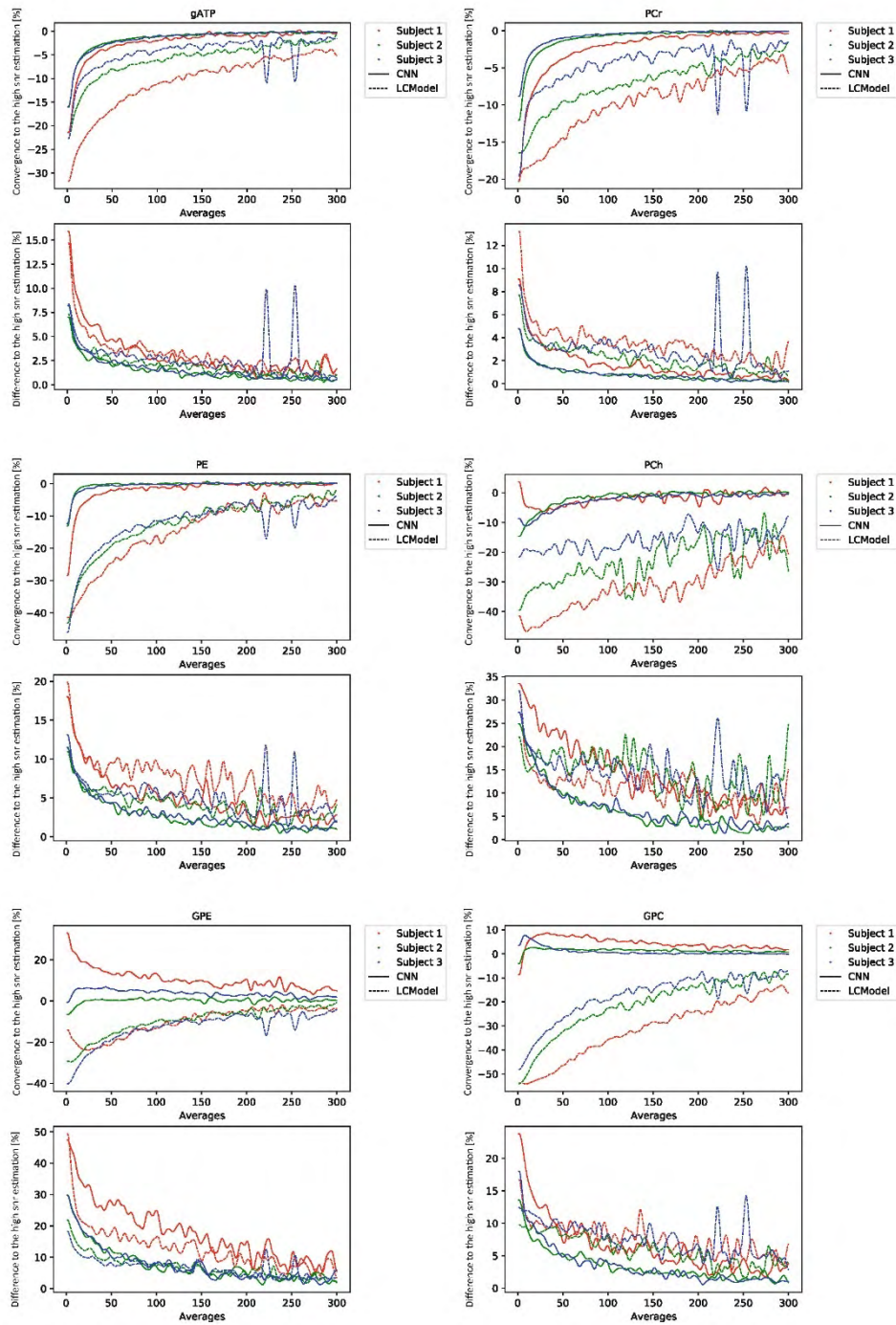


**FIGURE 7** Results from unlocalized FID data of the occipital lobe. Comparison of metabolite concentration estimation by SPAWNN and LCModel. The reference value is the estimate obtained with the average of the full acquisition (600 spectra). The plots show the convergence and the difference in estimation of each model with respect to the highest SNR estimate.



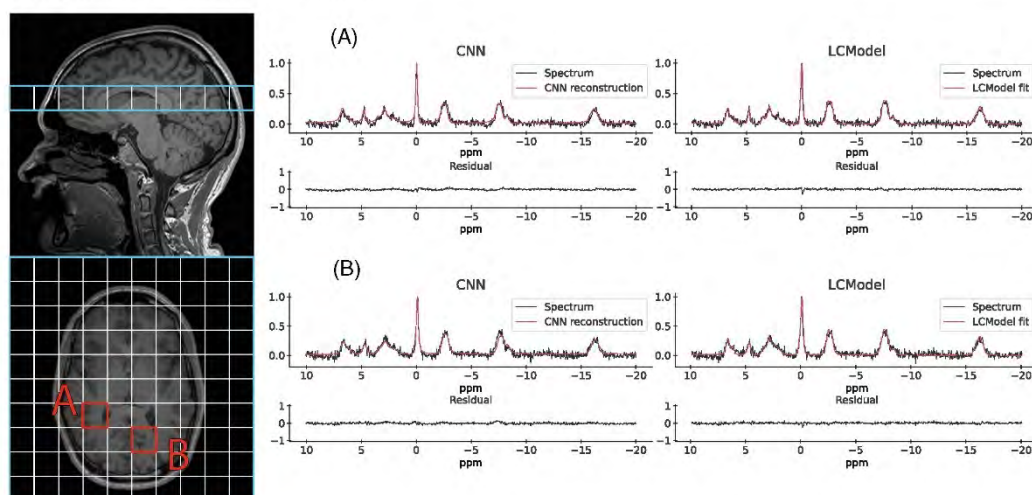


FIGURE 8 Examples of SPAWNN evaluation of a 3D  $^{31}\text{P}$ -MRSI acquired on a human brain. The figure shows two spectra (TR = 1.5 s, TE = 0.5 ms, 24 weighted averages) arising from two brain regions. The T1 MP-RAGE  $^1\text{H}$  MRI is displayed on the left, indicating the slice position and voxel locations. The voxel has a resolution of 25 mm isotropic. The spectra on the left represent the SPAWNN reconstruction with the measurement data, and the spectra on the right the LCModel fitting for voxels A and B.

with a narrower parameter distribution could induce a bias in the analysis of specific conditions or pathologies that strongly affects the metabolism. Moreover, in a situation where data are acquired with parameters outside the training range (e.g., strong artifact), the results of the analysis should be discarded. The spectral reconstruction based on estimates is an important tool to visually validate whether the neural network estimate matches the in vivo spectrum, in which case the results should be discarded. In this study, we chose to train the networks over a very wide range of parameter values to avoid this limitation. This wide range does not compromise the quantification accuracy while avoiding bias.

On the simulated data, SPAWNN compared favorably to LCModel in terms of precision. The coefficient of determination  $R^2$  per metabolites, as a whole, was similar for both approaches (Figure 4B). Of the 11 metabolites, only three significantly differed between the two methods. SPAWNN performed better for tNAD and GPC, while LCModel showed better performance on MP. NAD $^+$  and NADH can be accurately estimated with LCModel at 7T,<sup>48</sup> due to the higher signal and greater chemical shift dispersion. By contrast, at 3T without proton decoupling, the distinction between NAD $^+$  and NADH is more difficult, as illustrated by the results where tNAD was estimated with the least accuracy. MPs were also estimated with low accuracy by both SPAWNN and LCModel. This is due to the larger peak width that makes the distinction between the baseline and noise difficult. Figure 4B shows that with bootstrap statistics, the standard deviation of the

coefficient of determination of the LCModel was larger than that of SPAWNN for all metabolites. In addition, SPAWNN estimates remained accurate ( $R^2 > 0.8$ ) for most metabolites at a very low SNR (Figure 4C), highlighting the robustness of the method.

In vivo data (Figures 5 and 8) showed that SPAWNN can estimate the spectral parameters with good accuracy, since the reconstruction of the spectra based on these estimates closely matched the measured data. An example of analysis with both methods for a volunteer is presented in Figure 5. The data were obtained by summing 8 neighbor voxels in the occipital region. By contrast, an analysis with both methods for singles voxels of the volunteer data is shown in Figure 8. The individual signals of each metabolite as estimated by SPAWNN and LCModel are displayed in Figures 5 and 8. The two methods showed consistent signal for each metabolite. The residuals are low with both approaches but nevertheless slightly higher with SPAWNN. This is explained by the fact that LCModel is a fitting algorithm while SPAWNN does not aim at minimizing the residuals. Figure 6 presents the concentration ratio values of the metabolites obtained on 8 averaged voxels from the occipital region of each subject. The results are in very good agreement with the values reported using PCR as internal reference.<sup>46,49,50</sup> The Bland-Altman plot shows that the mean difference of the two methods was much smaller than the standard deviation and demonstrates the absence of bias. The outlier points in Subject #9 could be explained by poor B0 homogeneity during the acquisition. By contrast, Subject #7 was the one with



the best B0 homogeneity and showed close estimation with both methods. Table 1 reveals that all relative standard deviations were greater than the relative differences, indicating that inter-subject variation was greater than between-method variation.

Figure 7 shows the convergence toward the estimated value at high SNR by SPAWNN and LCModel. The data originate from unlocalized FID with 600 averages acquired from three volunteers. Unlocalized FID was used instead of MRSI in order to get optimum SNR with reasonable acquisition duration considering 600 averages. The plots aim to present the convergence of both models toward the reference value estimated at the highest SNR, corresponding to the spectra obtained with 600 averages. For high-signal metabolites, such as PCr and ATPs, both models displayed similar speed of convergence. For lower-signal metabolites, such as PCh and GPC, the estimation with LCModel differed by more than 10% from the high SNR value even with high numbers of averages. SPAWNN showed faster asymptotic convergence toward the concentration reference. Both SPAWNN and LCModel demonstrated similar precisions, with more variation across subjects than across methods. Spectra from Subject #1 had more noise and half lower SNR compared with the other two subjects, which can be due to worst shimming. The discontinuities observed in Subject #2 are attributable to LCModel failure to converge ("fatal errors") and were considered as outliers. Over all the metabolites, SPAWNN displayed more consistency and stability, especially at low SNR. This result suggests that the SPAWNN approach is more robust at low SNR than LCModel, thus implying a fewer number of averages to match the results of traditional fitting methods. This could translate into shorter acquisition time in a clinical setting or higher reconstruction resolution for MRSI.

SPAWNN training time was 4 and 6 h for the two sub-models. Nevertheless, once the weights were computed, spectral analysis with SPAWNN was almost instantaneous. Indeed, the evaluation of  $10^5$  spectra required approximately 5 min. This could be useful in the prospect of applying the method to 3D metabolite mapping, which requires the analysis of the full dataset. As illustrated in Figure 8, the  $10^3$  voxels of the dataset were analyzed in a few minutes, whereas the same analysis performed by LCModel lasted almost 1 h. Faster computing time is a clear advantage for clinical applications where a fast online processing is highly desired.

Our study results compared with those of previously published works that used neural network approaches to analyze MRS.<sup>14,23,24</sup> Das et al.<sup>14</sup> presented a method using random forest machine learning, while Hatami et al.<sup>23</sup> used a DL CNN model for quantification. Compared with both methods, the physical model proposed

here for generating the simulated training set includes a larger number of parameters, which should result in a more complete variety of spectra, as well as artifacts and distortions, as observed *in vivo*. The approach proposed by Lee et al.<sup>24</sup> aimed to learn the reconstruction of the spectral real part, while ours aimed to learn the metabolite concentration and parameters directly, without optimized reconstruction. Other studies used a different approach to applying AI to NMR, such as the one conducted by Da-Wei et al.<sup>51</sup> who used a neural network approach to perform deconvolution on overlapping peaks.

The analysis was performed without measuring a reference signal, with therefore no possibility of absolute quantification, and LCModel was used as a fair reference for comparison of metabolite ratios. In a possible perspective, both models could be compared for absolute quantification with the measurement of an *in vitro* reference with a known concentration. The influence of the training parameter ranges over SPAWNN robustness and stability remains to be established. As mentioned above, narrow specific parameter ranges might improve accuracy but SPAWNN results would be unreliable for spectral parameters falling outside the training range. Possible improvements of SPAWNN can be explored: the physical model could notably be improved by taking into account more distortions, such as eddy current effects. Future developments also include implementing SPAWNN for metabolite mapping and determining a confidence interval for the estimated values.

In conclusion, we presented a DL method of evaluation, quantification, and baseline estimation for <sup>31</sup>P-MRS, combined with a reconstruction pipeline for spectral reconstruction. The proposed SPAWNN method had a high accuracy and robustness overall, especially at low SNR, thereby allowing higher resolution reconstruction in MRSI schemes. Our proposed approach had an extremely fast computation time that offers the ability to analyze large <sup>31</sup>P-MRSI datasets almost instantaneously, which is a significant advantage for possible applications in a clinical setting.

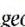

#### ACKNOWLEDGMENTS

This study was supported by the Swiss National Science Foundation (320030\_182658). We gratefully acknowledge NVIDIA Corporation for the donation of the Titan V GPU used for this research. Open access funding provided by Universite de Geneve.

#### DATA AVAILABILITY STATEMENT

The source code for the proposed 31P-SPAWNN model can be downloaded from this link: <https://gitlab.unige.ch/Julien.Songeon/31P-SPAWNN>.



**ORCID**Julien Songeon  <https://orcid.org/0000-0001-8760-6862>Lijing Xin  <https://orcid.org/0000-0002-5450-6109>Antoine Klausner  <https://orcid.org/0000-0003-3019-9914>**REFERENCES**

1. Reto B, Dieter M, Ernst M, Peter B. Assessment of absolute metabolite concentrations in human tissue by <sup>31</sup>P MRS in vivo part II: muscle, liver, kidney. *Magn Reson Med*. 1994;32:453-458.
2. Chmelik M, Schmid A, Gruber S, et al. Three-dimensional high-resolution magnetic resonance spectroscopic imaging for absolute quantification of <sup>31</sup>P metabolites in human liver. *Magn Reson Med*. 2008;60:796-802.
3. Webb Graham A, ed. Methods and applications of phosphorus NMR spectroscopy in vivo. *Annual Reports on NMR Spectroscopy*. Vol 75. Academic Press; 2012.
4. Jong-Hee H, Soo CC. Use of in vivo magnetic resonance spectroscopy for studying metabolic diseases. *Exp Mol Med*. 2015;47:e139.
5. Rudin M, ed. *In-Vivo Magnetic Resonance Spectroscopy III: In-Vivo MR Spectroscopy: Potential and Limitations*. Springer Berlin Heidelberg; 1992.
6. Boulangé CL. Nuclear magnetic resonance spectroscopy-applicable elements| Phosphorus-31. *Reference Module in Chemistry, Molecular Sciences and Chemical Engineering*. Elsevier; 2017.
7. Maudsley AA, Hilal SK, Perman WH, Simon HE. Spatially resolved high resolution spectroscopy by "four-dimensional" NMR. *J Magn Reson*. 1983;51:147-152.
8. Thulborn KR, Atkinson IC. Quantitative metabolic magnetic resonance imaging of sodium, oxygen, phosphorus and potassium in the human brain. *Magnetic Resonance Spectroscopy*. Elsevier; 2014:291-311.
9. Hongyan Q, Xiaoliang Z, Zhu X-H, Fei D, Wei C. In vivo <sup>31</sup>P MRS of human brain at high/ultrahigh fields: a quantitative comparison of NMR detection sensitivity and spectral resolution between 4T and 7T. *Magn Reson Imaging*. 2006;24:1281-1286.
10. Ladislav V, Marek C, Martin M, et al. Dynamic <sup>31</sup>P-MRSI using spiral spectroscopic imaging can map mitochondrial capacity in muscles of the human calf during plantar flexion exercise at 7T. *NMR Biomed*. 2016;29:1825-1834.
11. Goldenberg S, Larry NG, Salcudean Septimiu E. A new era: artificial intelligence and machine learning in prostate cancer. *Nat Rev Urol*. 2019;16:391-403.
12. Scott K. Feature learning and deep learning architecture survey. *Computer Vision Metrics: Textbook Edition*. Springer International Publishing; 2016:375-514.
13. Jinchao L, Margarita O, Lorna A, Michael F, Solomon Christopher J, Gibson Stuart J. Deep convolutional neural networks for Raman spectrum recognition: a unified solution. *Analyst*. 2017;142:4067-4074.
14. Dhritiman D, Eduardo C, Schulte Rolf F, Menze Bjoern H. Quantification of metabolites in magnetic resonance spectroscopic imaging using machine learning. *Medical Image Computing and Computer Assisted Intervention - MICCAI 2017*. Springer International Publishing; 2017:462-470.
15. Provencher S. Automatic quantitation of localized in vivo <sup>1</sup>H spectra with LCModel. *NMR Biomed*. 2001;14:260-264.
16. Pierre-Gilles H, Gülin Ö, Stephen P, Rolf G. Toward dynamic isotopomer analysis in the rat brain in vivo: automatic quantitation of <sup>13</sup>C NMR spectra using LCModel. *NMR Biomed*. 2003;16:400-412.
17. Kumar DD, Tra-My N, Xiao-Hong Z, Fanny M, Pierre-Gilles H. Quantification of in vivo <sup>31</sup>P NMR brain spectra using LCModel. *NMR Biomed*. 2015;28:633-641.
18. Selvikvåg LA, Arvid L. An overview of deep learning in medical imaging focusing on MRI. *Z Med Phys*. 2019;29:102-127.
19. Singh SP, Lipo W, Sukrit G, Haveesh G, Parasuraman P, Balázs G. 3D deep learning on medical images: a review arXiv e-prints, arXiv:2004.00218.
20. Marina C, Simone S, Francesco S, Trimboli Rubina Manuela. Artificial intelligence for breast MRI in 2008–2018: a systematic mapping review. *Am J Roentgenol*. 2019;212:280-292.
21. Aurélien B, Niccolo F, Botnar René M, Claudia P. From compressed-sensing to artificial intelligence-based cardiac MRI reconstruction. *Front Cardiovascular Med*. 2020;7:17.
22. Fan L, Yudu L, Guo R, Bryan C, Zhi-Pei L. Ultrafast magnetic resonance spectroscopic imaging using SPICE with learned subspaces. *Magn Reson Med*. 2019;83:377-390.
23. Nima H, Michaël S, Hélène R. Magnetic resonance spectroscopy quantification using deep learning. *Medical Image Computing and Computer Assisted Intervention - MICCAI 2018*. Springer International Publishing; 2018:467-475.
24. Hun LH, Hyeonjin K. Deep learning-based target metabolite isolation and big data-driven measurement uncertainty estimation in proton magnetic resonance spectroscopy of the brain. *Magn Reson Med*. 2020;84:1689-1706.
25. Fan L, Yahang L, Xi P. Constrained magnetic resonance spectroscopic imaging by learning nonlinear low-dimensional models. *IEEE Trans Med Imaging*. 2020;39:545-555.
26. Courvoisier S, Klausner A, Lazeyras F. High-resolution magnetic resonance spectroscopic imaging quantification by convolutional neural network. Proceedings of the 2019 Annual Meeting of the International Society for Magnetic Resonance in Medicine (ISMRM). 2019; 27: 0519.
27. Varanavasi G, Karl Y, Maudsley Andrew A. Proton NMR chemical shifts and coupling constants for brain metabolites. *NMR Biomed*. 2000;13:129-153.
28. Ernst RR, Bodenhausen G, Wokaun A. *Principles of Nuclear Magnetic Resonance in One and Two Dimensions*. Vol 7. Wiley; 1988:158-165.
29. Lecun Y, Bottou L, Bengio Y, Haffner P. Gradient-based learning applied to document recognition. *Proc IEEE*. 1998;86:2278-2324.
30. Olaf R, Philipp F, Thomas B. U-net: convolutional networks for biomedical image segmentation. *LNCIS*. 2015;9351: 234-241.
31. Bhargab BM, Dinthisrang D, Khwairakpam A, Debdatta K. Handwritten character recognition from images using CNN-ECOC. *Procedia Comput Sci*. 2020;167:2403-2409.
32. Shengnan C, Heng Z, Yang X, et al. Raman spectroscopy reveals abnormal changes in the urine composition of prostate cancer: an application of an intelligent diagnostic model with a deep learning algorithm. *Adv Intel Syst*. 2021;3:2000090.
33. Dicheng C, Wang Z, Guo D, Vladislav O, Xiaobo Q. Review and prospect: deep learning in nuclear magnetic resonance spectroscopy. arXiv e-prints, arXiv:2001.04813.
34. Albawi S., Mohammed T.A. and Al-Zawi S. Understanding of a convolutional neural network. Proceedings of the

- 2017 International Conference on Engineering and Technology (ICET), 2017, pp. 1-6.
35. Zhang Z, Liu Q, Wang Y. Road extraction by deep residual U-net. *IEEE Geosci Remote Sens Lett.* 2018;15:749-753.
  36. Zohaib I, Dan N, Albert TM, Steve J. Deep learning can accelerate and quantify simulated localized correlated spectroscopy. *Sci Rep.* 2021;11:8727.
  37. Kyathanahally SP, Döring A, Kreis R. Deep learning approaches for detection and removal of ghosting artifacts in MR spectroscopy. *Magn Reson Med.* 2018;80:851-863.
  38. Zahangir AM, Chris Y, Mahmudul H, Taha Tarek M, Asari Vijayan K. Recurrent residual U-net for medical image segmentation. *J Med Imag.* 2019;6:1.
  39. Smith SA, Levante TO, Meier BH, Ernst RR. Computer simulations in magnetic resonance. An object-oriented programming approach. *J Magn Reson A.* 1994;106:75-105.
  40. Kingma DP, Jimmy B. ADAM: a method for stochastic optimization. arXiv:1412.6980. 2014.
  41. Ida T, Ando M, Toraya H. Extended pseudo-Voigt function for approximating the Voigt profile. *J Appl Crystallogr.* 2000;33:1311-1316.
  42. Provencher Stephen W. Estimation of metabolite concentrations from localized in-vivo proton NMR spectra. *Magn Reson Med.* 1993;30:672-679.
  43. Rolf P, Markus K. Accurate phosphorus metabolite images of the human heart by 3D acquisition-weighted CSI. *Magn Reson Med.* 2001;45:817-826.
  44. Davide C, Warrens Matthijs J, Giuseppe J. The coefficient of determination R-squared is more informative than SMAPE, MAE, MAPE, MSE and RMSE in regression analysis evaluation. *Peer J Comput Sci.* 2021;7:e623.
  45. Efron B. Bootstrap methods: another look at the Jackknife. *Anna Stat.* 1979;7:1-26.
  46. Andreas R, Ruth S, Stephanie M, et al. Energy metabolism measured by 31P magnetic resonance spectroscopy in the healthy human brain. *J Neuroradiol.* 2022.
  47. Gout E, Rebeille F, Douce R, Bligny R. Interplay of mg<sup>2+</sup>, ADP, and ATP in the cytosol and mitochondria: unravelling the role of mg<sup>2+</sup> in cell respiration. *Proc Natl Acad Sci U S A.* 2014;111:E4560-E4567.
  48. Xin L, Ipek Ö, Beaumont M, et al. Nutritional ketosis increases NAD<sup>+</sup>/NADH ratio in healthy human brain: an in vivo study by 31P-MRS. *Front Nutr.* 2018;5:62.
  49. Jensen J, Eric DDJ, Menon Ravi S, Williamson Peter C. In vivo brain 31P-MRS: measuring the phospholipid resonances at 4 tesla from small voxels. *NMR Biomed.* 2002;15:338-347.
  50. Jimin R, Dean SA, Malloy Craig R. 31P-MRS of healthy human brain: ATP synthesis, metabolite concentrations, pH, and T1 relaxation times. *NMR Biomed.* 2015;28:1455-1462.
  51. Da-Wei L, Hansen Alexander L, Chunhua Y, Lei B-L, Rafael B. DEEP picker is a DEEP neural network for accurate deconvolution of complex two-dimensional NMR spectra. *Nat Commun.* 2021;12:5229.

**How to cite this article:** Songeon J, Courvoisier S, Xin L, et al. In vivo magnetic resonance <sup>31</sup>P-Spectral Analysis With Neural Networks: 31P-SPAWN. *Magn Reson Med.* 2023;89:40-53. doi: 10.1002/mrm.29446



# Cystathionine- $\gamma$ -lyase overexpression modulates oxidized nicotinamide adenine dinucleotide biosynthesis and enhances neovascularization

Kevin Kiesworo, MS,<sup>a,b</sup> Michael R. MacArthur, PhD,<sup>c</sup> Peter Kip, MD, PhD,<sup>d</sup> Thomas Agius, MS,<sup>a,b</sup> Diane Macabrey, MS,<sup>a,b</sup> Martine Lambelet, BS,<sup>a,b</sup> Lauriane Hamard, PhD,<sup>e</sup> C. Keith Ozaki, MD,<sup>d</sup> James R. Mitchell, PhD,<sup>c</sup> Sébastien Déglise, MD,<sup>a,b</sup> Sarah J. Mitchell, PhD,<sup>c</sup> Florent Allagnat, PhD,<sup>a,b</sup> and Alban Longchamp, MD, PhD,<sup>a,b</sup> *Lausanne and Zurich, Switzerland; and Boston, MA*

## ABSTRACT

**Objective:** Hydrogen sulfide is a proangiogenic gas produced primarily by the transsulfuration enzyme cystathionine- $\gamma$ -lyase (CGL). CGL-dependent hydrogen sulfide production is required for neovascularization in models of peripheral arterial disease. However, the benefits of increasing endogenous CGL and its mechanism of action have not yet been elucidated.

**Methods:** Male whole body CGL-overexpressing transgenic (CGL<sup>Tg</sup>) mice and wild-type (WT) littermates (C57BL/6J) were subjected to the hindlimb ischemia model (age, 10-12 weeks). Functional recovery was assessed via the treadmill exercise endurance test. Leg perfusion was measured by laser Doppler imaging and vascular endothelial-cadherin immunostaining. To examine the angiogenic potential, aortic ring sprouting assay and postnatal mouse retinal vasculature development studies were performed. Finally, comparative metabolomics analysis, oxidized/reduced nicotinamide adenine dinucleotide (NAD<sup>+</sup>/NADH) analysis, and quantitative real-time polymerase chain reaction were performed on CGL<sup>WT</sup> and CGL<sup>Tg</sup> gastrocnemius muscle.

**Results:** The restoration of blood flow occurred more rapidly in CGL<sup>Tg</sup> mice. Compared with the CGL<sup>WT</sup> mice, the median  $\pm$  standard deviation running distance and time were increased for the CGL<sup>Tg</sup> mice after femoral artery ligation (159  $\pm$  53 m vs 291  $\pm$  74 m [ $P < .005$ ] and 17  $\pm$  4 minutes vs 27  $\pm$  5 minutes [ $P < .05$ ], respectively). Consistently, in the CGL<sup>Tg</sup> ischemic gastrocnemius muscle, the capillary density was increased fourfold (0.05  $\pm$  0.02 vs 0.20  $\pm$  0.12;  $P < .005$ ). Ex vivo, the endothelial cell (EC) sprouting length was increased in aorta isolated from CGL<sup>Tg</sup> mice, especially when cultured in VEGFA (vascular endothelial growth factor A)-only media (63  $\pm$  2 pixels vs 146  $\pm$  52 pixels;  $P < .05$ ). Metabolomics analysis demonstrated a higher level of niacinamide, a precursor of NAD<sup>+</sup>/NADH in the muscle of CGL<sup>Tg</sup> mice (61.4  $\times 10^6 \pm 5.9 \times 10^6$  vs 72.4  $\pm 7.7 \times 10^6$  area under the curve;  $P < .05$ ). Similarly, the NAD<sup>+</sup> salvage pathway gene expression was increased in CGL<sup>Tg</sup> gastrocnemius muscle. Finally, CGL overexpression or supplementation with the NAD<sup>+</sup> precursor nicotinamide mononucleotide improved EC migration in vitro (wound closure: control, 35%  $\pm$  9%; CGL, 55%  $\pm$  11%; nicotinamide mononucleotide, 42%  $\pm$  13%;  $P < .05$ ).

**Conclusions:** Our results have demonstrated that CGL overexpression improves the neovascularization of skeletal muscle on hindlimb ischemia. These effects correlated with changes in the NAD pathway, which improved EC migration. (JVS—Vascular Science 2023;4:1-10.)

**Clinical Relevance:** Peripheral arterial disease (PAD) currently affects >200 million people worldwide and is anticipated to increase with the aging population. In the present study, we outlined the beneficial effects of cystathionine- $\gamma$ -lyase (CGL) overexpression in improving neovascularization and functional recovery in a murine PAD model. Taken together with other reported studies, our findings further highlight the untapped potential of targeting CGL for therapeutic interventions in patients with PAD.

**Keywords:** Hydrogen sulfide; CGL; Peripheral arterial disease; Endothelial cells

From the Department of Vascular Surgery, Lausanne University Hospital,<sup>a</sup> the Department of Biomedical Sciences, University of Lausanne,<sup>b</sup> Lausanne; the Department of Health Sciences and Technology, ETH Zurich, Zurich;<sup>c</sup> the Department of Surgery and Heart and Vascular Center, Brigham & Women's Hospital and Harvard Medical School, Boston;<sup>d</sup> and the Department of Medicine, Lausanne University Hospital, Lausanne.<sup>e</sup>

The present study was supported by the Swiss National Science Foundation (grant PZ00P3-185927 to A.L. and grant 310030\_176158 to F.A. and S.D.); the National Institutes of Health (grant F31 AG064863/AG/NIA to M.R.M. and grant R01 DK090629/DK/NIDDK to J.R.M.); the Leenaards Foundation, Novartis Foundation for Medical-Biological Research, and Foundation Pierre Mercier pour la Science (all to A.L.); and the Foundation pour la Recherche en Chirurgie Thoracique et Vasculaire (to A.L., F.A., and S.D.).

Author conflict of interest: none.

Correspondence: Alban Longchamp, MD, PhD, Department of Vascular Surgery, Lausanne University Hospital, Rue du Bugnon 46, Lausanne 1011, Switzerland (e-mail: [alban.longchamp@chuv.ch](mailto:alban.longchamp@chuv.ch)).

The editors and reviewers of this article have no relevant financial relationships to disclose per the JVS-Vascular Science policy that requires reviewers to decline review of any manuscript for which they may have a conflict of interest. 2666-3503

Copyright © 2023 by the Society for Vascular Surgery. Published by Elsevier Inc. This is an open access article under the CC BY license (<http://creativecommons.org/licenses/by/4.0/>). <https://doi.org/10.1016/j.jvssci.2022.11.003>

Peripheral arterial disease (PAD) currently affects >200 million people worldwide and is anticipated to increase with the aging population.<sup>1</sup> PAD can lead to severe complications such as chronic limb threatening ischemia and amputation and has been associated with high rates of cardiovascular events and death. Clinical management of PAD aims to improve patients' functional capacity and maintain limb viability.<sup>2</sup> During PAD, occlusion of the arteries can cause a series of compensatory events, such as arteriogenesis and angiogenesis, to restore perfusion to the ischemic tissue.<sup>3,4</sup> One therapeutic strategy that has been explored for PAD has been to enhance the formation of a new capillary network through administration of growth factors and vasculogenic cells and subsequent activation, proliferation, and migration of endothelial cells (ECs). Although some success with angiogenic therapy has been reported in young and healthy animal models of acute artery ligation, these therapies have not yet demonstrated therapeutic efficacy when translated to patient cohorts.<sup>5,6</sup>

In mammals, hydrogen sulfide (H<sub>2</sub>S) is a ubiquitous redox modifying gasotransmitter that has numerous physiologic roles across various organ systems, including the cardiovascular system.<sup>7,8</sup> H<sub>2</sub>S is produced through the transsulfuration pathway by the concerted effort of three enzymes: cystathionine-γ-lyase (CGL), cystathionine-β-synthase (CBS), and 3-mercaptopyruvate sulfurtransferase.<sup>9</sup> In the cardiovascular system, CGL is thought to be the principal enzyme responsible for the production of H<sub>2</sub>S.<sup>10</sup> *In vitro* and *in vivo* H<sub>2</sub>S promotes angiogenesis.<sup>8,9</sup> In mice, whole body knockout of CGL impaired recovery in a murine model of PAD,<sup>11,12</sup> and the administration of an H<sub>2</sub>S pro-drug has been shown to improve neovascularization in a porcine PAD model.<sup>13</sup> In humans, endogenous H<sub>2</sub>S bioavailability is attenuated in the setting of chronic limb threatening ischemia and in patients with diabetes-related vascular inflammation.<sup>14</sup> Moreover, our group recently demonstrated that circulating H<sub>2</sub>S levels will be lower in patients with atherosclerotic disease and that patients undergoing surgical revascularization with lower H<sub>2</sub>S production capacity will have higher rates of postoperative mortality.<sup>15</sup>

H<sub>2</sub>S-associated angiogenesis is thought to be driven by stimulation of the vascular endothelial growth factor A (VEGFA) pathway in ECs via activation of the VEGFR2 (vascular endothelial growth factor receptor 2) through sulfhydrylation.<sup>16</sup> H<sub>2</sub>S further increases EC glucose uptake and adenosine triphosphate production, which allows for rapid energy generation, supporting migration during angiogenesis.<sup>17</sup> A few studies have suggested an interplay between H<sub>2</sub>S and the redox couple oxidized/reduced nicotinamide adenine dinucleotide (NAD<sup>+</sup>/NADH). NAD<sup>+</sup> is an essential coenzyme for cellular redox reactions, such as glycolysis and fatty acid oxidation, making it central to energy metabolism. Moreover, it also functions as a substrate for nonredox enzymes,

## ARTICLE HIGHLIGHTS

- **Type of Research:** Basic research in mice.
- **Key Findings:** CGL overexpression improves the neovascularization of skeletal muscle upon hindlimb ischemia. CGL overexpression increased endothelial cell migration and was associated with changes in the NAD pathway.
- **Take Home Message:** The results of our study indicate that hydrogen sulfide and CGL might facilitate recovery upon limb ischemia and during peripheral arterial disease.

such as sirtuins and poly(ADP-ribose) polymerases.<sup>18,19</sup> The H<sub>2</sub>S donor sodium hydrosulfide can also activate the NAD<sup>+</sup> dependent histone deacetylase sirtuin 1 (SIRT1) and augment the proangiogenic effects of the NAD<sup>+</sup> precursor nicotinamide mononucleotide (NMN) in primary ECs<sup>20-22</sup> and elderly mice.<sup>20</sup> In muscle, supplementation with a NAD<sup>+</sup> precursor, nicotinamide riboside, also accelerated regeneration in young and aged mice in a model of cardiotoxin-induced muscle damage.<sup>23</sup> However, the intricacies of the interaction between H<sub>2</sub>S and NAD<sup>+</sup> have not yet been elucidated.

To investigate the effect of H<sub>2</sub>S on neovascularization, we used a model of limb ischemia and transgenic mice overexpressing CGL (CGL<sup>T9</sup>). We identified CGL as a potent proangiogenic trigger *in vivo*, which was associated with changes in the NAD<sup>+</sup> pathway.

## METHODS

The materials and reagents used are described in [Supplementary Tables I-IV](#) (online only).

**Mice.** Male mice, aged 10 to 12 weeks, both wild type (WT) and CGL<sup>T9</sup> on a C57BL/6J genetic background, were used for all experiments. The CGL<sup>T9</sup> mice have been previously described.<sup>24</sup> All mice were housed in standard housing conditions (22°C, 12-hour light/dark cycle), with ad libitum access to water and a regular diet (SAFE 150 SP-25 vegetal diet; SAFE Diets, Augy, France). All animal experiments conformed to the U.S. National Research Council's *Guide for the Care and Use of Laboratory Animals*.<sup>25</sup> The Lausanne University Hospital and the Cantonal Veterinary Office approved all animal care, surgery, and euthanasia procedures (SCAV-EXPANIM, authorization nos. 3258 and 3504).

**Hindlimb ischemia model.** The hindlimb ischemia model was performed as previously described.<sup>17</sup> In brief, the mice were anesthetized with isoflurane (2.5% with 2.5 L of oxygen), and the body temperature was maintained on a circulating heated pad. After a 1-cm groin incision, the neurovascular pedicle was visualized under



a microscope (Z2 Zoom Stereo Microscope; LW Scientific, Lawrenceville, GA). The femoral nerve and vein were separated from the femoral artery. The femoral artery was ligated proximally and above both the proximal caudal femoral and superficial caudal epigastric arteries, allowing for electrocoagulation of the left common femoral artery and sparing the vein and nerve.<sup>26</sup> Buprenorphine (Temgesic; 0.1 mg/kg; Reckitt Benckiser AG, Wallisellen-Zürich, Switzerland) was provided before surgery, with an analgesic administered postoperatively every 12 hours for 36 hours.

**Laser Doppler perfusion imaging.** Laser Doppler perfusion imaging (LDPI) was performed as described previously.<sup>17</sup> In brief, the mice were kept under isoflurane anesthesia, and the body temperature was maintained using a circulating heated pad. Once unconscious, we subjected the mouse hindlimbs to LDPI (Moor Instruments Ltd, Axminster, UK) with a low-intensity (2 mW) laser light beam (wavelength 632.8 nm). The hindlimb blood flow was recorded as a two-dimensional color-coded image, with a scan setting of 2 ms/pixel. Blood flow recovery was monitored at baseline and on days 0 (immediately after surgery), 1, 3, 5, 7, 10, and 14. The LDPI intensity of the ischemic foot was normalized to the corresponding contralateral foot and expressed as ratio between the ischemic and nonischemic limb.

**Treadmill test.** At 14 days after hindlimb ischemia, the mice were acclimated to the treadmill (six-lane treadmill; Columbus Instruments, Columbus, OH) at 8 m/min for 5 minutes for 5 days before exercise testing. The next day, the mice were run until exhaustion at a 5° incline at 8 m/min for 10 minutes, followed by 10 m/min for 5 minutes, with a 2-m/min increase in speed every 5 minutes until exhaustion. Exhaustion was defined as follows: the mice had remained on the electric grid for 5 seconds, had remained on the electric grid for 25 seconds in total, had received >25 shocks in 3 minutes, or had received >200 shocks in total.

**H<sub>2</sub>S production assay.** Measurement of the H<sub>2</sub>S production capacity in tissues was performed as previously described.<sup>17,27</sup> In brief, 80 μg of protein was incubated in 10 mM L-cysteine and 1 mM pyridoxal 5'-phosphate hydrate (Sigma-Aldrich, St Louis, MO), or 20 μL of plasma was incubated in 100 mM L-cysteine and 10 mM pyridoxal 5'-phosphate hydrate. This mixture was sealed under lead acetate paper and incubated until black lead sulfide precipitate was detected, but not saturated. The lead sulfide presence was quantified using Fiji software, version 1.53f51 (available at: <http://fiji.sc/Fiji>).

**NAD<sup>+</sup>/NADH quantification.** The NAD<sup>+</sup>/NADH level was determined using the NAD/NADH assay kit (Abcam, Cambridge, UK) according to the manufacturer's instructions. Pulverized tissue (20 mg) was dissolved in the assay buffer

from the kit as suggested by the manufacturer and normalized to the protein content using the Pierce BCA protein assay kit (Thermo Fisher Scientific, Waltham, MA), with 250 μg of protein used for each reaction. The NAD<sup>+</sup> and NADH concentrations are expressed as ng/mg protein.

**Metabolomics.** Polar metabolite profiling was performed as described previously.<sup>28</sup> In brief, 20 mg of mouse gastrocnemius tissue was homogenized on dry ice in 80% methanol and kept at -80°C overnight. The debris was pelleted and the methanol suspension dried under nitrogen. The resulting pellet was resuspended in water, and the metabolites were measured using targeted tandem mass spectrometry with polarity switching and selected reaction monitoring with an AB/SCIEX 6500 QTRAP mass spectrometer.

**Immunohistochemistry.** Immunohistochemistry was performed on 10-μm frozen sections of gastrocnemius muscle. After 5 minutes of fixation in 4% paraformaldehyde and rinsing in phosphate-buffered saline (PBS), immunostaining was performed as previously described.<sup>17,29</sup> The slides were incubated overnight with vascular endothelial-cadherin (VE-cad; 1:200; CD144; BD Pharmingen; BD Biosciences, Franklin Lakes, NJ) rat anti-mouse primary antibody, followed by AlexaFluor 488 anti-rat secondary antibody, and washed and mounted in DAPI (4',6'-diamidino-2-phenylindole)-containing Vectashield fluorescent mounting medium (Vector Laboratories, Burlingame, CA). The sections were then scanned using an Axioscan microscope (Carl Zeiss, Oberkochen, Germany). The VE-cad-positive area of whole muscle was quantified blindly using Fiji software, version 1.53f51 (available at: <http://fiji.sc/Fiji>). Quantifications are expressed as a percentage of the VE-cad-positive area to the total surface area of the gastrocnemius muscle.

**Immunostaining of whole retina mounts.** The eyes from 5-day-old pups were harvested and fixed for 2 hours at 4°C in 1% to 4% paraformaldehyde, under gentle stirring. The retinas were isolated, stored in methanol at -20°C, and immunostained according to the reported protocols.<sup>30-32</sup> The permeabilized retinas were incubated overnight at 4°C with biotinylated isolectin B4 (B-1205, diluted 1:500; Vector Laboratories). The retinas were imaged using a Zeiss LSM 780 GaAsp inverted laser scanning fluorescence microscope (Carl Zeiss). The vascular radial extension was quantified by dividing the area labeled by isolectin B4 by the total area of the retina using the angiogenesis analyzer plugin on Fiji (available at: <http://fiji.sc/Fiji>).

**Aortic ring sprouting assay.** The aortic ring assay was performed as previously described.<sup>33</sup> In brief, mouse thoracic aortas were isolated and cut into 1-mm-wide rings and embedded in Matrigel (Corning, Corning, NY) and incubated in EBM-2 (Lonza Inc, Basel, Switzerland)



supplemented with VEGFA alone or full EC growth medium-2 (EGM-2) containing VEGFA, fibroblast growth factor, epidermal cell growth factor, and insulin-like growth factor-1 (Lonza Inc). The media were replaced every 2 days. For each sample, the length of eight sprouts at days 6 and 8, originating from the aorta, were quantified using the Fiji software (available at: <http://fiji.sc/Fiji>) from brightfield images taken at 2× magnification.

**Cell culture.** Pooled human umbilical vein ECs (HUVECs; Lonza Inc) were maintained in EGM-2 (Bullet-Kit; Lonza Inc) at 37°C, with 5% carbon dioxide and 5% oxygen, as previously described.<sup>29</sup> Passages 1 to 8 were used for the described experiments.

**Cell migration assay.** HUVECs were grown to confluence in a 12-well plate, and a scratch wound was created using a sterile P200 pipette tip, as previously described.<sup>17</sup> Repopulation of the wound in the presence of mitomycin C was recorded using phase-contrast microscopy for 16 hours in a Nikon Ti2-E live-cell microscope (Nikon, Tokyo, Japan). The denuded area was measured at 0 hours and 10 hours after wound creation and quantified using ImageJ software, version 1.53f51 (available at: <http://fiji.sc/Fiji>). Data are expressed as a ratio of the healed area over the initial wound area.

**Cell proliferation assay.** HUVECs were grown at 80% confluence ( $5 \times 10^3$  cells per well) on glass coverslips in a 24-well plate and starved overnight in serum-free medium (EBM-2; Lonza Inc). Next, they were incubated for 24 hours in EGM-2 containing 10  $\mu$ M bromodeoxyuridine. Immunostaining was performed on cells washed and fixed for 5 minutes in  $-20^\circ\text{C}$  methanol, air-dried, rinsed in PBS, and permeabilized for 10 minutes in PBS supplemented with 2% bovine serum albumin and 0.1% Triton X-100. Bromodeoxyuridine-positive nuclei were automatically detected in ImageJ software, version 1.53f51 (available at: <http://fiji.sc/Fiji>) and normalized to the total number of DAPI-positive nuclei.<sup>29</sup>

**Western blotting.** Gastrocnemius and soleus muscle samples were collected and flash-frozen in liquid nitrogen, ground to powder, and resuspended in sodium dodecyl sulfate (SDS) lysis buffer (62.5 mM TRIS; pH 6.8; 5% SDS; 10 mM EDTA [ethylenediaminetetraacetic acid]). The protein concentration was determined using the DC (detergent compatible) protein assay (Bio-Rad Laboratories, Reinach, Switzerland), and 10 to 20  $\mu$ g of protein were loaded per well. The primary cells were washed once with ice-cold PBS and directly lysed with Laemmli buffer, as previously described.<sup>29,34</sup> The lysates were resolved using SDS-PAGE (polyacrylamide gel electrophoresis) and transferred to a PVDF (polyvinylidene fluoride) membrane (Immobilon-P; Millipore AG, Aldorf, Switzerland). Immunoblot analyses were performed as previously described using the antibodies

listed in **Supplementary Table I** (online only).<sup>34</sup> Membranes were revealed by enhanced chemiluminescence (Immobilon; Millipore) using the Azure 280 device (Azure Biosystems, Dublin, CA) and analyzed using Fiji (ImageJ, version 1.53c). Protein abundance was normalized to total protein using the Pierce reversible protein stain kit for PVDF membranes (catalog no. 24,585; Thermo Fisher Scientific).

**Reverse transcription and quantitative polymerase chain reaction.** Pulverized frozen gastrocnemius muscles were homogenized in Tripure isolation reagent (Roche, Basel, Switzerland), and total RNA was extracted as previously described.<sup>17</sup> After RNA reverse transcription (Prime Script RT reagent; Takara Bio, Shagara, Japan), cDNA levels were measured using quantitative polymerase chain reaction (PCR) and the Fast SYBR Green Master Mix (reference no. 4,385,618; Applied Biosystems; Thermo Fisher Scientific) in a Quant Studio 5 Real-Time PCR System (Applied Biosystems, Thermo Fisher Scientific), using the primers detailed in **Supplementary Table II** (online only).

**Statistical analysis.** The data are displayed as the mean  $\pm$  standard error of the mean. Statistical significance was assessed in GraphPad Prism, version 9.1.0 (GraphPad, San Diego, CA) using the Student *t* test or one-way or two-way analysis of variance, unless otherwise specified. A *P* value of  $\leq .05$  was deemed statistically significant. Metabolomics data were analyzed using MetaboAnalyst software, version 5.0.<sup>35</sup>

## RESULTS

First, we characterized CGL expression in the gastrocnemius muscles from WT (CGL<sup>WT</sup>) and CGL<sup>T9</sup> mice under baseline (nonischemic) conditions. As expected, CGL, but not CBS or 3-mercaptopyruvate sulfurtransferase, mRNA expression was increased in CGL<sup>T9</sup> muscle (**Fig 1, A**). Consistently, the CGL protein levels were 4.8-fold higher in the CGL<sup>T9</sup> gastrocnemius muscle (**Fig 1, B**). CGL immunostaining further showed that in the gastrocnemius muscle, CGL was mostly expressed by ECs and increased specifically in VE-cad<sup>+</sup> ECs on CGL overexpression (**Fig 1, C**). The number of VE-cad<sup>+</sup> ECs in the gastrocnemius muscle was similar in both CGL<sup>WT</sup> and CGL<sup>T9</sup> mice (**Fig 1, C** and **Supplementary Fig 1**, online only). CGL overexpression correlated with an increase in H<sub>2</sub>S production in the whole muscle (1.5-fold; **Fig 1, D**) and serum (**Fig 1, E**). CGL and H<sub>2</sub>S production were also increased in the liver (**Supplementary Fig 2, A and D**, online only), kidney (**Supplementary Fig 2, B and E**, online only), and aorta (**Supplementary Fig 2, C and F**, online only) of CGL<sup>T9</sup> mice.

We previously reported that H<sub>2</sub>S/CGL triggers angiogenesis under amino acid restriction.<sup>17</sup> We tested whether CGL overexpression alone was sufficient to



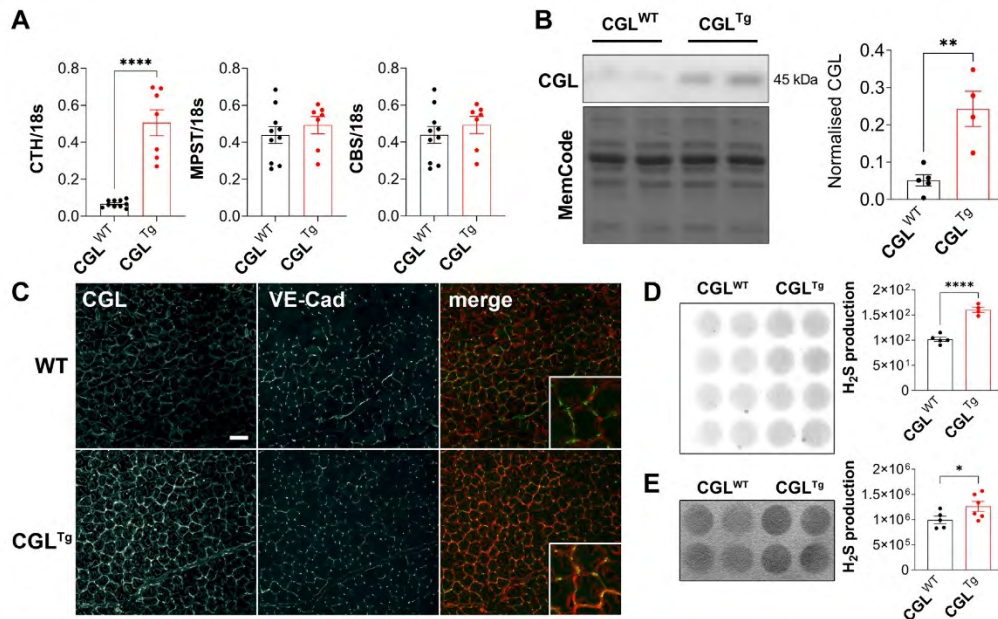


**Fig 1.** Hydrogen sulfide (H<sub>2</sub>S) production is enhanced in cystathionine-γ-lyase (CGL)-overexpressing (CGL<sup>Tg</sup>) gastrocnemius muscle. **A**, Quantitative real-time polymerase chain reaction (PCR) gene expression analysis of H<sub>2</sub>S-generating enzymes (CGL [CTH], 3-mercaptopyruvate sulfur transferase [MPST], and cystathionine-β-synthase [CBS]) in gastrocnemius muscle at baseline, normalized to 18S expression (n = 7-10 mice/group). **B**, CGL protein abundance in gastrocnemius muscle of CGL wild-type (CGL<sup>WT</sup>) and CGL<sup>Tg</sup> mice at baseline by Western blot (Pierce reversible protein stain [Thermo Fisher Scientific] served as the loading control; n = 4-5 mice/group). **C**, Representative images of baseline gastrocnemius muscle sections (original magnification ×20) immunostained with CGL and vascular endothelial-cadherin (VE-cad) antibodies. Baseline CGL-mediated H<sub>2</sub>S production capacity in CGL<sup>WT</sup> and CGL<sup>Tg</sup> mice gastrocnemius muscle (**D**) and plasmatic H<sub>2</sub>S production (**E**) detected by lead acetate assay (n = 5-6 mice/group). Data presented as mean ± standard error of the mean \*\*P < .01 and \*\*\*\*P < .0001, Student's *t* test.

promote neovascularization in the hindlimb ischemia model.<sup>17</sup> Although the blood flow had been similarly interrupted in all mice immediately after ligation (day 0), the return of blood flow was accelerated in the CGL<sup>Tg</sup> mice (Fig 2, A). The improvement in leg perfusion correlated with an increased running duration and distance run on a treadmill at 14 days after ligation (Fig 2, B). Immunostaining of gastrocnemius muscle sections at 21 days after ischemia induction indicated increased VE-cad-positive EC in the ischemic legs of the CGL<sup>Tg</sup> mice (Fig 2, C) and reduced the muscle damage (Fig 2, D).

Next, we sought to better characterize the effects of CGL overexpression on sprouting angiogenesis using an aortic ring assay. In both complete EGM-2 and VEGFA-only media, vessel sprouting from aortic explants was significantly increased in the CGL<sup>Tg</sup> mice compared with the CGL<sup>WT</sup> mice, with a greater magnitude of increase with the VEGFA-only media (Fig 3, A and B). Developmental angiogenesis was not affected by CGL

overexpression, as demonstrated by the pup retina vascular network at postnatal day 5 (Fig 3, C).

To elucidate the mechanism of CGL-dependent angiogenesis, we performed targeted metabolomics on the baseline (nonischemic) CGL<sup>WT</sup> and CGL<sup>Tg</sup> mice. This revealed only three significantly differentially abundant metabolites; betaine (0.28 log<sub>2</sub>-fold change), kynurenic acid (-0.71 log<sub>2</sub>-fold change), and niacinamide (0.4 log<sub>2</sub>-fold change; Fig 4, A and Supplementary Table III, online only). The increase in niacinamide was of particular interest because of its role as a key precursor of NAD<sup>+</sup>/NADH.<sup>20</sup> Consistently, the NADH level had increased twofold, and the NAD<sup>+</sup> level had decreased equally in the gastrocnemius muscle (Fig 4, B) and liver (Fig 4, C) of the CGL<sup>Tg</sup> mice. Quantitative PCR analyses of the genes associated with NAD<sup>+</sup>/NADH metabolism revealed increased expression of the NAD<sup>+</sup> salvage pathway genes *Nmnat1*, *Nmnat2*, and *Nmnat3* (Fig 4, D). Expression of *SIRT1*, a major NAD<sup>+</sup> consuming enzyme, was also increased in the CGL<sup>Tg</sup> mice (Fig 4, D).

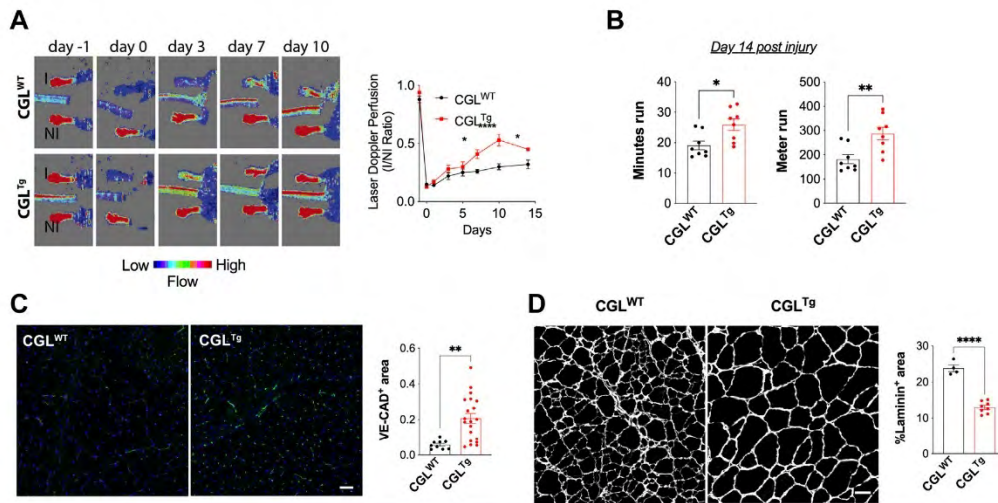


**Fig 2.** Cystathionine- $\gamma$ -lyase (CGL)-overexpressing (CGL<sup>T9</sup>) mice showed improved protection from hindlimb ischemia (HLI). **A**, Superficial perfusion of mouse hindlimb measured by laser Doppler perfusion imaging (LDPI). Results illustrated by representative LDPI images (Left) and ratio of LDPI perfusion quantification in ischemic and nonischemic limbs (Right;  $n = 8$ /group). **B**, Time (Left) and distance (Right) run on incremental speed test at day 14 after HLI ( $n = 8$ /group). **C**, Gastrocnemius muscle tissue perfusion 21 days after HLI shown in representative images and quantification (Right) of transverse sections stained with vascular endothelial-cadherin (VE-cad;  $n = 10$ -20/group). Scale bar = 50  $\mu$ m. **D**, Representative transverse sections (Left) and quantification (Right) of laminin staining of gastrocnemius muscle at 21 days after HLI ( $n = 4$ -8/group). Scale bar = 50  $\mu$ m. Data presented as mean  $\pm$  standard error of the mean \* $P < .05$  and \*\* $P < .01$ , Student's  $t$  test.

Further *in vitro* experiments conducted in human ECs (HUVECs) indicated that adenoviral-mediated CGL overexpression or treatment with the NAD<sup>+</sup> precursor NMN promoted HUVEC migration. However, the combination of CGL overexpression and NMN did not result in further improvement, suggesting a redundant effect on migration (Fig 4, E). CGL overexpression or NMN treatment had no effect on cell proliferation (Supplementary Fig 3, online only).

## DISCUSSION

In the present study, we have demonstrated a beneficial role for CGL overexpression in a murine model of PAD. In addition, CGL overexpression modulated the NAD<sup>+</sup>/NADH biosynthesis pathway, which improved EC migration, angiogenesis, and recovery from hindlimb ischemia.

Our *in vivo* findings have built on previous work suggesting that H<sub>2</sub>S is beneficial for neovascularization of the ischemic hindlimb.<sup>11,13,36</sup> CGL overexpression predominantly promoted VEGFA-dependent sprouting angiogenesis, building on our previous findings that amino acid restriction induces CGL overexpression and H<sub>2</sub>S production, which stimulates VEGFA-dependent EC migration and angiogenesis<sup>17</sup> via persulfidation of VEGFR2.<sup>16,37</sup>

We observed that the NAD<sup>+</sup>/NADH precursor niacinamide was increased in the muscle of CGL-overexpressing mice and that the NAD<sup>+</sup>/NADH balance had shifted. Moreover, the expression of several key enzymes within the NAD<sup>+</sup>/NADH biosynthesis pathway changed in response to CGL expression. Prior *in vitro* studies of HUVECs demonstrated a transient increase in the NAD<sup>+</sup> concentration during sodium hydrosulfide treatment.<sup>20</sup> In the present study, the NAD<sup>+</sup>/NADH ratio was decreased in the gastrocnemius of the CGL-overexpressing mice. Our measurements of the steady state metabolite levels limited our interpretations, because differences could exist in the rate of NAD<sup>+</sup> turnover or with differences in the shorter vs longer term effects of H<sub>2</sub>S augmentation. Further experiments using flux measurements with stable isotope-labeled substrate are required to determine the exact relationships and interplay between H<sub>2</sub>S and NAD<sup>+</sup>. An alternative explanation for the CGL-mediated reduced NAD<sup>+</sup>/NADH ratio could stem from an enhancement of glycolysis<sup>17,58</sup> because glycolysis consumes NAD<sup>+</sup> as a coenzyme.<sup>19</sup> Thus, the increase in relative abundance of NADH in the CGL<sup>T9</sup> muscle might represent an increase in glycolysis-related NAD<sup>+</sup> consumption. We previously demonstrated that CGL overexpression in ECs increased glycolysis and adenosine triphosphate production.<sup>17</sup>



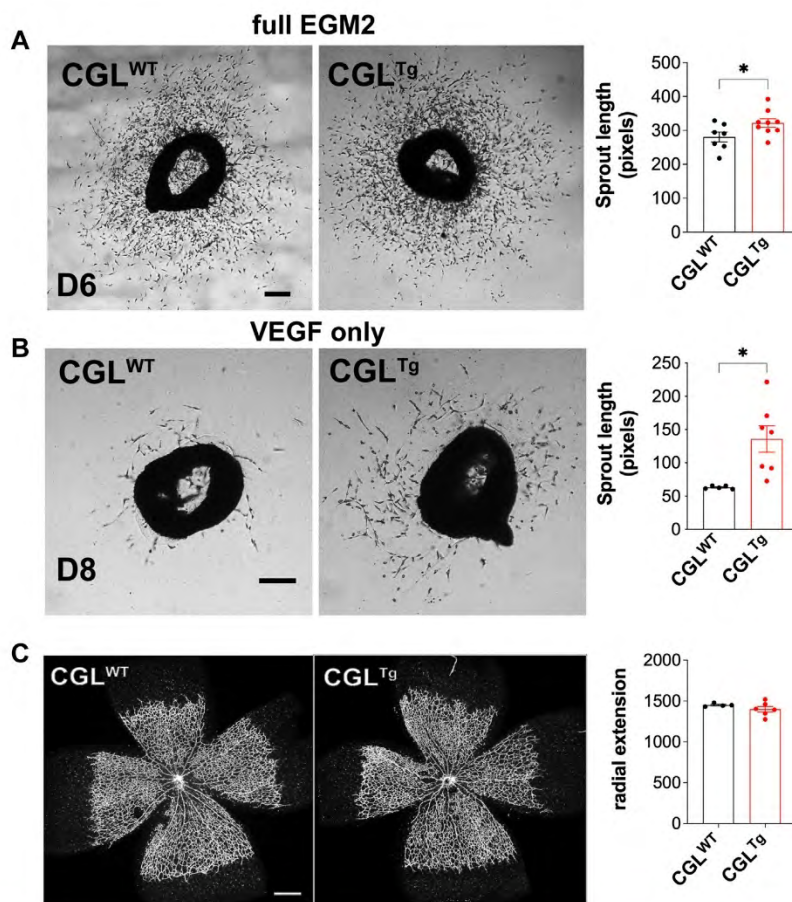


**Fig 3.** Vascular sprouting was accelerated in cystathionine- $\gamma$ -lyase (CGL)-overexpressing (CGL<sup>Tg</sup>) mice. **A**, Average length of microvessel sprouting from aortic ring explants from wild-type CGL (CGL<sup>WT</sup>) and CGL<sup>Tg</sup> mice incubated in full endothelial cell growth medium-2 (EGM-2; n = 7/group). Scale bar = 100  $\mu$ m. **B**, Average length of microvessel sprouting from aortic ring explants from CGL<sup>WT</sup> and CGL<sup>Tg</sup> mice incubated in vascular endothelial growth factor A (VEGFA)-only EBM-2 (n = 7/group). Scale bar = 200  $\mu$ m. **C**, Radial extension of developing mouse retina at postnatal day (D) 5, with representative images (Left) and quantification of radial extension (Right) of whole retina mounts stained with isolectin B4 (n = 4-5/group). Scale bar = 100  $\mu$ m. Data presented as mean  $\pm$  standard error of the mean \*P  $\leq$  .05, Student's t test.

Thus, it is likely that NADH accumulation is driven by NAD<sup>+</sup> consumption, which is known to play a key role in neovascularization during limb ischemia.<sup>20</sup> Despite our observations, the mechanistic understanding of the interplay between H<sub>2</sub>S and the NAD<sup>+</sup>/NADH system is still incomplete and warrants further investigation. Additionally, although the present study has demonstrated that CGL is sufficient in inducing the observed phenotype, it has not demonstrated that CGL is essential for NAD<sup>+</sup> biosynthesis and neovascularization.<sup>11</sup>

In addition, SIRT1 gene expression was increased in CGL<sup>Tg</sup> gastrocnemius. EC-specific SIRT1 knockout

mice have impaired neovascularization and muscle endurance after hindlimb ischemia.<sup>39</sup> Thus, the increased SIRT1 expression seen in CGL-overexpressing mice might support neovascularization. As a NAD<sup>+</sup>-consuming enzyme, SIRT1 increased expression could further reduce the NAD<sup>+</sup> concentration in CGL<sup>Tg</sup> mice. On a cellular level, we found that boosting H<sub>2</sub>S and NAD<sup>+</sup>/NADH production enhanced EC migration but not proliferation in vitro. This is consistent with prior studies, which highlighted substantial improvements in EC migration with H<sub>2</sub>S supplementation.<sup>17,40</sup> In addition, boosting both H<sub>2</sub>S and NAD<sup>+</sup>/NADH

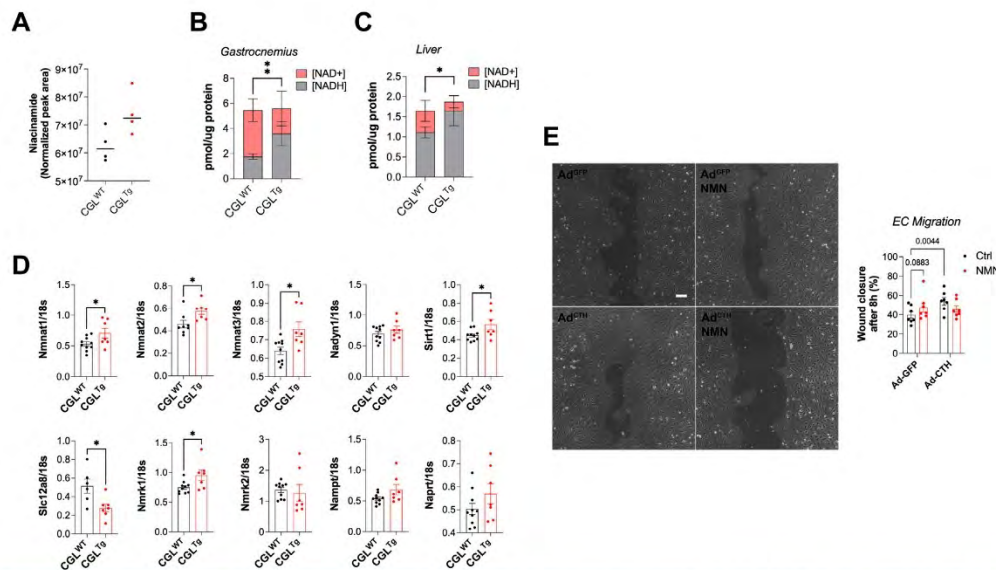


**Fig 4.** Beneficial effects seen in cystathionine- $\gamma$ -lyase (CGL)-overexpressing (CGL<sup>Tg</sup>) mice was associated with changes in oxidized/reduced nicotinamide adenine dinucleotide (NAD<sup>+</sup>/NADH) pathways. **A**, Niacinamide level in CGL wild-type (CGL<sup>WT</sup>) and CGL<sup>Tg</sup> gastrocnemius muscle (n = 4).  $P = .0569$ , Student's *t* test. **B**, Quantification of NAD<sup>+</sup> and NADH concentration in gastrocnemius muscle (n = 5). Data presented as mean  $\pm$  standard deviation.  $**P \leq .01$  (Student's *t* test), comparing NADH abundance between groups. **C**, Quantification of NAD<sup>+</sup> and NADH concentration in liver (n = 5). Data presented as mean  $\pm$  standard deviation.  $*P \leq .05$  (Student's *t* test), comparing NADH abundance between groups. **D**, Quantitative real-time polymerase chain reaction (PCR) gene expression analysis of enzymes associated with the NAD<sup>+</sup>/NADH pathway in gastrocnemius muscle. NAD-generating enzymes: Nmnat1, Nmnat2, Nmnat3, and Nadsyn1. NAD salvage pathway: Slc12a8, Nmrk1, Nmrk2, and Nampt. Preiss-Handler pathway: Naprt. NAD-consuming enzyme: SIRT1. All genes were normalized to 18S expression (n = 7-10/group). **E**, Endothelial cell (EC) migration across scratch with representative image (Left: original magnification,  $\times 10$ ) and quantification (Right) of human umbilical vein ECs (HUVECs) infected with green fluorescent protein (GFP)- or CGL-expressing adenovirus (Ad), with or without nicotinamide mononucleotide (NMN) supplementation, as indicated (n = 7/group). Scale bar = 100  $\mu$ m. Data presented as mean  $\pm$  standard error of the mean.  $*P \leq .05$ , Student's *t* test. Ctrl, Control.

pathways simultaneously did not have a synergistic effect on EC migration, suggesting that the promigratory effects of H<sub>2</sub>S and NAD<sup>+</sup>/NADH occur through the same mechanism. Endothelial tip cell migration drives sprouting angiogenesis,<sup>41</sup> and we previously showed that H<sub>2</sub>S promotes VEGFA-dependent tip-cell migration.<sup>17</sup> Thus, we propose that CGL overexpression drives VEGFA-induced tip-cell migration and sprouting angiogenesis to improve neovascularization of the ischemic muscle.

Although our study focused on changes within the NAD<sup>+</sup>/NADH pathways, our metabolomics analysis revealed two other significantly differentially abundant metabolites: betaine (0.28 log<sub>2</sub>-fold change) and kynurenic acid (−0.71 log<sub>2</sub>-fold change). Betaine is a part of the transsulfuration pathway, allowing regeneration of methionine from homocysteine via the betaine homocysteine methyltransferase.<sup>9</sup> Betaine accumulation is consistent with a shift toward the use of homocysteine

to generate cysteine via CGL. The accumulation of kynurenic acid suggests a shift in the kynurenine pathway, outlining the conversion of tryptophan to NAD<sup>+</sup>. Most enzymes in this pathway are dependent on vitamin B<sub>6</sub> pyridoxal 5'-phosphate, similar to the transsulfuration pathway enzymes CGL and CBS. Accumulation of kynurenic acid could have resulted from reduced kynurenine pathway activity due to NAD<sup>+</sup> accumulation or increased pyridoxal 5'-phosphate usage by CGL. Both the betaine and tryptophan/kynurenic acid pathways are important in the regulation of immune cells. Previous studies have shown that macrophages are polarized toward the pro-repair M2 phenotype in the presence of betaine.<sup>42</sup> Moreover, the same phenomenon was observed in the context of indoleamine 2,3-dioxygenase overexpression, a key enzyme driving the catabolism of tryptophan to kynurenic acid.<sup>43</sup> The M2 macrophage phenotype has been shown to be vital to neovascularization in the context of the hindlimb ischemia model<sup>44</sup>



and could, hence, posit a plausible mechanism of action to explain the improvements in neovascularization with CGL overexpression.

Although our findings have given us cause to be optimistic, we are aware of our study's limitations. We endeavored to replicate PAD pathology with our hindlimb ischemia procedure. Although it might be the reference standard in replicating the pathology *in vivo*, it does not reflect the chronic nature of PAD development. We recently demonstrated that the H<sub>2</sub>S production capacity and plasma sulfide concentrations were reduced in patients with PAD.<sup>15</sup> The chronicity of PAD might allow for the development of compensatory adaptations, absent in the hindlimb ischemia model. Furthermore, we have yet to fully characterize the potential off-target effects of CGL overexpression, which might induce adaptations independently of H<sub>2</sub>S. Thus, one could anticipate changes in the relative levels of sulfur-containing amino acids, which could have unforeseen effects on the ischemic adaptations. From our study, we only drew conclusions regarding the effects of the global increase in CGL; however, it remains to be seen whether the protection is due to CGL overexpression locally within ECs or due to distal systemic CGL overexpression. Because our long-term goal is to offer therapeutic angiogenesis, it will be important to identify the cell types and organ systems that drive the proangiogenic phenotype. In addition, EC migration assays were performed of HUVECs because they are readily available and able to migrate.<sup>17,20</sup> However, HUVECs might not be representative of the actual *in vivo* conditions because they derive from immune-privileged fetal tissue. Thus, these data should be reproduced in arterial ECs (eg, human aortic ECs), which might be more closely related to what occurs in patients with PAD. Finally, only male mice were used in the present study; thus, the response to CGL overexpression might be different in female mice and deserves investigation in the future.

## CONCLUSIONS

In the present study, we have outlined the beneficial effects of CGL overexpression in improving neovascularization and functional recovery in a murine PAD model. Taken together with other reported studies, our study has further highlighted the untapped potential of targeting CGL for therapeutic interventions in patients with PAD.

## AUTHOR CONTRIBUTIONS

Conception and design: KK, MM, PK, CO, JM, SD, SM, FA, AL  
Analysis and interpretation: KK, MM, PK, TA, SM, FA, AL  
Data collection: KK, MM, PK, TA, DM, ML, LH, FA, AL  
Writing the article: KK, MM, TA, SM, FA, AL  
Critical revision of the article: KK, PK, DM, ML, LH, CO, JM, SD, SM, AL

Final approval of the article: KK, MM, PK, TA, DM, ML, LH, CO, JM, SD, SM, FA, AL

Statistical analysis: KK, MM, FA, AL

Obtained funding: MM, JM, SD, FA, AL

Overall responsibility: AL

FA and AL contributed equally to this article and share co-senior authorship.

## REFERENCES

1. Fowkes FGR, Rudan D, Rudan I, Aboyans V, Denenberg JO, McDermott MM, et al. Comparison of global estimates of prevalence and risk factors for peripheral artery disease in 2000 and 2010: a systematic review and analysis. *Lancet* 2013;382:1329-40.
2. Kullo IJ, Rooke TW. Peripheral artery disease. *N Engl J Med* 2016;374:861-71.
3. Dragneva G, Korpisalo P, Yla-Herttuala S. Promoting blood vessel growth in ischemic diseases: challenges in translating preclinical potential into clinical success. *Dis Model Mech* 2013;6:312-22.
4. Couffinhal T, Silver M, Zheng L, Kearney M, Witzenzon B, Isner J. Mouse model of angiogenesis. *Am J Pathol* 1998;152:1667-79.
5. Iyer SR, Annex BH. Therapeutic angiogenesis for peripheral artery disease: lessons learned in translational science. *JACC Basic Transl Sci* 2017;2:503-12.
6. Kusumanto Y, Van Weel V, Mulder N, Smit A, Van Den Dungen J, Hooymans J, et al. Treatment with intramuscular vascular endothelial growth factor gene compared with placebo for patients with diabetes mellitus and critical limb ischemia: a double-blind randomized trial. *Hum Gene Ther* 2006;17:683-91.
7. Giroud S, Hahad C, Nespolo RF, Mejias C, Terrier J, Logan SM, et al. The torpid state: recent advances in metabolic adaptations and protective mechanisms<sup>1</sup>. *Front Physiol* 2020;11:623665.
8. Li L, Rose P, Moore PK. Hydrogen sulfide and cell signaling. *Annu Rev Pharmacol Toxicol* 2011;51:169-87.
9. Wallace JL, Wang R. Hydrogen sulfide-based therapeutics: exploiting a unique but ubiquitous gasotransmitter. *Nat Rev Drug Discov* 2015;14:329-45.
10. Yang C, Wu L, Jiang B, Yang W, Qi J, Cao K, et al. H<sub>2</sub>S as a physiologic vasorelaxant: hypertension in mice with deletion of cystathionine gamma-lyase. *Science* 2008;322:587-90.
11. Kolluru GK, Bir SC, Yuan S, Shen X, Pardue S, Wang R, et al. Cystathionine gamma-lyase regulates arteriogenesis through NO-dependent monocyte recruitment. *Cardiovasc Res* 2015;107:590-600.
12. Mani S, Li H, Untereiner A, Wu L, Yang G, Austin RC, et al. Decreased endogenous production of hydrogen sulfide accelerates atherosclerosis. *Circulation* 2013;127:2523-34.
13. Rushing AM, Donnarumma E, Polhemus DJ, Au KR, Victoria SE, Schumacher JD, et al. Effects of a novel hydrogen sulfide prodrug in a porcine model of acute limb ischemia. *J Vasc Surg* 2019;69:1924-35.
14. Jain SK, Bull R, Rains JL, Bass PF, Levine SN, Reddy S, et al. Low levels of hydrogen sulfide in the blood of diabetes patients and streptozotocin-treated rats causes vascular inflammation? *Antioxid Redox Signal* 2010;12:1333-7.
15. Longchamp A, MacArthur MR, Trocha K, Ganahl J, Mann CG, Kip P, et al. Plasma hydrogen sulfide is positively associated with post-operative survival in patients undergoing surgical revascularization. *Front Cardiovasc Med* 2021;8:750926.
16. Tao BB, Liu SY, Zhang CC, Fu W, Cai WJ, Wang Y, et al. VEGFR2 functions as an H<sub>2</sub>S-targeting receptor protein kinase with its novel Cys1045-Cys1024 disulfide bond serving as a specific molecular switch for hydrogen sulfide actions in vascular endothelial cells. *Antioxid Redox Signal* 2013;19:448-64.
17. Longchamp A, Mirabella T, Arduini A, MacArthur MR, Das A, Trevino-Villarreal JH, et al. Amino acid restriction triggers angiogenesis via GCN2/ATF4 regulation of VEGF and H<sub>2</sub>S production. *Cell* 2018;173:117-29.e14.
18. Covarrubias AJ, Perrone R, Grozio A, Verdin E. NAD(+) metabolism and its roles in cellular processes during ageing. *Nat Rev Mol Cell Biol* 2021;22:119-41.
19. Xie N, Zhang L, Gao W, Huang C, Huber PE, Zhou X, et al. NAD(+) metabolism: pathophysiologic mechanisms and therapeutic potential. *Signal Transduct Target Ther* 2020;5:227.

20. Das A, Huang GX, Bonkowski MS, Longchamp A, Li C, Schultz MB, et al. Impairment of an endothelial NAD(+)-H2S signaling network is a reversible cause of vascular aging. *Cell* 2018;173:74-89.e20.
21. Hu M, Zhou B, Mao H, Sheng Q, Du B, Chen J, et al. Exogenous hydrogen sulfide postconditioning protects isolated rat hearts from ischemia/reperfusion injury through SIRT1/PGC-1 $\alpha$  signaling pathway. *Int Heart J* 2016;57:477-82.
22. Borradaile NM, Pickering JG. Nicotinamide phosphoribosyltransferase imparts human endothelial cells with extended replicative lifespan and enhanced angiogenic capacity in a high glucose environment. *Aging Cell* 2009;8:100-12.
23. Zhang H, Ryu D, Wu Y, Gariani K, Wang X, Luan P, et al. NAD<sup>+</sup> repletion improves mitochondrial and stem cell function and enhances life span in mice. *Science* 2016;352:1436-43.
24. Trocha KM, Kip P, Tao M, MacArthur MR, Trevino-Villarreal JH, Longchamp A, et al. Short-term preoperative protein restriction attenuates vein graft disease via induction of cystathionine gamma-lyase. *Cardiovasc Res* 2020;116:416-28.
25. National Research Council (US) Committee for the Update of the Guide for the Care and Use of Laboratory Animals. *Guide for the Care and Use of Laboratory Animals*. National Academies Press; 2011.
26. Kochi T, Imai Y, Takeda A, Watanabe Y, Mori S, Tachi M, et al. Characterization of the arterial anatomy of the murine hindlimb: functional role in the design and understanding of ischemia models. *PLoS One* 2013;8:e84047.
27. Hine C, Harputlugil E, Zhang Y, Ruckenstein C, Lee BC, Brace L, et al. Endogenous hydrogen sulfide production is essential for dietary restriction benefits. *Cell* 2015;160:132-44.
28. Yuan M, Breitkopf SB, Yang X, Asara JM. A positive/negative ion-switching, targeted mass spectrometry-based metabolomics platform for bodily fluids, cells, and fresh and fixed tissue. *Nat Protoc* 2012;7:872-81.
29. Longchamp A, Kaur K, Macabrey D, Dubuis C, Corpataux JM, Deglise S, et al. Hydrogen sulfide-releasing peptide hydrogel limits the development of intimal hyperplasia in human vein segments. *Acta Biomater* 2019;97:374-84.
30. Hamard L, Santoro T, Allagnat F, Meda P, Nardelli-Haeffliger D, Alonso F, et al. Targeting connexin37 alters angiogenesis and arteriovenous differentiation in the developing mouse retina. *FASEB J* 2020;34:8234-49.
31. Haeffliger JA, Allagnat F, Hamard L, Le Gal L, Meda P, Nardelli-Haeffliger D, et al. Targeting Cx40 (connexin 40) expression or function reduces angiogenesis in the developing mouse retina. *Arterioscler Thromb Vasc Biol* 2017;37:2136-46.
32. Pitulescu ME, Schmidt I, Benedito R, Adams RH. Inducible gene targeting in the neonatal vasculature and analysis of retinal angiogenesis in mice. *Nat Protoc* 2010;5:1518-34.
33. Baker M, Robinson SD, Lechertier T, Barber PR, Tavora B, D'Amico G, et al. Use of the mouse aortic ring assay to study angiogenesis. *Nat Protoc* 2011;7:89-104.
34. Allagnat F, Dubuis C, Lambelet M, Le Gal L, Alonso F, Corpataux JM, et al. Connexin 37 reduces smooth muscle cell proliferation and intimal hyperplasia in a mouse model of carotid artery ligation. *Cardiovasc Res* 2017;113:805-16.
35. Pang Z, Chong J, Zhou G, de Lima Morais DA, Chang L, Barette M, et al. MetaboAnalyst 5.0: narrowing the gap between raw spectra and functional insights. *Nucleic Acids Res* 2021;49:W388-96.
36. Xia H, Li Z, Sharp TE III, Polhemus DJ, Carnal J, Moles KH, et al. Endothelial cell cystathionine gamma-lyase expression level modulates exercise capacity, vascular function, and myocardial ischemia reperfusion injury. *J Am Heart Assoc* 2020;9:e017544.
37. Saha S, Chakraborty PK, Xiong X, Dwivedi SK, Mustafi SB, Leigh NR, et al. Cystathionine beta-synthase regulates endothelial function via protein S-sulfhydration. *FASEB J* 2016;30:441-56.
38. De Bock K, Georgiadou M, Schoors S, Kuchnio A, Wong BW, Cantelmo AR, et al. Role of PFKFB3-driven glycolysis in vessel sprouting. *Cell* 2013;154:651-63.
39. Potente M, Ghaeni L, Baldessari D, Mostoslavsky R, Rossig L, Dequiedt F, et al. SIRT1 controls endothelial angiogenic functions during vascular growth. *Genes Dev* 2007;21:2644-58.
40. Macabrey D, Longchamp A, MacArthur MR, Lambelet M, Urfer S, Deglise S, et al. Sodium thiosulfate acts as a hydrogen sulfide mimetic to prevent intimal hyperplasia via inhibition of tubulin polymerisation. *EBioMedicine* 2022;78:103954.
41. De Bock K, Georgiadou M, Carmeliet P. Role of endothelial cell metabolism in vessel sprouting. *Cell Metab* 2013;18:634-47.
42. Chen A, An Y, Huang W, Xuan T, Zhang Q, Ye M, et al. Highly water-preserving zwitterionic betaine-incorporated collagen sponges with anti-oxidation and anti-inflammation for wound regeneration. *Front Cell Dev Biol* 2020;8:491.
43. Wang XF, Wang HS, Wang H, Zhang F, Wang KF, Guo Q, et al. The role of indoleamine 2,3-dioxygenase (Ido) in immune tolerance: focus on macrophage polarization of THP-1 cells. *Cell Immunol* 2014;289:42-8.
44. Zhang J, Muri J, Fitzgerald G, Gorski T, Gianni-Barrera R, Masschelein E, et al. Endothelial lactate controls muscle regeneration from ischemia by inducing M2-like macrophage polarization. *Cell Metab* 2020;31:1136-53.

Submitted Jul 1, 2022; accepted Nov 10, 2022.



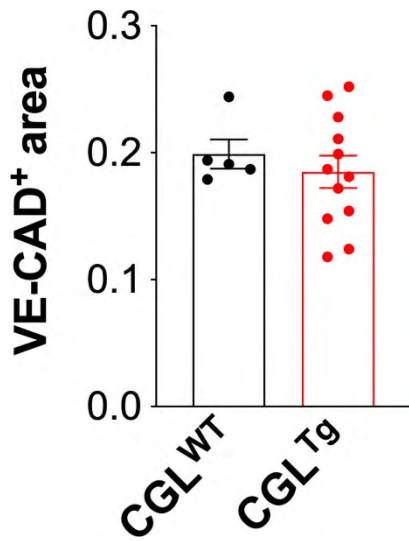


Figure S1.

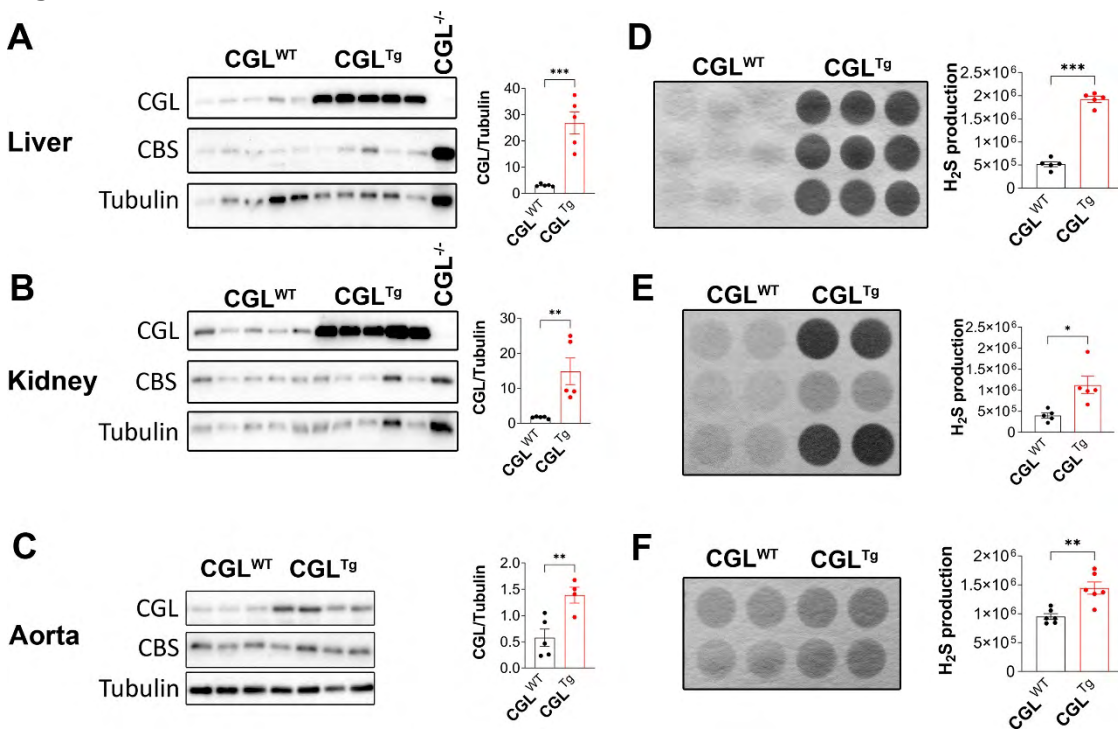


Figure S2.

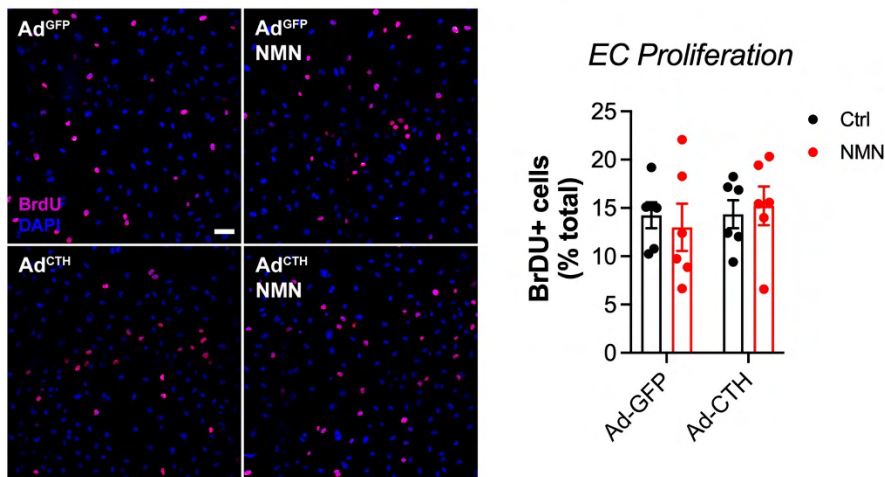


Figure S3.

1 **Association of Kidney Graft 10-Year Outcome with Recipient Cystathionine Gamma-Lyase**  
2 **Polymorphisms and Hydrogen Sulfide Levels: A Cohort Study**

3

4 Matthieu Halfon<sup>1\*</sup>, Raffaella Emsley<sup>2\*</sup>, Thomas Agius<sup>2</sup>, Arnaud Lyon<sup>1,2</sup>, Sébastien Déglise<sup>2</sup>, Manuel  
5 Pascual<sup>1</sup>, Korkut Uygun<sup>3</sup>, James F. Markmann<sup>3</sup>, Pierre-Yves Bochud<sup>4</sup>, Dela Golshayan<sup>1#</sup>, Alban  
6 Longchamp<sup>2,3#</sup>, and the Swiss Transplant Cohort Study <sup>§</sup>

7

8 ORCID ID

9 D Golshayan 0000-0001-5631-6096

10 A Longchamp 0000-0002-1743-4935

11

12 <sup>1</sup>Department of Medicine, Transplantation Centre and Transplantation Immunopathology Laboratory,  
13 Lausanne University Hospital and University of Lausanne, Lausanne, Switzerland

14 <sup>2</sup>Department of Vascular Surgery, Lausanne University Hospital and University of Lausanne, Lausanne,  
15 Switzerland

16 <sup>3</sup>Division of Transplant Surgery, Massachusetts General Hospital, Boston, MA, United States

17 <sup>4</sup>Department of Medicine, Infectious Diseases Service, Lausanne University Hospital and University of  
18 Lausanne, Lausanne, Switzerland.

19

20 *\*Contributed equally*

21

22 *#Correspondence to:*

23 alongchamp@mgh.harvard.edu

24 Division of Transplantation, Massachusetts General Hospital

25 55 Fruit Street, Boston, Massachusetts 02114, USA.

26

27 dela.golshayan@chuv.ch

28 Transplantation center, CHUV

29 Rue du Bugnon 46, Lausanne 1011, Switzerland

30

31 **Word count:** 3493

32 **Running headline:** Kidney graft outcome and cystathionine gamma-lyase polymorphisms

33 **Keywords:** hydrogen sulfide, cystathionine gamma-lyase, kidney transplantation, ischemia-reperfusion,  
34 single nucleotide polymorphism.

- 35 **Abbreviations list in alphabetical order:**
- 36 Autosomal dominant polycystic kidney disease: ADPKD
- 37 Body mass index: BMI
- 38 Coronary artery disease: CAD
- 39 Cystathionine gamma-lyase: CGL
- 40 Donation after brain death: DBD
- 41 Donation after cardiocirculatory death: DCD
- 42 Diabetes mellitus: DM
- 43 Ethylenediaminetetraacetic acid: EDTA
- 44 End stage kidney disease: ESKD
- 45 Estimated glomerular filtration rate: eGFR
- 46 Delayed graft function: DGF
- 47 Glomerulonephritis: GN
- 48 Human leucocyte antigen: HLA
- 49 Hydrogen sulfide: H<sub>2</sub>S
- 50 Ischemia-reperfusion injury: IRI
- 51 Major adverse cardiovascular events: MACE
- 52 Phosphate buffered saline: PBS
- 53 Single nucleotide polymorphism: SNP
- 54 Swiss Transplant Cohort Study: STCS
- 55 University of Wisconsin: UW
- 56 Wildtype: WT
- 57

58 **ABSTRACT**

59 Hydrogen sulfide (H<sub>2</sub>S) produced endogenously by the *CTH* gene-encoded cystathionine gamma-lyase  
60 protects from renal ischemia-reperfusion injury in preclinical models. Here, we hypothesized that *CTH*  
61 gene polymorphisms (SNP) and recipient H<sub>2</sub>S serum levels influence kidney graft outcomes after  
62 transplantation. We included all consecutive recipients of a first kidney transplant in the Swiss Transplant  
63 Cohort Study and with available genotyping. In addition, 192 deceased-donor kidney transplants  
64 recipients were randomly selected to measure baseline serum H<sub>2</sub>S levels. The primary composite  
65 endpoint was transplantation failure (graft loss, eGFR<30 ml/min/m<sup>2</sup> or proteinuria>1 g/day) during follow-  
66 up. 604/1243 (48%) patients harbored the *CTH* \*592C>T mutation. During median follow-up (66.5  
67 months, IQR:47.6-106.2), transplantation failure occurred in 499 (40%) patients. Transplantation failure-  
68 free survival at 10 years was improved in SNP carriers (56% vs.52% for the controls, *p*=0.023), with a  
69 robust association after correction for potential confounders (HR=0.83, 95%CI:0.69-0.99, *p*=0.038).  
70 Interestingly, in patients with delayed graft function, high serum H<sub>2</sub>S levels correlated with improved  
71 transplant survival (HR=4.92, 95%CI:1.07-22.5, *p*=0.04). Thus, kidney transplant outcome was  
72 associated with the *CTH* genotype and, to some extent, H<sub>2</sub>S serum levels. Further research is needed to  
73 define the underlying protective mechanisms.

74



75 **INTRODUCTION**

76 In patients suffering from end-stage renal disease, kidney transplantation provides superior survival and  
77 better quality of life compared to dialysis, but is currently limited by the number of available organs <sup>1</sup>. To  
78 address the disparity between organ supply and demand, there has been a growing utilization of donation  
79 after circulatory death (DCD) and extended criteria donors (ECD). However, DCD and ECD kidneys are  
80 more susceptible to ischemia reperfusion injury (IRI), manifest as delayed graft function (DGF), which is  
81 a risk factor for subsequent graft failure/loss <sup>2</sup>. IRI is unavoidable during solid organ transplantation, and  
82 occurs in two steps. First, during ischemia cells switch from an aerobic to an anaerobic metabolism, which  
83 results in a decrease in adenosine triphosphate (ATP) production, intracellular acidosis, leakage of  
84 lysosomal enzymes, breakdown of the cytoskeleton and inhibition of membrane-bound Na<sup>+</sup>/K<sup>+</sup> ATPase  
85 activity <sup>3</sup>. It is however during reperfusion that most of the damage occurs, with production of large  
86 amounts of reactive oxygen species, together with a reduction in the antioxidant capacity <sup>4</sup>. Altogether,  
87 implementing strategies that can either predict or reduce IRI holds great promise in enhancing both graft  
88 and patient survival following kidney transplantation.

89

90 Hydrogen sulfide (H<sub>2</sub>S) is a gas that is produced endogenously by the cystathionine gamma-lyase (CGL)  
91 enzyme, encoded on the *CTH* gene. H<sub>2</sub>S has anti-inflammatory, antioxidant and cytoprotective properties  
92 <sup>5,6</sup>. Mice lacking CTH were more prone to IRI, while systemic adenoviral overexpression of *CTH* was  
93 protective <sup>7</sup>. In pre-clinical models, exogenous H<sub>2</sub>S protected from renal IRI <sup>8</sup> and improved graft survival  
94 after kidney transplantation <sup>9-11</sup>, possibly via the regulation of mitochondrial energy metabolism (ATP) <sup>12</sup>.  
95 In human, circulating H<sub>2</sub>S levels correlate positively with vascular health (e.g., blood pressure, limb  
96 ischemia) and post-operative survival <sup>13-16</sup>. Thus, CTH and H<sub>2</sub>S emerged as important regulators of  
97 ischemia and reperfusion <sup>12,13</sup>. In human, mutations in the *CTH* gene leading to reduced enzymatic activity  
98 provided the genetic basis for cystathioninuria, an autosomal recessive metabolic disorder. Similarly, a  
99 common non-synonymous single nucleotide polymorphism (SNP) 1364G>T (Rs1021737) in exon 12 was

100 associated with higher plasma homocysteine levels <sup>17,18</sup>, and was more frequent in patients with  
101 cardiovascular diseases <sup>19</sup>.

102

103 While mutations in CTH were associated with alterations in homocysteine levels and cardiovascular  
104 diseases, its specific role during kidney transplantation is unknown. Additionally, while H<sub>2</sub>S emerged as  
105 a significant regulator of IRI in preclinical models, its relevance in humans has yet to be established. In  
106 this study, we hypothesized that recipient polymorphisms in *CTH* and H<sub>2</sub>S serum levels could impact  
107 kidney graft function.

108

109 **MATERIALS AND METHODS**

110 **Study design and clinical data collection**

111 The study followed the principles of the Declaration of Helsinki and was approved by the local Ethics  
112 committee (GER-VD, 2019-00457). This study (project number FUP126) was part of the Swiss Transplant  
113 Cohort Study (STCS), a prospective nationwide longitudinal cohort study in solid organ and  
114 hematopoietic stem cells transplantation in Switzerland, approved by all the participating centers' Ethical  
115 committees (2018-02394)<sup>20-22</sup>. All patients enrolled in the STCS signed an informed consent and agreed  
116 to the prospective collection of clinical and biological data. Patients were included if they were > 18 years  
117 old and underwent a first kidney transplant between May 2008 and December 2021, and with available  
118 data regarding the Rs6677781 SNP in the *CTH* gene (NM\_001902.6(*CTH*):c.\*592C>T). Patients were  
119 excluded if they were <18 years, had previous kidney transplant or multi-organ transplantation.

120

121 Within the STCS, patient and transplantation-specific data are collected at baseline (day 0 before  
122 transplantation surgery), then prospectively at month 6 and 12, and yearly using standardized case-report  
123 forms (CRF). The following baseline donor and recipient data were extracted for our study: sex, age,  
124 body mass index (BMI), type of donation (living or cadaveric donor, pre-emptive or not), cause of end-  
125 stage kidney disease (ESKD), type of dialysis, and cardiovascular co-morbidities (hypertension,  
126 peripheral artery disease, cerebrovascular disease, coronary heart disease). Transplantation-related  
127 data further included: cold ischemia time, HLA mismatches, immunosuppressive induction treatment.  
128 Follow-up data included: graft function (serum creatinine,  $\mu\text{mol/l}$ , and proteinuria, g/day), graft loss (and  
129 cause of loss), patient's death (and cause of death), cardiovascular complications, and the occurrence  
130 of DGF defined as the need for dialysis in the first 7 days post transplantation.

131

132 The primary endpoints were death-censored transplantation failure and death-censored graft loss during  
133 follow-up (up to 10 years post transplantation), according to the presence of the Rs6677781 *CTH*  
134 \*592C>T SNP or based on recipient H<sub>2</sub>S levels. Secondary endpoints included patient's survival and the

135 occurrence of major adverse cardiovascular events (MACE) during follow-up (up to 10 years post  
136 transplantation). Transplantation failure was defined as a composite endpoint of graft loss, an estimated  
137 glomerular filtration rate (eGFR, as calculated with the Chronic Kidney Disease Epidemiology  
138 collaboration, CKD-EPI, equation) below 30 ml/min/m<sup>2</sup> or proteinuria of more than 1 g/day, during follow-  
139 up after kidney transplant. Graft loss was defined as the return to dialysis or re-transplantation. MACE  
140 was defined as a composite endpoint of acute myocardial infarction, stroke, or cardiovascular death.

141

#### 142 **DNA sequencing**

143 For all STCS recipients, DNA samples were collected and stored the day of and prior to transplantation  
144 (day 0). DNA was extracted from blood samples, as previously described<sup>23</sup>. To limit the risk of population  
145 stratification bias, genetic analyses were performed in Caucasian patients only. A whole genome  
146 sequencing was performed with ~1,000,000 SNPs by the genomics platform of the National Center of  
147 Competence in Research (NCCR) "Frontiers in Genetics" at the University of Geneva (Geneva,  
148 Switzerland) using Illumina human1M-Duo BeadChips using Illumina human1M-Duo BeadChips.  
149 Genotype calling and quality control filters were applied in the cohort. Genotype calling was performed  
150 with the default settings of the BeadStudio software (Illumina). For genetic markers, we discarded SNPs  
151 with: (1) a genotype clustering score (i.e., the Illumina GenTrain score, which quantifies for a given SNP  
152 the quality of clustering of samples in 3 separate genotypes) <0.2, (2) a call rate <90%, (3) a minor allele  
153 frequency (MAF) <1%, and (4) a Hardy-Weinberg value <10<sup>-7</sup>. Quality control filtering led to a total of  
154 912,765 high-quality SNPs. In this cohort, we identified the Rs6677781 SNP for the gene encoding the  
155 H<sub>2</sub>S producing enzyme CTH (chr 1). NM\_001902.6(CTH):c.\*592C>T). Briefly, genomic DNA was isolated  
156 from frozen human blood using a Puregene DNA isolation kit (Gentra Systems Minneapolis, MN),  
157 according to the manufacturer's instructions. To genotype *CTH* \*592C>T, the amplification primers were  
158 5'-GGA CTT CTT GAG GAG TTG AAG C-3' and 5'-AAT CTC ACC TCC TTC AGA GGC-3'. Then samples  
159 were electrophoresed on a Prism 377 DNA Sequencer and analyzed with GeneScan analysis software  
160 (both from PE-Applied Biosystems, Mississauga, Ontario, Canada).

7



161 **Hydrogen sulfide measurements**

162 To evaluate circulating H<sub>2</sub>S levels in recipients with or without the \*592C>T SNP we randomly selected  
163 192 recipients of cadaveric kidney transplantation with the following criteria: 50% men, 50% women.  
164 Additionally, we excluded living donors in the serum cohort as we hypothesized that the benefits of H<sub>2</sub>S  
165 might be more pronounced after severe IRI. This sub-cohort is thereafter referred to as the “serum  
166 cohort”. Similar to DNA samples, peripheral venous blood was collected into ethylenediaminetetraacetic  
167 acid (EDTA) collection tubes was collected and stored the day of and prior to transplantation (day 0).  
168 Samples were centrifuged at room temperature for 15 minutes at 2000g and the obtained plasma was  
169 stored at -80°C for future analysis. All samples were then thawed and processed at once to ensure  
170 uniformity. H<sub>2</sub>S levels were measured using the lead acetate method as described previously <sup>12,24</sup>. In  
171 brief, plasma was mixed with 80μl freshly prepared reaction mixture, containing 100 mM L-cysteine and  
172 0.5 mM pyridoxal 5'-phosphate (PLP, aka Vitamin B6) in phosphate buffered saline (PBS) in a plastic  
173 384-well plate. The plate was then incubated at 37°C with lead acetate embedded filter paper on top.  
174 Upon the reaction of H<sub>2</sub>S with the lead acetate paper, a dark lead sulfide precipitate is produced. The  
175 paper was then incubated for 6 hours, until a detectable, but non-saturated signal was seen. The amount  
176 of lead sulfide captured on the paper was quantitated using the IntDen measurement function in ImageJ®  
177 software and normalized after subtracting the background. An empty well without plasma was used as  
178 blank value for background measurement. These measurements were assessed by 2 independent  
179 investigators blinded to group assignment. High and low H<sub>2</sub>S levels/free sulfide groups were divided by  
180 median split, which was arbitrary (**Figure S1A**).

181

182 **Statistical analysis**

183 Descriptive statistics were used to report demographic and baseline data, with results expressed as  
184 medians and interquartile ranges (IQR) or means and standard deviations (SD), as appropriate.  
185 Categorical variables were summarized as numbers and percentages. The Kaplan-Meier method was  
186 used to estimate survival in WT and recipient with *CTH* \*592C>T SNP as well as in high and low H<sub>2</sub>S

187 levels/free sulfide groups. Groups were compared using log-rank test. A logistic regression analysis was  
188 used to analyze the association of H<sub>2</sub>S levels with kidney function (eGFR) at various time-points after  
189 kidney transplantation. Cox proportional hazard models were fit to estimate mortality hazard ratios  
190 between WT and SNP groups, corrected for potentially confounding variables at the time of  
191 transplantation (donor type, recipient H<sub>2</sub>S levels, recipient sex, hypertension, coronary artery disease,  
192 peripheral artery disease and the use of anti-thymocyte globulin). Both unadjusted and adjusted Cox  
193 proportional hazard models met assumptions of proportional hazard. Analysis was performed with R  
194 (RStudio 2022.07.1.) using the following packages: survival, survminer, ggplot2, table1 and epitools. All  
195 reported *p* values are based on 2-sided tests and *p* values of less than 0.05 were considered statistically  
196 significant.

197 **RESULTS**

198 **Study population.**

199 We included 1243 patients who underwent kidney transplantation between May 2008 and December  
200 2022 in Switzerland. In the list of variants reported for the CTH gene, we only identified the \*592C>T  
201 polymorphism (Rs6677781), which was present in 604 (48%) kidney transplant recipient. Thereafter, the  
202 CTH 592C genotype is referred to as "wildtype" (WT), and CTH \*592C>T polymorphism as "SNP".  
203 Baseline patient characteristics are shown in **Table 1**. The median recipient age was 56 (range 46-64)  
204 and 55 (range 45-63) years old for the WT and SNP groups, respectively ( $p=0.43$ ). In both the WT and  
205 SNP groups, there were no significant differences in the age of the donor, the type of donation (deceased  
206 versus living), the total ischemia time, recipient baseline comorbidities, the cause of end stage kidney  
207 disease, HLA mismatches and the use of anti-thymocyte globulin as induction immunosuppressive  
208 therapy (**Table 1**).

209

210 **Graft outcome is improved in carriers of the CTH \*592C>T polymorphism.**

211 During the follow-up (median 66.5 months, IQR: 47.6-106.2), transplantation failure and graft loss  
212 occurred in 499 (40%) and 129 (10.3%) patients, respectively. Transplantation failure-free survival at 1,  
213 2, 5, and 10 years was 0.83, 0.77, 0.66, 0.52 for the WT group, and 0.98, 0.82, 0.72, 0.56 for the SNP  
214 group, respectively ( $p=0.023$ , **Figure 1A**). Consistently, freedom from graft loss was 0.96, 0.95, 0.91,  
215 0.84 and 0.98, 0.97, 0.94, 0.89 at 1, 2, 5, and 10 years in absence (WT) and presence of the SNP,  
216 respectively ( $p=0.012$ , **Figure 1B**). Thus, in kidney transplant recipients with the CTH \*592C>T  
217 polymorphism, the hazard ratio (HR) of transplantation failure and graft loss was 0.85 (95% CI: 0.71-  
218 1.01,  $p=0.064$ ) and 0.64 (95% CI: 0.45-0.92,  $p=0.015$ ), respectively.

219

220 DGF was previously shown to reduce both short- and long-term graft survival after kidney transplantation,  
221 even in patients without rejection episodes. Thus, we next examined the impact of CTH \*592C>T  
222 polymorphism and the occurrence of DGF on subsequent graft outcome. In patients without DGF, the

223 occurrence of transplantation failure (HR=0.83, 95% CI: 0.68-1.00,  $p=0.055$ , **Figure 2A**) and graft loss  
224 was lower in carriers of the *CTH* \*592C>T polymorphism (HR=0.56, 95% CI: 0.37-0.85,  $p=0.007$ , **Figure**  
225 **2B**). In contrast, in patients with DGF the presence or absence of the *CTH* \*592C>T polymorphism did  
226 not impact on transplantation failure ( $p=0.65$ ) and graft loss ( $p=1$ , **Figure 2C, D**), consistent with the  
227 importance of CTH during IRI.

228

229 Next, we evaluated the impact of this polymorphism in subgroups of patients who received a kidney from  
230 a deceased or a living donor. In deceased-donor (DBD/DCD) kidney transplant recipients, the presence  
231 of the *CTH* \*592C>T polymorphism improved graft outcome (transplantation failure HR=0.82, 95% CI:  
232 0.66-1.02,  $p=0.035$ ; graft loss HR=0.70, 95% CI: 0.47-1.05,  $p=0.08$ , **Figure 3A, B**). However, in living-  
233 donor recipients *CTH* \*592C>T polymorphism did not influence both transplantation failure (HR 0.9, 95%  
234 CI: 0.67-1.21,  $p=0.33$ , **Figure 3C**) and graft loss (HR=0.51, 95% CI: 0.25-1.06  $p=0.05$ , **Figure 3D**). The  
235 probability of patient survival and the occurrence of MACE were not different between the WT and SNP  
236 groups ( $p=0.4$  and  $p=0.9$ , respectively) (**Figure S1**).

237

238 To further assess the robustness of the *CTH* \*592C>T polymorphism as a predictor of graft survival after  
239 transplantation, we generated Cox proportional hazard models to adjust for potential confounding  
240 variables. When adjusted for donor type, recipient sex, hypertension, coronary artery disease, peripheral  
241 artery disease and the use of anti-thymocyte globulin, *CTH* \*592C>T polymorphism remained  
242 significantly associated with both transplantation failure (HR=0.88, 95% CI: 0.69-0.99,  $p=0.037$ ; **Figure**  
243 **4**), and graft loss (HR=0.61, 95% CI: 0.43-0.88,  $p=0.007$ ; **Figure 5**). Altogether, these data demonstrate  
244 that graft outcome after kidney transplantation is improved in carriers of the *CTH* \*592C>T polymorphism.

245

#### 246 **Serum H<sub>2</sub>S levels do not correlate with *CTH* \*592C>T polymorphism.**

247 To assess the association between recipient baseline serum H<sub>2</sub>S levels with *CTH* \*592C>T polymorphism  
248 and clinical outcome, 192 recipients were randomly extracted from the cohort (see methods) and referred



249 thereafter as the “serum cohort”. Baseline patient characteristics are shown in **Table S1**. Median H<sub>2</sub>S  
250 levels were 5599.2 a.u. (IQR: 4786.5-6585.7, **Figure S2A**). Counterintuitively, *CTH \*592C>T*  
251 polymorphism did not impact recipient serum H<sub>2</sub>S levels prior transplantation (**Figure S2B**,  $p=0.74$ ).  
252 When patients were divided into high versus low H<sub>2</sub>S groups (using a median split), there was no  
253 difference in the risk of transplantation failure ( $p=0.69$ ), graft loss ( $p=0.13$ ), and patient survival ( $p=0.087$ )  
254 during follow-up (**Figure 6A–C**). Similarly, we did not find any correlation between recipient baseline H<sub>2</sub>S  
255 serum levels and eGFR post-transplantation (**Figure S3**). In preclinical models, H<sub>2</sub>S administration limit  
256 renal IRI, that manifests clinically as early DGF after transplantation. Thus, we hypothesized that higher  
257 levels of H<sub>2</sub>S could improve recovery in patients with initial DGF. Consistent with our hypothesis,  
258 recipients with a clinical diagnosis of DGF, transplant survival was improved in the presence of higher  
259 H<sub>2</sub>S levels (HR=4.92, 95% CI: 1.07 - 22.5,  $p=0.04$ , **Figure S4A**). On the other hand, baseline H<sub>2</sub>S levels  
260 did not influence graft outcome in the absence of DGF (HR=0.73, 95% CI: 0.43 - 1.26,  $p=0.3$ , **Figure**  
261 **S4B**).  
262

263 **DISCUSSION**

264 In a prospective cohort, kidney transplant recipients harboring the *CTH* \*592C>T polymorphism had  
265 better overall graft outcome, while this SNP did not influence patient survival or MACE during follow-up.  
266 Surprisingly, *CTH* \*592C>T polymorphism did not correlate with recipient serum H<sub>2</sub>S. However higher  
267 preoperative H<sub>2</sub>S levels were associated with better 10-year graft survival in patients who suffered from  
268 DGF.

269

270 Our findings are clinically relevant as recipient *CTH* \*592C>T polymorphism was a frequent trait (48%).  
271 in our cohort. This could constitute a novel measurable marker. Such markers could be utilized for  
272 allocation and post-transplant management strategies, or even aid in determining the prognosis for  
273 kidney transplant recipients. It might even lead to more personalized and effective approaches to improve  
274 long-term graft success and overall patient outcomes. To date, only a few recipient factors are known to  
275 have an impact on kidney graft outcome. Among them, recipient age was associated with 1-year graft  
276 failure <sup>25 26</sup>. Other recipient-related factors include the cause of renal failure, as patients with  
277 glomerulonephritis or diabetic nephropathy experience worst outcomes <sup>26,27</sup>. While the presence or  
278 absence of *CTH* \*592C>T polymorphism is not modifiable *per se*, further work should identify its  
279 functional consequences, that could be amenable to interventions (e.g., H<sub>2</sub>S or glutathione  
280 supplementation).

281

282 Our results provide the first evidence in human that *CTH* polymorphism can impact kidney graft function  
283 and survival. Here, we hypothesize that the protective effect on graft survival was mainly by mitigating  
284 IRI. Consistent with this hypothesis, the *CTH* \*592C>T polymorphism was more pronounced in deceased  
285 donor kidney transplants. Similarly, in patients who already suffered from DGF, the *CTH* \*592C>T  
286 polymorphism did not impact graft survival. While the underlying mechanism associated with *CTH*  
287 \*592C>T polymorphism is unknown, H<sub>2</sub>S was demonstrated to reduce mitochondrial metabolism,  
288 apoptosis, oxidative stress, reduced IRI, and improved kidney survival <sup>9,10,28-30</sup>.

289

290 Of interest, *CTH* \*592C>T mutation has not been previously associated with a clinically relevant  
291 phenotype. Another SNP in exon 12 of *CTH*, 1364 G>T (Rs1021737), was associated with plasma  
292 homocysteine concentrations in Caucasians<sup>18</sup>. In addition, *CTH* 1364 G>T allele frequency was  
293 increased in patients with cardiovascular diseases, while *CTH* 356C>T (Rs28941785) and 874C>G  
294 (Rs28941786) were not associated with cardiovascular outcomes<sup>19</sup>. Of note, the Rs6677781 SNP  
295 investigated in our cohort was not examined in neither of these studies. Surprisingly, *CTH* \*592C>T  
296 polymorphism did not correlate with serum H<sub>2</sub>S levels (as measured using the lead acetate method), nor  
297 cardiovascular events (MACE). The lead acetate method measures only relative differences in H<sub>2</sub>S  
298 between individuals and groups, and not absolute differences. Likewise, it primarily serves as a surrogate  
299 for the actual amount of H<sub>2</sub>S produced from available substrates in plasma<sup>13</sup>. Consistent, while most  
300 tests assess sulfide release from bound sulfide reserves, more specific assays might better capture  
301 distinct biological phenomena with clinical relevance. Important questions remain about what specific  
302 components of the plasma determine and regulate H<sub>2</sub>S levels. One theory revolves around the sulfur-  
303 containing amino acid homocysteine, which in itself has been long associated with the risk of  
304 cardiovascular diseases, but the physiologic mechanisms are not well understood<sup>31</sup>. In addition, it might  
305 be that the observed effect of the *CTH* \*592C>T polymorphism on graft outcome in our cohort is  
306 independent of H<sub>2</sub>S levels, as *CTH* impacts cell redox balance during glutathione and homocysteine  
307 metabolism<sup>18,32</sup>. Of interest, hyperhomocysteinemia has been shown to trigger the expression of cellular  
308 communication network factor 2 (CCN2) in vascular cells<sup>18,33</sup>, and is associated with fibrosis and cellular  
309 senescence following kidney transplant<sup>34</sup>. Interestingly, administration of H<sub>2</sub>S was reported to reduce  
310 CCN2 expression<sup>35</sup>, and could be used to reduce IRI and possibly DGF after kidney transplant.

311

312 In a subgroup of patients who suffered from DGF, higher preoperative levels of H<sub>2</sub>S were associated with  
313 improved kidney graft outcome. This is relevant in an era where marginal donors are increasingly used  
314<sup>1</sup>. Thus, organs that are at great risk of DGF could be preferentially allocated to recipients with high

14

315 baseline H<sub>2</sub>S levels. On the other hand, patients with low preoperative H<sub>2</sub>S, and suffering from DGF might  
316 benefit from H<sub>2</sub>S administration (e.g., clinically available H<sub>2</sub>S donors such as zofenopril, sodium  
317 thiosulfate)<sup>36,37</sup>. Alternatively, H<sub>2</sub>S-based therapeutic strategies could also be envisaged during organ  
318 preservation and *ex-vivo* organ perfusion<sup>2</sup>, limiting systemic side-effects.

319

320 The limitations of our study need to be acknowledged. First, we had a relatively small cohort for genetic-  
321 association studies. Second, the quantification of H<sub>2</sub>S using the lead acetate method measures only  
322 relative differences in H<sub>2</sub>S between individuals and groups, and not absolute differences. Likewise, it  
323 primarily serves as a surrogate for the actual amount of H<sub>2</sub>S produced from available substrates in  
324 plasma. Future work is therefore needed to validate these findings in larger cohorts. In addition, we  
325 previously demonstrated that dietary restriction and the hypothalamic-pituitary axis were important  
326 regulators of endogenous H<sub>2</sub>S levels and downstream signaling<sup>7,38,39</sup>. Thus, specific dietary interventions  
327 could be envisaged in a prospective randomized controlled study of patient undergoing kidney  
328 transplantation. Third, homocysteine levels were not available in this cohort, which would have been of  
329 great interest as it is linked to *CTH* polymorphism, cardiovascular health and kidney function<sup>18</sup>. Lastly,  
330 additional studies distinguishing specific inorganic and organic per/polysulfide such as cysteine or  
331 glutathione-related sulfur species are needed to better understand the relationship of these metabolites  
332 with *CTH* polymorphism and their role in kidney transplantation.

333

334 In conclusion, in a cohort of 1243 patients who underwent kidney transplantation, *CTH* \*592C>T  
335 polymorphism was associated with improved transplantation and graft survival. This finding may enable  
336 improved risk stratification and better tailoring of treatment for IRI, which ultimately should improve the  
337 overall success of kidney transplantation.

338



339 **ACKNOWLEDGMENTS**

340 This work was supported by the Swiss National Science Foundation (SNSF PZ00P3-185927), the  
341 Leenaards and Mercier Foundation, and The Mendez National Institute of Transplantation Foundation to  
342 AL, the Faculty of biology and medicine of the University of Lausanne and the STCS to AL and DG, and  
343 the Medi-CAL Futur Foundation to DG. We thank all patients who participate in the Swiss Transplant  
344 Cohort Study, the study nurses, the central and local data managers and all the investigators involved in  
345 the STCS<sup>§</sup>.

346

347 <sup>§</sup>Swiss Transplant Cohort Study Collaborators: Patrizia Amico, John-David Aubert, Vanessa Banz, Sonja  
348 Beckmann, Guido Beldi, Christoph Berger, Ekaterine Berishvili, Annalisa Berzigotti, Isabelle  
349 Binet, Pierre-Yves Bochud, Sandra Branca, Heiner Bucher, Emanuelle Catana, Anne Cairoli, Yves  
350 Chalandon, Sabina De Geest, Olivier De Rougemont, Sophie De Seigneux, Michael Dickenmann, Joëlle  
351 Lynn Dreifuss, Michel Duchosal, Thomas Fehr, Sylvie Ferrari-Lacraz, Christian  
352 Garzoni, Dela Golshayan, Nicolas Goossens, Fadi Haidar, Jörg Halter, Dominik Heim, Christoph  
353 Hess, Sven Hillinger, Hans H Hirsch, Patricia Hirt, Günther Hofbauer, Uyen Huynh-Do, Franz  
354 Immer, Michael Koller, Mirjam Laager, Bettina Laesser, Frédéric Lamothe, Roger Lehmann, Alexander  
355 Leichtle, Oriol Manuel, Hans-Peter Marti, Michele Martinelli, Valérie McLin, Katell Mellac, Aurélie  
356 Mercay, Karin Mettler, Antonia Müller, Nicolas J Müller, Ulrike Müller-Arndt, Beat Müllhaupt, Mirjam  
357 Nägeli, Graziano Oldani, Manuel Pascual, Jakob Passweg, Rosemarie Pazeller, Klara Posfay-  
358 Barbe, Juliane Rick, Anne Rosselet, Simona Rossi, Silvia Rothlin, Frank Ruschitzka, Thomas  
359 Schachtner, Urs Schranz, Stefan Schaub, Alexandra Scherrer, Aurelia Schnyder, Macé  
360 Schuurmans, Simon Schwab, Thierry Sengstag, Federico Simonetta, Susanne Stampf, Jürg  
361 Steiger, Guido Stirnimann, Ueli Stützinger, Christian Van Delden, Jean-Pierre Venetz, Jean  
362 Villard, Julien Vionnet, Madelaine Wick, Markus Wilhelm, Patrick Yerly

363

364

365 **DISCLOSURES**

366 The authors of this manuscript have no conflicts of interest to disclose as described by the American  
367 Journal of Transplantation.

368

369 **DATA AVAILABILITY STATEMENT**

370 The anonymized data are available upon reasonable request for a collaborative research project. Please  
371 contact the corresponding author for all requests regarding data sharing.

372

373 **FIGURE LEGENDS**

374 **Figure 1. Ten-years risk of transplantation failure and graft loss according to recipient *CTH***  
375 **\*592C>T polymorphism in 1243 kidney transplant recipients.** (A) Probability of transplantation (Tx)  
376 failure, (B) Probability of graft loss, according to the presence (blue line) or absence of *CTH* \*592C>T  
377 polymorphism (red line). Shaded regions indicate 95% confidence intervals. Death censored. *P* value  
378 calculated from log-rank test.

379

380 **Figure 2. Ten-years risk of transplantation failure and graft loss according to the presence or**  
381 **absence of delayed graft function and recipient *CTH* \*592C>T polymorphism.** (A) Probability of  
382 transplantation (Tx) failure in patients without delayed graft function (DGF), (B) Probability of graft loss in  
383 patients without DGF, (C) Probability of transplantation failure in patients with DGF, (D) Probability of  
384 graft loss in patients with DGF; according to the presence (blue line) or absence (red line) of *CTH*  
385 \*592C>T polymorphism. Shaded regions indicate 95% confidence intervals. Death censored. *P* value  
386 calculated from log-rank test.

387

388 **Figure 3. Ten-years risk of transplantation failure and graft loss according to the type of donation**  
389 **and recipient *CTH* \*592C>T polymorphism.** (A) Probability of transplantation (Tx) failure in patients  
390 with deceased donation, (B) Probability of graft loss in patients with deceased donation, (C) Probability  
391 of transplantation failure in patients with living donation, (D) Probability of graft loss in patients with living  
392 donation. Blue line: presence of *CTH* \*592C>T polymorphism, red line: absence of \*592C>T  
393 polymorphism. Shaded regions indicate 95% confidence intervals. Death censored. *P* value calculated  
394 from log-rank test.

395

396 **Figure 4. Hazard ratios of death-censored transplantation failure during follow up period.**

397 Hazard ratio estimates and 95% confidence intervals for clinically relevant parameters and *CTH*  
398 \*592C>T polymorphism (SNP). CAD=coronary artery disease. PAD=peripheral artery disease. *P* value  
399 calculated from log-rank test.

400

401 **Figure 5. Hazard ratios of death-censored graft loss during follow up period.** Hazard ratio  
402 estimates and 95% confidence intervals for clinically relevant parameters and *CTH* \*592C>T  
403 polymorphism (SNP). CAD=coronary artery disease. PAD=peripheral artery disease. *P* value calculated  
404 from log-rank test.

405

406 **Figure 6. Ten-years risk of transplantation failure, graft loss and patient survival according to H<sub>2</sub>S**  
407 **levels. (A)** Probability of transplantation (Tx) failure, **(B)** Probability of graft loss, **(C)** Patient survival; in  
408 recipient with low (blue line) or high (red line) H<sub>2</sub>S levels. Shaded regions indicate 95% confidence  
409 intervals. Death censored. *P* value calculated from log-rank test.

410



411 TABLES

412

|   | WT<br>(N=639)     | SNP<br>(N=604)    | P-value |
|---|-------------------|-------------------|---------|
| <b>Recipient sex</b>                        |                   |                   |         |
| Male  | 420 (65.7%)       | 407 (67.4%)       | 0.548   |
| Female                                      | 219 (34.3%)       | 197 (32.6%)       |         |
| <b>Donor age (years)</b>                    |                   |                   |         |
| Median [Q1, Q3]                             | 55.0 [45.0, 64.0] | 55.0 [45.0, 63.0] | 0.549   |
| <b>Donor type</b>                           |                   |                   |         |
| DBD   | 338 (52.9%)       | 296 (49.0%)       | 0.0936  |
| DCD   | 19 (3.0%)         | 31 (5.1%)         |         |
| Living                                      | 282 (44.1%)       | 277 (45.9%)       |         |
| <b>Cold ischemia time (min)</b>             |                   |                   |         |
| Median [Q1, Q3]                             | 363 [90.0, 626]   | 323 [90.0, 580]   | 0.151   |
| <b>Delayed graft function</b>               |                   |                   |         |
| Yes   | 77 (12.1%)        | 66 (10.9%)        | 0.594   |
| No  | 562 (88.0%)       | 538 (89.1%)       |         |
| <b>Recipient age</b>                        |                   |                   |         |
| Median [Q1, Q3]                             | 56.0 [46.0, 64.0] | 55.0 [45.0, 63.3] | 0.429   |
| <b>BMI</b>                                  |                   |                   |         |
| Median [Q1, Q3]                             | 26.0 [23.0, 29.0] | 25.5 [22.6, 29.1] | 0.318   |
| <b>Hypertension</b>                         |                   |                   |         |
| No  | 110 (17.2%)       | 107 (17.7%)       | 0.823   |
| Yes   | 529 (82.8%)       | 497 (82.3%)       |         |
| <b>Coronary artery disease <sup>a</sup></b> |                   |                   |         |
| No  | 592 (92.6%)       | 563 (93.2%)       | 0.741   |
| Yes   | 47 (7.4%)         | 41 (6.8%)         |         |
| <b>Peripheral artery disease</b>            |                   |                   |         |
| No  | 549 (85.9%)       | 526 (87.1%)       | 0.562   |
| Yes   | 90 (14.1%)        | 78 (12.9%)        |         |
| <b>Dialysis type</b>                        |                   |                   |         |
| HD  | 437 (68.4%)       | 408 (67.5%)       | 0.898   |
| PD  | 74 (11.6%)        | 75 (12.4%)        |         |
| None, preemptive transplantation            | 128 (20.0%)       | 121 (20.0%)       |         |
| <b>Cause of end stage kidney disease</b>    |                   |                   |         |
| ADPKD                                       | 139 (21.8%)       | 136 (22.5%)       | 0.568   |

20

|  | WT<br>(N=639)     | SNP<br>(N=604)    | P-value |
|--|-------------------|-------------------|---------|
| Diabetic nephropathy                             | 65 (10.2%)        | 48 (7.9%)         |         |
| Glomerulonephritis                               | 161 (25.2%)       | 161 (26.7%)       |         |
| Other  | 274 (42.9%)       | 259 (42.9%)       |         |
| <b>HLA mismatch</b>                              |                   |                   |         |
| Median [Q1, Q3]                                  | 4.00 [3.00, 5.00] | 4.00 [3.00, 5.00] | 0.168   |
| <b>Anti-thymocyte globulin induction therapy</b> |                   |                   |         |
| Yes  | 140 (21.9%)       | 141 (23.3%)       | 0.587   |
| No   | 499 (78.1%)       | 463 (76.7%)       |         |
| <b>H<sub>2</sub>S levels</b>                     |                   |                   |         |
| Not measured                                     | 590 (92.3%)       | 555 (91.9%)       | 0.898   |
| High   | 28 (4.4%)         | 26 (4.3%)         |         |
| Low  | 21 (3.3%)         | 23 (3.8%)         |         |

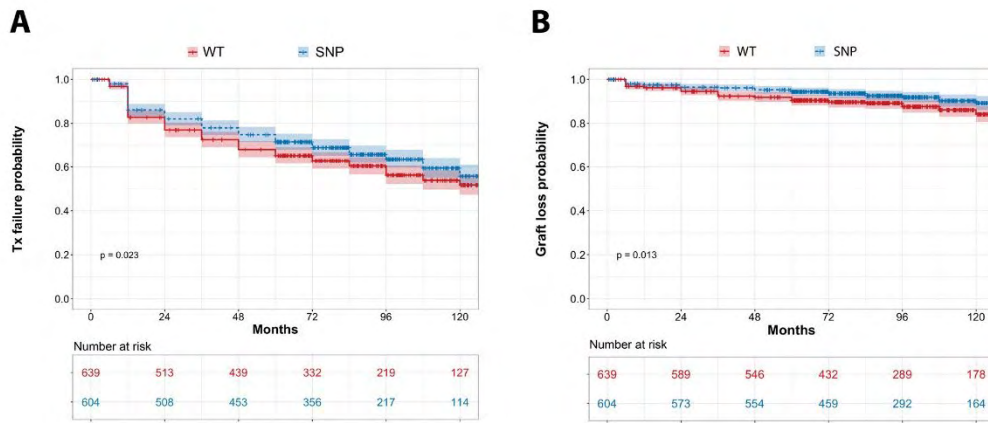
413

414 **Table 1. Characteristics of the study population at the time of transplantation.** Patients were  
415 stratified based on the absence (WT) or presence of the *CTH* \*592C>T polymorphism (SNP). Fisher test or *t*-test  
416 were used when appropriate. ADPKD: autosomal dominant polycystic kidney disease, BMI: body mass index,  
417 DBD: donation after brain death, DCD: donation after cardiocirculatory death, HD: hemodialysis, H<sub>2</sub>S: hydrogen  
418 sulfide, HLA: human leukocyte antigen, PD: peritoneal dialysis.

419

420 FIGURES

421

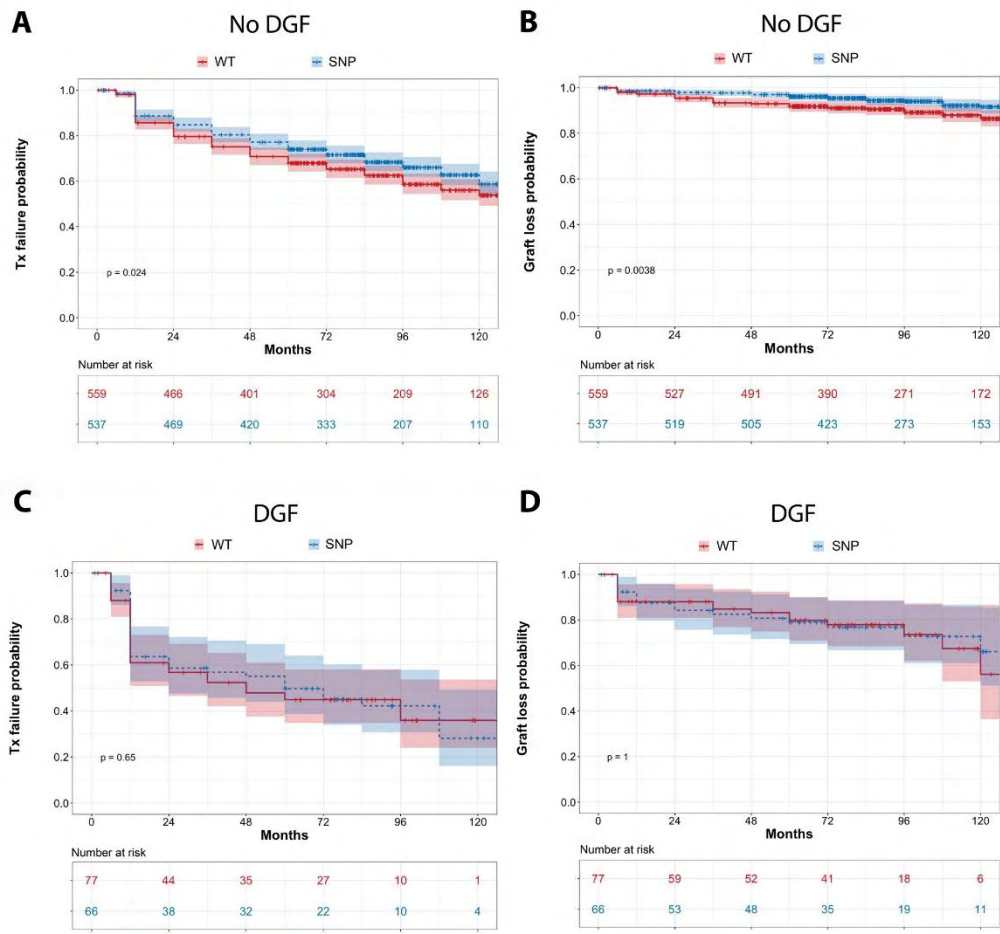


422

423 Figure 1

424

425



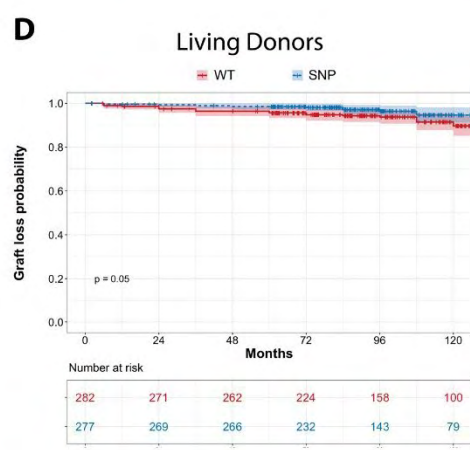
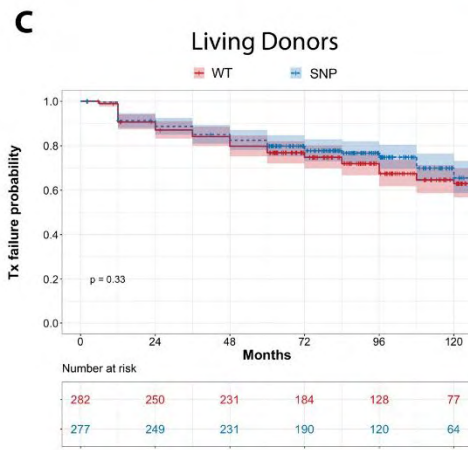
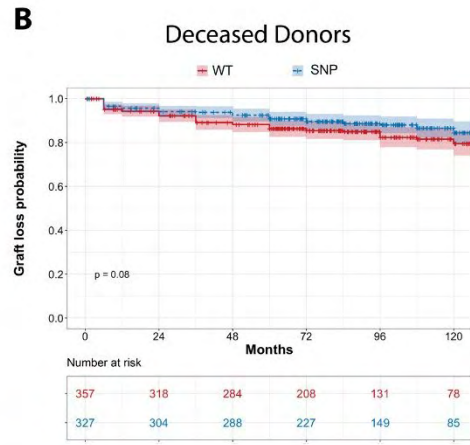
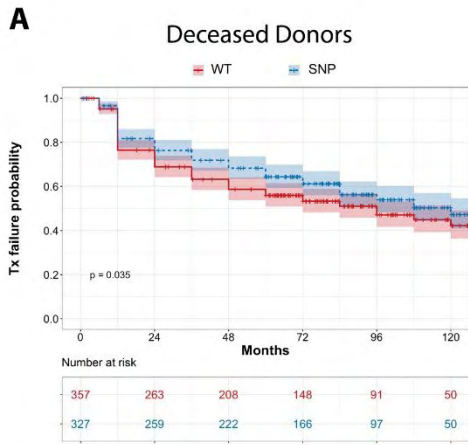
426

427

Figure 2

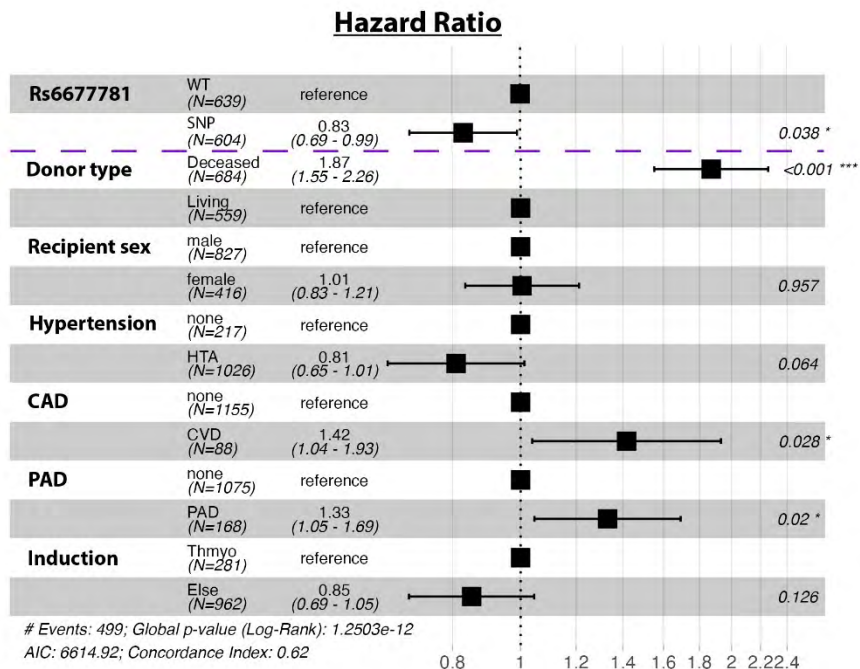
428



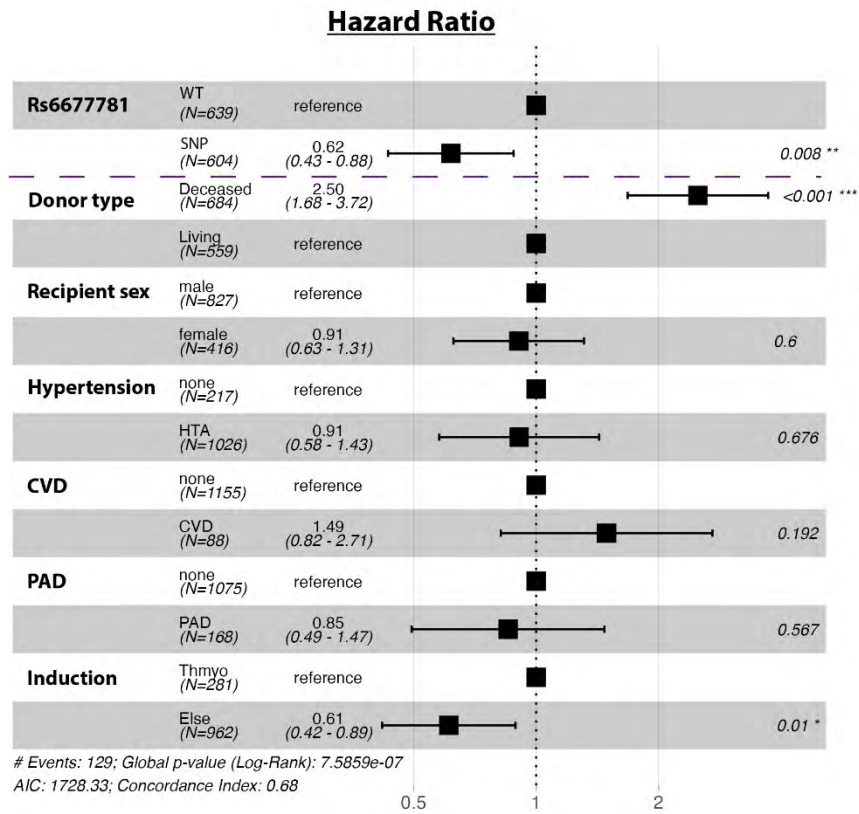


429  
430  
431  
432

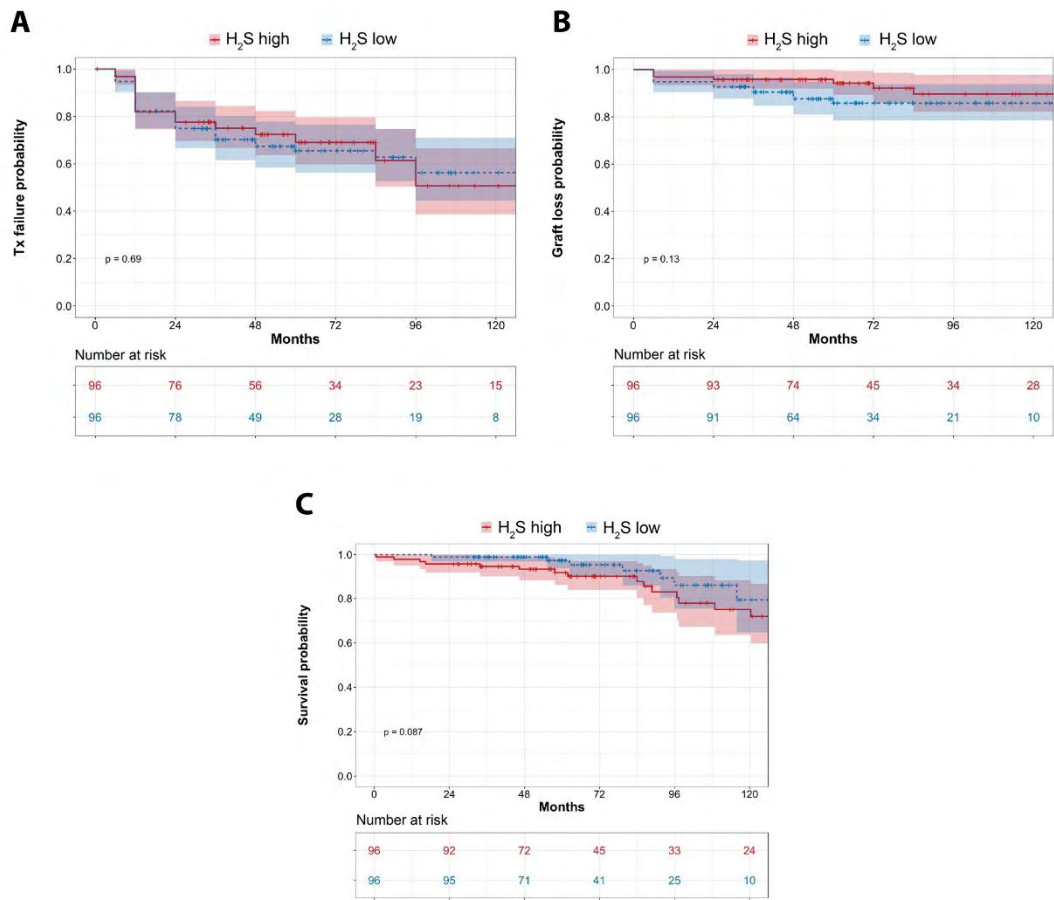
**Figure 3**



433  
434 **Figure 4**  
435



436 Figure 5  
437



438  
439  
440  
441

Figure 6



442 SUPPORTING INFORMATION  
 443  
 444

|  | High H <sub>2</sub> S<br>(N=96) | Low H <sub>2</sub> S<br>(N=96) | P-value |
|--|---------------------------------|--------------------------------|---------|
| <b>Recipient sex</b>                     |                                 |                                |         |
| Male                                     | 61 (63.5%)                      | 62 (64.6%)                     | 1       |
| Female                                   | 35 (36.5%)                      | 34 (35.4%)                     |         |
| <b>Donor age</b>                         |                                 |                                |         |
| Median [Q1, Q3]                          | 54.0 [40.8, 65.0]               | 55.0 [45.8, 66.0]              | 0.579   |
| <b>Donor type</b>                        |                                 |                                |         |
| DBD                                      | 85 (88.5%)                      | 88 (91.7%)                     | 0.63    |
| Living                                   | 0 (0%)                          | 0 (0%)                         |         |
| DCD                                      | 11 (11.5%)                      | 8 (8.3%)                       |         |
| <b>Cold ischemia time (min)</b>          |                                 |                                |         |
| Median [Q1, Q3]                          | 560 [442, 698]                  | 494 [404, 671]                 | 0.116   |
| <b>Delayed graft function</b>            |                                 |                                |         |
| Yes                                      | 8 (8.3%)                        | 13 (13.5%)                     | 0.355   |
| No                                       | 88 (91.7%)                      | 83 (86.5%)                     |         |
| <b>Recipient age</b>                     |                                 |                                |         |
| Median [Q1, Q3]                          | 56.5 [45.0, 64.0]               | 58.0 [45.8, 66.3]              | 0.48    |
| <b>BMI</b>                               |                                 |                                |         |
| Median [Q1, Q3]                          | 25.6 [22.3, 28.9]               | 25.8 [22.9, 28.7]              | 0.702   |
| <b>Hypertension</b>                      |                                 |                                |         |
| No                                       | 12 (12.5%)                      | 11 (11.5%)                     | 1       |
| Yes                                      | 84 (87.5%)                      | 85 (88.5%)                     |         |
| <b>Coronary artery disease</b>           |                                 |                                |         |
| No                                       | 90 (93.8%)                      | 89 (92.7%)                     | 1       |
| Yes                                      | 6 (6.3%)                        | 7 (7.3%)                       |         |
| <b>Peripheral artery disease</b>         |                                 |                                |         |
| No                                       | 82 (85.4%)                      | 82 (85.4%)                     | 1       |
| Yes                                      | 14 (14.6%)                      | 14 (14.6%)                     |         |
| <b>Dialysis type</b>                     |                                 |                                |         |
| HD                                       | 77 (80.2%)                      | 72 (75.0%)                     | 0.245   |
| PD                                       | 16 (16.7%)                      | 15 (15.6%)                     |         |
| None                                     | 3 (3.1%)                        | 9 (9.4%)                       |         |
| <b>Cause of end-stage kidney disease</b> |                                 |                                |         |

|  | High H <sub>2</sub> S<br>(N=96) | Low H <sub>2</sub> S<br>(N=96) | P-value |
|--|---------------------------------|--------------------------------|---------|
| ADPKD  | 16 (16.7%)                      | 17 (17.7%)                     | 0.932   |
| Diabetic nephropathy                             | 11 (11.5%)                      | 12 (12.5%)                     |         |
| Glomerulonephritis                               | 24 (25.0%)                      | 20 (20.8%)                     |         |
| Other  | 45 (46.9%)                      | 47 (49.0%)                     |         |
| <b>HLA mismatch</b>                              |                                 |                                |         |
| Median [Q1, Q3]                                  | 4.00 [4.00, 5.00]               | 4.00 [3.00, 5.00]              | 0.43    |
| <b>Anti-thymocyte globulin induction therapy</b> |                                 |                                |         |
| Yes  | 47 (49.0%)                      | 35 (36.5%)                     | 0.108   |
| No   | 49 (51.0%)                      | 61 (63.5%)                     |         |
| <b>rs6677781</b>                                 |                                 |                                |         |
| Absent   | 28 (29.2%)                      | 21 (21.9%)                     | 0.839   |
| SNP  | 26 (27.1%)                      | 23 (24.0%)                     |         |

445

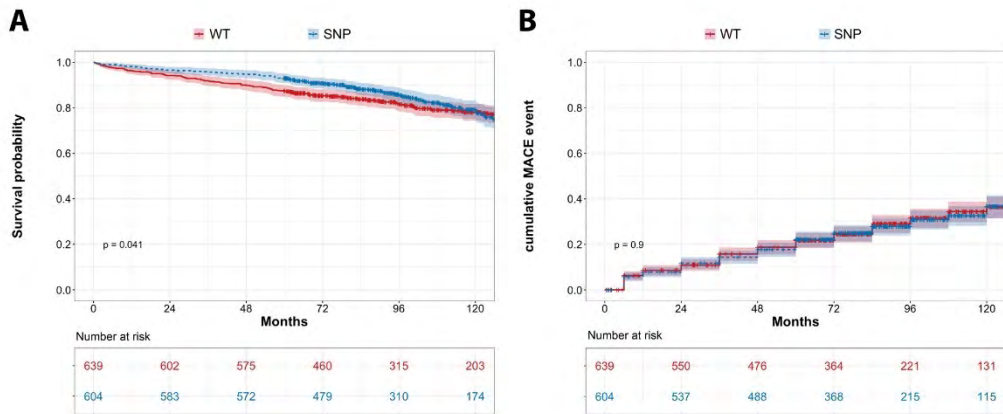
446 **Table S1. Baseline characteristics of the recipients based on measured H<sub>2</sub>S serum levels (“serum**  
447 **cohort”).** Patients were stratified based on low or high H<sub>2</sub>S levels. Fisher test or *t*-test were used when appropriate.

448 ADPKD: autosomal dominant polycystic kidney disease, BMI: body mass index, DBD: donation after brain death,

449 DCD: donation after cardiocirculatory death, HD: hemodialysis, H<sub>2</sub>S: hydrogen sulfide, HLA: human leukocyte

450 antigen, PD: peritoneal dialysis.

451

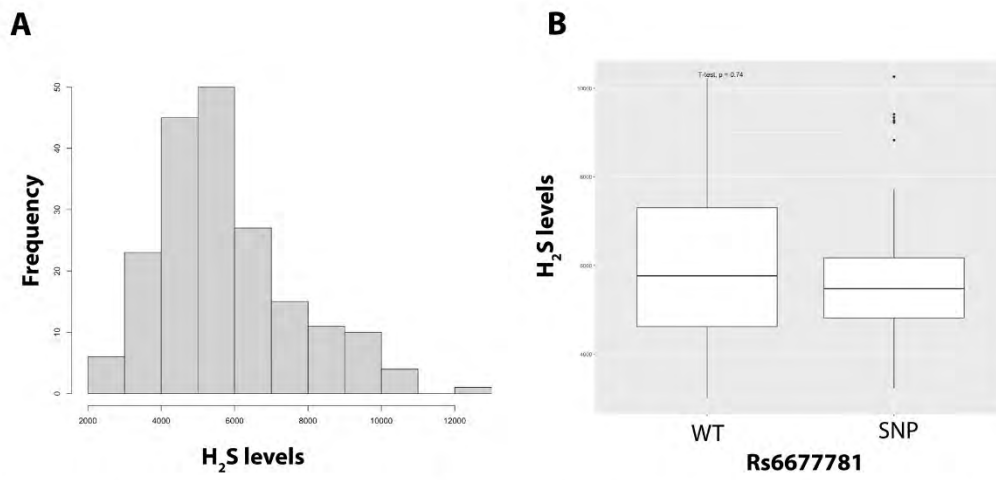


452

453 **Figure S1. Ten-years risk of patient death and major cardiovascular events (MACE) according to**  
 454 **the recipient *CTH* \*592C>T polymorphism in 1243 kidney transplant recipients. (A) Probability of**  
 455 **patient survival, (B) cumulative composite endpoint of incident cerebrovascular disease, coronary heart**  
 456 **disease and cardiovascular death, according to the presence (blue line) or absence of *CTH* \*592C>T**  
 457 **polymorphism (red line). Shaded regions indicate 95% confidence intervals. Death censored. *P* value**  
 458 **calculated from log-rank test.**

30

459



460

461 **Figure S2. Lead acetate measurements and distribution of H<sub>2</sub>S levels in the serum cohort. (A)**

462 Histogram of H<sub>2</sub>S levels in 192 deceased-donor kidney transplants recipients. (B) H<sub>2</sub>S levels in kidney

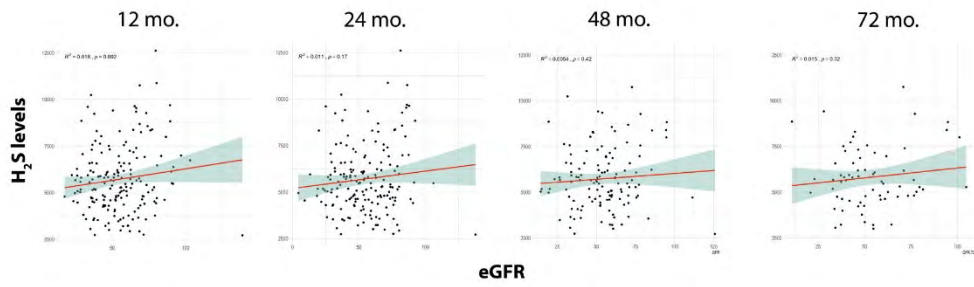
463 transplant recipient according to the recipient *CTH* \*592C>T polymorphism. Error bars indicate SD. *P* =

464 t-test.

465

31



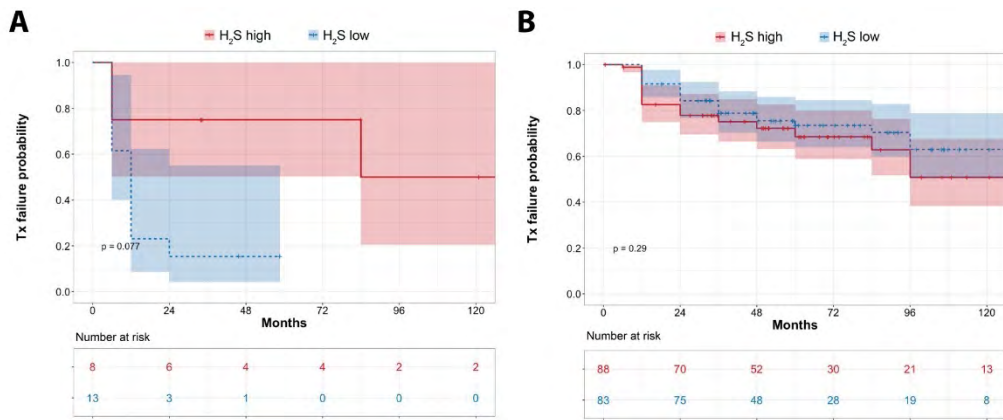


466

467 **Figure S3. Correlation between H<sub>2</sub>S levels and eGFR after kidney transplantation.** From left to right:  
 468 Correlation between H<sub>2</sub>S levels and eGFR at 12, 24, 48 and 72 months post-transplantation. Shaded  
 469 regions indicate 95% confidence intervals. R<sup>2</sup> = square of the Pearson correlation coefficient r.

470

471



472

473 **Figure S4. Ten-years risk of transplantation failure according to the presence or absence of**

474 **delayed graft function and by H<sub>2</sub>S levels in 196 kidney transplant recipients.** Probability of

475 transplantation (Tx) failure in **(A)** patients with delayed graft function (DGF), **(B)** patients without DGF,

476 and with high H<sub>2</sub>S (red line) or low (blue line) levels. Shaded regions indicate 95% confidence intervals.

477 Death censored. *P* value calculated from log-rank test.

478

479 **REFERENCES**

480

- 481 1. Tullius SG, Rabb H. Improving the Supply and Quality of Deceased-Donor Organs for  
 482 Transplantation. *N Engl J Med.* May 17 2018;378(20):1920-1929. doi:10.1056/NEJMra1507080
- 483 2. Longchamp A, Markmann JF. Kidney Preservation Strategies to Improve Transplant Outcomes.  
 484 *Clin J Am Soc Nephrol.* May 23 2023;doi:10.2215/CJN.0000000000000212
- 485 3. Nieuwenhuijs-Moeke GJ, Pischke SE, Berger SP, et al. Ischemia and Reperfusion Injury in  
 486 Kidney Transplantation: Relevant Mechanisms in Injury and Repair. *J Clin Med.* Jan 17  
 487 2020;9(1)doi:10.3390/jcm9010253
- 488 4. Chouchani ET, Pell VR, Gaude E, et al. Ischaemic accumulation of succinate controls  
 489 reperfusion injury through mitochondrial ROS. *Nature.* Nov 20 2014;515(7527):431-435.  
 490 doi:10.1038/nature13909
- 491 5. Wang R. Physiological implications of hydrogen sulfide: a whiff exploration that blossomed.  
 492 *Physiol Rev.* Apr 2012;92(2):791-896. doi:10.1152/physrev.00017.2011
- 493 6. Das A, Huang GX, Bonkowski MS, et al. Impairment of an Endothelial NAD(+)-H2S Signaling  
 494 Network Is a Reversible Cause of Vascular Aging. *Cell.* Mar 22 2018;173(1):74-89 e20.  
 495 doi:10.1016/j.cell.2018.02.008
- 496 7. Hine C, Harputlugil E, Zhang Y, et al. Endogenous hydrogen sulfide production is essential for  
 497 dietary restriction benefits. *Cell.* Jan 15 2015;160(1-2):132-44. doi:10.1016/j.cell.2014.11.048
- 498 8. Bos EM, Wang R, Snijder PM, et al. Cystathionine gamma-lyase protects against renal  
 499 ischemia/reperfusion by modulating oxidative stress. *J Am Soc Nephrol.* Apr 2013;24(5):759-70.  
 500 doi:10.1681/ASN.2012030268
- 501 9. Hosgood SA, Nicholson ML. Hydrogen sulphide ameliorates ischaemia-reperfusion injury in an  
 502 experimental model of non-heart-beating donor kidney transplantation. *Br J Surg.* Feb 2010;97(2):202-  
 503 9. doi:10.1002/bjs.6856
- 504 10. Bos EM, Leuvenink HG, Snijder PM, et al. Hydrogen sulfide-induced hypometabolism prevents  
 505 renal ischemia/reperfusion injury. *J Am Soc Nephrol.* Sep 2009;20(9):1901-5.  
 506 doi:10.1681/ASN.2008121269
- 507 11. Lobb I, Jiang J, Lian D, et al. Hydrogen Sulfide Protects Renal Grafts Against Prolonged Cold  
 508 Ischemia-Reperfusion Injury via Specific Mitochondrial Actions. *Am J Transplant.* Feb 2017;17(2):341-  
 509 352. doi:10.1111/ajt.14080
- 510 12. Longchamp A, Mirabella T, Arduini A, et al. Amino Acid Restriction Triggers Angiogenesis via  
 511 GCN2/ATF4 Regulation of VEGF and H2S Production. *Cell.* Mar 22 2018;173(1):117-129.e14.  
 512 doi:10.1016/j.cell.2018.03.001
- 513 13. Longchamp A, MacArthur MR, Trocha K, et al. Plasma Hydrogen Sulfide Is Positively  
 514 Associated With Post-operative Survival in Patients Undergoing Surgical Revascularization. *Front*  
 515 *Cardiovasc Med.* 2021;8:750926. doi:10.3389/fcvm.2021.750926
- 516 14. Islam KN, Polhemus DJ, Donnarumma E, Brewster LP, Lefer DJ. Hydrogen Sulfide Levels and  
 517 Nuclear Factor-Erythroid 2-Related Factor 2 (NRF2) Activity Are Attenuated in the Setting of Critical  
 518 Limb Ischemia (CLI). *J Am Heart Assoc.* May 2015;4(5)doi:10.1161/JAHA.115.001986
- 519 15. Kondo K, Bhushan S, King AL, et al. H<sub>2</sub>S protects against pressure overload-induced heart  
 520 failure via upregulation of endothelial nitric oxide synthase. *Circulation.* Mar 2013;127(10):1116-27.  
 521 doi:10.1161/CIRCULATIONAHA.112.000855
- 522 16. Polhemus DJ, Kondo K, Bhushan S, et al. Hydrogen sulfide attenuates cardiac dysfunction after  
 523 heart failure via induction of angiogenesis. *Circ Heart Fail.* Sep 1 2013;6(5):1077-86.  
 524 doi:10.1161/CIRCHEARTFAILURE.113.000299
- 525 17. Wang J, Hegele RA. Genomic basis of cystathioninuria (MIM 219500) revealed by multiple  
 526 mutations in cystathionine gamma-lyase (CTH). *Hum Genet.* Apr 2003;112(4):404-8.  
 527 doi:10.1007/s00439-003-0906-8

- 528 18. Wang J, Huff AM, Spence JD, Hegele RA. Single nucleotide polymorphism in CTH associated  
529 with variation in plasma homocysteine concentration. *Clin Genet*. Jun 2004;65(6):483-6.  
530 doi:10.1111/j.1399-0004.2004.00250.x
- 531 19. Rajpal S, Katikaneni P, Deshotels M, et al. Total sulfane sulfur bioavailability reflects ethnic and  
532 gender disparities in cardiovascular disease. *Redox Biol*. May 2018;15:480-489.  
533 doi:10.1016/j.redox.2018.01.007
- 534 20. Koller. STCS annual report. 2020;
- 535 21. Stampf S, Mueller NJ, van Delden C, et al. Cohort profile: The Swiss Transplant Cohort Study  
536 (STCS): A nationwide longitudinal cohort study of all solid organ recipients in Switzerland. *BMJ Open*.  
537 Dec 15 2021;11(12):e051176. doi:10.1136/bmjopen-2021-051176
- 538 22. Koller MT, van Delden C, Muller NJ, et al. Design and methodology of the Swiss Transplant  
539 Cohort Study (STCS): a comprehensive prospective nationwide long-term follow-up cohort. *Eur J*  
540 *Epidemiol*. Apr 2013;28(4):347-55. doi:10.1007/s10654-012-9754-y
- 541 23. Wojtowicz A, Gresnigt MS, Lecompte T, et al. IL1B and DEFB1 Polymorphisms Increase  
542 Susceptibility to Invasive Mold Infection After Solid-Organ Transplantation. *J Infect Dis*. Nov 14  
543 2014;doi:10.1093/infdis/jiu636
- 544 24. Hine C, Mitchell JR. Endpoint or Kinetic Measurement of Hydrogen Sulfide Production Capacity  
545 in Tissue Extracts. *Bio Protoc*. Jul 5 2017;7(13)doi:10.21769/BioProtoc.2382
- 546 25. Foroutan F, Friesen EL, Clark KE, et al. Risk Factors for 1-Year Graft Loss After Kidney  
547 Transplantation: Systematic Review and Meta-Analysis. *Clin J Am Soc Nephrol*. Nov 7  
548 2019;14(11):1642-1650. doi:10.2215/CJN.05560519
- 549 26. Beerli N, Denhaerynck K, Binet I, et al. Age at Time of Kidney Transplantation as a Predictor for  
550 Mortality, Graft Loss and Self-Rated Health Status: Results From the Swiss Transplant Cohort Study.  
551 *Transpl Int*. 2021;35:10076. doi:10.3389/ti.2021.10076
- 552 27. Pruthi R, McClure M, Casula A, et al. Long-term graft outcomes and patient survival are lower  
553 posttransplant in patients with a primary renal diagnosis of glomerulonephritis. *Kidney Int*. Apr  
554 2016;89(4):918-26. doi:10.1016/j.kint.2015.11.022
- 555 28. Sekijima M, Sahara H, Miki K, et al. Hydrogen sulfide prevents renal ischemia-reperfusion injury  
556 in CLAWN miniature swine. *J Surg Res*. Nov 2017;219:165-172. doi:10.1016/j.jss.2017.05.123
- 557 29. Ahmad A, Olah G, Szczesny B, Wood ME, Whiteman M, Szabo C. AP39, A Mitochondrially  
558 Targeted Hydrogen Sulfide Donor, Exerts Protective Effects in Renal Epithelial Cells Subjected to  
559 Oxidative Stress in Vitro and in Acute Renal Injury in Vivo. *Shock (Augusta, Ga)*. 2016;45:88-97.  
560 doi:10.1097/SHK.0000000000000478
- 561 30. Marko L, Szijarto IA, Filipovic MR, et al. Role of Cystathionine Gamma-Lyase in Immediate  
562 Renal Impairment and Inflammatory Response in Acute Ischemic Kidney Injury. *Sci Rep*. Jun 8  
563 2016;6:27517. doi:10.1038/srep27517
- 564 31. Beard RS, Jr., Bearden SE. Vascular complications of cystathionine beta-synthase deficiency:  
565 future directions for homocysteine-to-hydrogen sulfide research. *Am J Physiol Heart Circ Physiol*. Jan  
566 2011;300(1):H13-26. doi:10.1152/ajpheart.00598.2010
- 567 32. Jurkowska H, Kaczor-Kaminska M, Bronowicka-Adamska P, Wrobel M. [Cystathionine gamma-  
568 lyase]. *Postepy Hig Med Dosw (Online)*. Jan 15 2014;68:1-9. gamma-Liaza cystationinowa.  
569 doi:10.5604/17322693.1085372
- 570 33. Liu X, Luo F, Li J, Wu W, Li L, Chen H. Homocysteine induces connective tissue growth factor  
571 expression in vascular smooth muscle cells. *J Thromb Haemost*. Jan 2008;6(1):184-92.  
572 doi:10.1111/j.1538-7836.2007.02801.x
- 573 34. Valentijn FA, Knoppert SN, Marquez-Exposito L, et al. Cellular communication network 2  
574 (connective tissue growth factor) aggravates acute DNA damage and subsequent DNA damage  
575 response-senescence-fibrosis following kidney ischemia reperfusion injury. *Kidney Int*. Jul 31  
576 2022;doi:10.1016/j.kint.2022.06.030



- 577 35. Li X, Du J, Jin H, Geng B, Tang C. Sodium hydrosulfide alleviates pulmonary artery collagen  
578 remodeling in rats with high pulmonary blood flow. *Heart Vessels*. Nov 2008;23(6):409-19.  
579 doi:10.1007/s00380-008-1059-4
- 580 36. Macabrey D, Deslarzes-Dubuis C, Longchamp A, et al. Hydrogen Sulphide Release via the  
581 Angiotensin Converting Enzyme Inhibitor Zofenopril Prevents Intimal Hyperplasia in Human Vein  
582 Segments and in a Mouse Model of Carotid Artery Stenosis. *Eur J Vasc Endovasc Surg*. Feb  
583 2022;63(2):336-346. doi:10.1016/j.ejvs.2021.09.032
- 584 37. Macabrey D, Longchamp A, MacArthur MR, et al. Sodium thiosulfate acts as a hydrogen sulfide  
585 mimetic to prevent intimal hyperplasia via inhibition of tubulin polymerisation. *EBioMedicine*. Apr  
586 2022;78:103954. doi:10.1016/j.ebiom.2022.103954
- 587 38. Hine C, Kim HJ, Zhu Y, et al. Hypothalamic-Pituitary Axis Regulates Hydrogen Sulfide  
588 Production. *Cell Metab*. Jun 6 2017;25(6):1320-1333 e5. doi:10.1016/j.cmet.2017.05.003
- 589 39. Bithi N, Link C, Henderson YO, et al. Dietary restriction transforms the mammalian protein  
590 persulfidome in a tissue-specific and cystathionine gamma-lyase-dependent manner. *Nat Commun*.  
591 Mar 19 2021;12(1):1745. doi:10.1038/s41467-021-22001-w  
592